
**Geology, Geochemistry and Metallogenesis of Selected
Sediment-hosted Gold Deposits in the Central Gold
Belt, Peninsular Malaysia**

Charles Makoundi

MSc



**A research thesis submitted in partial fulfillment of the
requirements for the degree of Master of Science**



**School of Earth Sciences, CODES Centre of Excellence in Ore
Deposits, University of Tasmania**

April 2012

Abstract

The Tersang, Selinsing, and Penjom gold deposits are located at the east of the Bentong-Raub Suture Zone in the State of Pahang, Central Malaysia. The Tersang gold deposit is hosted in sandstone, breccia and felsic rhyolite of probably Triassic in age. LA ICP-MS U-Pb zircon dating of the host sandstone at Tersang indicates a possible age that ranges from ca.319 Ma to ca.219 Ma. However, the age of the sandstone could be as young as Upper Triassic. The alkali rhyolite, which intruded the host sandstone sequence, yielded a Late Triassic age of 218.8 ± 1.7 Ma. Structural and textural investigation has shown two sets of NNW-SSE and ESE-WNW oriented mineralised veins at Tersang and ore minerals include pyrite, arsenopyrite, sphalerite, galena, geocronite [$\text{Pb}_{14}(\text{Sb}, \text{As})_6\text{S}_{23}$], covellite, and gold. Normalised quantitative analysis of gold grains in veins indicates two generations: high fineness gold (959 to 965) and low fineness gold (769 to 792). The argillic alteration is dominant in the Tersang deposit and characterised by an assemblage of sericite, illite, and montmorillonite.

Detailed paragenetic studies at Tersang revealed four pyrite types including euhedral to subhedral “spongy” pyrite with internal fracturing (pyrite 1), euhedral clean pyrite (pyrite 2) overgrown on pyrite 1, amorphous pyrite with high As and high Au (pyrite 3), crack-fill or vein pyrite with high As and low Au (pyrite 4). LA ICP-MS analysis of different pyrite types indicates that they are enriched in Au, As, Zn, Ni, Co, Sb, Tl, Se and depleted in Cu, Ag, Te, V, Bi, and Ag. Pyrite 1 and Pyrite 3 are particularly enriched in Au, As, Co, Ni, Se, and Tl. Pyrite 1 and pyrite 2 show zoning of

Co, Ni, As, and Se and they have low Ag/Au, and Ni/Co ratios indicating that these pyrites are likely of metamorphic origin.

Sulphur isotope composition of pyrite, arsenopyrite and galena has a range of $\delta^{34}\text{S}$ values from -6 to 2.5 ‰ at Tersang. Additionally, these sulphide minerals are associated with primary hematite indicating that the sulphur may have been derived from the oxidation of a magmatic hydrothermal fluid at Tersang. The Tersang ores contain lead isotope ratios of 18.59 for $\text{Pb}^{206}/\text{Pb}^{204}$ and 15.75 for $\text{Pb}^{207}/\text{Pb}^{204}$ suggesting that lead was probably derived from the lower crust source rocks. At Tersang, fluid-inclusion studies yielded a homogenisation temperature range from 210 to 348 °C with salinities between 2.41 and 8.95 wt % NaCl equiv. indicating magmatic input due to relatively high salinity. Laser Raman Spectrometry analysis indicates the presence of CO_2 (98.1 to 100 mol %) in fluids with a minor amount of CH_4 (0 to 1.9 mol %).

In comparison, the Selinsing gold deposit is hosted by phyllite, siltstone, cataclasite, mylonite and argillite units of probably Triassic in age. LA ICP-MS U-Pb zircon dating of the host siltstone indicated a maximum Carboniferous age between 324.1 ± 3.5 and 346 ± 6 Ma. Structural and paragenetic studies of quartz veins revealed two vein generations: NS-oriented early veins and NNW-SSE-trending pinch and swell structures formed during D2 extensional regime and later brecciated veins, which resulted from D3 compressional regime.

At Selinsing, ore minerals consist of pyrite, arsenopyrite, galena, sphalerite, chalcopyrite, pyrrhotite and gold. Metal distribution in drill holes shows that economic mineralisation is mostly found in cataclasite and breccia units suggesting a structural control on gold mineralisation. The host sequences are altered to quartz-ankerite

alteration in the high-grade zones in the catalasite units. However, sericite and illite alteration is present in phyllite and siltstone units. Detailed textural and chemical studies revealed seven pyrite types, which include framboidal pyrite (pyrite 1), rounded recrystallised pyrite (pyrite 2), euhedral clean pyrite (pyrite 3), euhedral to subhedral with inclusions (pyrite 4), overgrown pyrite (pyrite 5), euhedral to subhedral overgrown pyrite (pyrite 6), and euhedral overgrown on pyrite 6 (pyrite 7).

LA ICP-MS analysis of the pyrite types indicates that they are enriched in Au, Pb, As, Zn, Ni, Co, and Sb and depleted in Mo, Te, V, Bi, and Ag relative to the Tersang pyrites. Pyrite 1 and pyrite 2 have almost the same trace element assemblages. Compared to pyrite 1, pyrite 2 shows slight enrichment in Bi, Te, and Se and depletion in Co and Mo. However, Pyrite 3 and pyrite 6 are particularly enriched in Au, As, Cu and Ni, whereas pyrite 7 is enriched in Pb and Mo. Sulphur isotope composition of ores from the Selinsing deposit ranges from 1.5 to 9.2 ‰. In addition, Pb isotope values of pyrite range from 18.94 to 19.10 for Pb^{206}/Pb^{204} and from 15.72 to 15.73 for Pb^{207}/Pb^{204} suggesting a high uranium source rock of the lead. Fluid-inclusion in quartz at Selinsing yielded a homogenisation temperature range from 194 to 348 °C and salinities between 1.23 and 9.98 wt % NaCl equiv. Similar to Tersang, Laser Raman Spectrometric analysis revealed CO₂-rich (95 to 100 mol %) inclusions with minor amount of N₂ (0 to 5 mol %).

A limited study was undertaken at the Penjom gold deposit. This deposit is hosted in Permian tuffaceous siltstone, carbonaceous shale, and tuffaceous conglomerate sequence that is intruded by rhyodacitic and trachyandesitic igneous rocks. LA ICP-MS U-Pb zircon dating of the host tuffaceous siltstone and tuffaceous breccia indicated ages ranging from 264.9 ± 2.6 to 259.8 ± 4.9 Ma (Permian). Gold mineralisation occurs in

carbonate-rich zones hosted within dilated quartz veins, which contain disseminated pyrite and arsenopyrite. These veins are found in NS and NE trending shears which dip 60-75° to the east. Sulphur isotope composition at the Penjom deposit ranges from -8.4 to -3.9 ‰. The Pb isotope composition from galena ranges from 18.54 to 18.57 for Pb^{206}/Pb^{204} and 15.70 for Pb^{207}/Pb^{204} . This Pb isotopic signature is less radiogenic indicating a lower crust source rock. Fluid inclusion studies at Penjom yielded a homogenisation temperature range from 260 to 300 °C and salinities between 6.30 and 8.68 wt % NaCl equiv.

The geological, structural, geochemical and isotopic data together with mineral paragenesis, pyrite chemistry and ore fluid characteristics of the Tersang, Selinsing and Penjom gold deposits indicate that they are comparable to Bendigo and Meguma type deposits. The geochemical and isotopic evidence also suggests that the ore fluids have been predominantly derived from a mixture of magmatic and metamorphic sources with a minor meteoric fluid. The ore fluids ascended and deposited in structurally favorable traps, such as shear zones, saddle reefs, and fold hinges during metamorphism and deformation. The source of Au is still conjectural; however, LA ICP-MS pyrite geochemistry indicates multiple stages of Au enrichment and remobilisation from diagenetic conditions. The enrichment of VAMSNZ (V, As, Mo, Se, Ni, Ag and Zn) metals implies a possibility of diagenetic origin of the gold. Pyrite chemistry, alteration, Pb isotopes and structural setting at Tersang, Selinsing, and Penjom provide exploration guides. Elements such as As, Sb, Pb, Ag, Co, Ni, Tl, Te, Se, Zn, Mo, U and V occurring together with Au can be used as pathfinders and vectoring tools. Occurrences of quartz-ankerite and quartz-illite-chlorite alteration assemblages are also indicative of potentially

Au enriched geological terrains. Additionally, Pb isotope ratios for $\text{Pb}^{206}/\text{Pb}^{204}$ that varies from 15.72 to 19.10 are useful geochemical criteria to search for gold.

Declaration of Originality

This thesis contains no information that has been accepted for the award of any other degree or diploma in any tertiary institution around the world. To the best of my knowledge and belief, it contains no material pre-published or written by another individual, apart from due reference made in the text of the paper.

Signed

Charles Makoundi
B.Sc. M.Sc (UMNG), M.Sc (UM)
(April, 2012)

Authority of access

This thesis may be made available for loan and limited copying in accordance with the Copyright Act 1968.

Signed

Charles Makoundi
B.Sc. M.Sc (UMNG), M.Sc (UM)
(April, 2012)

TABLE OF CONTENTS

ABSTRACT.....	ii
DECLARATION.....	vi
CONTENTS.....	vii
LIST OF FIGURES.....	xi
LIST OF TABLES.....	xviii
ACKNOWLEDGEMENTS.....	xx

Chapter 1: Introduction

1.1 Prelude.....	1
1.2 Location, topography and climate.....	1
1.3 Exploration and mining history.....	3
1.4 Aims.....	6
1.5 Thesis organisation.....	7

Chapter 2: Tectonic and district-scale setting

2.1 Introduction.....	10
2.2 Tectonic setting.....	10
2.2.1 Sibumasu terrane.....	11
2.2.2 Indochina, South China and East Malaya terranes.....	12
2.2.3 West Sumatra terrane.....	13
2.2.4 West Burma terrane and the Mogok belt.....	13
2.2.5 Woyla terrane.....	14
2.2.6 Medial Sumatra Tectonic Zone (MSTZ).....	14
2.2.7 Bentong-Raub Suture Zone.....	14
2.3 Metallogenic belts of Malaysia.....	18
2.3.1 The Western tin belt.....	18
2.3.2 The Central gold belt.....	18
2.3.3 The Eastern tin belt.....	20
2.4 District-scale geology.....	21

Chapter 3: Local geology and geochronology

3.1 Introduction.....	25
3.2 Methods of study.....	25
3.2.1 Fieldwork.....	25
3.2.2 Laboratory methods.....	27
3.3 Geology of the Tersang deposit.....	30
3.3.1 Sandstone unit.....	30
3.3.2 Felsic intrusion unit.....	30
3.3.3 Breccia unit.....	34
3.4 Geology of the Selinsing deposit.....	34
3.4.1 Phyllite unit.....	34
3.4.2 Siltstone unit.....	37
3.4.3 Fault-related rocks.....	37

3.4.3.1 Cataclasite unit.....	37
3.4.3.2 Mylonite unit.....	37
3.4.4 Argillite unit.....	38
3.4.5 Limestone unit.....	38
3.5 Geometry of the Selinsing orebody.....	40
3.6 Geology of the Penjom deposit.....	43
3.6.1 Tuffaceous siltstone unit.....	43
3.6.2 Intrusion unit.....	43
3.6.3 Carbonaceous shale unit.....	44
3.6.4 Tuffaceous conglomerate unit.....	44
3.7 Age of host rocks.....	49
3.8 Geochemical classification of intrusive rocks.....	54
3.9 Discussion.....	55
3.10 Conclusion.....	56

Chapter 4: Structural setting

4.1 Introduction.....	57
4.2 Geometry of vein sets at Tersang.....	57
4.3 Selinsing.....	60
4.3.1 Surface structures.....	60
4.3.2 Subsurface structures.....	63
4.4 Vein paragenesis at Tersang and Selinsing.....	64
4.4.1 Vein paragenesis at Tersang.....	64
4.4.2 Vein paragenesis at Selinsing.....	66
4.5 Deformational history at Selinsing.....	69
4.6 Discussion.....	72

Chapter 5: Mineralogy, alteration, paragenesis and metal distribution

5.1 Introduction.....	75
5.2 Methods of study.....	75
5.3 Alteration.....	77
5.3.1 Tersang deposit.....	77
5.3.2 Selinsing deposit.....	78
5.4 Ore mineralogy and paragenesis at Tersang deposit.....	80
5.4.1 Pyrite.....	80
5.4.1.1 Euhedral to subhedral spongy pyrite (pyrite 1).....	82
5.4.1.2 Euhedral overgrown/clean pyrite (pyrite 2).....	82
5.4.1.3 Vein and intrusion hosted pyrite (pyrite 1 and pyrite 2).....	82
5.4.1.4 Amorphous pyrite (pyrite 3) and fracture-filled (pyrite 4).....	84
5.4.2 Gold.....	84
5.4.2.1 Gold in vein.....	84
5.4.2.2 Alluvial gold.....	88
5.4.3 Arsenopyrite.....	90
5.4.4 Sphalerite.....	92
5.4.5 Galena.....	92
5.4.6 Geochronite.....	92

5.4.7 Covellite.....	92
5.4.8 Ilmenite and rutile.....	93
5.4.9 Hematite.....	93
5.5 Ore mineralogy and paragenesis at the Selinsing deposit.....	95
5.5.1 Pyrite.....	95
5.5.1.1 Framboidal pyrite (pyrite 1).....	95
5.5.1.2 Recrystallised pyrite (pyrite 2).....	98
5.5.1.3 Euhedral clean pyrite (pyrite 3).....	98
5.5.1.4 Composite pyrites.....	98
5.5.2 Arsenopyrite and galena.....	99
5.5.3 Sphalerite and chalcopyrite.....	101
5.5.4 Pyrrhotite.....	101
5.5.5 Gold.....	102
5.5.6 Hematite and rutile.....	102
5.5.7 Chlorite.....	105
5.6 Metal distribution.....	105
5.7 Discussion.....	112
5.8 Conclusions.....	115

Chapter 6: Pyrite geochemistry

6.1 Introduction.....	116
6.2 Method of study.....	116
6.3 Processing of trace element maps.....	117
6.4 Pyrite geochemistry at the Tersang gold deposit.....	118
6.4.1 Pyrite trace element mapping at Tersang.....	118
6.4.2 Trace element distribution at Tersang.....	125
6.5 Pyrite geochemistry at the Selinsing gold deposit.....	128
6.5.1 Trace element distribution at Selinsing.....	136
6.6 Comparative trace element distribution at Tersang and Selinsing.....	141
6.7 Discussion.....	146
6.8 Conclusions.....	148

Chapter 7: Sulphur and lead isotopes

7.1 Introduction.....	149
7.2 Sulphur isotopes.....	149
7.2.1 Previous studies.....	150
7.2.2 Methods.....	150
7.2.3 Sulphur isotope compositions.....	151
7.2.3.1 Tersang.....	151
7.2.3.2 Selinsing.....	151
7.2.3.3 Penjom.....	154
7.2.4 Discussion.....	154
7.3 Lead isotopes.....	158
7.3.1 Methods.....	158

7.3.2 Lead isotope compositions.....	159
7.3.3 Discussion.....	162

Chapter 8: Fluid inclusions

8.1 Introduction.....	164
8.2 Methodology.....	164
8.2.1 Microthermometric method.....	165
8.2.2 Laser Raman Spectrometry method.....	166
8.3 Inclusion petrography.....	167
8.4 Microthermometric results.....	171
8.5 Laser Raman results.....	177
8.6 Discussion.....	179

Chapter 9: Discussion, Genetic models and Exploration implications

9.1 Introduction.....	186
9.2 Summary of results.....	186
9.2.1 Geological setting.....	186
9.2.2 Structural setting.....	187
9.2.3 Alteration and ore minerals.....	188
9.2.4 Pyrite chemistry.....	189
9.2.5 Sulphur isotopes.....	190
9.2.6 Pb isotopes.....	191
9.2.7 Fluid characteristics.....	191
9.3 Ore deposit models.....	192
9.3.1 Tersang deposit model.....	192
9.3.2 Selinsing deposit model.....	196
9.3.3 Penjom deposit model.....	198
9.4 Exploration implications.....	200

References.....	202
------------------------	------------

Appendix A: Rock catalogue

Appendix B: X-ray fluorescence (XRF)

Appendix C: LA ICP-MS data

Appendix D: Statistical analysis of gold in pyrite and silicates

LIST OF FIGURES

Chapter I

- 1.1 Location of the Tersang, Selinsing and Penjom gold deposits in mainland Southeast Asia.....2
- 1.2 Location of gold deposits in the State of Pahang, Peninsular Malaysia.....4

Chapter II

- 2.1 Distribution of continental blocks and suture zones in Southeast Asia region. ...11
- 2.2 Hypothetical plate tectonic reconstruction of the distribution of the continents between 280 and 210 million years ago.....16
- 2.3 Cross-section illustrating plate tectonic evolution of the Malay Peninsular and Singapore.....17
- 2.4 Map of the metallogenic belts of Peninsular Malaysia.....19
- 2.5 District-scale geological map showing location of the gold deposits, Central Malaysia.....22

Chapter III

- 3.1 Geological map of the Tersang gold deposit showing the main lithologic units.....31
- 3.2 Field view and outcrop photographs at Tersang.....32
- 3.3 Lithological characteristics of Host rock and intrusion at the Tersang gold deposit.....33
- 3.4 Geological map of the Selinsing gold deposit showing the main lithologies, Central Malaysia.....35
- 3.5 Lithological characteristics of host sequence at the Selinsing gold deposit.....36
- 3.6 Lithological characteristics of host sequence and limestones at the Selinsing gold deposit.....39
- 3.7 Characteristics of the orebody at the Selinsing gold deposit.41

3.8	Cross-sections across the Selinsing deposit site.....	41
3.9	Main cross-section of the Selinsing gold deposit.....	42
3.10	Geological map of the Penjom gold deposit.....	45
3.11	Lithological and textural characteristics of Host rocks and intrusion at the Penjom gold deposit.....	46
3.12	Lithological and textural characteristics of tuffaceous conglomerate at Penjom, Central Malaysia.....	47
3.13	Field view and outcrop photographs at Penjom, Central Malaysia.....	48
3.14	Age of the host sandstone at the Tersang gold deposit.....	50
3.15	Age of felsic intrusion at the Tersang gold deposit Central Malaysia.....	51
3.16	Age of Host rock at the Selinsing gold deposit.....	52
3.17	Age of the host tuffaceous conglomerate at Penjom.....	53
3.18	Age of the host tuffaceous siltstone at Penjom.....	53
3.19	Zr/Ti and Nb/Y discrimination diagram for the Tersang and Penjom intrusive rocks, Central Malaysia.....	54

Chapter IV

4.1	Structural features of Host rock and vein assemblages at Tersang gold deposit.....	58
4.2	Structural setting at Tersang.....	59
4.3	Structural features of Host rock at the Selinsing gold deposit.....	61
4.4	Structural features of Host rock and vein assemblages at the Selinsing gold deposit.....	62
4.5	Structural features of barren quartz veins at the Selinsing Gold deposit.....	63
4.6	Vein stages at the Tersang gold deposit.....	65

4.7	Vein stages at the Selinsing gold deposit.....	67
4.8	Shear sense characteristics at the Selinsing gold deposit.....	68
4.9	Structural map of the Selinsing gold deposit.....	71
4.10	Gold mineralisation at the Selinsing gold deposit.....	73
4.11	Gold mineralisation at the Selinsing gold deposit.....	74

Chapter V

5.1	Alteration mineral assemblages at the Tersang gold deposit.....	78
5.2	Alteration assemblages at the Selinsing gold deposit.....	79
5.3	Textural characteristics of different types of pyrite at the Tersang gold deposit.....	83
5.4	Gold occurrence at the Tersang deposit.....	85
5.5	Gold occurrence at the Tersang deposit	86
5.6	Gold occurrence at the Tersang deposit.....	87
5.7	SEM images showing morphology of alluvial gold grains at the Tersang deposit.....	89
5.8	Ore minerals at the Tersang deposit.....	91
5.9	Back-scattered electron images of ore and gangue minerals at the Tersang gold deposit.....	94
5.10	Textural characteristics of pyrite at the Selinsing gold deposit.....	97
5.11	Ore minerals at the Selinsing deposit.....	100
5.12	Gold occurrence at the Selinsing gold deposit.....	103
5.13	Ore and gangue minerals at the Selinsing deposit.....	104
5.14	Lithologic log of the drillhole SEL-DD0001.....	107
5.15	Lithologic log of the drillhole SEL-DD0002.....	108

5.16	Lithologic log of the drillhole SEL-DD0003.....	109
5.17	Lithologic log of the drillhole SEL-DD0007	110
5.18	Lithologic log of the drillhole SEL-DD0009.....	111
5.19	Binary plot of Au and Ag contents in vein and alluvial gold grains at the Tersang deposit.....	113

Chapter VI

6.1	LA-ICPMS images of trace elements in pyrite 1 and pyrite 2 (Sample No. TER-R007) at the Tersang gold deposit.....	119
6.2	LA-ICPMS images of trace elements in vein-hosted pyrite 1 (Sample No. TER-R039) at the Tersang gold deposit.....	120
6.3	LA-ICPMS images of trace elements in wallrock-hosted pyrite 1 and pyrite 2 (Sample No. TER-R007B) at the Tersang gold deposit.....	121
6.4	LA-ICPMS images of trace elements intrusion-hosted pyrite (pyrite 2) (Sample No. TER-R033) at the Tersang gold deposit.....	122
6.5	LA-ICPMS images of trace elements in pyrite 1, pyrite 3 and pyrite 4 (Sample No. TER-R007B) at the Tersang gold deposit.....	123
6.6	Attribute map of pyrite grains and gold solubility diagram at Tersang.....	124
6.7	Periodic table of chemical elements.....	125
6.8	Normalised quantitative analysis of trace elements for all pyrite types at the Tersang gold deposit, Central Malaysia.....	126
6.9	Trace element ratios at the Tersang gold deposit.....	127
6.10	Framboidal pyrite textures and LA ICP-MS spot analysis at Selinsing.....	129
6.11	LA-ICPMS images of trace elements in pyrite 3 (Sample No. SEL-R039) at the Selinsing deposit.....	130
6.12	LA-ICPMS images of trace elements in pyrite 4, pyrite 5, and pyrite 6 (Sample No. SEL-R006) at the Selinsing deposit.....	131
6.13	LA-ICPMS images of trace elements in pyrite 5, pyrite 6 (Sample No. SEL-R006) at the Selinsing gold deposit, Central Malaysia.....	132

6.14	LA-ICPMS images of trace element of zoned hydrothermal Pyrites (pyrite 4, pyrite 5, pyrite 6, and pyrite 7) at the Selinsing gold deposit.....	133
6.15	LA-ICPMS images of trace elements in pyrite 4 and pyrite 5 (Sample No. SEL-R054C) at the Selinsing gold deposit, Central Malaysia.....	134
6.16	LA-ICPMS images of trace elements in pyrite 4 and pyrite 5 (Sample No. SEL-R009) in black shale at the Selinsing gold deposit.....	135
6.17	Attribute map of pyrite grains and gold solubility diagram at Selinsing.....	136
6.18	Normalised quantitative analysis of trace elements for all pyrite types at the Selinsing gold deposit.....	137
6.19	Normalised quantitative analysis of framboidal pyrites (pyrite 1 and pyrite 2) at the Selinsing gold deposit, Central Malaysia.....	137
6.20	Binary plot of Au against Bi (A) and Te (B) in all pyrite types at the Selinsing gold deposit, Central Malaysia.....	138
6.21	Ratio of trace elements at the Selinsing gold deposit, Central Malaysia.....	139
6.22	Line ablation line across pyrite 4 and pyrite 5 at the Selinsing gold deposit.....	140
6.23	Box plots showing mean concentrations of Au, Co, and Ni in pyrite for both the Tersang and Selinsing gold deposit.....	141
6.24	Box plots showing mean concentrations of Cu, Zn, and Se in pyrite for both the Tersang and Selinsing gold deposits.....	142
6.25	Box plots showing mean concentrations of Sb, Tl, and Pb in pyrite for both the Tersang and Selinsing gold deposits.....	143
6.26	Box plots showing mean concentrations of Bi, Ti, and Ag in pyrite for both the Tersang and Selinsing gold deposits.....	144
6.27	Point density maps of main Au-As concentration	145

Chapter VII

7.1	Histograms showing the $\delta^{34}\text{S}$ compositions of sulphides from the Tersang, Selinsing and Penjom deposits, Malaysia.....	153
7.2	Sulphur isotope composition at the Tersang, Selinsing and Penjom deposits, Central Malaysia.....	156
7.3	Pb isotope ratio for pyrites from the Selinsing, Tersang and Penjom gold deposits, Malaysia.....	161
7.4	Plot of lead isotopic compositions for $\text{Pb}^{208}/\text{Pb}^{204}$ versus $\text{Pb}^{206}/\text{Pb}^{204}$ from the Tersang, Selinsing, and Penjom deposit.....	161
7.5	Pb isotope compositions for $\text{Pb}^{207}/\text{Pb}^{204}$ versus $\text{Pb}^{206}/\text{Pb}^{204}$ for the Tersang, Selinsing, and Penjom deposits, Central Malaysia.....	162

Chapter VIII

8.1	Photomicrographs of fluid inclusions at the Tersang gold deposit, Central Malaysia.....	168
8.2	Photomicrographs of fluid inclusions in quartz veins at the Selinsing gold deposit.....	169
8.3	Photomicrographs of fluid inclusions at the Penjom gold deposit, Central Malaysia.....	170
8.4	Histogram of homogenisation temperature of Type I inclusions at the Tersang gold deposit, Central Malaysia.....	174
8.5	Histogram of salinities of Type I inclusions at the Tersang gold deposit, Central Malaysia.....	174
8.6	Histogram of homogenisation temperature of Type I inclusions at the Selinsing gold deposit, Central Malaysia.....	175
8.7	Histogram of salinities of Type I inclusions at the Selinsing gold deposit, Central Malaysia.....	175
8.8	Histograms of homogenisation temperature at the Penjom gold deposit, Central Malaysia.....	176
8.9	Histogram of salinities for the Type III fluid inclusions from the Penjom gold deposit, Central Malaysia.....	177

8.10	Plot of molar percent of H ₂ O against homogenisation temperature at the Tersang gold deposit.....	181
8.11	Plot of molar percent of H ₂ O against homogenisation temperature at the Selinsing gold deposit.....	181
8.12	Plot of molar percent of H ₂ O against homogenisation temperature at the Penjom gold deposit.....	182
8.13	Plot of homogenisation temperatures and salinities for the Tersang, Selinsing and Penjom deposit, Central Malaysia.....	184

Chapter IX

9.1	Cartoon showing a simplified ore deposit model of the Tersang gold deposit, Malaysia.....	195
9.2	A two-stage genetic model of the Selinsing gold deposit, Central Malaysia.....	197
9.3	Deposit model of the Penjom gold deposit, Central Malaysia	199

LIST OF TABLES

Chapter IV

- 4.1 Deformation history at the Selinsing gold deposit, Central Malaysia.....70

Chapter V

- 5.1 Mineral paragenesis at the Tersang gold deposit, Central Malaysia.....81
- 5.2 Normalised quantitative analysis of gold in veins at Tersang.....88
- 5.3 Normalised quantitative analysis of alluvial gold at Tersang.....90
- 5.4 Mineral paragenesis at the Selinsing gold deposit, Central Malaysia.....96

Chapter VII

- 7.1 Sulphur isotope composition for the Tersang, Selinsing, and Penjom deposits...152
- 7.2 Lead isotope composition for the Selinsing, Tersang, and Penjom deposits.....159

Chapter VIII

- 8.1 Summary of homogenization temperature and salinity at the Selinsing, Tersang, and Penjom deposits.....172
- 8.2 Laser Raman Spectrometry Results for the Tersang gold deposit.....178
- 8.3 Laser Raman Spectrometry Results for the Selinsing gold deposit.....178
- 8.4 Laser Raman Spectrometry Results for the Penjom gold deposit.....179

Chapter IX

- 9.1 Comparison of the Selinsing, Tersang, and Penjom Au deposits in Central Malaysia.....193
- 9.2. Comparison of the gold deposits in Malaysia with other deposits.....194

ACKNOWLEDGMENTS

Special thanks to my supervisor Assoc. Prof. Dr. Khin Zaw, who tirelessly guided me right from choosing the research project and methods for my research, from the data collection to writing and completion of this thesis. I also strongly thank him for his advice and constructive criticism during my study. In my weak moments, he motivated me to keep going and be strong regardless of what I could face. He also taught me to be consistent in the process of tidying up my thesis. I had many fruitful discussions with my co-supervisor Prof. R.R. Large, in particular on pyrite geochemistry. His ideas were a driving force that made me enjoyed writing on various aspects of pyrite chemistry.

During my field work, exploration and mine geologists of Monument Mining Ltd, Malaysia gave me a hand through sampling, sample preparation, and packaging. To these folks I am indebted. I am grateful to Mr. Zaidi Harun, Managing Director of Monument Mining Ltd Company who permitted me to carry out my project at the Selinsing gold mine.

Thanks to Dr. Teh Gua Hoe, Research Fellow at the University of Malaya, who played an important role of motivating me in the early days of my field work in Malaysia. My gratitude also goes to Dato's Andrew Kam, CEO of Peninsular Gold Ltd Company for allowing me to get access into the Tersang mine area. Thanks to the staff of Penjom gold mine for granting me permission to collect hand specimen samples at the Penjom mine-site.

I am also thankful to Dr. Sebastien Meffre who provided me with new ideas on how to write a good piece of pyrite chemistry by processing pyrite mapping data using ioGAS software. He also reviewed my research work on structural geology and

facilitated the dating of my samples. Christine Cook and Karsten Goemann at the Central Science Laboratory are thanked for the sulphur isotope conventional analysis and SEM and microprobe analysis. Many thanks to Dr. Zhaoshan Chang with whom I spent quite a bit of time on analyzing clay minerals using PIMA instrument. This study is financially supported by CODES Scholarships, Monument Mining and CODES Industry funded “Ore Deposits of SE Asia” Project.

I also thank Phil Robinson and Katie McGoldrick for their work on XRF analysis. This study was undertaken with financial and logistical support from Monument Mining Ltd, CODES Scholarships and Ore Deposits of SE Asia” Project. During my candidature at CODES, many colleagues have been a source of psychological support such as Takayuki Manaka, Matthieu Agenau, Jeff Steadman, Abhisi Salam, Mohd Basril, Kit, Yungu, and Hugo Galvan to name a few. Thanks to Christian McKenzie and his team for helping on technical issues related to information technology.

Many thanks also go to the administrative staff at CODES, University of Tasmania: Nilar Hlaing, Sarah Gilbert, Simon Stephens, Peter Cornish, Isabella von Lichtan, Christine Higgins, Karen Mollross, Deborah Macklin, Helen Scott, and Rose Pongratz.

CHAPTER 1 INTRODUCTION

1.1. Prelude

Gold deposits are widely distributed in Peninsular Malaysia. To date, these deposits have received little scientific study using modern analytical techniques, especially the nature of ore fluids, geochronology, geochemistry, mineralogy and paragenesis, and trace element concentration of pyrites to constrain the source of metal and ore-forming fluids. There were only few limited studies done by Wan Fuad and Heru (2002), Jasmi (2007), and Kamar Shah and Hewson (2007) on the compositions of sulphide minerals and host rocks.

1.2. Location, topography and climate

The research area is located at approximately 150 km north of Kuala Lumpur, the capital city of Peninsular Malaysia (Fig 1.1). It is situated between latitude 3°30' and 4°42' N, and longitude 101°30' and 103°E in the State of Pahang, Peninsular Malaysia. The study area comprises of the Tersang gold deposit, the Selinsing gold deposit, and the Penjom gold deposit. The overall topography varies from 368 to 2107 m above sea level. The western and eastern boundaries are elevated due to the presence of intrusive rocks. The central part of the area is relatively flat. A warm climate with consistent temperatures ranging from 21 °C to 32 °C is common all year long within the project area.

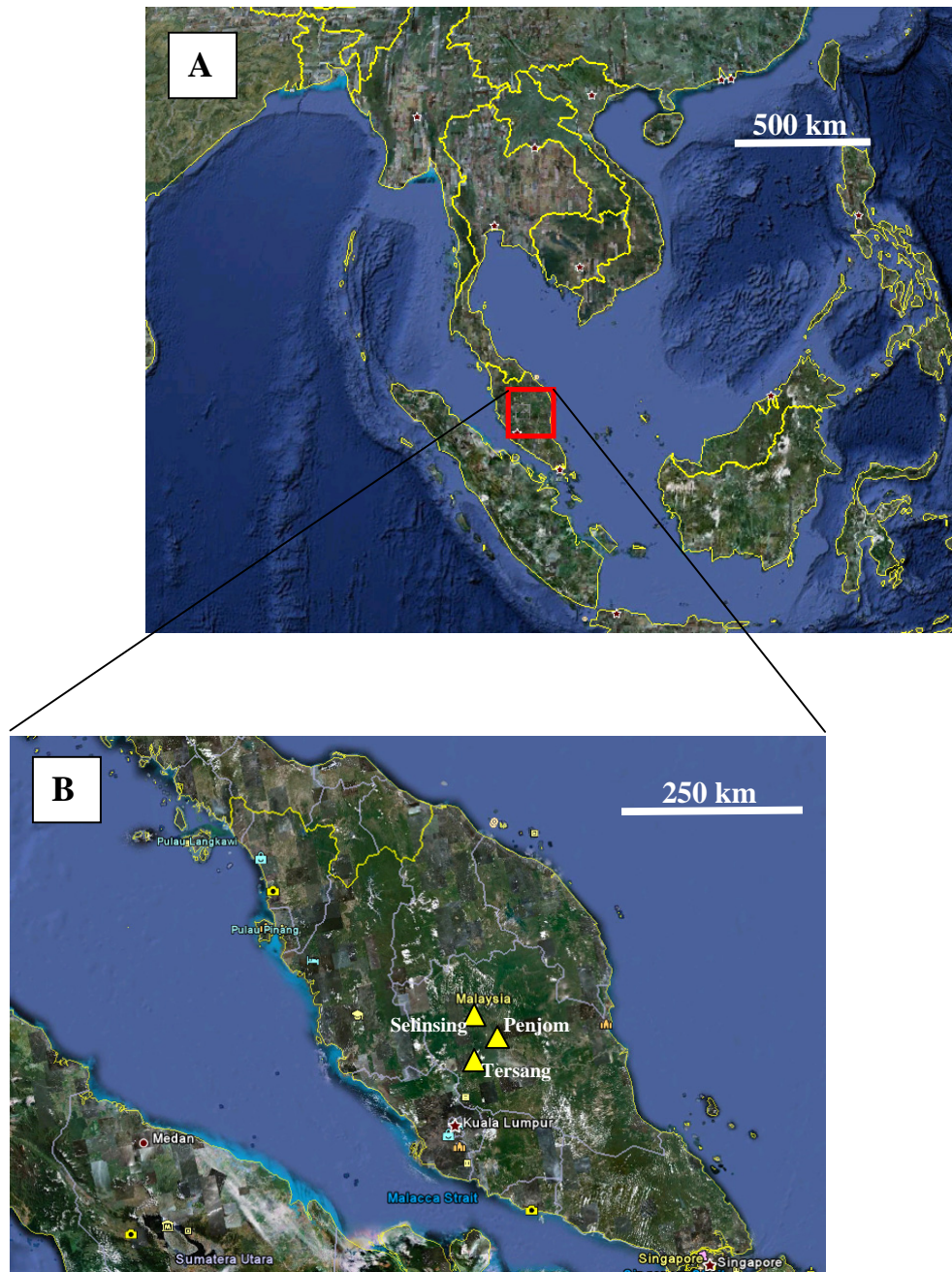


Fig. 1.1. Location of the Tersang, Selinsing and Penjom gold deposits in mainland Southeast Asia. **A.** Location of Peninsular Malaysia in Southeast Asia. **B.** Location of the Selinsing, Tersang and Penjom gold deposits in Central Malaysia (from Google Earth, 2011).

A dry and warm season occurs from January to April, whilst the wet season takes place from May to December. Yearly, rainfall varies from 2032 mm to 2540 mm with humidity between 82 to 86 %. The vegetation is characterised by tropical forests and oil palm plantation.

1.3. Exploration and mining history

Locations of the gold deposits mentioned in this thesis are shown in Fig. 1.2. In Malaysia, no records of gold production were made prior to the establishment of the British administration in the State of Pahang in 1888 (Richardson, 1949). In the Kuala Lipis area, about 50 km north of Raub Town, gold exploration and mining have been undertaken for at least a century. Between 1885 and 1941 gold was mined from both underground and open-pit workings at Kecaui, 2 km north of Kuala Lipis. Over the years, several alluvial gold occurrences have been found in Peninsular Malaysia, and more than one million ounces of gold have been recovered from them. Up to the end of 1940, most prospected areas for gold have been concentrated largely near igneous intrusions. About volume of 34,535 troy ounces of gold bullion were produced from the Selinsing Gold Mine, located south of the Buffalo Reef prospect, between 1898 and 1904 and 413 ounces were obtained in 1939 (Richardson, 1939). Between 1903 and 1904, the tailings at Selinsing Gold Mine were cyanided for a reported production of 3,535 troy ounces of gold bullion.

In January 1998, Asia Mining Services NL, a predecessor of Selinsing Mining Sdn Bhd (the present vendors to Monument), reported a revised resource estimate for the

Chapter 1: Introduction

Selinsing deposit to be 340,000 ounces from 4.8 million tonnes of tailings and open pit ore (<http://www.monumentmining.com>).

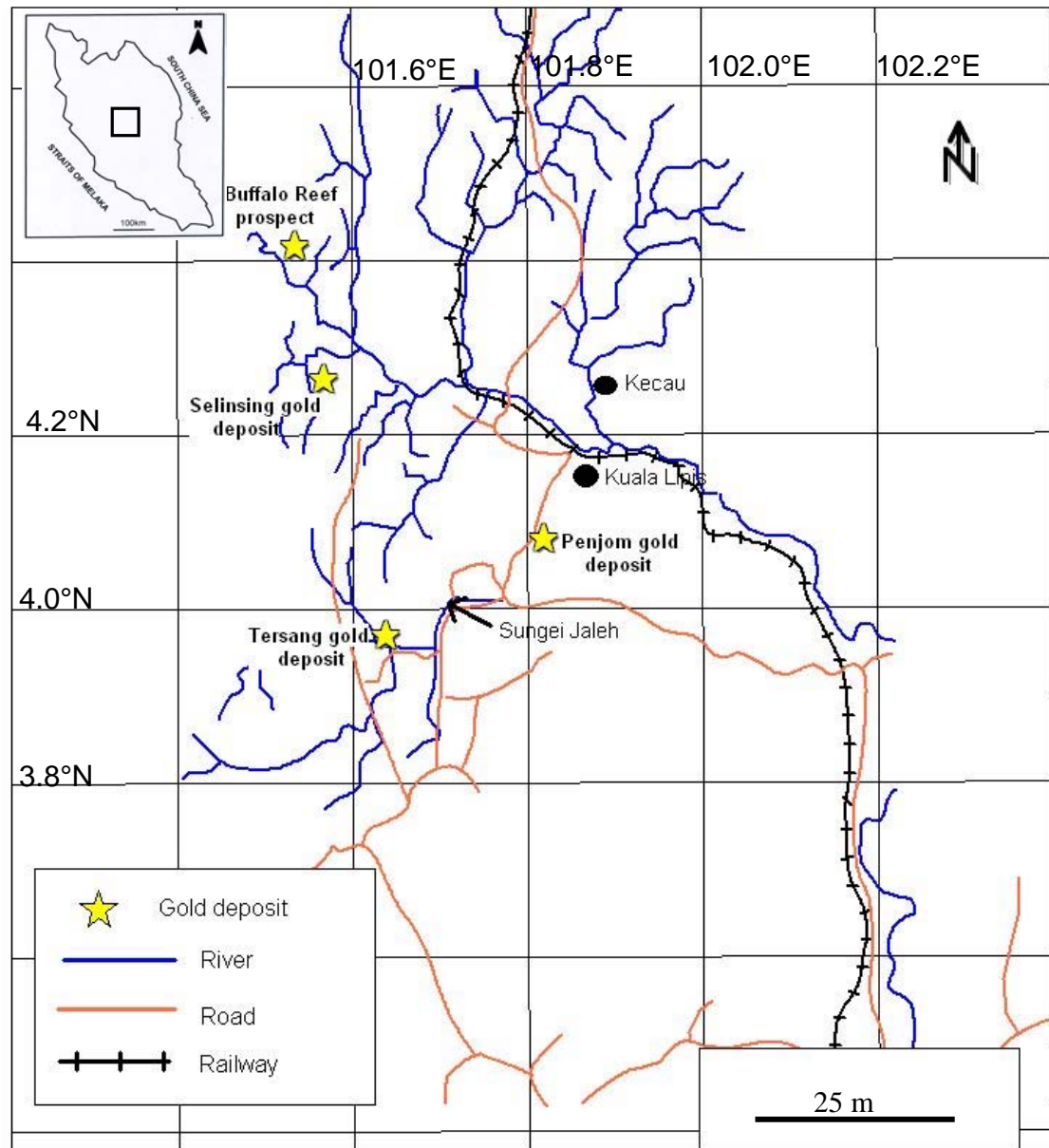


Fig. 1.2. Location of gold deposits in the State of Pahang, Peninsular Malaysia.

Chapter 1: Introduction

In 2009, open-pit mining started at the Selinsing Gold Mine. In early 2010, Monument Mining commenced the construction of the Carbon-in leach (CIL) Plant. Additionally, in 2010, Monument Mining Company has completed 165 RC drillholes for a total of about 11,880 metres at the Selinsing mine-site. From September 2010, Monument Mining drilled 22 drillholes comprising 1,000 metres of Reverse Circulation (RC) holes and 3000 metres of diamond holes.

In the early 1900's, small-scale mining had commenced in the initial exploration stage in the Buffalo Reef area at the north of the Selinsing deposit. By June 2011, Monument mining drilled 15 drillholes which comprise of 3,012 m. The results have shown significant drill intercepts (>1 g/t Au) at depth. As a result, a new resource estimate is being assessed, which would likely extend the gold resource from the existing orebody. In 1934, a British company had completed 1,000 m of underground mining in the Buffalo Reef area. In early 1993, modern exploration started in the Buffalo Reef prospect by the Company Damar Consolidated Exploration Sdn Bhd Company. In 2005, a total of 29 RC holes comprising of 3,222 m were drilled by Avocet.

Since 1886, small-scale underground and alluvial gold mining have been undertaken in the Penjom area (Proctor, 1972; Gunn et al., 1993). It is also reported that small-scale alluvial mining was carried out in the 1970's and 1980's by Banka drilling method in the Valley of Sungei Jaleh, and its tributaries. The Penjom Gold Mine started open-pit gold mining in 1996 by Avocet Mining. A reserve estimation of 3.99 million

tonnes of ore grading 3.78 g/t Au with 484100 ounces of gold were reported (Flindell, 2003, quoted in Kamar, 2007).

In 1937 at Tersang, a quantity of 70,000 cubic yards of alluvium were mined and 588.71 ounces were recovered (Richardson, 1939). It is also reported that gold bearing-quartz veins were found in quartz-muscovite rocks in the northern part of the Tersang river by a late prospector Mr. F.G.W. Dunsford (Richardson, 1939). Currently, Peninsular Gold Limited owns the Tersang gold prospect. This Company estimates that the deposit could host an inferred resource of 528,000 ounces of gold. It also claims that the deposit could host up to 1 million ounces of gold after additional exploration and drilling (<http://www.peninsulargold.com>).

1.4. Aims

The proposed research comprises of the following aims:

1. To undertake deposit-scale studies characterising local geology, mineral paragenesis, alteration patterns by surface sampling, petrographic and textural studies.
2. To study micro-structures at a local scale. This will help reveal structural deformation that affected the ore bodies and establish structural control and history of the deposits.
3. To do quantitative chemical analysis of host rocks and intrusions by using XRF.

4. To document age relationships using LA ICP-MS and U-Pb geochronology to constrain the timing of magmatism and mineralisation.
5. To undertake LA ICP-MS trace element analysis and imaging of pyrite types to constrain the source of metal and ore fluids.
6. To carry out sulphur and lead isotope and fluid-inclusions studies and discuss sources of metals and ore fluids.
7. To construct an ore deposit model of the gold deposits and discuss exploration implications.

1.5. Thesis organisation

This thesis is focused on the Tersang and Selinsing gold deposits; however geological information for the Penjom deposit from previous workers is added wherever possible to understand the nature and metallogenic relation of the gold systems in Central Malaysia. The Buffalo Reef prospect is not part of this thesis. The thesis structure comprises of the following Chapters:

- Chapter 2 documents the continental terranes or blocks and sutures of the mainland Southeast Asia including metallogenic belts of Malaysia.
- Chapter 3 provides deposit-scale geology for the Tersang, Selinsing and Penjom gold deposits. Petrographic and textural characteristics of the lithologic units of these gold deposits have been included. The ages of host rocks and intrusions have been added by using LA ICP-MS U-Pb zircon dating.

- Chapter 4 documents the structural setting of the Tersang and Selinsing gold deposits. Vein paragenesis and associated mineralisation have been described. The structural control of mineralisation and deformational history of the gold deposits were discussed.
- Chapter 5 presents the nature of mineralisation for the Tersang and Selinsing gold deposits. It also describes alteration and mineral paragenesis including gold distribution in drillholes at the Selinsing gold deposit.
- Chapter 6 documents pyrite chemistry for the Tersang and Selinsing gold deposits. In addition, this Chapter emphasizes on enrichment, depletion trends, zonation and distribution of trace elements and gold in different pyrite types.
- Chapter 7 interprets sulphur and lead isotope composition from the Tersang, Selinsing and Penjom gold deposits to infer possible sources of metals.
- Chapter 8 describes fluid inclusion petrography for both the Tersang and Selinsing gold deposits. This Chapter includes homogenisation temperatures, salinities and gas composition of ore fluids combined with fluid inclusion data from the Penjom gold deposit by previous workers.
- Chapter 9 is the synthesis of this thesis. Firstly, the Chapter summarises the main conclusions from each Chapter. Secondly, it discusses on comparison between the Tersang, Selinsing and Penjom gold deposits based on ore mineralogy, trace element associations, sulphur isotopes, age of intrusions and host rocks and fluid inclusion data. Finally, the Chapter proposes genetic models for the Tersang,

Chapter 1: Introduction

Selinsing and Penjom gold deposits and some exploration implications in terms of trace elements associated with the gold mineralisation.

CHAPTER 2

TECTONIC SETTING AND DISTRICT-SCALE GEOLOGY

2.1. INTRODUCTION

This Chapter summarizes the continental terranes or blocks, suture zones, and fold belts that make up the present tectonic framework of Southeast Asia. The terranes include Sibumasu, Indochina, East Malaya, South China, West Sumatra, West Burma and Woyla. The Bentong-Raub Suture Zone and the Medial Sumatra Tectonic Zone, which are located west of the Central gold belt of Malaysia, are also described in Figure. 2.1. In addition, the Chapter documents the metallogenic belts of Peninsular Malaysia and completes on the district-scale geology.

2.2. TECTONIC SETTING

The mainland Southeast Asia is characterised by a number of continental blocks or terranes, fold belts, and suture zones. The major continental blocks includes: Indochina, South China and Sibumasu (Fig. 2.1). The Indochina block, which forms the core of Southeast Asia, separated from Gondwana in the Late Devonian, moved northwards, driven by the expansion of Palaeo-Tethys, to collide and amalgamate with the South China Block in the Early Carboniferous (Barber and Crow, 2007). In the following sections, geological and palaeogeographic settings of these terranes will be described.

2.2.1. Sibumasu terrane

In the Permian, 280 Ma ago, Siam, Burma, Western Malaya, and Sumatra (Sibumasu) were part of the supercontinent called Gondwana.

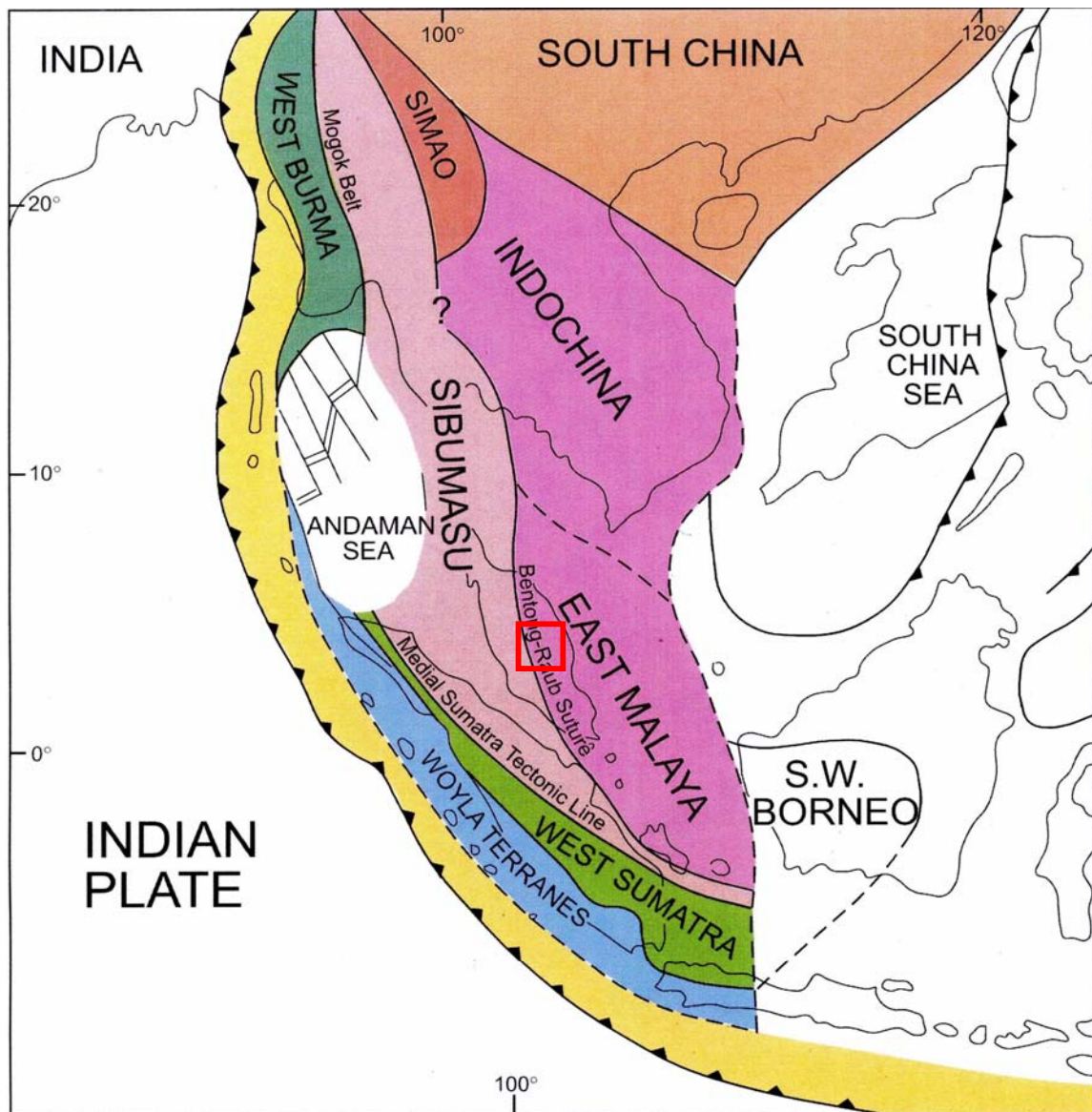


Fig. 2.1. Distribution of continental blocks and suture zones in Southeast Asia region from Barber and Crow (2007). The red square represents the study area in Central Malaysia.

This terrane is characterised by pebbly mudstones, interpreted as glaciogenic diamictites or tillites (Stauffer and Lee, 1986; Hirsch et al., 2006; Barber and Crow, 2007). These pebbly mudstones are Late Carboniferous-Early Permian in age. The Sibumasu terrane was separated from northern Gondwana during that time and a glacial environment was dominated with the opening of Mesotethys in the Early Permian.

The break-up between Sibumasu and northern Gondwana terranes gives insights to constrain the timing of rifting. Biogeographic evidence indicates that Sibumasu was attached to Gondwana until the Early Permian (Carter et al., 2001). Metcalfe (2002) later constrained this to the Sakmarian Stage, which is approximately 295-285 Ma. Barber and Crow (2007) also reported that Sibumasu moved to the north to collided and joined with the Indochina Block in the Late Permian.

2.2.2. Indochina, South China and East Malaya terranes

Metcalfe (1996, 2005) indicates that the Indochina block or terrane, which forms the core of Southeast Asia, separated from Gondwana in Late Devonian. This terrane moved to the north by the expansion of Paleotethys and collided with the South China Block in the Early Carboniferous. This block also includes the eastern part of Peninsular Malaya, or East Malaya, which hosts the Central Gold Belt. The Indochina block is characterised by a Permian flora and fauna (Barber and Crow, 2007). Carter et al. (2001) also agreed that Indochina and South China were in contact during the Middle Carboniferous on the basis of lithological, palaeobiogeographic and tectonic data.

In addition, they also argued that while the Palaeo-Tethys was closing, the Indochina-South China “super-terrane” was rotating clockwise.

2.2.3. West Sumatra terrane

The West Sumatra block or terrane is located to the west of the Sibumasu terrane and is characterised by Permian volcanic and volcanoclastic rocks. Barber and Crow (2007) indicated that a right lateral transcurrent faulting along the highly strained zone, termed the Medial Sumatra Tectonic Zone allowed the emplacement of the West Sumatra block or terrane in southern Southeast Asia. Barber and Crow (2007) also argued that the Medial Sumatra Tectonic Zone is a major shear zone that separates the Gondwana Sibumasu Block from the West Sumatra Block of derived Cathaysian origin.

2.2.4. West Burma terrane and the Mogok Belt

In Myanmar, the Mogok Belt separates the Sibumasu Block from the West Burma Block. The belt is made up of high grade metamorphic rocks, such as marbles, augen gneisses, schists and mylonite (Mitchell et al., 2007). It is argued that before the opening of the Andaman Sea in the Miocene (Curry, 2005) the West Burma Block was continuous with the West Sumatra Block (Fig. 2.1). The augen gneisses have recorded Middle Jurassic isotopic ages (Mitchell et al., 2007) and are viewed as granitic intrusions into an active shear zone. Barber and Crow (2007) have indicated that the Mogok Metamorphic Belt is the northward extension of the Medial Tectonic Zone of Sumatra.

2.2.5. Woyla terrane

In Sumatra, the West Sumatra Block is structurally overlain by the Woyla Nappe or Woyla terrane (Fig. 2.1). The Woyla terrane is characterised by a Jurassic-Cretaceous intra-oceanic island arc with fringing reefs and an associated subduction complex (Barber and Crow, 2007). Metcalfe (2005) pointed out that the Sikuleh terranes, incorporated in the Woyla Terrane and West Burma Terrane separated from Gondwana in the Late Triassic to Early Jurassic. These terranes accreted to the southwest boundary of Southeast Asia in the Mid-Cretaceous.

2.2.6. Medial Sumatra Tectonic Zone (MSTZ)

The Medial Sumatra Tectonic Zone represents the contact between the Sibumasu Block and the West Sumatra Block (Fig. 2.1). It is recognised as a zone of intensely strained rocks. This zone is composed of schists and gneisses and covers the entire length of Sumatra (Hutchison 1994; Barber and Crow 2003; Barber et al., 2005; Barber and Crow 2007). This zone is not a suture zone as it does not contain important ophiolitic components. Nevertheless, the strong deformation of the rocks points to a major shear zone. Evidence of syntectonic granitoids with a tin anomaly linked to the zone supports the view of a shear zone on a crustal scale (Stephenson et al., 1982; Barber et al., 2005).

2.2.7. Bentong-Raub Suture Zone

The Selinsing, Tersang, and Penjom are major gold deposits in Central Malaysia and they are located along the Bentong-Raub Suture Zone suture zone. Following Tjia

(1987), Metcalfe (1988) and Hutchison (1993), Wakita and Metcalfe (2005) interpreted that the Bentong-Raub Suture Zone is the boundary between Sibumasu and the East Malaya Terrane (Indochina) and represents the location of closure of the Palaeo-Tethys Ocean. This suture zone is characterised by a *mélange* zone ranging in width from 13 to 20 km (Metcalfe, 2000). This zone also hosts ribbon-bedded cherts and schists containing elongated blocks of serpentinised mafic and ultramafic rocks. Back in the Permian, 280Ma (Fig. 2.2A), Siam, Burma, Western Malaysia and Sumatra (Sibumasu) was part of the supercontinent called Gondwana, and located near NW Australia. By the Upper Triassic, 210Ma (Fig. 2.2B), Sibumasu had split from Gondwanaland, drifted across the Palaeo-Tethys Ocean and collided with Central and Eastern Malaysia along the Bentong-Raub suture zone (Fig. 2.2).

The formation of the Bentong-Raub Suture Zone is illustrated in the cross-section as shown in Fig. 2.3. The Figure 2.3A shows the drifting of Sibumasu from Gondwana. The Palaeo-Tethys Ocean was consumed under the East Malaya down a shallow dipping subduction zone. This subduction event triggered the melting of the mantle and production of granite intrusions into the crust of the Eastern granitoid Belt of Malaysia as well as volcanism. In addition, the formation of the Bentong-Raub Suture Zone was probably coeval with the emplacement of major faults that were conduits for most of mineralising fluids.

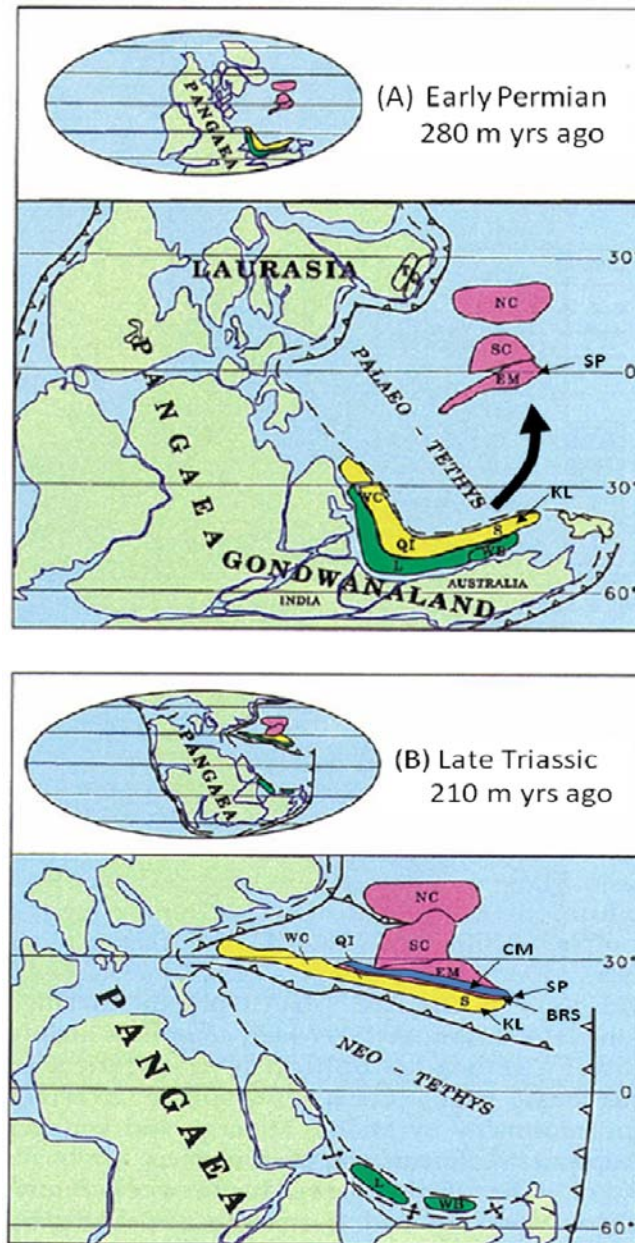


Figure 2.2. Hypothetical plate tectonic reconstruction of the distribution of the continents between 280 and 210 million years ago according to Wakita and Metcalfe (2005). Key: BRS = Bentong-Raub Suture Zone. CM = Central Malaysia. EM = Eastern Malaysia. KL = Kuala Lumpur. L = Ladak. NC = North China. QI = Qing-Tan. S = Sibumasu. SC = South China. SP = Singapore. WB = West Burma. WC = Western Cimmerian Continent.

Chapter 2: Tectonic setting and district-scale geology

The Fig. 2.3B illustrates how the Palaeo-Tethys shrunk as Sibumasu drifted towards East Malaya. This caused the steepening of the subduction zone under East Malaya forming granite plutons and volcanism in the Central Belt. In Fig. 2.3C, Sibumasu collided with East Malaya during the Upper Triassic and the subduction zone steepened further and melting occurred. Quartz veins probably formed during the Upper Triassic.

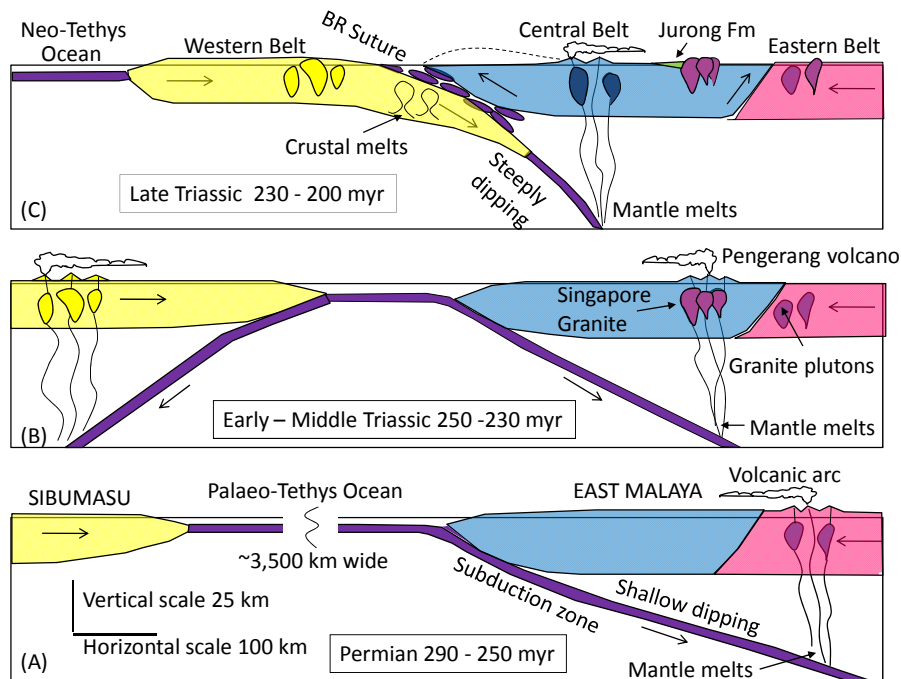


Fig. 2.3. Cross-section illustrating plate tectonic evolution of the Malay Peninsular and Singapore. Note continental plates drift across Oceans and collide with each other. BR Suture = Bentong-Raub Suture Zone. Explanation of the cross-section is given in the text (after Oliver et al., 2011)

The deep water rocks in the Palaeo-Tethys Ocean were fractured inside the Bentong-Raub Suture Zone. In addition, plutonism and volcanism progressed through time in the Central Belt of Malaysia.

2.3. METALLOGENIC BELTS OF MALAYSIA

It is widely accepted that Peninsular Malaysia comprises of three main geological domains that strike parallel to the Peninsula. Yeap (1993) defines these as the Western Tin Belt, Central Gold Belt and Eastern Tin Belt after Scrivenor (1928) (Fig. 2.4).

2.3.1 The Western Tin Belt

The Western Tin Belt occupies west of Malaysia and is characterised by Early Palaeozoic continental margin sequences, Late Palaeozoic platform carbonates, Triassic platform carbonates and deep basinal clastic sequences, and Jurassic-Cretaceous continental deposits (Fig. 2.3). The Western Tin Belts is associated with the Main Range Granitoid Province which is a large plutonic belt that extends to the southern Peninsular Thailand and central Thailand. Tin deposits are associated with these granites contributed 55% of the historic tin production of Southeast Asia (Schwartz et al., 1995).

2.3.2 The Central Gold Belt

The Central Gold Belt comprises mainly Permo-Triassic metasediments, and deep to shallow marine sedimentary rocks (Kobayashi and Tamura, 1968; Makoundi, 2004) (Fig. 2.4). This belt also contains limestones with intermediate to felsic volcanic and volcanoclastic rocks, which were deposited in a fore-arc portion of the palaeo-arc basin (Richardson, 1939; Proctor, 1972; Gobbett and Hutchison, 1973; Tan, 1984; Leman, 1994; Metcalfe, 2002).

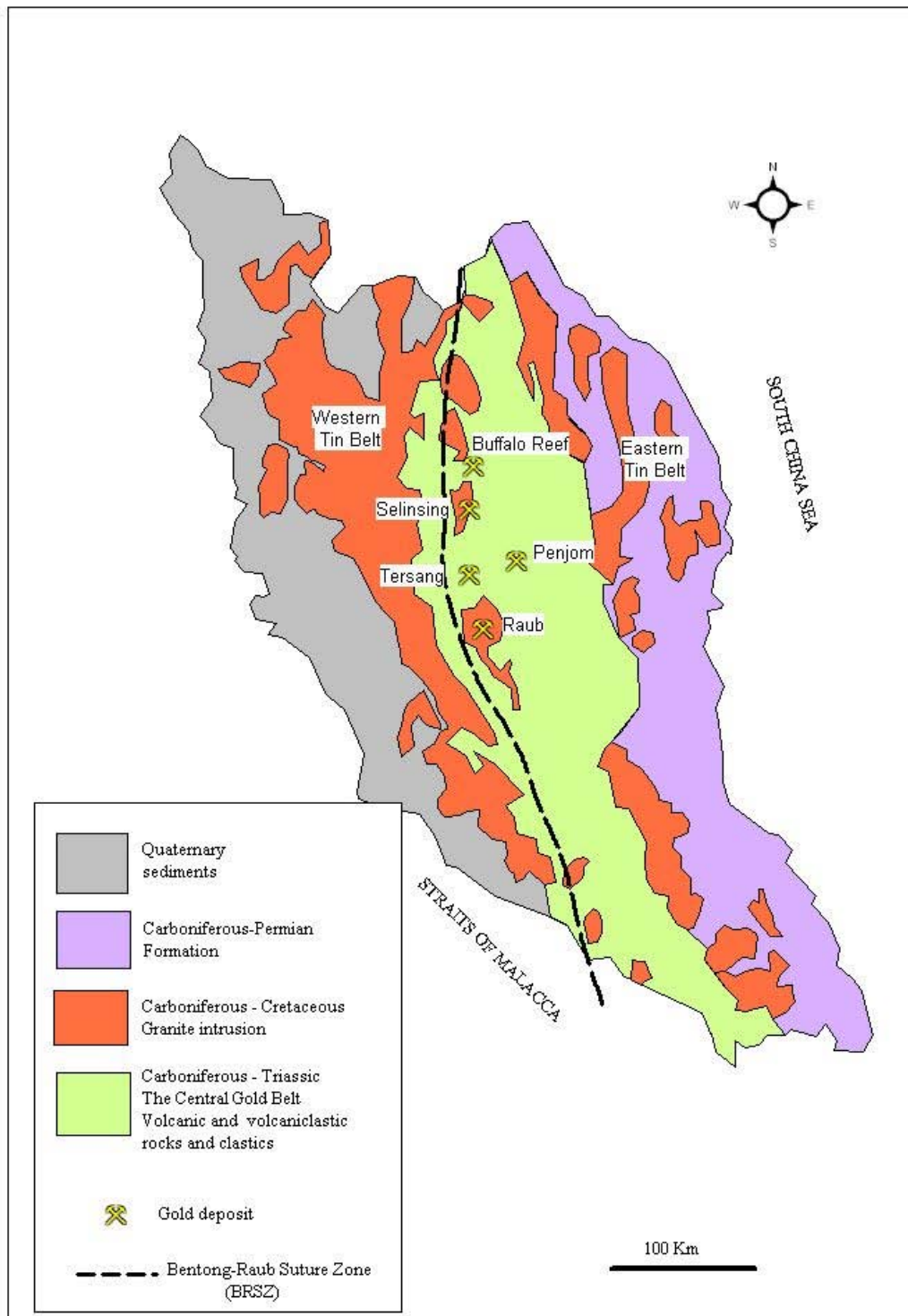


Fig. 2.4. Map of the metallogenic belts of Peninsular Malaysia.

Chapter 2: Tectonic setting and district-scale geology

The basement of the Central Belt consists of a Carboniferous-Permian sequence composed of felsic to intermediate volcanic rocks, limestone, shale and subordinate sandstone, siltstone and conglomerate (Mustaffa Kamal and Abdul Hadi, 1999). This belt is characterised by major gold deposits such as the Penjom, Tersang, Raub and Buffalo Reefs deposits as shown on Fig. 2.4.

2.3.3 The Eastern Tin Belt

The Eastern Tin Belt is characterised by poly-deformed Late Palaeozoic sequence, overlain unconformably by Late Permian continental conglomerate and Jurassic-Cretaceous continental deposits (Fig. 2.4). The granitoids in this belt cover a wide compositional range from biotite granite to hornblende-biotite granite/granodiorite and diorite-gabbro (Schwartz et al., 1995). Tin deposits are associated with biotite granite in the Eastern Coast Belt and account for up to 3% of tin production.

In addition, this belt includes a suite of shoshonitic trachyte in the Segamat area (Johor) which has been dated by K/Ar dating and returned an age of 62 Ma (Bignell and Snelling, 1977). In addition, the Eastern Belt plutons consist of $^{87}\text{Sr}/^{86}\text{Sr}$ initial ratio (less than 0.712) biotite or hornblende-biotite-bearing I-type granitoids with Triassic Rb-Sr ages. I-type granitoids are typical of modern day Andean-type active margins where oceanic plates are subducted under continental margins or island arcs producing andesite volcanoes. Additionally, Liew and McCulloch (1985) obtained U-Pb zircon ages of ~260 Ma and ~220 Ma (i.e. Upper Permian to Middle Triassic) from I-type granites from the Easter Province. The Eastern Belt plutons represent the magmatism associated with the

subduction of an ancient ocean (Palaeo-Tethys Ocean) under the Central and Eastern Belts.

2.4 District-scale Geology

The district-scale geology of the study area is comprised by three main formations including the Kaling Formation, Gua Musang Formation, the Semantan Formation, and intrusive rocks (Fig. 2.5). Stratigraphically, the Semantan Formation is overlain by the Kaling Formation. The Gua Musang Formation was reported to be transitional into the overlying Semantan Formation. The Semantan Formation, which is Middle to Upper Triassic in age consists of alternating sequences of carbonaceous shale, siltstone, and rhyolitic tuffs with lenses of chert and crystalline limestone. Jaafar (1976) divided the Semantan Formation into four facies:

- An argillaceous facies that is composed of shale, siltstone interbedded with rhyolite tuffs. In this facies, tuffaceous shale and tuffaceous siltstone are developed where argillaceous and pyroclastic strata are closely interbedded.
- A pyroclastic facies that consists of well-bedded medium to fine-grained rhyolitic tuff.
- A limestone facies that is made up of lenses of crystalline limestone. It contains lenticular segregations of carbonaceous materials.

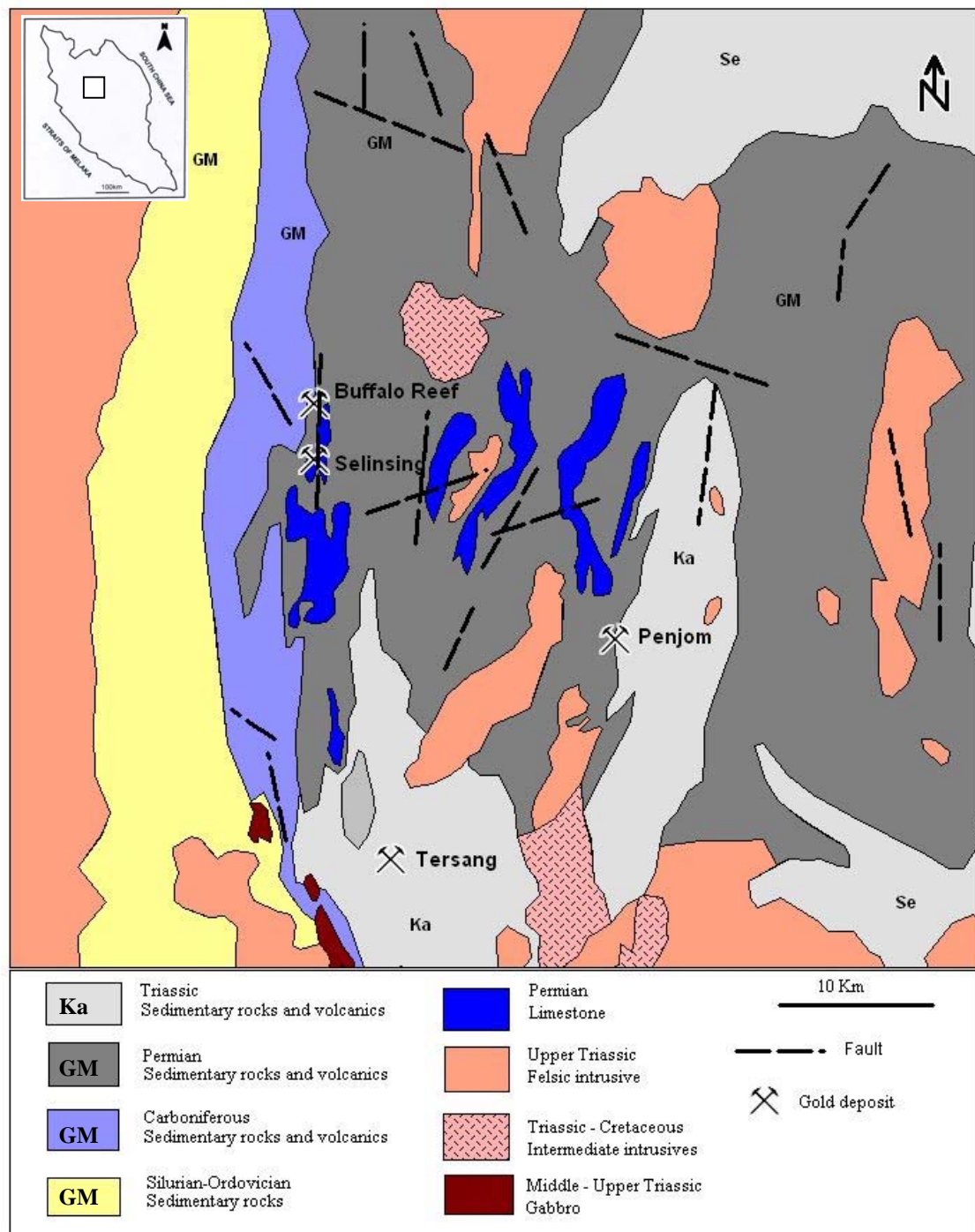


Fig. 2.5. District-scale geological map showing location of the gold deposits, Central Malaysia. Key: Ka: Kaling Formation; GM: Gua Musang Formation; Se: Semantan Formation.

- A chert facies that occurs as lenses of carbonaceous chert interbedded with shale and rhyolite tuffs. The Semantan Formation outcrops in the Penjom area and is predominantly composed of black shale overlain by sequences of fine-grained turbidites. The turbidite sequences are made up of interbedded black mudstone and sometimes pebbly siltstone with minor occurrence of sandstone. The Semantan Formation contains *Halobia* and *Daonella* beds that represent off-shore depositional environment.

In addition, the Semantan Formation also contains *Myophoria strata* indicating a near-shore environment. The presence of plant fossils in the carbonaceous shale probably suggests a shallow water environment (Kobayashi and Tamura, 1968). Rocky (1980) recognised the following units for the Semantan Formation:

- The Belengu member (youngest)

This member comprises black Carboniferous shale with some sandstone laminae. This member is 2100 m thick.

- The Cheriau member

This member shows alternation of sandstone and siltstone associated with thinly bedded and tuffaceous shale. This member is 1400 m in thickness.

- The Sanggang member (Oldest)

This member is composed of interbedded shale and siltstone sequences with some interbeds of tuffs. This member is 500 m thick.

Chapter 2: Tectonic setting and district-scale geology

The Kaling Formation is arenaceous and argillaceous and composed of sandstone, subgreywacke and quartzite with some conglomerate, shale, and rhyolitic tuffs. The conglomerate occurs as lenticular bodies interbedded with sandstone and shale. The arenaceous facies is made up of sandstone, orthoquartzite, and subgreywacke. The argillaceous facies consists of interbeds of shale and siltstone. Most of these strata are carbonaceous. The Kaling Formation is characterised by marine fauna of Triassic age and is interpreted as having been deposited in littoral environment (Alexander, 1959).

The Gua Musang Formation, which is Ordovician-Permian in age (Leman 1993), is composed of shale, slate, and limestone. This formation is poorly exposed in the region due to intense weathering. In this formation, the argillaceous facies is associated with calcareous facies which make up the prominent limestone hills. The limestone is interpreted as having been deposited in shallow water environment (Richardson, 1939).

CHAPTER 3

LOCAL GEOLOGY AND GEOCHRONOLOGY

3.1. Introduction

This Chapter documents the local geological setting of the Selinsing and Tersang gold deposits on the basis of the author's geological mapping and logging of drill cores. The geology of the nearby Penjom gold deposit was described by Kamar Shah and Hewson (2007), and their geological information are combined with the Selinsing and Tersang data to delineate the nature and setting of the gold system in the district. The lithology of the different units has also been examined under the microscope to document their petrographic and textural characteristics. The ages of host rocks and intrusions have been determined using LA ICP-MS U-Pb zircon dating. A geochemical classification of intrusive rocks from the Tersang and Penjom gold deposits is also presented in this Chapter and discussed in detail. No geochemical analysis was undertaken for the Selinsing deposit due to lack of intrusive exposures.

3.2. Methods of study

The methods of study are field and laboratory works were done at CODES ARC Centre of Excellence in Ore Deposit Research, University of Tasmania.

3.2.1. Fieldwork

A detailed field mapping was carried out recording lithology and structures on 1:2,000 and 1:250 scales for the Selinsing and Tersang deposits. A GPS (Global Positioning System) was used to provide a relatively accurate position, usually in order of 3 to 10 m depending on the signal reception quality. The signal reception was fairly good

Chapter 3: Local geology and geochronology

in open field (no vegetation coverage) and provided reliable positions. But in the forested area, the GPS usually encountered difficulties to acquire satellite signals thereby causing poor GPS coverage. Weather, steep terrain and vegetation conditions also influenced the quality of satellite reception. A time gap of about 5 to 10 minutes was needed to acquire satellite data before recording X, Y, and Z coordinates. The GPS Receiver also helped to generate waypoints (or positions), tracks and routes for mapping purposes. Apart from using a handheld compass, the GPS Receiver helped move around in the field because of its electronic compass capability. Field data such as sample ID, easting/northing coordinates (X, Y), and the Z position (elevation) were computerised for mapping purposes. In this study, coordinate systems are in UTM (Universal Transverse Mercator), zone 47, northern hemisphere (Map datum-WGS 84), latitude-longitude (Map datum-Kertau 1948), and RSO (Rectified Skew Orthomorphic) system. If UTM and RSO systems were used, the coordinates were shown as northing and easting, typically in meters. At some locations, standard mine grids were converted to RSO or UTM for accurate locations of the mapped areas. In addition, eleven 1:250 bench maps were created for the Selinsing gold deposit. Fifty-seven outcrop samples and 112 core samples were collected from the Selinsing gold deposit. These core samples were taken from ten drill holes to cover the entire deposit. The drill holes were logged and emphasis was placed on lithology, distribution of quartz vein, sulphide and gold mineralisation. Forty outcrop samples were also collected from the Tersang gold deposit. These samples were from quartz veins, intrusion and host rock. There were no more core samples available from the Tersang deposit. Twenty-two outcrop samples have been collected from the Penjom gold deposit. As a whole, 231 samples were collected for this study.

3.2.2. Laboratory Methods

Laboratory analyses were undertaken at the CODES ARC Centre of Excellence in Ore Deposit Research (CODES), University of Tasmania. Petrographic and textural studies were made using Nikon and Olympus microscopes. Scanning electron microscope was applied for mineral composition and identification to establish paragenesis at the deposit scale. These analyses were particularly useful to detect mineral inclusions in sulphide grains since they are difficult to find using normal optical microscope.

The following procedure was applied for U-Pb dating. Approximately 100 g of rock was repeatedly sieved and crushed in a Cr-steel ring mill to a grain size <400 micron. Non magnetic heavy minerals were then separated using a gold pan and a Fe-B-Nd hand magnet. The zircons were hand picked from the heavy mineral concentrate under the microscope in cross-polarised transmitted light. The selected crystals were placed on double sided sticky tape and epoxy glue was then poured into a 2.5 cm diameter mould on top of the zircons. The mount was dried for 12 hours and polished using clean sandpaper and a clean polishing lap. The samples were then washed in distilled water in an ultrasonic bath. The standard procedure for the Laser ICP-MS zircon dating is performed on an Agilent 7500cs quadrupole ICPMS with a 193 nm Coherent Ar-F gas laser and the Resonetics M50 ablation cell at CODES, University of Tasmania.

The downhole fractionation, instrument drift and mass bias correction factors for Pb/U ratios on zircons were calculated using two analyses on the primary (91500 standard of Wiendenbeck et al. 1995) and one analysis on each of the secondary standard zircons (Temora standard of Black et al., 2003 and Jackson et al., 2004) analysed at the beginning of the session and every 12 unknown zircons (roughly every 1/2 hour) using

Chapter 3: Local geology and geochronology

the same spot size and conditions as used on the samples. Additional secondary standards (The Mud Tank Zircon of Black and Gulson 1978) were also analysed. The correction factor for the $^{207}\text{Pb}/^{206}\text{Pb}$ ratio was calculated using 3 large spot of NIST610 analysed at the beginning and end of the day and corrected using the values recommended by Baker et al. (2004). Each analysis on the zircons began with a 30 second blank gas measurement followed by a further 30 seconds of analysis time when the laser was switched on. Zircons were sampled on 32 micron spots using the laser at 5 Hz and a density of approximately 1.5 J/cm^2 . A flow of He carrier gas at a rate of 0.6 litres/minute carried particles ablated by the laser out of the chamber to be mixed with Ar gas and carried to the plasma torch.

Elements measured include ^{49}Ti , ^{96}Zr , ^{146}Nd , ^{178}Hf , ^{202}Hg , ^{204}Pb , ^{206}Pb , ^{207}Pb , ^{208}Pb , ^{232}Th and ^{238}U with each element being measured sequentially every 0.16 s with longer counting time on the Pb isotopes compared to the other elements. The data reduction used was based on the method outlined in detail in Meffre et al. (2008) similar to that outlined in Black et al. (2004) and Paton et al. (2010). Element abundances on zircons were calculated using the method outlined by Kosler (2001) using Zr as the internal standard element, assuming stoichiometric proportions and using the 91500 to standard correct for mass bias.

Eight samples of intrusion rocks were analysed by X-ray fluorescence analysis to obtain whole rock major and trace elements composition. The instrument used for this analysis is PANalytical Axios Advanced X-Ray Spectrometer. It is equipped with X-Ray Tubes of 4kW maximum and a Rh anode end window. The element analysed are: F, Na, Mg, Al, Si, P, S, K, Ca, Ti, Mn, Fe and trace elements Sc, V, Cr, Co, Ni, Cu, Zn, Ga, Ge,

Chapter 3: Local geology and geochronology

As, Se, Br, Rb, Sr, Y, Zr, Nb, Mo, Ag, Cd, Sn, Sb, Te, I, Ba, La, Ce, Nd, W, Tl, Pb, Bi, Th and U. The instrument also has the following parts: Crystals: PX-10, LiF 220, PX-1 (for F, Na and Mg), curved PE002, curved Ge111. The collimators are coarse (0.7mm), fine (0.3mm) with high resolution (0.15mm). The detectors are Gas flow proportional counters with P10 gas (10% methane argon), a sealed Xe Duplex and Scintillation Counter. The sample changer is PANalytical X-Y sample changer with capacity for 96 fusion discs and 64 pills.

In sample preparation for the major elements, 32mm fusion discs were prepared at 1100 degrees C in 5% Au/95% Pt crucibles 0.500g sample, 4.500g 12-22 Flux (Lithium Tetraborate-Metaborate mix), 0.0606g LiNO₃ for silicates. Platinum/5% gold moulds were used for cooling. Sulphide bearing samples had a different mix with more LiNO₃ as oxidising agent and the mix is pre-ignited at 700 degrees C for 10 minutes. Ore samples and ironstones used 12/22 flux and a higher flux/sample ratio. Dolomites and limestones needed pure lithium tetraborate as a flux. Iodine vapour was used as a releasing agent to remove discs from the mould. For the trace elements, 32mm diameter pressed powder pills (10g, 3.5 tons/cm⁻²) were used and a sample Binder PVP-MC. Corrections for mass absorption were calculated using PANalytical Super-Q software with its Classic calibration model and alpha coefficients. In house inter-element corrections were also applied. Calibration was done on pure element oxide mixed in pure silica, along with International and Tasmanian reference rocks.

3.3. Geology of the Tersang deposit

The geology at the Tersang gold deposit is presented in Fig. 3.1. The main lithologies at the Tersang gold deposit consist of grey-coloured sandstone and breccia, which are cross-cut by a felsic intrusion. The ore zone is characterised by the presence of sheeted quartz veins and sulphide mineralisation hosted in the sandstone. Outcrop photographs of the main lithological units and the ore zone are presented in Fig. 3.2. The ore zone is located in the south of the mine-site (Fig. 3.2A). A close-up view of the felsic intrusion is shown in Fig. 3.2B. The contact zone between the felsic intrusion and the host sandstone is found in Fig. 3.2C. The outcrop photograph of the breccia unit is shown in Fig. 3.2D.

3.3.1. Sandstone unit

The sandstone is pinkish to yellowish brown in colour when weathered and greenish grey when fresh and crops out from the central part to the south of the deposit. This unit also crops out in the northwest and northeast of the deposit where it is in contact with the felsic intrusion. The sandstone is fine-grained and poorly sorted. The rock contains visible pyrite veins. Under microscope, the rock is composed of K-feldspar grains (40-50 vol. %), quartz (20 vol. %), biotite (20 vol. %), and disseminated pyrite (up to 10 vol. %) of various textures (Figs. 3.3A and B).

3.3.2. Felsic intrusion unit

The massive felsic intrusion measures approximately 600 m long and 400 m wide and is exposed in the central and northern part of the deposit area. Stratigraphically, the

Chapter 3: Local geology and geochronology

unit occurs in the form of sills sandwiched along bedding planes in the sandstone unit.

The felsic intrusion is grey when fresh and yellow when weathered.

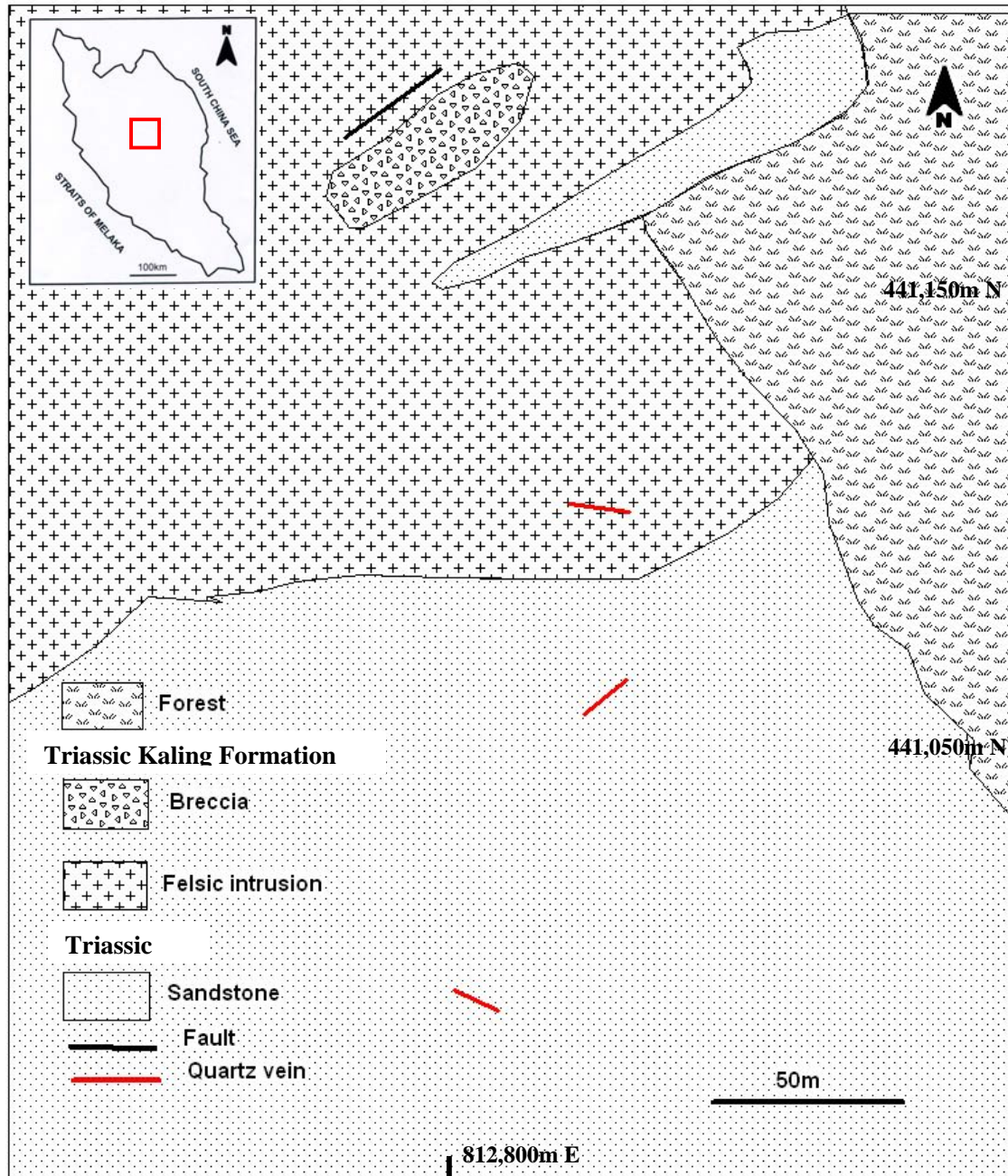


Fig. 3.1. Geological map of the Tersang gold deposit showing the main lithologic units.

Chapter 3: Local geology and geochronology

Under the microscope, the intrusion is composed of quartz (20 vol. %), K-feldspar (30 vol. %), and muscovite (35 vol. %) phenocrysts. Muscovite occurs in the form of laths and interstitial infillings. The sample is also composed of vesicles (up to 5 vol. %) and disseminated fresh pyrite (up to 5 vol. %) (Figs. 3.3C and D).

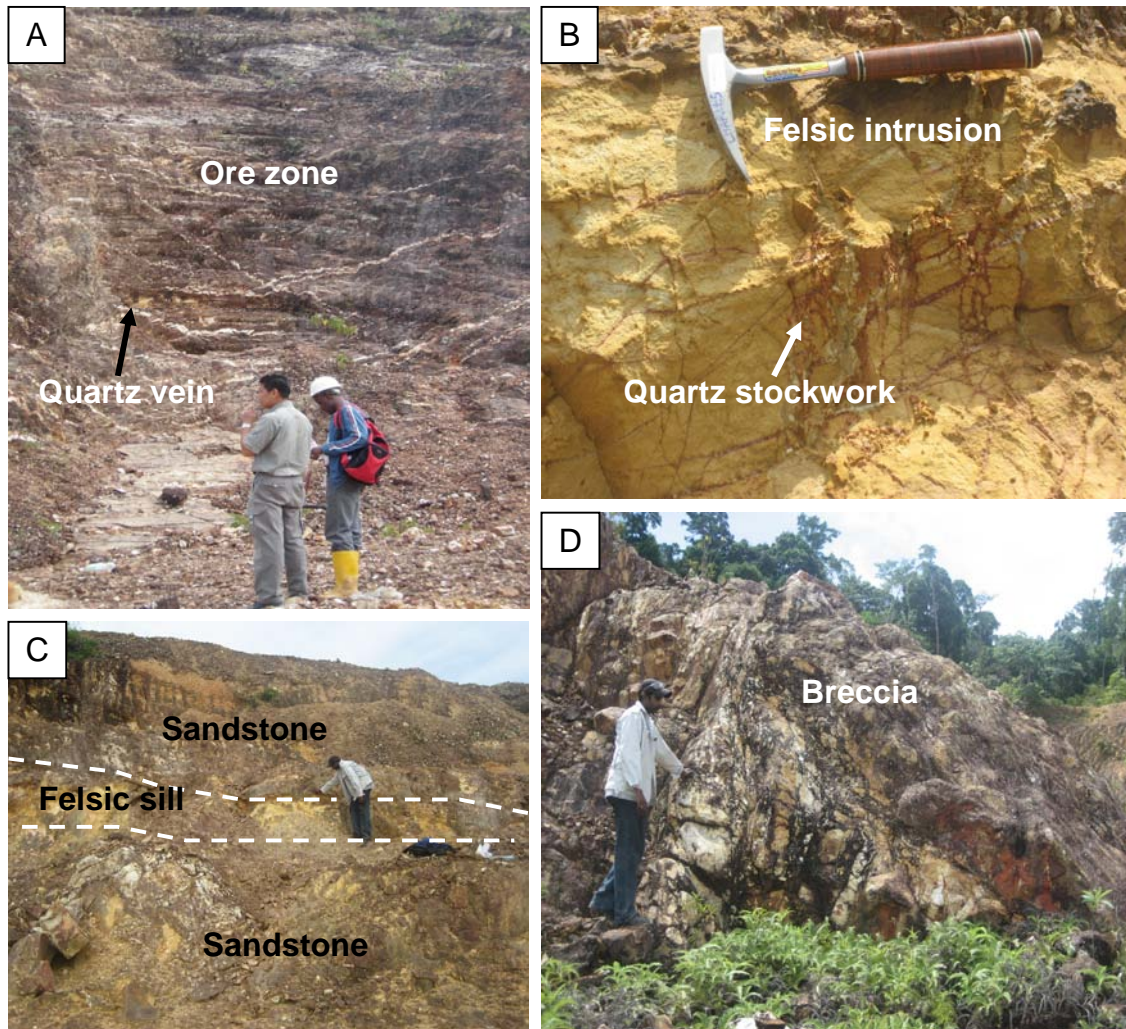


Fig. 3.2. Field view and outcrop photographs at Tersang. **A.** view of the Tersang gold deposit showing the location of the ore zone. **B.** Felsic intrusion with quartz stockwork. **C.** Outcrop of the host sandstone and felsic sill. **D.** Exposure of Triassic breccia in the Kaling Formation.

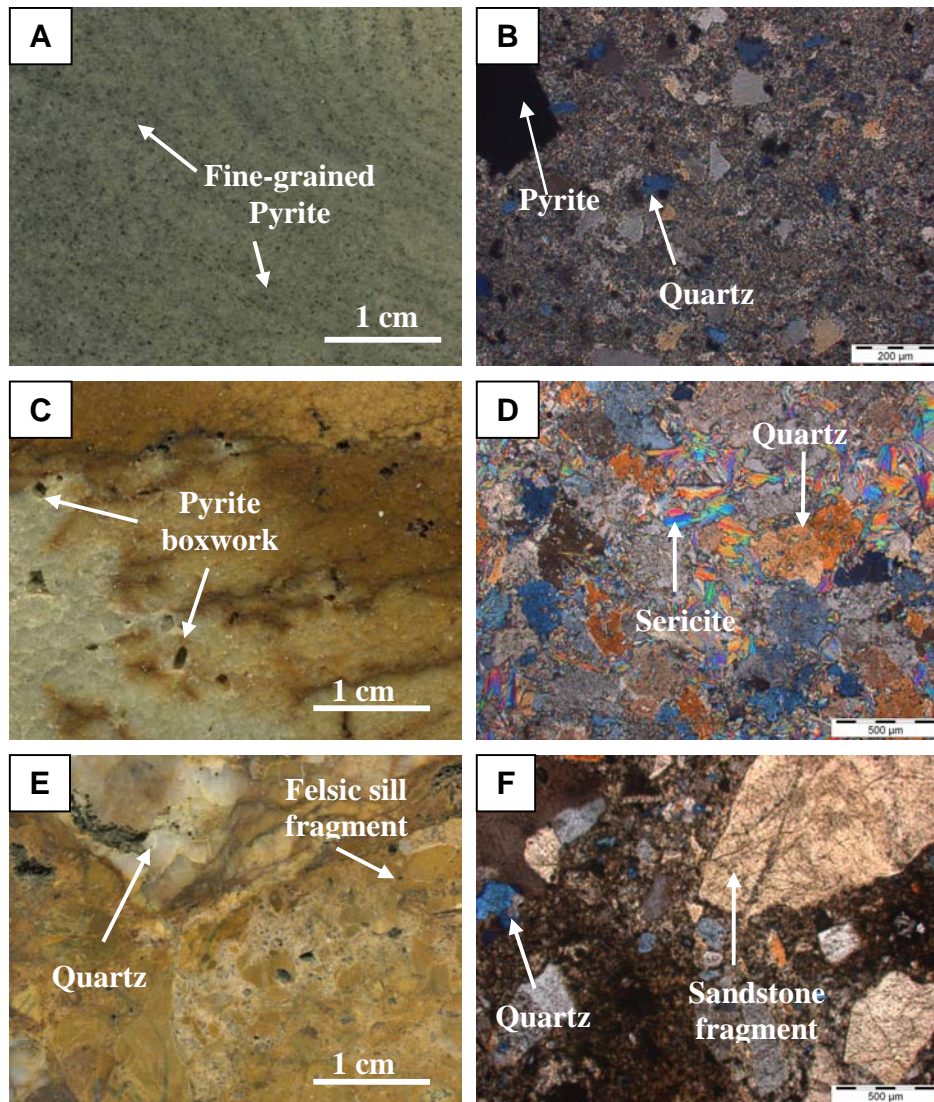


Fig. 3.3. Lithological characteristics of Host rock and intrusion at the Tersang gold deposit. **A.** Photograph of Host sandstone (Sample No. TER-R007). **B.** Photomicrograph of Host sandstone (Sample No. TER-R007). **C.** Felsic intrusion (Sample No. TER-R033). **D.** Photomicrograph of the intrusion (Sample No. TER-R033). **E.** Photograph of breccia (Sample No. TER-R032). **F.** Photomicrograph of the breccia. All thin sections were viewed in transmitted light (XPL).

3.3.3. Breccia unit

A grayish brown oxidised breccia unit of 40-50 m in length and 20-25 m in width within the felsic unit. This unit contains polymictic fragments (0.5-3 cm) of felsic and probably volcanoclastic rock (55 vol. %). Small-scale stockwork of quartz veinlets (up to 200µm thick) is found in the rock fragments. Oxidised pyrite grains occupy interstices within the rock fragments. The sample also contains altered biotite (10 vol. %), feldspar (30 vol. %), and vesicles (up to 5 vol. %) in a silicified fine-grained quartz matrix (Figs. 3.3E and F). The breccia was formed during the emplacement of the intrusion within the sandstone unit. It may be interpreted as tectonic breccia or dilational breccia.

3.4. Geology of the Selinsing deposit

Geological setting of the Selinsing gold deposit is shown in Fig. 3.4. The deposit geology is composed of purplish grey to yellowish grey phyllite, siltstone and fault-related rocks such as cataclasite and mylonite. The textural characteristics of these lithologic units are shown in Fig. 3.5.

3.4.1. Phyllite unit

Phyllite units have been found interbedded with mylonite and cataclasites. They have variable thickness ranging from 2 to 10 metres. Phyllite layers mostly trend N160° and dip 60°-78° to the east. Under the microscope, the phyllite is composed of entirely clay mineral (90 vol. %) with minute grains of zircon and euhedral to subhedral grains of pyrite (up to 10 vol. %), which are up to 5 µm in diameter and preserved in the clay matrix. Some silt-size quartz grains are also present (Figs. 3.5A and B).

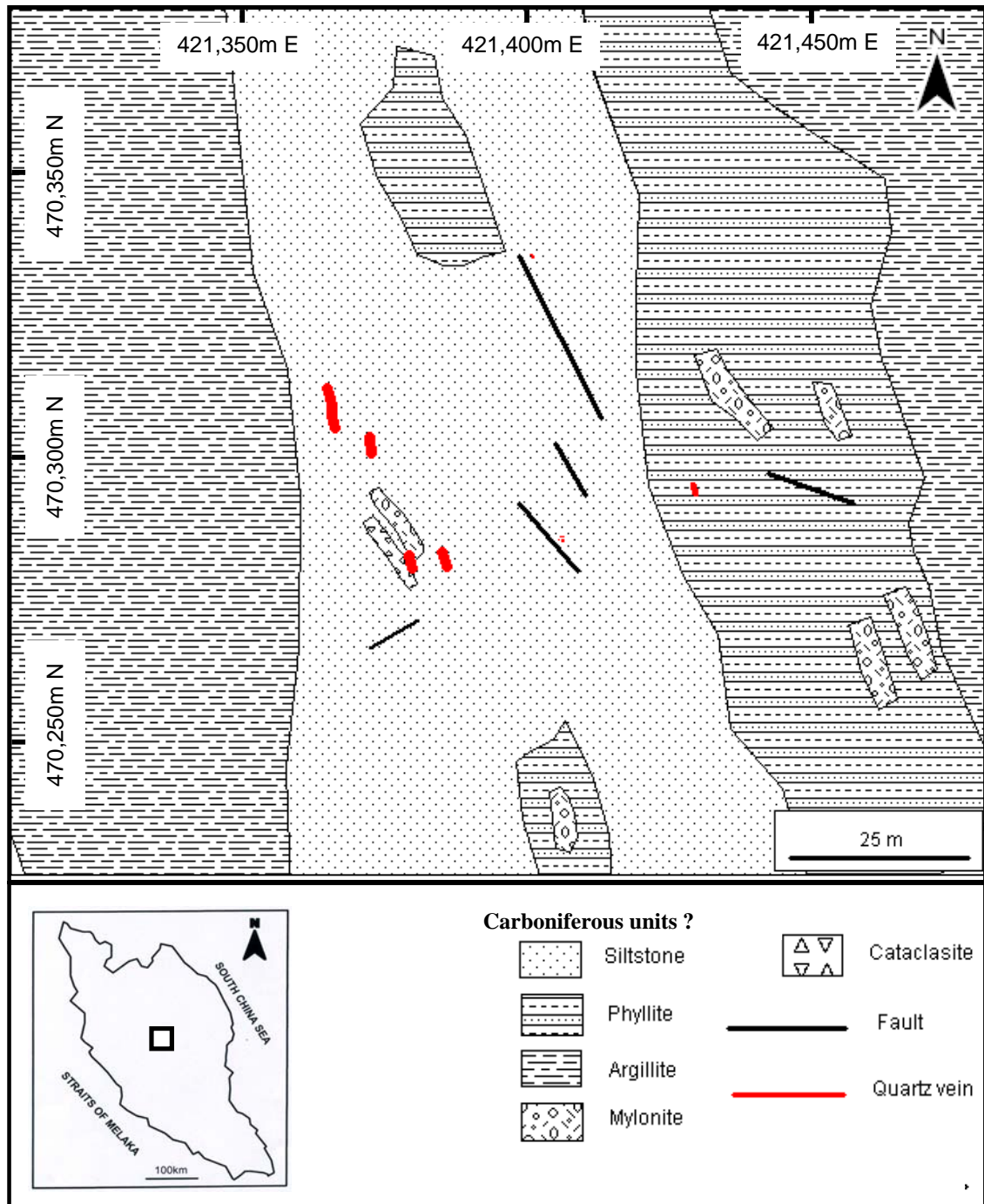


Fig. 3.4. Geological map of the Selinsing gold deposit showing the main lithologies, Central Malaysia. Note that the siltstone, phyllite, argillite and mylonite belong to the Gua Musang Formation.

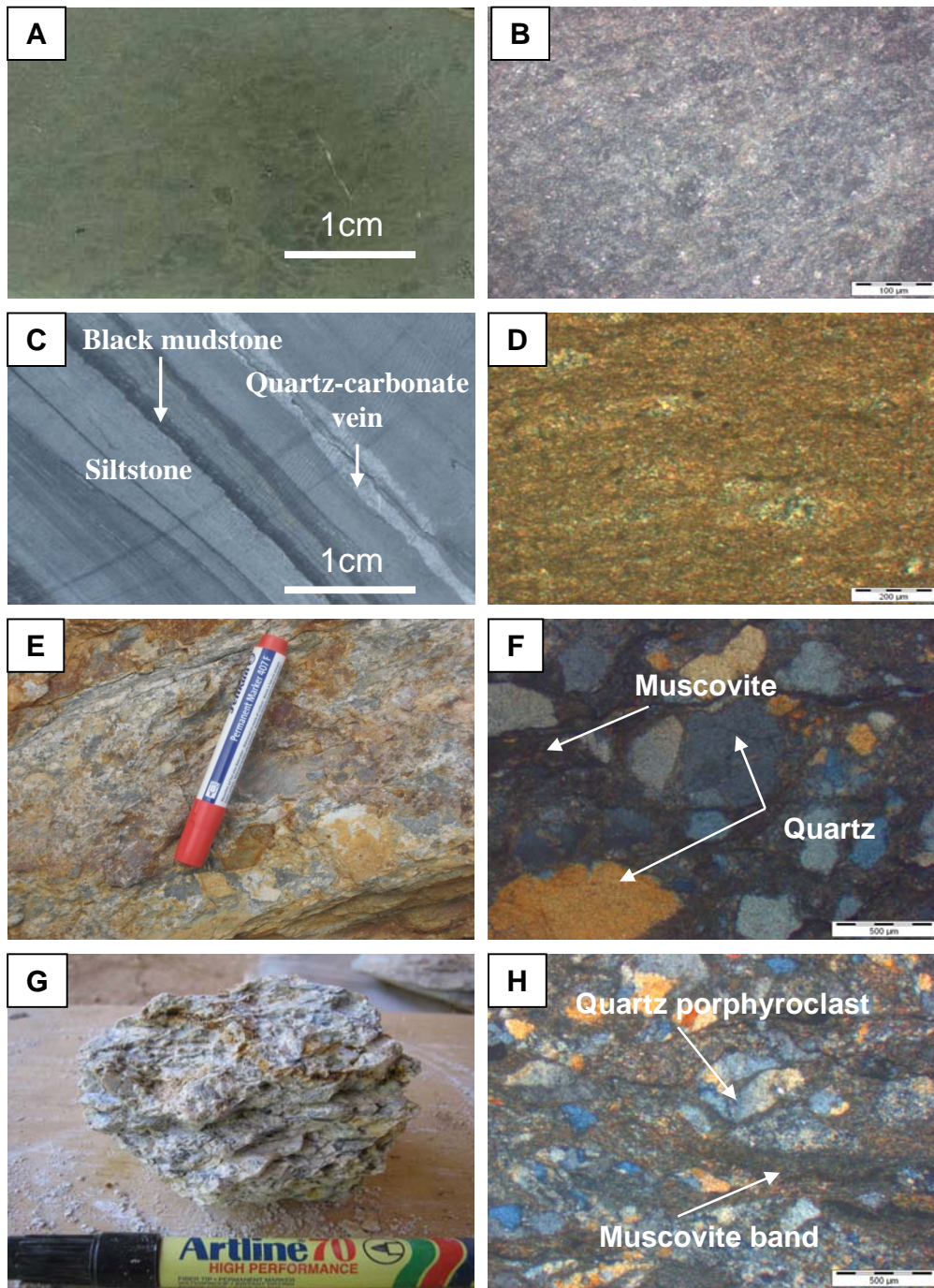


Fig. 3.5. Lithological characteristics of host sequence at the Selinsing gold deposit. **A.** Phyllite hand specimen (Sample No. SR12B). **B.** Photomicrograph of phyllite (Sample No. SR12). **C.** Interbedded siltstone and mudstone (Sample No. SEL-R009). **D.** Photomicrograph of siltstone. **E.** Cataclasite outcrop. **F.** Photomicrograph of cataclasite (Sample No. SEL-R032). **G.** Mylonite hand specimen (Sample No. SEL-R008). **H.** Photomicrograph of mylonite (Sample No. SEL-R008). All photomicrographs were taken in transmitted light (XPL).

3.4.2. Siltstone unit

The siltstone unit crops out in the western part of the Selinsing gold deposit with thickness reaching up to 20 m. The siltstone unit is composed of sub-rounded to rounded single quartz grains (30 vol. %). Polycrystalline quartz is common. The rock is weakly foliated with muscovite laths (up to 50 vol. %), which are deformed. The foliation is strong and parallel to the 3-4 mm thick quartz veins. Pressure shadows are common around pyrite grains. This suggests that the pyrite grains probably were formed prior to or during deformation. A few grains of biotite are present (up to 10 vol. %) in the siltstone. In crossed-nicol, a few opaque minerals are visible (Figs. 3.5C and D). The siltstone unit contains sub-rounded crystal clear quartz grains, which probably point to a volcanic origin.

3.4.3. Fault-related rocks

The fault-related rocks are cataclasite and mylonite mostly found in the ore zone.

3.4.3.1. Cataclasite unit

Cataclasite units are massive and are contained within the siltstone unit. They usually crop out in fault zones where they display discontinuous bands and thin out along the strike. In thin section, cataclasite is composed of angular quartz grains (up to 45 vol. %), some rock fragments of schist and siltstone (25 vol. %), altered muscovite (30 vol. %), phenoclasts of calcite (5 vol. %), and minute chlorite grains (Figs. 3.5E and F).

3.4.3.2. Mylonite unit

Mylonite units are within the phyllite, siltstone, and argillite units. In addition, mylonite outcrops in areas that are strongly deformed. They display foliation plans that

trend 160° and dip 64° east. Under the microscope, mylonite is composed of polycrystalline quartz (45 vol. %) porphyroclasts, muscovite bands (50 vol. %) and rock fragments (5 vol. %) (Figs. 3.5G and H).

3.4.4. Argillite unit

The argillite unit is composed of purple shale and mainly is exposed in the eastern side of the deposit (Fig. 3.4). The rocks are strongly weathered and show a saprolitic texture throughout the deposit site. In the northern part of the deposit towards the Buffalo Reef prospect, purplish brown argillite units are exposed and interbedded with siltstone units with a few strongly weathered felsic lenses. No thin section has been made for this unit because the samples were soft.

3.4.5. Limestone unit

Dark grey limestone crops out in the eastern and western parts of the deposit. This unit is not shown on the deposit scale geological map (Fig. 3.4) but is visible in cross-section (Fig. 3.8). In thin section, the limestone from eastern hillside is heavily fractured, very fine-grained, and fossiliferous with carbonaceous stylolitic micrite but no bedding obvious. The rock is largely recrystallised with large calcite crystals. Calcite grains are from 1 to 5 mm in diameter. Carbonaceous material is concentrated along the boundaries of the stylolites. Although the limestone is fossiliferous, fossils are not well-preserved for identification. In term of genesis, this limestone facies may represent a very quiet marine environment but the water depth is indeterminate.

Chapter 3: Local geology and geochronology

The evidence seems to suggest that multiple episodes of fracturing and compression led to calcite veinlets being cross-cut by stylolites, and these stylolite veinlets are cut by late generation calcite veinlets (Figs. 3.6A and B). Under the microscope, the limestone from the western part of the deposit is very fine-grained, calcareous and micritic. The limestone shows no bedding and a few stylolites are faintly visible. There are no fossils present (Figs. 3.6C and D).

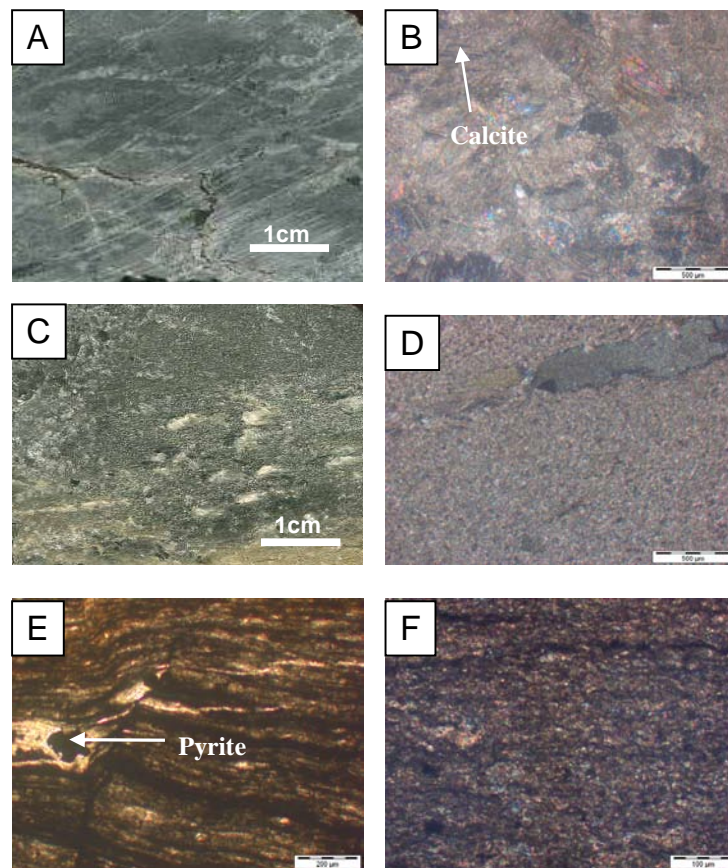


Fig. 3.6. Lithological characteristics of host sequence and limestones at the Selinsing gold deposit **A.** Eastern limestone hand specimen (Sample No. SR60). **B.** Photomicrograph of eastern limestone. **C.** Western limestone hand specimen (Sample No. SR61). **D.** Photomicrograph of western limestone. **E.** Photomicrograph of black mudstone (Sample No. SEL-R009). **F.** Photomicrograph of siltstone (Sample No. SEL-R009). All thin sections were viewed in transmitted light (XPL).

Chapter 3: Local geology and geochronology

In the subsurface zone, a few layers of siltstone interbedded with black mudstone have been found in core samples. These layers possibly represent remnants of turbidite sequences that had been disrupted by brittle and ductile deformation (Figs. 3.6E and F).

3.5. Geometry of the Selinsing orebody

The Selinsing ore body is composed of two sub-zones based on topography:

1. The lower ore zone to the east from reduced level RL 502.5-500 to RL 497.5-495 is composed dominantly of mylonite and cataclasite units mixed with oxidised weathered phyllite. The host rocks are phyllites that have been mylonitised.

2. The upper ore zone to the west from reduced level RL 560-557 to RL 540-537.5 is made up of dominantly of mylonite and cataclasite in purple weathered felsic tuff. The host rocks are mainly siltstone that has been mylonitised. A panoramic view of the Selinsing mine in Figure 3.7A shows zonation of the lower and upper ore zones gold bearing veins in phyllite and siltstone are shown in Figs. 3.7A-D.

The ore body lies within 40 m to 50 m thick shear zone that dips steeply east at angles between 60° and 70°. The length of the ore body is 250 m but only about 25 m long of ore zone is visible on Figure 3.4. The ore zone merges to the north and to the south along strike. Cross-sections that cut across the orebody were made (Figs. 3.8A and B). The cross-section in Fig. 3.8A shows high grade quartz veins, which contain pyrite boxworks. These veins are discordant to bedding (355°/50°E) in Figure 3.8A, and appear concordant to bedding in Figure 3.8B. The thickness of these veins varies from 1 to 1.5m. The veins also occur as boudins across the bedding S_0 and associated with reverse faults.

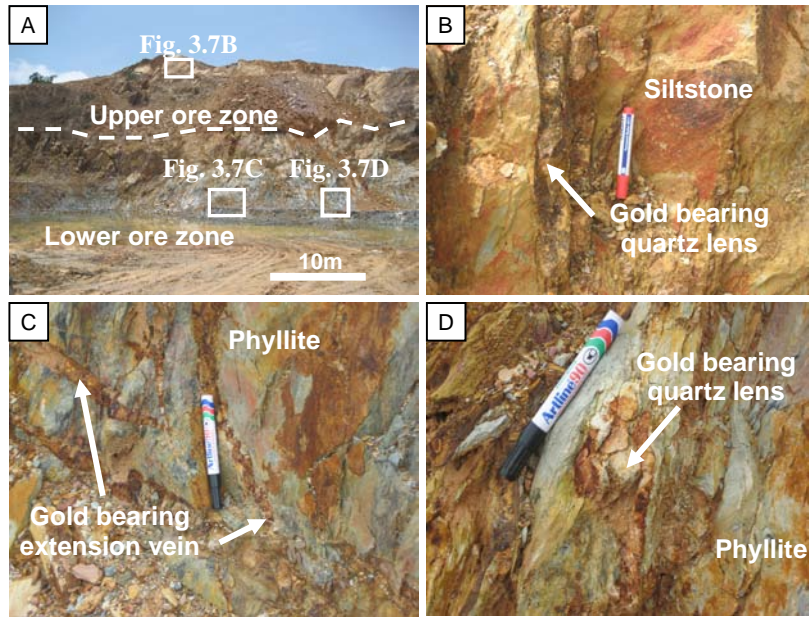


Fig. 3.7. Characteristics of the orebody at the Selinsing gold deposit. **A.** The upper zone is composed of siltstone associated with cataclasite and mylonite units. The lower zone is made up of mylonitised phyllite. Note the dotted line which is the inferred geological contact between the two distinct units. **B.** Vertically inclined gold bearing quartz vein in siltstone in the upper ore zone. **C.** Gold bearing extension veins in phyllite in the lower ore zone. **D.** Gold bearing quartz lens in phyllite in the lower ore zone.

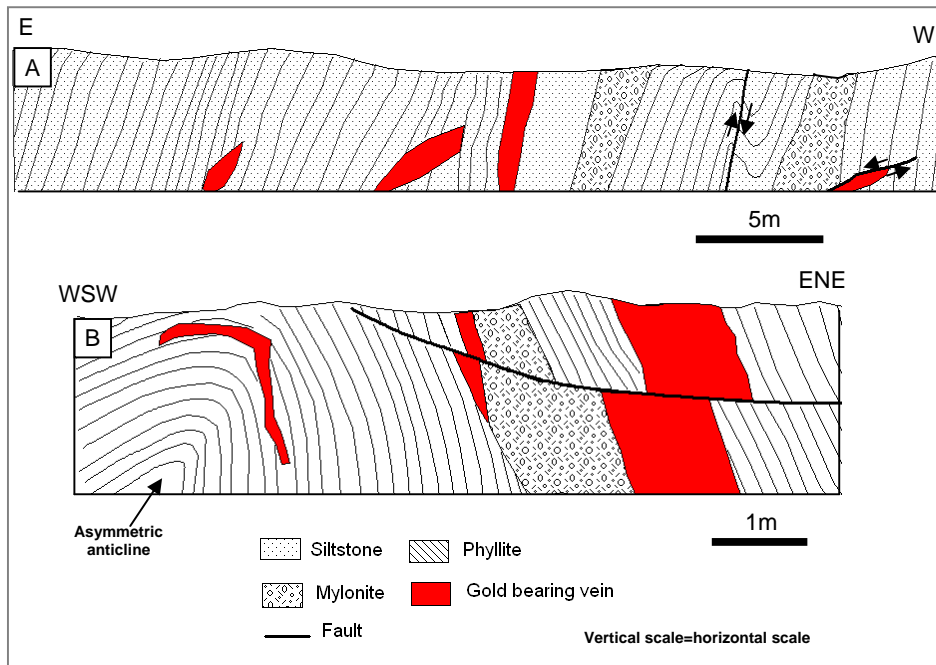


Fig. 3.8. Cross-sections across the Selinsing deposit site looking north. **A.** Mineralised quartz veins associated with reverse fault. **B.** Mineralised quartz veins combined with listric normal fault and saddle reef.

Chapter 3: Local geology and geochronology

Cross-section in Fig. 3.8B displays faulted high-grade veins which trend N060° and dip 60° to the northeast in phyllite. These 1 m thick veins are saddle reefs in small-scale asymmetric anticline (Figure 3.8B). The main cross-section that shows the interpreted ore zone is presented in Fig. 3.9.

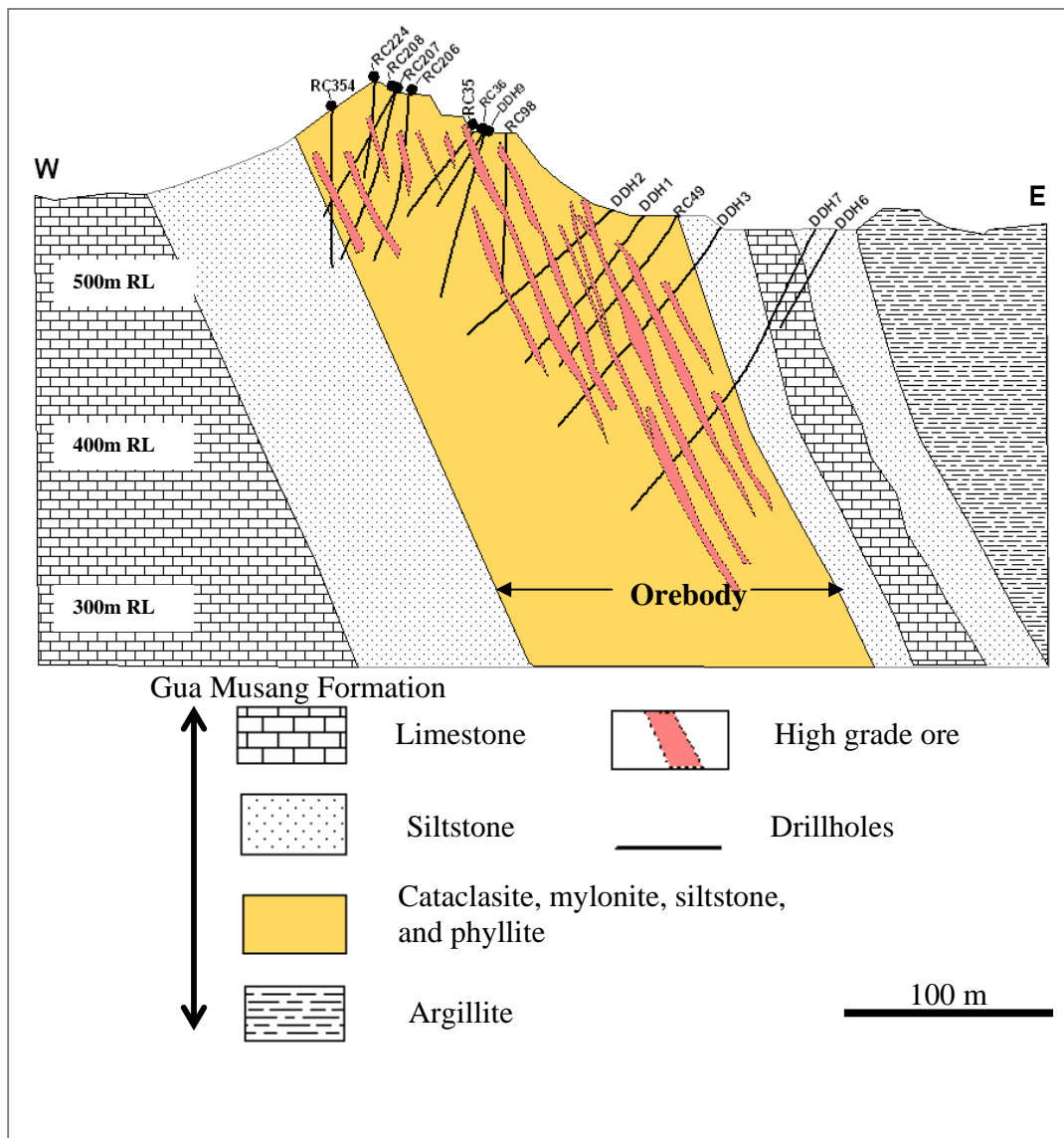


Fig. 3.9. Main cross-section looking north of the Selinsing gold deposit showing the orebody and high grade (1.5 g/t Au) ore zones, Central Malaysia.

3.6. Geology of the Penjom deposit

The geology of the Penjom gold deposit (Figure 3.10) is dominated by sequences of carbonaceous shale, tuffaceous conglomerate, tuffaceous siltstone and felsic sills and dykes associated with subordinate argillaceous limestone (Kamar Shah, 2007). The felsic intrusion is deformed within the host stratigraphy. In addition, the intrusion is faulted and brecciated in few areas across the mine. The Penjom geological map which shows the intrusion and carbonaceous shale as described above is presented in Fig. 3.10. The lithological and textural characteristics of the host rocks and intrusions are presented in Fig. 3.11.

3.6.1. Tuffaceous siltstone unit

Tuffaceous grey-coloured siltstones (Sample No. PEN-S3) are massive and contain quartz veinlets (1-3 mm) that cut across the bedding. Subhedral to euhedral pyrite grains are disseminated in these rocks (Fig. 3.11A and B). Sometimes, the siltstone (Sample No. PEN-S5) layers are brown in colour, massive and contain quartz veinlets (1-2 mm) that cross-cut the bedding (Fig. 3.11C). The siltstone also contains 3-4 mm glassy fragments of rocks probably of volcanic origin. Under the microscope, the sample contains quartz (80 vol. %), elongated crystal of biotite (10 vol. %), sericite (up to 5 vol. %) and disseminated pyrite (up to 5 vol. %) as shown in Fig. 3.11D.

3.6.2. Intrusive units

At the mine-site, intrusion occurs in the form of dykes and sills mostly within the carbonaceous shale and conglomerate units. The intrusive units (Sample No. PEN-R04)

Chapter 3: Local geology and geochronology

are composed of rounded to sub-rounded quartz grains (2-4 mm), which under the microscope represent about 80 vol. % of the rock (Fig. 3.11E). Some apatite inclusions in quartz grains are common. In addition, coarse K-feldspar grains make up to 10 vol. %. A few grains of amphibole showing cleavages at 120° are present (up to 5 vol. %) as shown in Fig. 3.11F.

3.6.3. Carbonaceous shale unit

The Carbonaceous shale unit (Sample No. PEN-R009) is black in colour and outcrops throughout the northern deposit site (Fig. 3.11G). Sometimes, the carbonaceous shales are white in colour when they are strongly weathered. They show no visible bedding or lamination. The rock is massive and displays a subtle schistosity under the microscope (Fig. 3.11H).

3.6.4. Tuffaceous conglomerate unit

Tuffaceous conglomerate is composed of sub-rounded to angular clasts of felsic intrusion and black shale and quartz carbonate veins which thickness ranges from 3 to 5 cm. Under the microscope, tuffaceous conglomerate is composed of rock fragments (80 vol. %), plagioclase (up to 5 vol. %), laths of muscovite (up to 5 vol. %) and disseminated pyrite (10 vol. %) as presented in Figs. 3.12A and B.

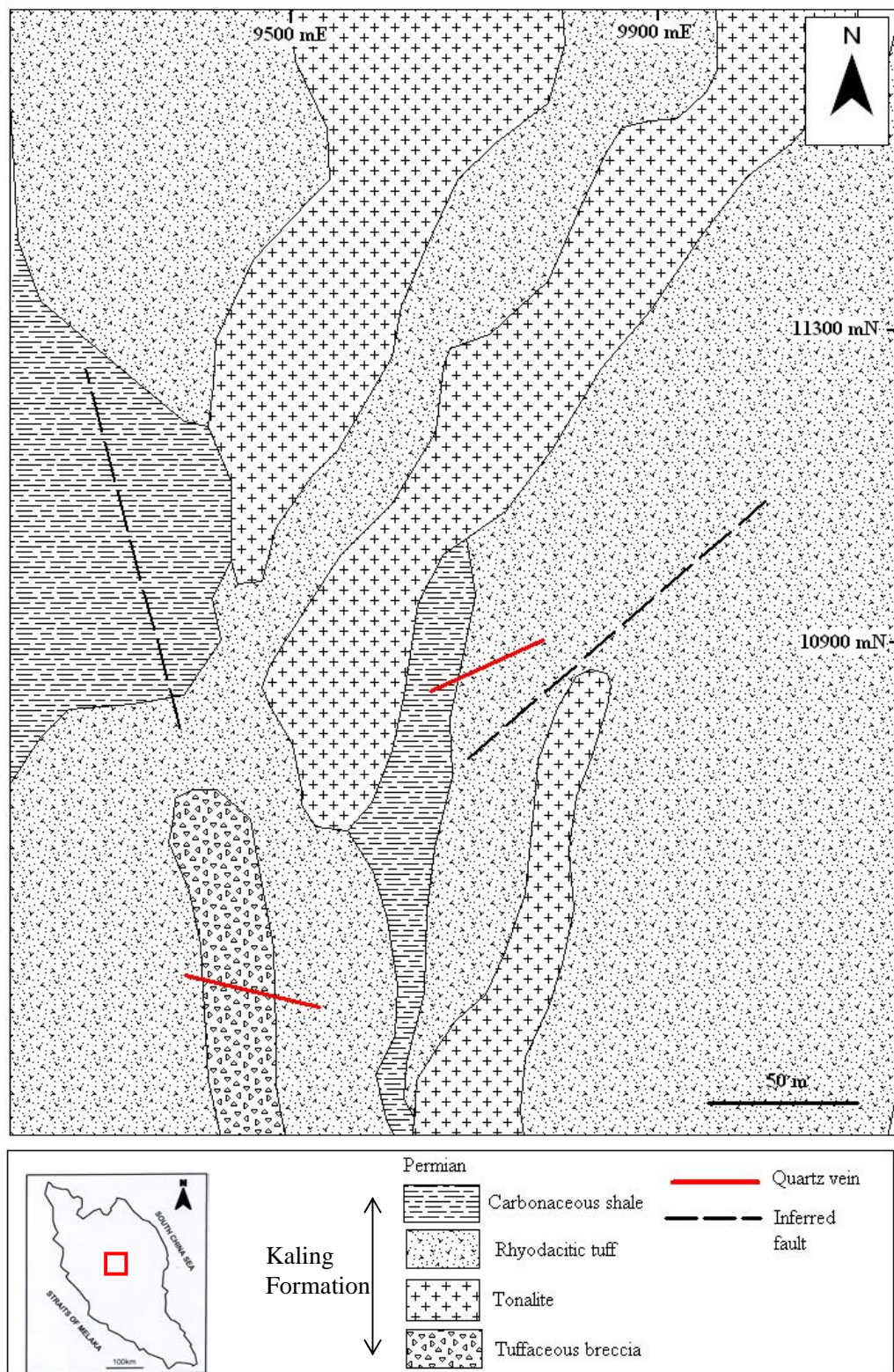


Fig. 3.10. Geological map of the Penjom gold deposit (Modified from Kamar Shah and Hewson, 2007)

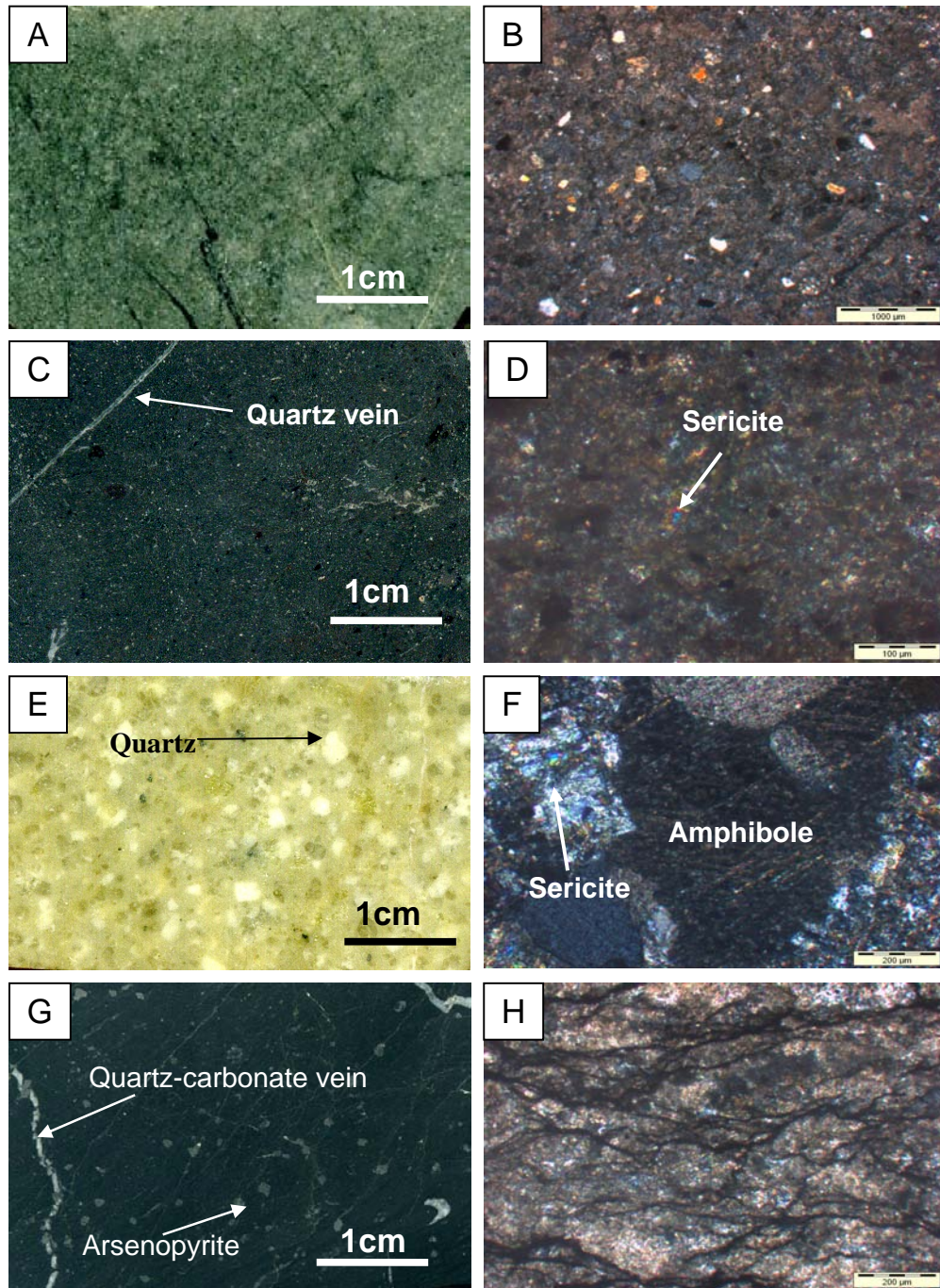


Fig. 3.11. Lithological and textural characteristics of Host rock and intrusion at the Penjom gold deposit. **A.** Hand specimen photograph of tuffaceous siltstone (Sample No. PEN-S3). **B.** Photomicrograph of the tuffaceous siltstone. **C.** Hand specimen photograph of the host siltstone (Sample No. PEN-S5). **D.** Photomicrograph of the host siltstone. **E.** Hand specimen photograph of the intrusion (Sample No. PEN-R04). **F.** Photomicrograph of the intrusion. **G.** Hand specimen photograph of the carbonaceous shale (Sample No. PEN-R009). **H.** Photomicrograph of the carbonaceous shale. All thin sections were viewed in transmitted light.

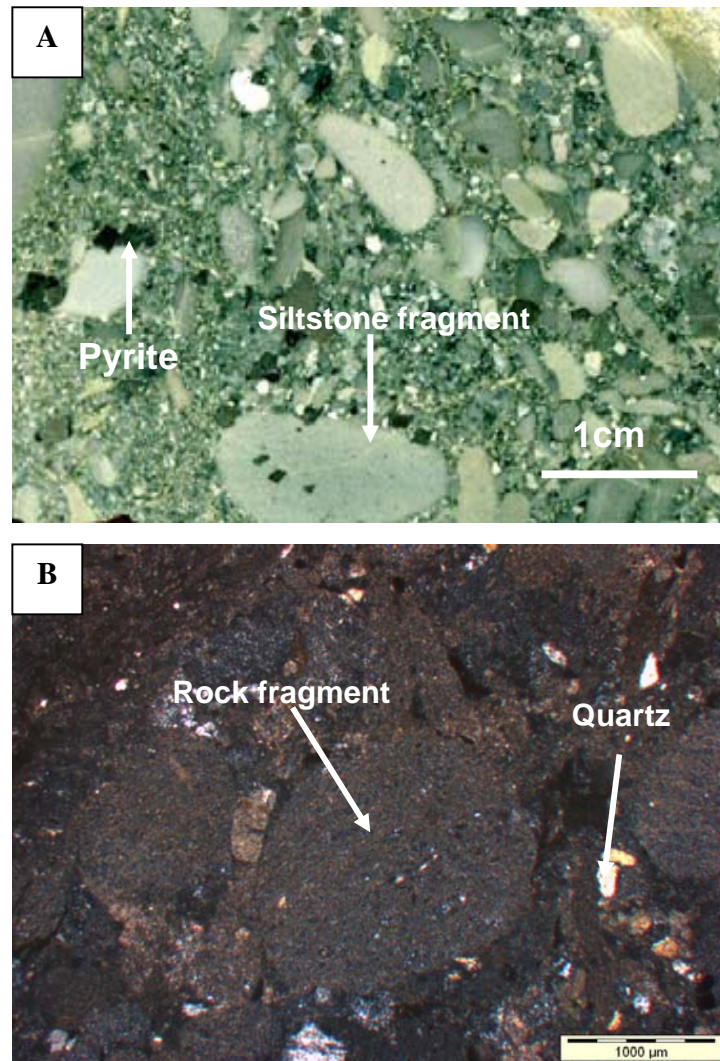


Fig. 3.12. Lithological and textural characteristics of the tuffaceous conglomerate at the Penjom gold deposit, Central Malaysia. **A.** Hand specimen of the tuffaceous conglomerate (Sample No. PEN-R12). **B.** Photomicrograph of the tuffaceous conglomerate. Thin section viewed in reflected light.

The view of the Penjom open pit with pictures of the dominant shale lithology and the felsic sills and dyke are also shown in Fig. 3.13A. A close-up view of the quartz-

Chapter 3: Local geology and geochronology

carbonate veins in brecciated zones is also presented in Fig. 3.13B. Sometimes, the felsic sills occur in the form of lenses as shown in Fig. 3.13C.

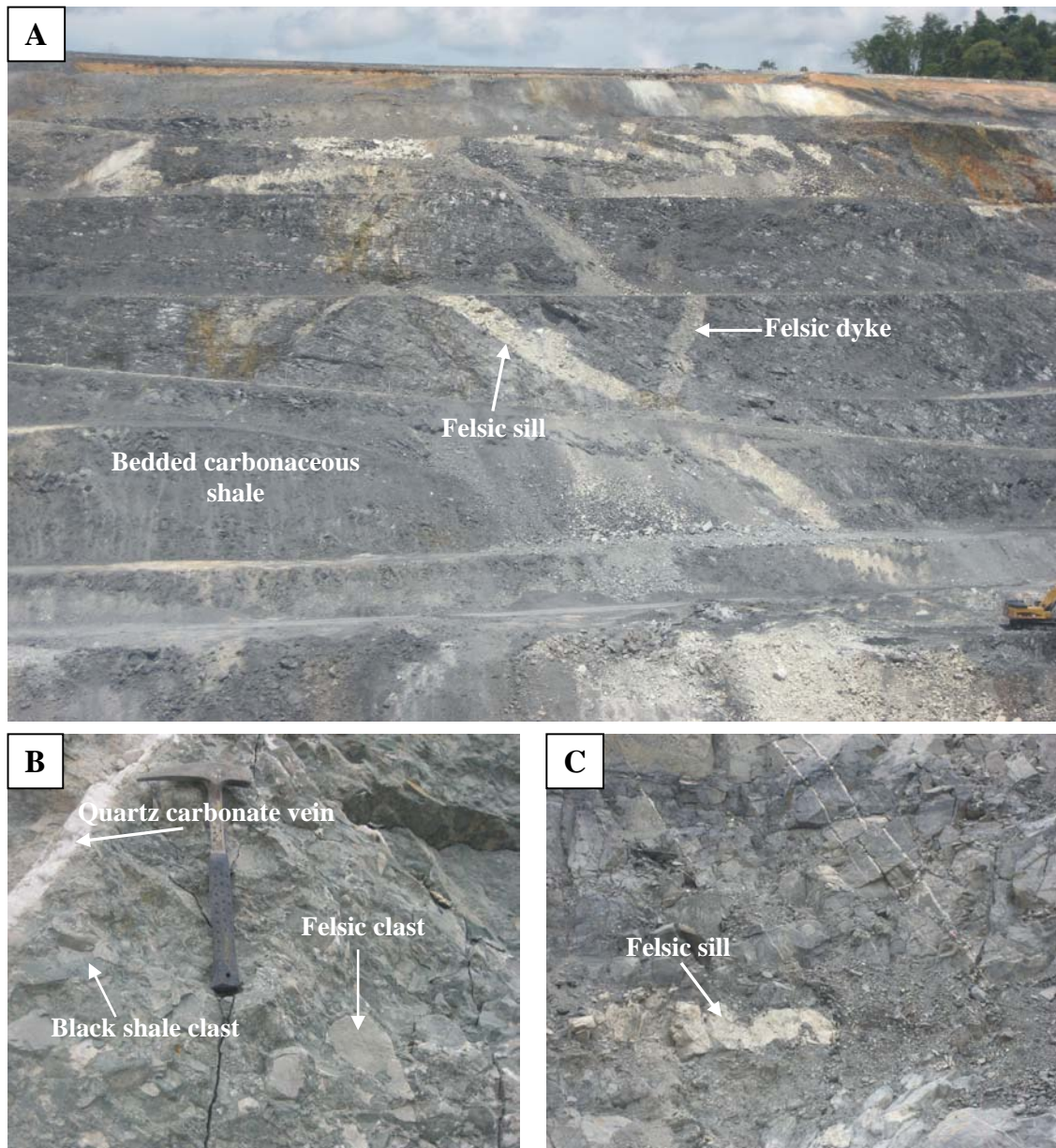


Fig. 3.13. Field view and outcrop photographs at Penjom, Central Malaysia. **A.** A view of the open pit facing north at the Penjom gold deposit. Note occurrence of felsic dyke and sill deformed within the host stratigraphy and carbonaceous shale, which is the dominant lithology. **B.** Outcrop of tuffaceous conglomerate. **C.** Close-up view of carbonaceous shale and felsic sill.

3.7. Age of host rocks

The age of host rock sequence from the Tersang, Selinsing and Penjom deposits were determined. Lithology of host sandstone and ages of younger zircon at Tersang are presented in Figs. 3.14 and 3.15. The maximum depositional age of the host sandstone unit ranges from 319.3 ± 5.9 to 337 ± 2.6 Ma (Carboniferous) evidenced by LA ICP-MS U-Pb zircon dating (Figs. 3.14A-E). In addition, LA ICP-MS U-Pb zircon analysis of the felsic sill that contains gold-bearing quartz gave ages of 218.8 ± 1.7 Ma (Late Triassic) as shown in Figs. 3.15A-D. Therefore, the age of the host sandstone could be as young as the age of the felsic sill which is Upper Triassic; possibly ranging from ca. 319 Ma to ca. 219 Ma.

Lithology of host siltstone and ages of younger zircon at Selinsing are presented in Figure 3.15. At the Selinsing deposit the dating of youngest zircons from the siltstone unit (Sample No. SM09-07 and SELDD1-102m) returned maximum ages, which range from 324 to 346 Ma (Figs. 3.16A-H). On a regional scale, to the north of the Selinsing area, the siltstone units are intruded by granite and syenite of Triassic age implying that the true age of the siltstone could be as young as Triassic.

Lithology of host rocks and ages of younger zircon at Penjom are presented in Figs 3.17 and 3.18. The age of host tuffaceous conglomerate is 264.9 ± 2.6 Ma indicated by LA ICP-MS U-Pb zircon age (Figs. 3.17A-C). Additionally, LA ICP-MS U-Pb zircon dating of host tuffaceous siltstone (Fig. 3.18D-F) returned Permian ages of 259.8 ± 4.9 Ma (Figs. 3.17A-C). This new finding has improved on previous studies done by some authors who suggested a Permo-Triassic age of the host rocks largely based on fossil evidence (Kamar Shah and Hewson, 2007).

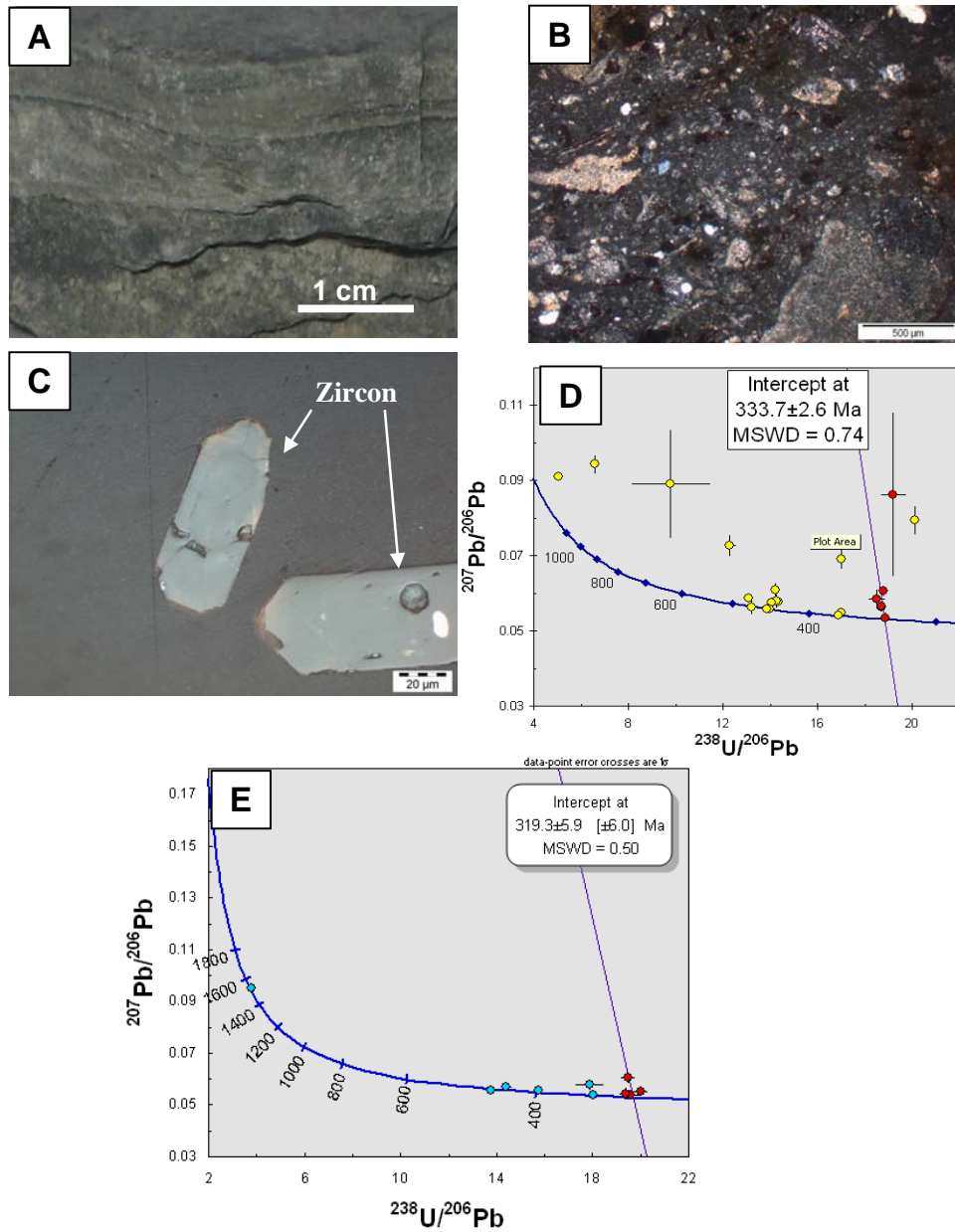


Fig. 3.14. Age of the Host sandstone at the Tersang gold deposit. **A.** Photograph of the host sandstone (Sample No. SM09-17). **B.** Photomicrograph of the sandstone. **C.** Photomicrograph of zircon from the host sandstone. **D.** Concordia plot of youngest zircon from the host sandstone. **E.** Concordia plot of youngest zircon from the host sandstone (Sample No. TER-R007).

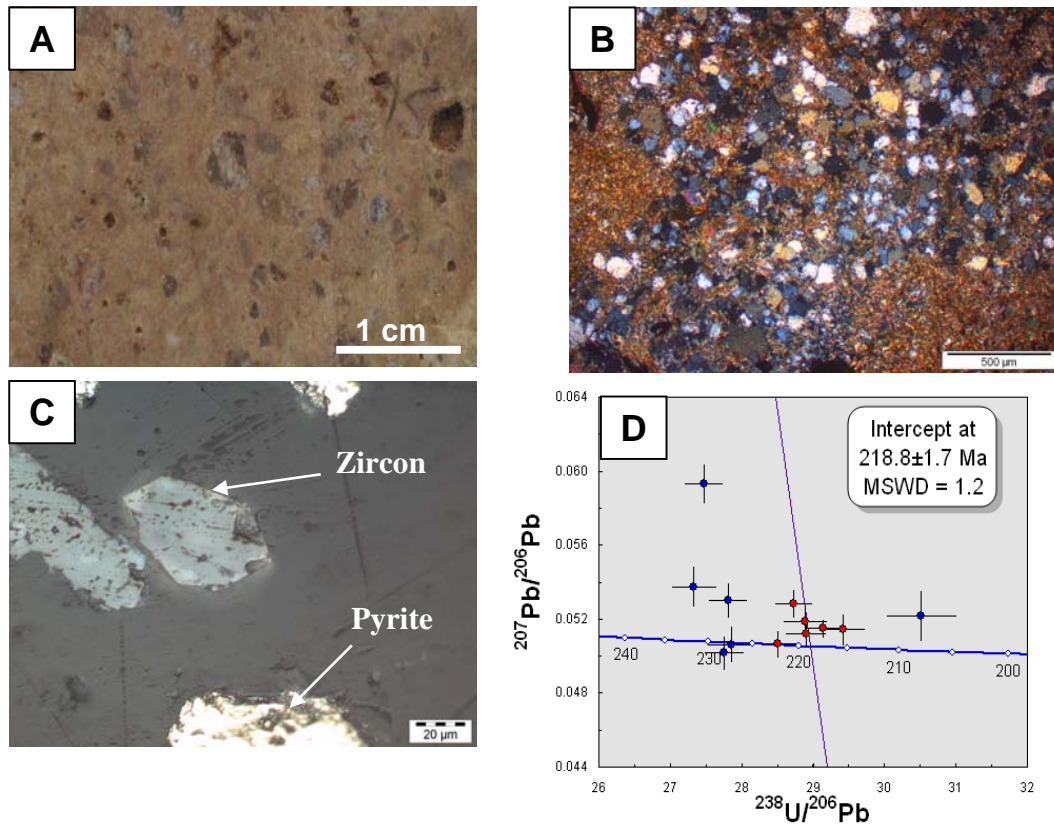


Fig. 3.15. Age of felsic intrusion at the Tersang gold deposit, Central Malaysia. **A.** Photograph of the felsic intrusion (Sample No. SM09-21). **B.** Photomicrograph of the felsic intrusion. **C.** Photomicrograph of zircon from the felsic intrusion. **D.** Concordia plot of youngest zircon from the felsic intrusion.

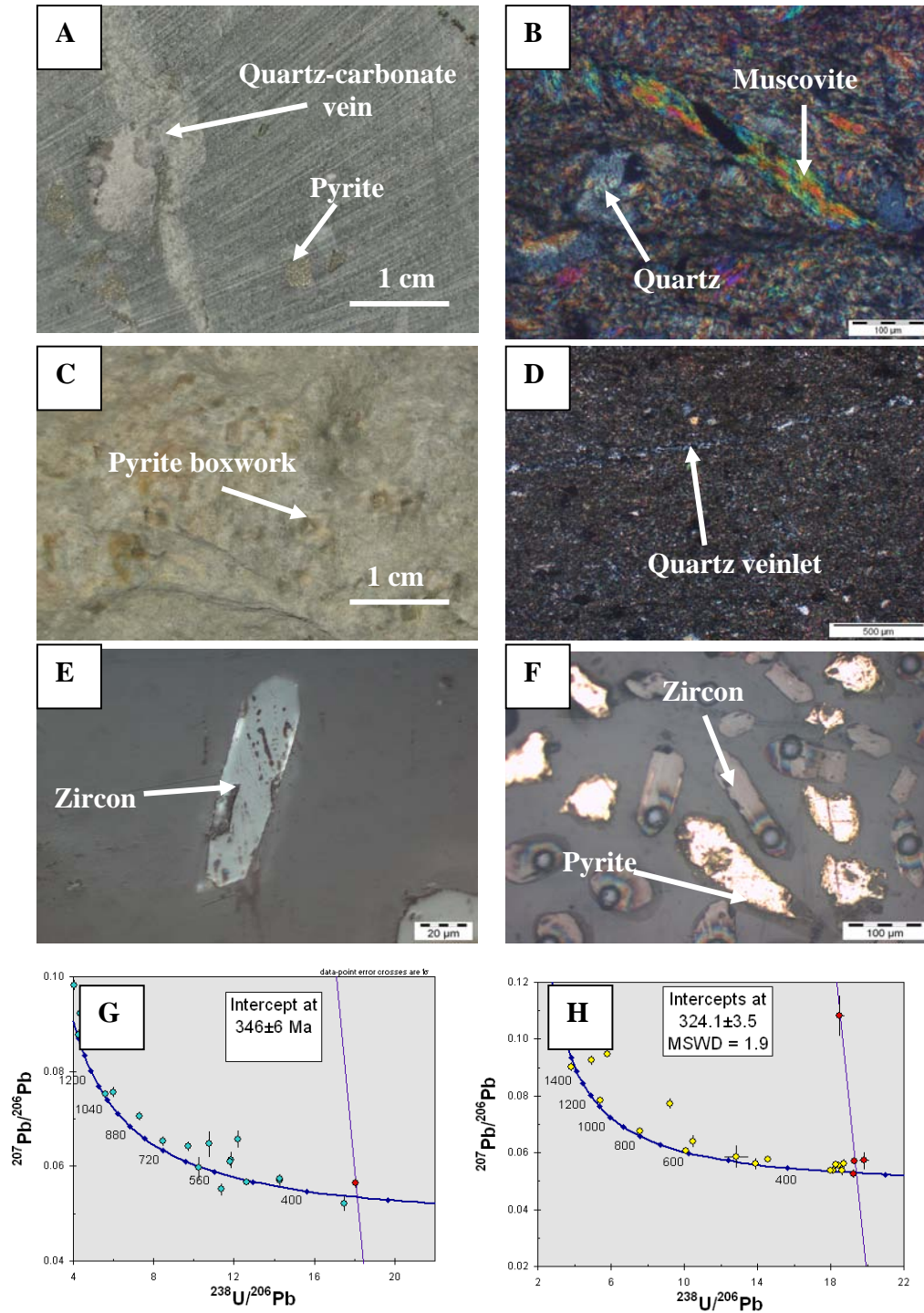


Fig. 3.16. Age of Host rock at the Selinsing gold deposit. **A.** Hand specimen of siltstone (Sample No. SELDD1-102m). **B.** Photomicrograph of the siltstone. **C.** Hand specimen of tuffaceous siltstone (Sample No. SM09-07). **D.** Photomicrograph of the tuffaceous siltstone. **E.** Photomicrograph of zircon from the siltstone. **F.** Photomicrograph of zircon from the tuffaceous siltstone **G.** Concordia plot of youngest zircon from the host siltstone (Sample No. SELDD1-102m). **H.** Concordia plot of youngest zircon from the tuffaceous siltstone (Sample No. SM09-07).

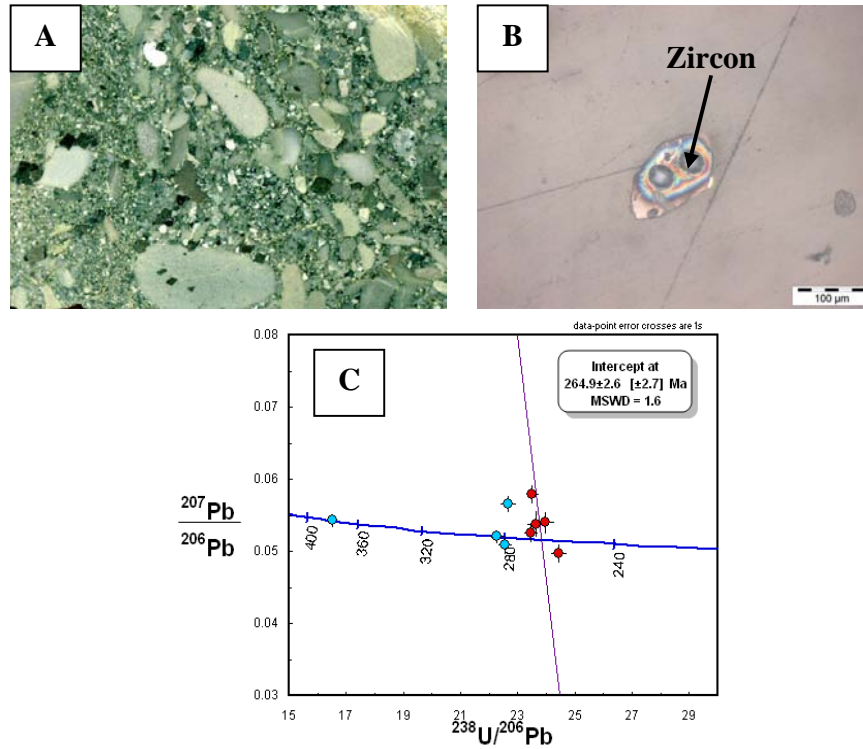


Fig. 3.17. Age of the host tuffaceous conglomerate at Penjom. **A.** Hand specimen of tuffaceous conglomerate (Sample No. PEN-R12). **B.** Photomicrograph of zircon. **C.** Concordia plot of younger zircon.

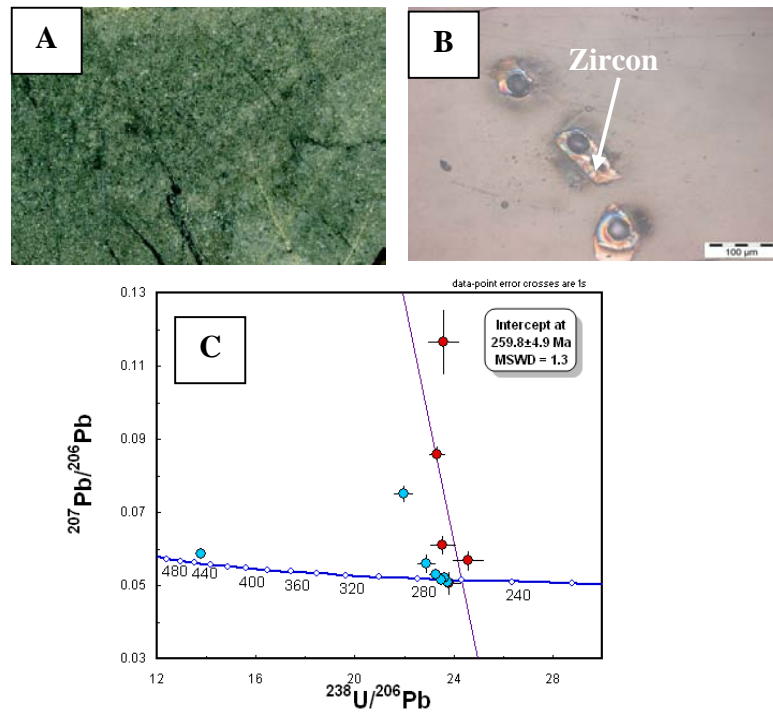


Fig. 3.18. Age of the host tuffaceous siltstone at Penjom. **A.** Hand specimen of Tuffaceous siltstone (Sample No. PEN-S3). **B.** Photomicrograph of zircon. **C.** Concordia plot of younger zircon.

3.8. Geochemical classification of intrusive rocks

Eight samples collected from the Tersang and Penjom intrusive exposures were analysed by X-ray fluorescence (XRF) and their compositions are presented in Figure.3.19. No intrusive rocks were found at the Selinsing mine-site during the period of fieldwork. In this study, the classification of Winchester and Floyd (1977) modified by Pearce (1996) for the volcanic rocks was used.

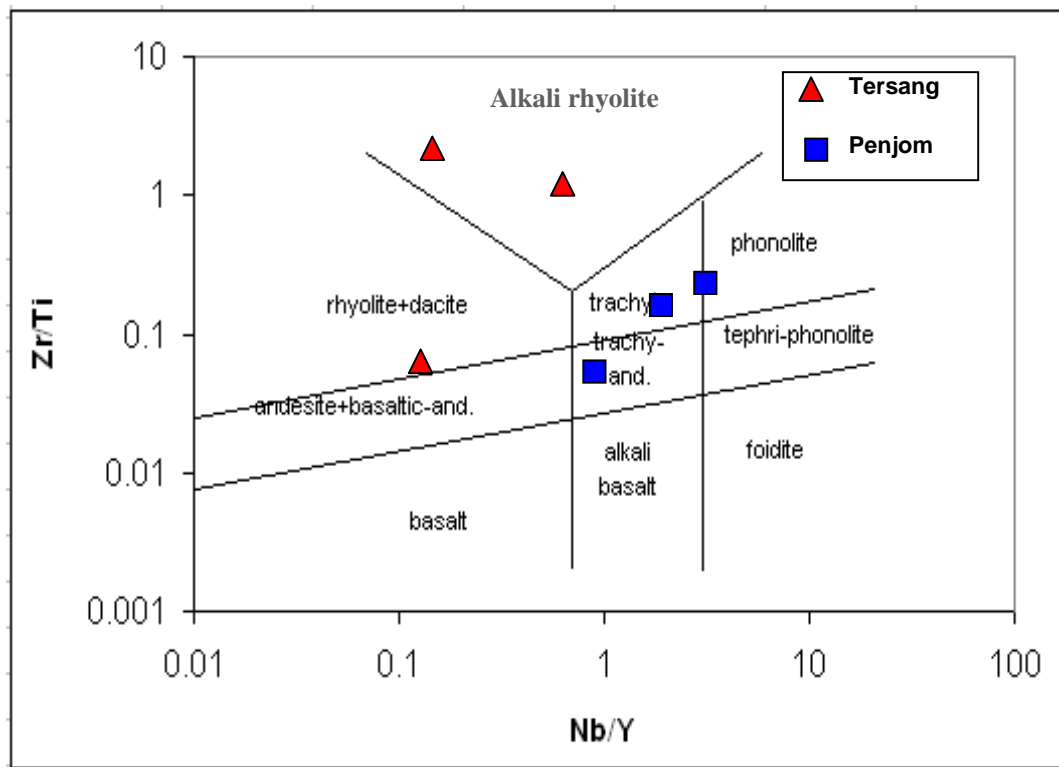


Fig. 3.19. Zr/Ti and Nb/Y discrimination diagram for the Tersang and Penjom intrusive rocks, Central Malaysia.

Chapter 3: Local geology and geochronology

Geochemical criteria that are not complying with this classification include the following: Al_2O_3 composition being more than 20 wt. %; Sc content more than 50 ppm and Ni content more than 200 ppm. Results of analysis are found at Appendix B.

3.9. Discussion

LA ICP-MS U-Pb zircon dating has shown that both the Selinsing and Tersang gold deposit host rocks contain detrital zircons that yield maximum age as old as Carboniferous. In comparison, the Penjom deposit is hosted in younger Permian age.

At the Tersang gold deposit, X-ray fluorescence analysis of intrusives has revealed a range of composition from alkali rhyolite to rhyolite-dacite compositions. In addition, the alkali rhyolite intrusion is Triassic in age and could be as young as the host sandstone. The rhyolite-dacite intrusion has not provided any zircon grain for dating and its timing is still unknown.

The composition of the alkali rhyolite probably points to an alkaline magmatism during late Triassic along the Bentong-Raub Suture Zone. This magmatism may be coeval to the Late Triassic crustally-derived granitoids for Peninsular Malaysia (Sevastjanova et al., 2010).

The Penjom intrusions have shown different compositions suggesting separate magmatic events. For instance, the first intrusion sample No. PEN-R04 collected at Kalompong east in the main pit has returned a trachyte composition (Fig. 3.19). The discrimination plot for Sample No. PEN-S1 has given a trachyandesite composition. However, the intrusion sample No. PEN-S2 collected from a sill structure has a trachyte composition. During fieldwork it was found that the trachyandesite dyke crosscuts the

trachyte sill suggesting that the emplacement of the volcanic rock of trachyandesite composition probably postdates the occurrence of the magma of trachyte composition.

3.10. Conclusions

- The Tersang gold deposit is hosted by sandstone and breccia that are cross-cut by felsic intrusion of alkali rhyolite and rhyodacite compositions.
- The Selinsing gold deposit is hosted by sequences of siltstone, argillite, and phyllite and the age of mineralisation is still unconstrained.
- The Penjom gold deposit is underlain by sequences of Permian shale, tuffaceous conglomerate, tuffaceous siltstone and tuffaceous breccia. These sequences are cross-cut by felsic intrusion of trachyte and trachyandesite compositions.
- At the Tersang gold deposit, the felsic sill that contains gold bearing quartz-sulphide veins has been dated using LA ICP-MS U-Pb zircon analysis and returned ages of 218.8 ± 1.7 Ma (Late Triassic). The age of mineralisation is thought to be Upper Triassic. The felsic sill age could also be the age of the host sandstone assuming provenance of detrital zircons from the surrounding felsic intrusion.
- At the Penjom gold deposit, the K-Ar age of sericite from tonalite intrusion gave a minimum age that ranges from 197 Ma to 199 Ma (Early Jurassic) and the mineralisation is thought to be coeval with the timing of tonalite emplacement (Per. com. Zakaria, 2010).

CHAPTER 4 STRUCTURAL SETTING

4.1. Introduction

This Chapter examines the nature, geometry, and morphology of different vein sets and their paragenesis at Tersang and Selinsing followed by discussion on the structural control of gold mineralisation at these deposits.

4.2. Geometry of vein sets at Tersang

Four orientation and style of veins are recorded at Tersang. The host sandstone sequence at Tersang strikes approximately N100° and dips 20°-28° to the south. This sandstone is intruded by a felsic intrusion, which occurs as a faulted sill (Fig. 4.1A). Both of these rock types are cross-cut by four different veins and their nature, morphology and distribution are discussed below.

The first set of quartz veins trend 060°-90° and dip 20° to the south or 30°-88° to the north and northeast. These veins vary in thickness from 20 to 45 cm and occur in the form of a hybrid extensional structure. The second set of quartz veins trends 098° to 104° and dips 50° to 64° to the north and thickness of these veins ranges from 4 cm to 1.2 m. The third set of quartz veins trends 108° to 118° and dips 54° to 88° to the north and northeast and these veins are 6-8 cm thick. The fourth set of quartz veins is orientated 148°-174° and dips 48°-70° to the northeast and the thickness of these veins ranges from 2 cm to 46 cm. This fourth set of veins also displays pinch and swell structures (Fig. 4.1B).

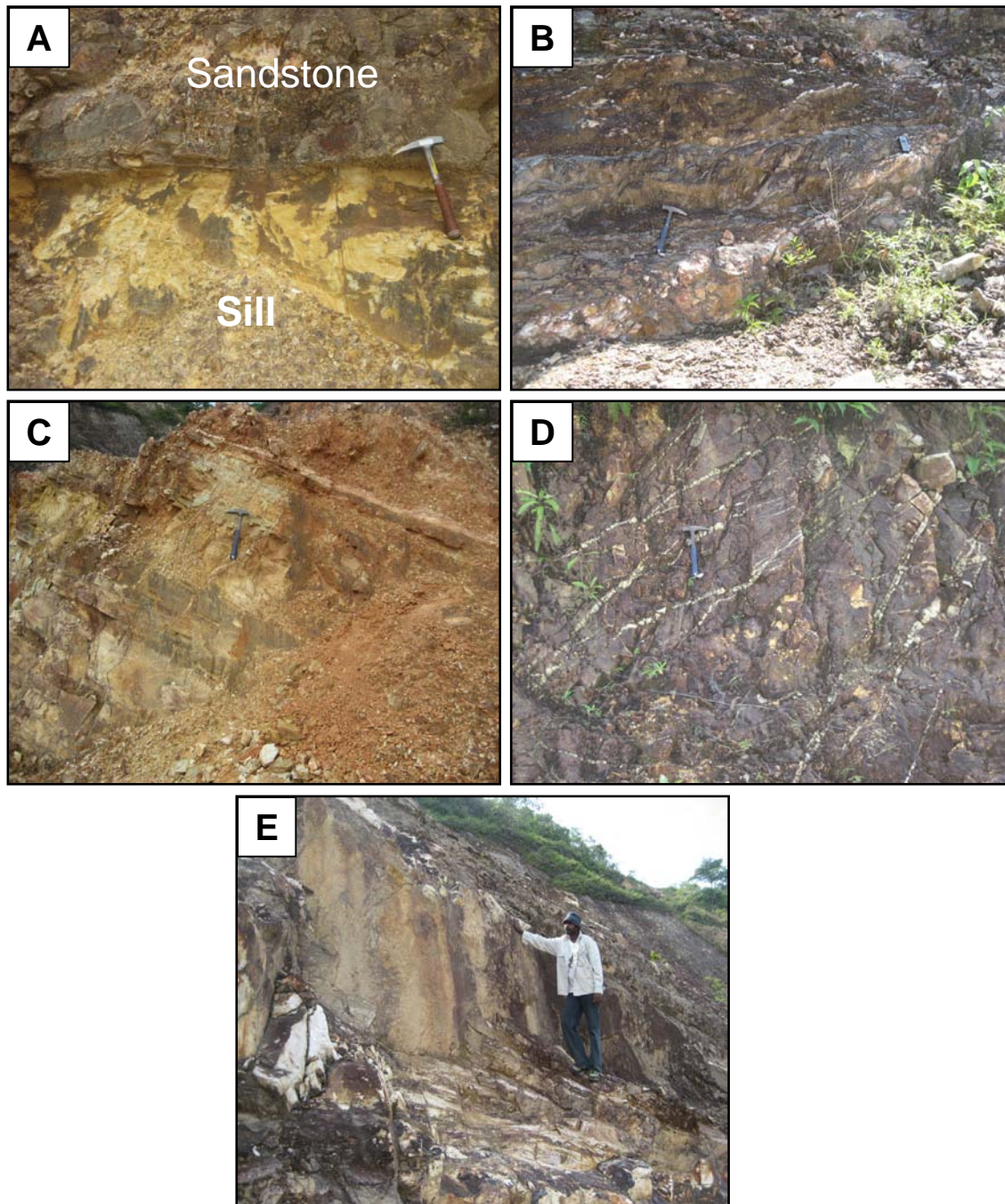


Fig. 4.1. Structural features of Host rock and vein assemblages at Tersang gold deposit. **A.** Felsic sill and host sandstone. **B.** Pinch and swell quartz vein. **C.** Quartz stringers cross-cutting bedding in weathered sandstone. **D.** Hybrid extensional quartz veins in sandstone. **E.** Close-up view of the fault plane held by the right hand of the observer.

Quartz stringers (2 mm to 1 cm thick) occur in the fourth set of veins (Fig. 4.1.C). Apart from these four sets of veins, some have a complex geometry called hybrid extensional veins (Fig. 4.1D). At the ore zone, a visible fault trending NS was found in the vicinity of the fourth set of veins that trends NNW-SSE. These veins are sub-parallel to the fault or cross-cutting it (Fig. 4.2A). The stereographic projection and the great circle plot of vein directions are shown in Figures. 4.2B and C.

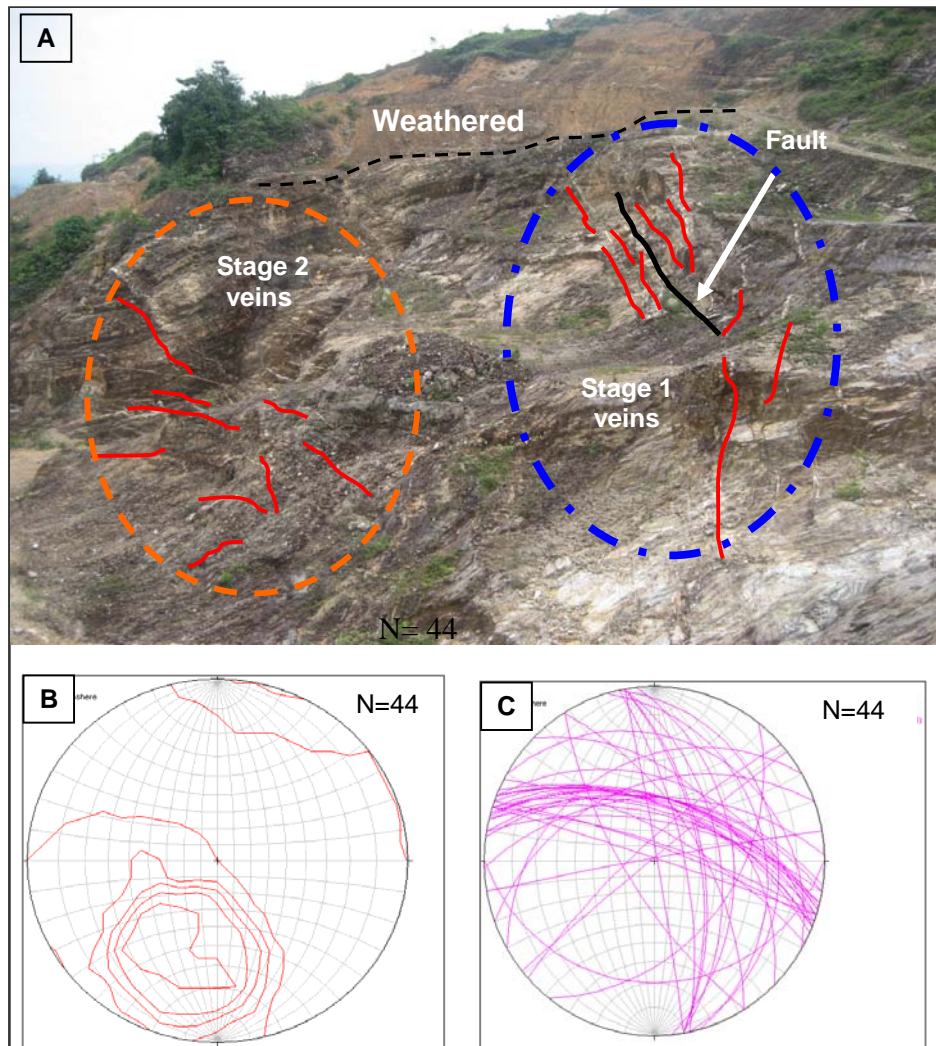


Fig. 4.2. Structural setting at Tersang. **A.** Field view of the different veins. **B.** Stereographic projection of the veins. **C.** Great circle plot diagram showing directions of the veins.

4.3. Selinsing structures

4.3.1. Surface structures

The host rocks at the Selinsing show different orientations from those at Tersang. In general, they are more deformed with much better defined fabrics and foliation. They strike 160° - 180° and dip 60° to 80° mostly to the east. Thrust faults are common in dark-grey to grey phyllite striking 160° and dipping 38° to the east, as well as recumbent folds, which are present in brownish grey siltstone (Figs. 4.3A-B). In addition, east plunging anticlinal folds and kink folding are common in phyllite (Figs. 4.3C-D). Sometimes, crenulation cleavage and asymmetric fold also were found in brownish to yellowish grey argillite (Figs. 4.3E-F).

More often, small anticlines are present in oxidised phyllite and argillite. They show fold axes orientated 050° and that plunge to the northeast (Figs. 4.4A-B). Some fault-related rocks such as mylonites occur in the form of lenticular bodies or boudins associated with quartz veins, the thickness of which range from 1cm to 20 cm in the shear zones (Fig. 4.4C). Near these mylonites, up to 4 m thick quartz veins which are in the form of pinch and swell crop out (Fig. 4.4D). Furthermore, these veins contain some films of the country rocks with thickness ranging from 2 mm to 4 mm. Further north away from the pinch and swell structures are found gash veins in weathered felsic dyke (Fig. 4.4E) and their presence suggests evidence of sinistral shear movement. Moreover, listric faults have been also found in mylonitised phyllite associated with faulted quartz veins (Fig. 4.4F).

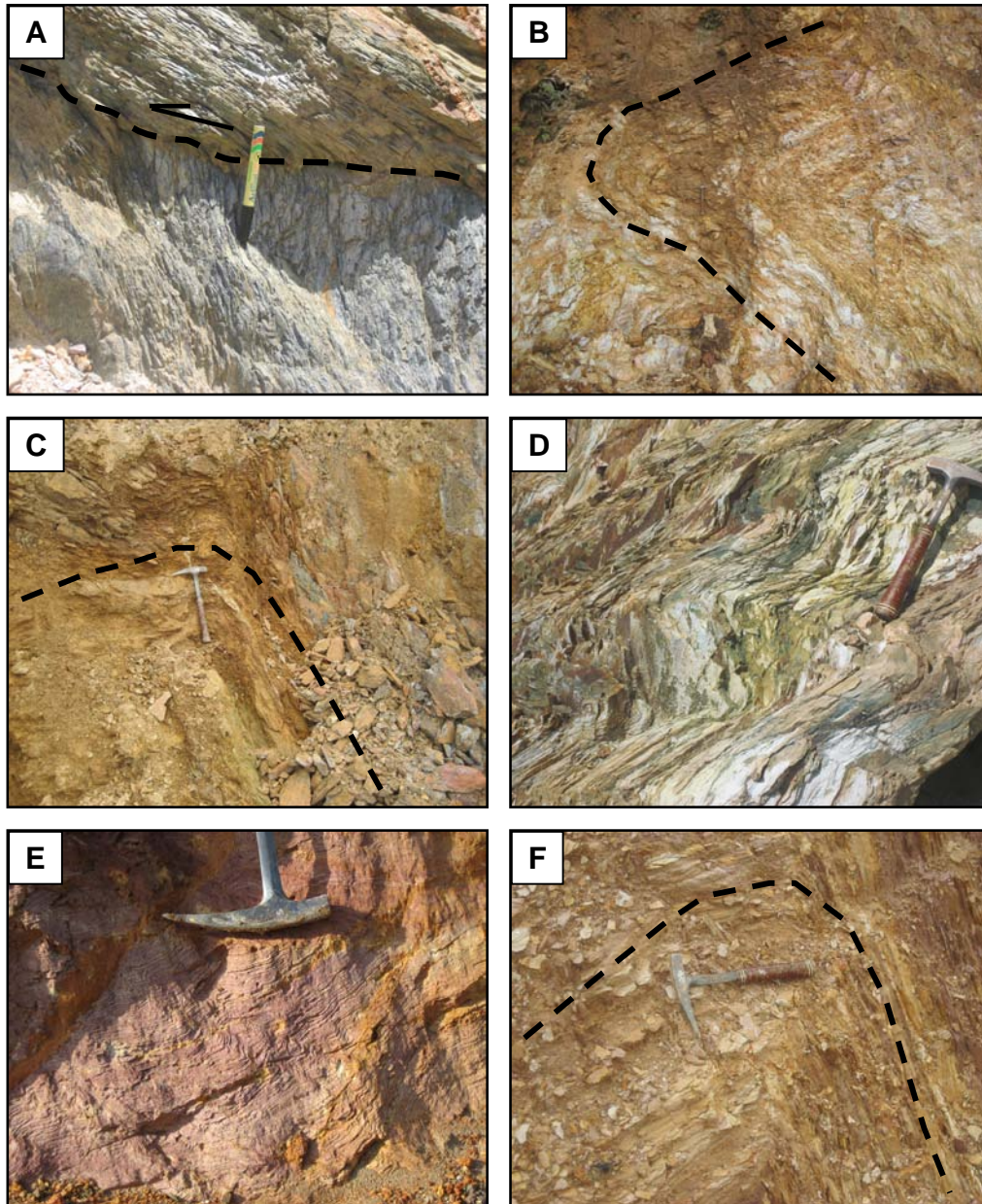


Fig. 4.3. Structural features of Host rock at the Selinsing gold deposit. **A.** Thrust fault in phyllite. Mylonite boundin in siltstone. **B.** Recumbent fold in siltstone. Pinch and swell quartz vein. **C.** Anticline in weathered phyllite and argillite. **D.** Kink fold in phyllite. **E.** Crenulation cleavage in argillite. **F.** Asymmetric anticline in argillite.

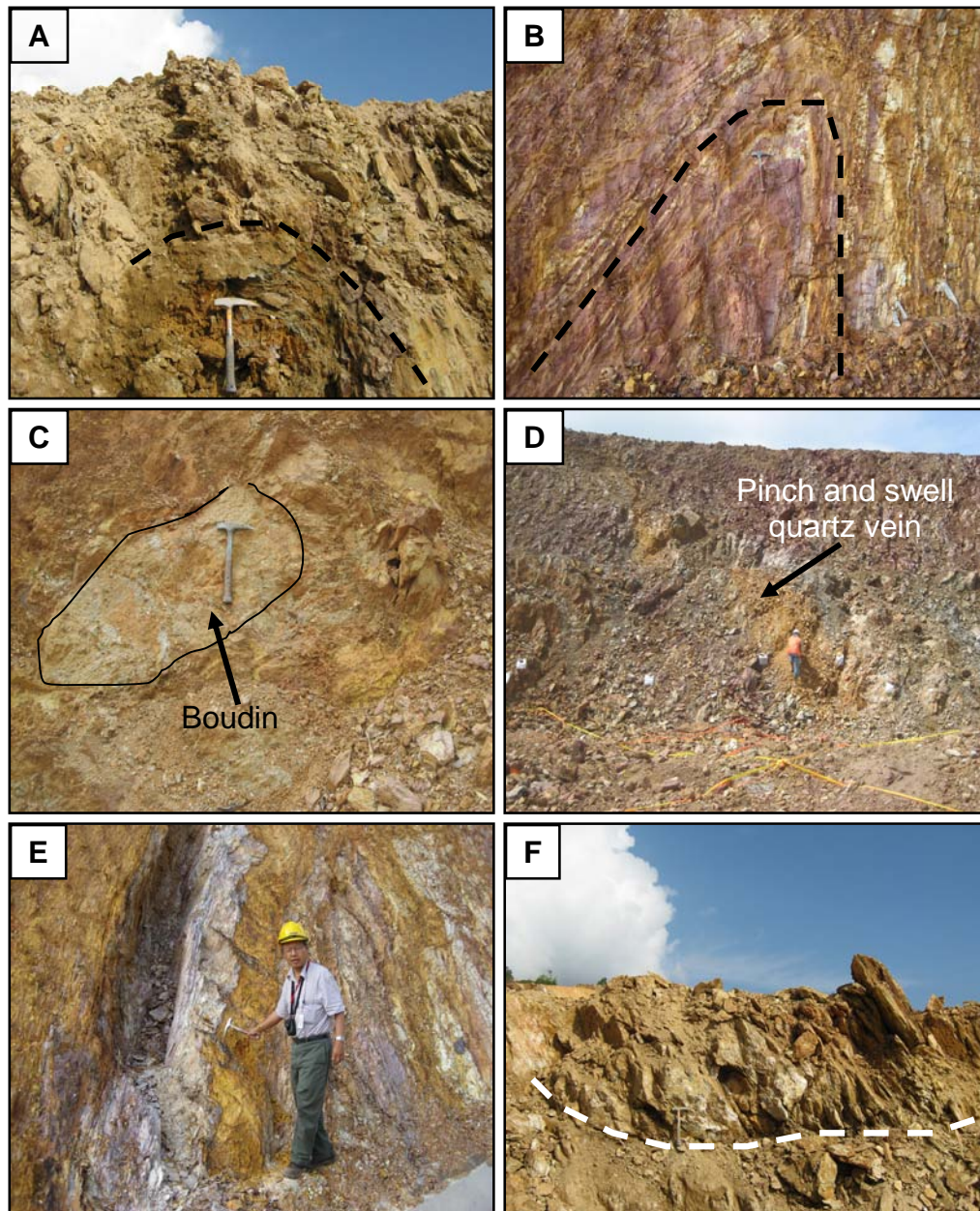


Fig. 4.4. Structural features of Host rock and vein assemblages at the Selinsing gold deposit. **A.** Anticline in weathered phyllite. **B.** Asymmetric anticline in argillite. **C.** Boudin of mylonite in host siltstone. **D.** Pinch and swell quartz vein in host siltstone. **E.** Gash veins in felsic dyke. **F.** Listric/detachment fault in a sequence of mylonite and phyllite.

4.3.2. Subsurface structures

The subsurface structures were observed in drill holes and shown in Fig. 4.5.

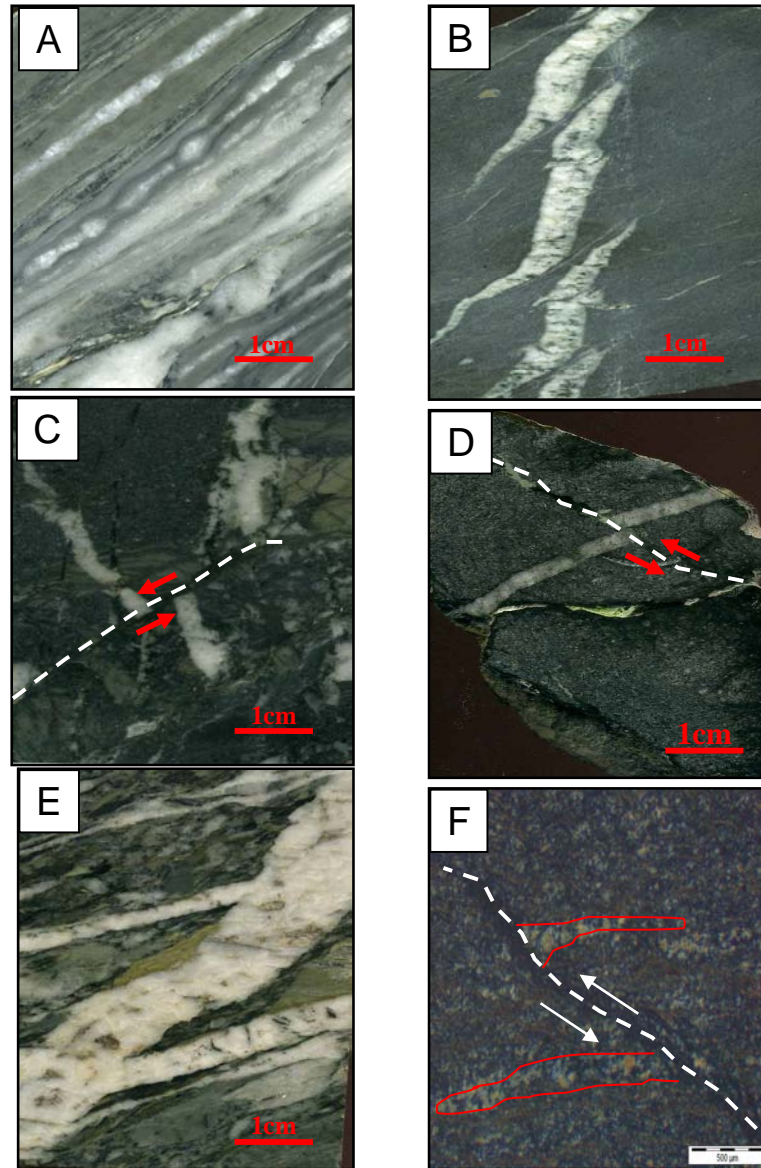


Fig. 4.5. Structural features of barren quartz veins at the Selinsing gold deposit. **A.** Pinch and swell quartz-carbonate veins in siltstone (Sample No. SEL-R107). **B.** En-echelon quartz vein in siltstone (Sample No. SEL-R038). **C.** Normal fault in siltstone (Sample No. SEL-R019). **D.** Reverse fault in siltstone (Sample No. SEL-R026). **E.** Extension vein in mylonite (Sample No. SEL-R012). **F.** Microscopic image of reverse fault cross-cutting extension vein in mylonite (Sample No. SEL-R027) as viewed in transmitted light.

The structures include (1) continuous to discontinuous pinch and swell quartz veins and lenses with variable thickness from 1mm to 4mm, (2) en-echelon quartz veins which are 1mm to 8 mm thick, (3) reverse and normal faults with limited extension, (4) the extension veins which are up to 1.5 cm in thickness and are the most abundant in core samples, and (5) faults of microscopic scale found in mylonite.

4.4. Vein paragenesis at Tersang and Selinsing

Paragenesis of quartz veins was established from cross-cutting relationships, replacement textures and gangue minerals found in hand specimen and thin sections.

4.4.1. Vein paragenesis at Tersang

At Tersang, two stages of mineralised veins have been found including the NNW-SSE orientated veins (stage 1) and the ESE-WNW orientated veins (stage 2). Stage 1 and 2 veins are presented in Fig. 4.6.

Stage 1 vein is characterised by quartz, pyrite, arsenopyrite, sphalerite and minor rutile. The earliest vein-fill material has made up this stage, which contains up to 90 % of the quartz formation. The sulphide grains account for approximately 10 % of the vein filling. The thickness of quartz veins varies up to 1.2 m as observed in the field. In hand-specimen, these quartz veins are milky to smoky in colour. In back-scattered electron images, there are a large number of fractured pyrite, arsenopyrite and sphalerite grains.

Chapter 4: Structural setting

The evidence suggests that sulphide grains have been subjected to a later brittle deformation within Stage 1 quartz veins. Stage 2 veins are probably the main stage gold event and contain pyrite, galena, geocronite $[\text{Pb}_{14}(\text{Sb,As})_6\text{S}_{23}]$, covellite, hematite, ilmenite, quartz and some silicates, amounting to 1-5% of the vein filling. Covellite and hematite were deposited during supergene processes.

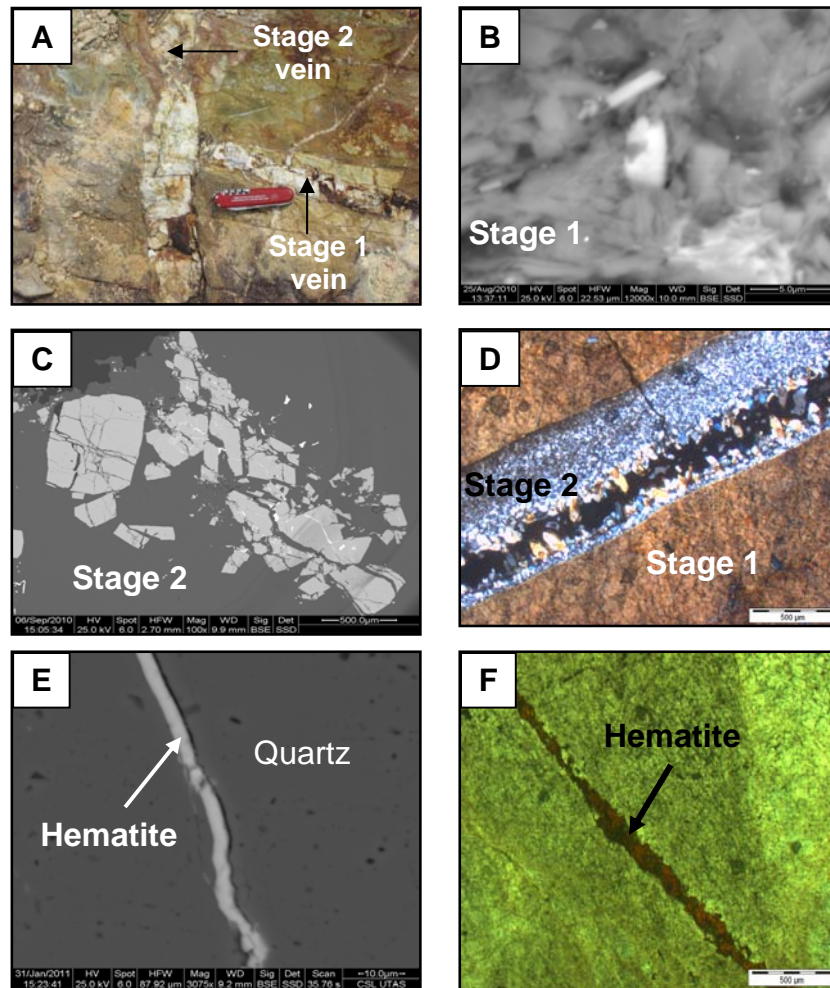


Fig. 4.6. Vein stages at the Tersang gold deposit. **A.** NNW-SSE and ESE-WNW quartz veins. **B.** Stage 1 quartz formation. **C.** Broken arsenopyrite in stage 2. **D.** Stage 1 and stage 2 veins. **E.** Back-scattered image of hematite vein in stage 2. **F.** Photomicrograph of hematite vein in quartz vein in cross polars.

In addition, the Stage 2 quartz grew syntaxially over periods of cracking and healing with hematite precipitation at a later stage. In back scattered images, sulphide minerals are found in the fracture filling suggesting that the later stage 2 was marked by subsequent brittle deformations that modified the preexisting sulphide textures.

4.4.2. Vein paragenesis at Selinsing

The Selinsing gold deposit is comprised of two generations of mineralised veins based on their mineral assemblage as described from core samples: early ductile-related veins are composed of quartz-carbonate \pm chlorite \pm sulphide and later brittle-related veins consists of quartz-sulphides \pm chlorite.

The earliest, ductile-related, stage 1 veins are milky white in colour and measuring 0.2-4 cm in width (Fig. 4.7A). These veins exhibit deformed pinch and swell structures at depth and contain pyrite, arsenopyrite and ankerite. Deformation of these veins suggests an early movement. In this stage, chlorite occurs in tiny deformed quartz stringers at depth. These veins are mostly sigmoidal in phyllites and are associated with economic mineralisation (Fig. 4.7).

The later, brittle-related, stage 2 veins are made up of veins which are milky to smoky in colour with width ranging from 0.3 to 13 cm. The veins contain fractures filled with sulphides and free gold. The sulphide minerals are mainly pyrite, arsenopyrite, and galena (Figs. 4.7B-D). In these veins, chlorite also occurs as tiny patches at the interface between wall rock and the veins called selvages. In addition, chlorite is confined to 1-4 mm wide short extension veins. The evidence seems to indicate that the later veins went

into cycles of subsequent brittle-ductile deformations evidenced by the repetitive occurrence of cataclasite in the orebody. The evidence suggests that much gold deposited during Stage 2 veins.

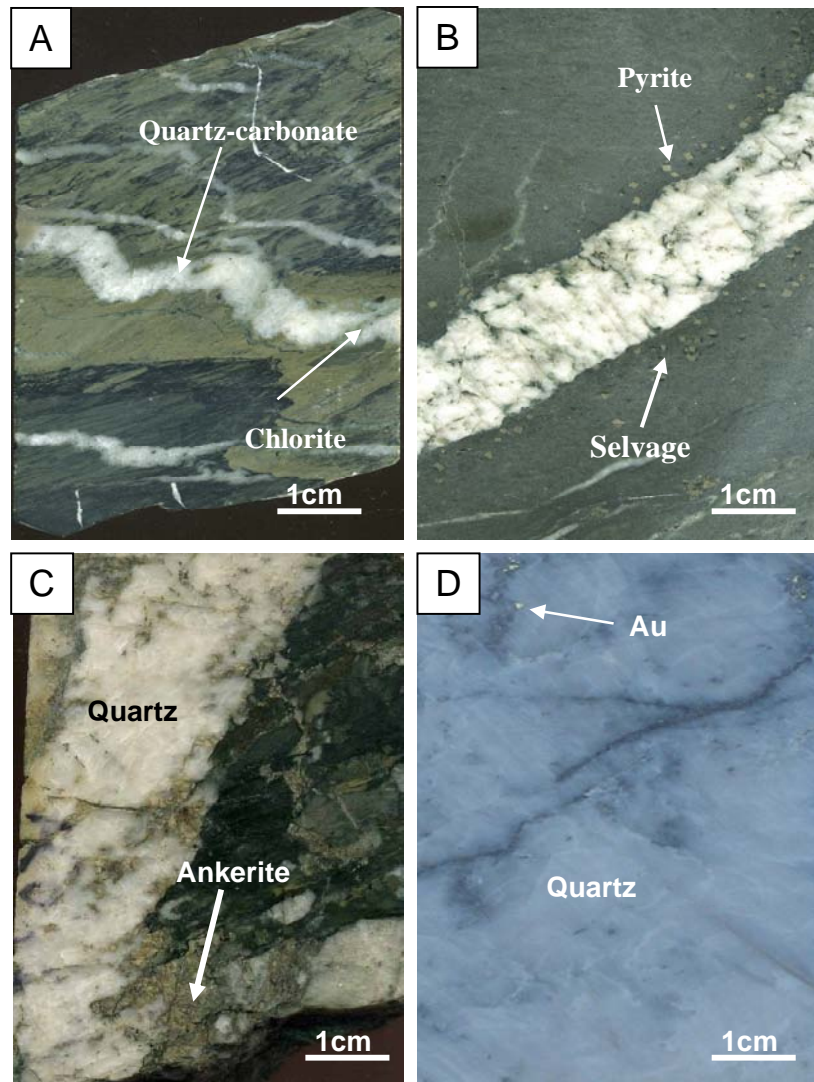


Fig. 4.7. Vein stages at the Selinsing gold deposit. **A.** Early-ductile deformed quartz-carbonate vein (Sample No. SEL-R047@ 121.9m). **B.** Late-brittle quartz-chlorite vein (Sample No. SEL-R036@ 31.9m). **C.** Stage 2 quartz-ankerite vein (Sample No. SEL-R041@ 80.10m). **D.** Late-brittle quartz-sulphide-gold vein (Sample No. SEL-R036@ 31.9m).

The shear sense of the veins is briefly discussed showing two types of deformation; a dextral and sinistral movements. The timing of each deformation was not established due to lack of close relationship (Fig. 4.8).

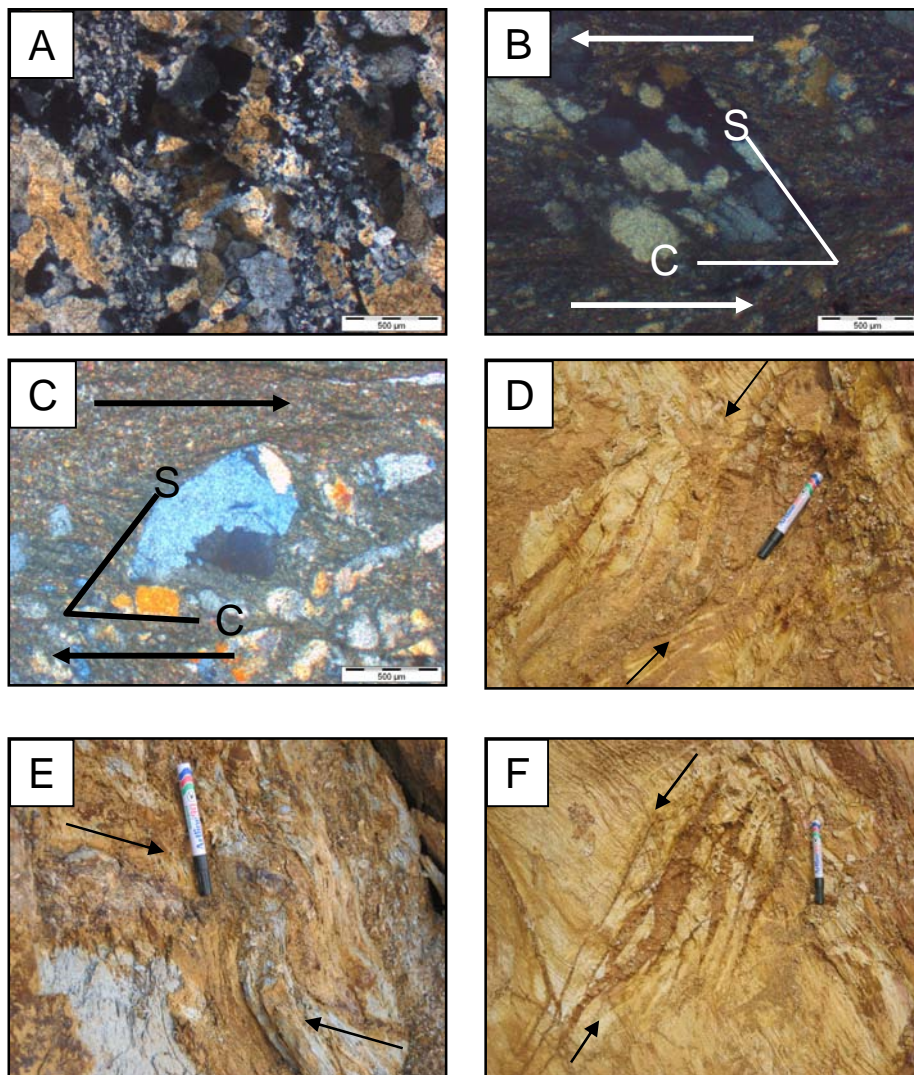


Fig. 4.8. Shear sense characteristics at the Selinsing gold deposit. **A.** Grain shape foliation in quartz vein. **B.** Sinistral shear sense in mylonite. **C.** Dextral shear sense in mylonite. **D.** Sinistral shear sense indicated by sigmoidal veins. **E.** Dextral shear sense indicated by sigmoidal veins in phyllite. **F.** Sinistral shear sense indicated by sigmoidal veins in siltstone. Note S-C fabrics in mylonite (photographs B and C).

4.5. Tectonic history at Selinsing

Tectonic evolution at Selinsing including events, detailed characteristics of related structures and types of vein is summarised in Table 4.1. Four main events can be distinguished at the Selinsing deposit. These deformations were formed during the collision of Sibumasu and East Malaya during Upper Triassic (Chapter 2). Firstly, there was deposition of the Permian sediments, which make up the Gua Musang Formation. Secondly, the D_1 deformation which produced quartz veins paralleling the bedding S_0 or foliation. The D_1 marks compression from the east when the thrust fault evolved and caused the formation of mylonite and cataclasite. Clues to support the D_1 event are the following: the presence of kink folds along margins of the ore body extending to the north within the argillite layers, first order reverse fault, which dips to the east, visible rotated porphyroclasts in mylonite and crenulation cleavage.

Thirdly, the D_2 deformation probably marks relaxation of the envelope of sheared rocks. Clues of relaxation or extension are the formation of dilation quartz veins. Formation of quartz veins cross-cutting foliation in boudins of mylonite also indicates reactivation. Formation of boudins is thought to have happened during extensional regime. The presence of pinch and swell quartz veins concordant to the bedding S_0 or foliation also marks relaxation. Mylonite layers have been stretched and deformed in envelopes of siltstone. As of normal faults, they are not common at the mine site. However, some of these faults were found in the core samples. They have been formed during relaxation (extension) or uplift. Listric normal faults are present indicating relaxation. D_1 , D_2 , and D_3 events are displayed on the structural map of the Selinsing gold

Chapter 4: Structural setting

deposit (Fig. 4.9). Lastly, the D₃ deformation is marked by formation of quartz veins during brittle regime and the presence of reverse faults that had cross-cut several portions of the orebody. D₃ is characterised by the presence of NW-SE and EW trending faults. D₃ event postdates the formation of sigmoidal quartz veins and possibly overprinted D₁ and D₂.

Table 4.1. Deformation history at the Selinsing gold deposit, Central Malaysia.

Event		Structure	Characteristics
Sedimentation		Bedding So mostly in shales and siltstones	Strike: N160-180°; dip: 60-80°E
D1 Compression		Thrust	Compression from the east; East dipping fault planes with listric character near surface
		Kink folds	Evolved in tuffaceous metasediments
		Reverse faults	Striking: N150°-165°; dipping: 40°-60°NE.
		Minor thrust fault	Fault plane trends NS and dips 20° to the east.
		Crenulation cleavage	Evolved in less competent strata such as shale
		Asymmetric anticlinal fold	Fold axis striking NS and dipping 65° to the east
		Mylonite and cataclasite formation	Lies along NS trending shear zone with lots of boudins.
D2 Extension	Ductile-related veins	Listric normal faults	Detachment fracture
		Pinch-swell quartz vein	Crosscut foliation/bedding in host rocks
		Sigmoidal quartz veins	Mostly crosscut bedding and foliation. Apparent sinistral shear.
		Normal microfaults	Centimetric in size
D3 Compression	Brittle-related veins	Quartz veins crosscut mylonite boudins	NNW-SSE & NNE-SSW trends, dipping 60°-78° to northeast, east or southwest
		Reverse faults	Possibly overriding D1 and D2; NE-SW trend and dips 20° to the southeast associated with low grade.

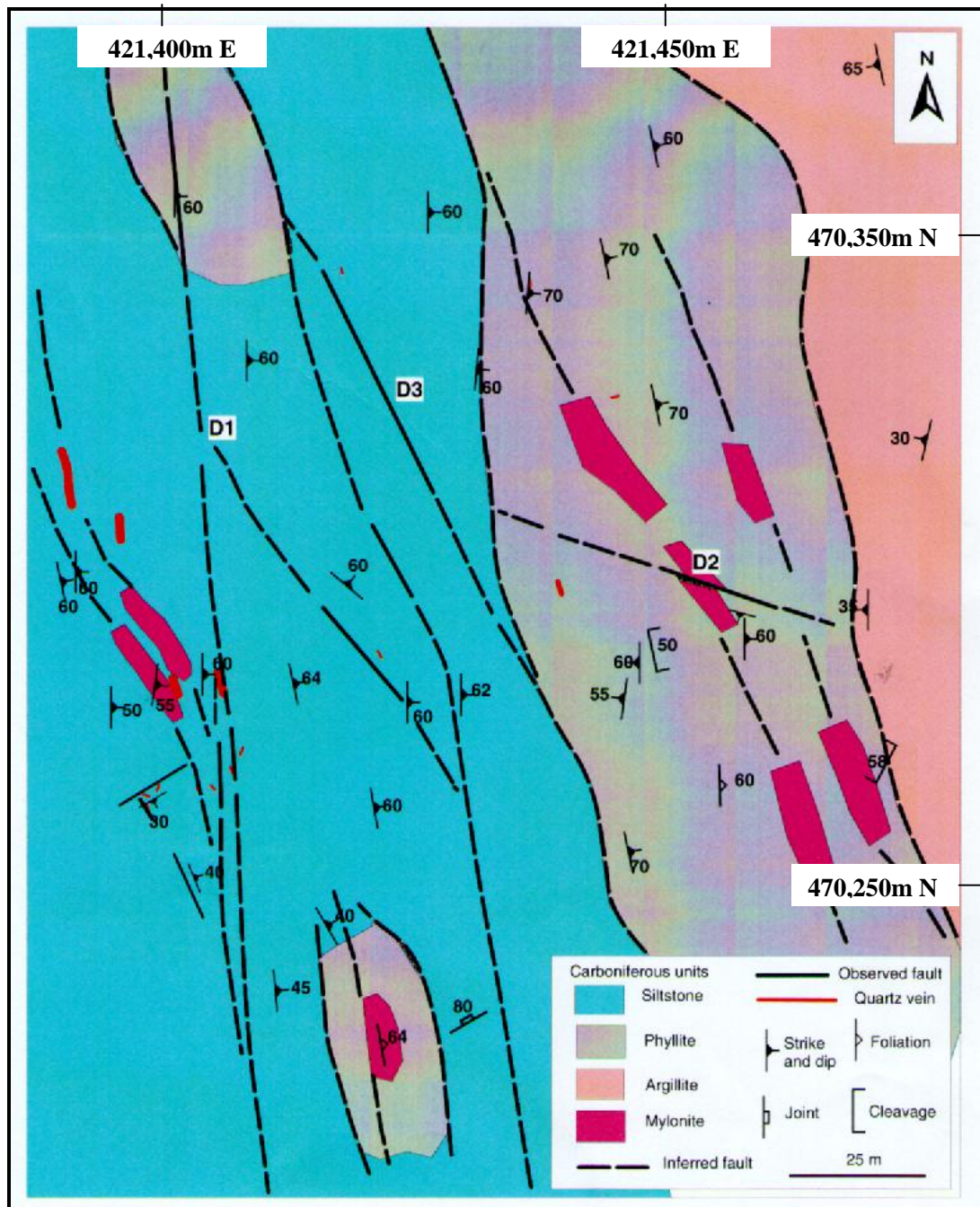


Fig. 4.9. Structural map of the Selinsing gold deposit displaying D₁, D₂, and D₃ deformation events, Central Malaysia.

4.6. Discussion

At the Tersang deposit, gold mineralisation is controlled by the 6 to 8 cm quartz veins (6 to 8 cm) that cross-cut the bedding and strike 108° - 118° and dip 28° - 78° to the northeast in the host sandstone. At Tersang, gold mineralisation is associated with Stage 2 veins, which are characterised by the occurrence of gold, pyrite, arsenopyrite, galena, geocronite, covellite and minor ilmenite.

At Selinsing, gold mineralisation is structurally controlled by the distribution of 2 to 5 m thick, NS and NNW-SSE trending pinch and swell structures in the host siltstone, by quartz stockwork and by extension veins that are contained within reverse faults. Grade control data across these veins shows high Au values in and around the veins. The Au grade drops away from these major structures (Figs. 4.10A and B). Gold grade ranges from 0.4 to 10 g/t for all the analysed samples. These veins cross-cut cataclasite units, which indicate that gold mineralisation occurred at some stage postdating faulting or the D_1 event.

Extension veins in mylonite also control gold mineralisation as confirmed by high grade Au values in these rocks (Fig. 4.11A). Similarly, quartz stockworks in phyllite also contain high gold values (Fig. 4.11B). However, quartz stockworks in argillite north of the orebody contain very low grade Au values (Figs. 4.11C-D). The evidence seems to indicate that there is a lithologic control of gold mineralisation at the Selinsing gold deposit.

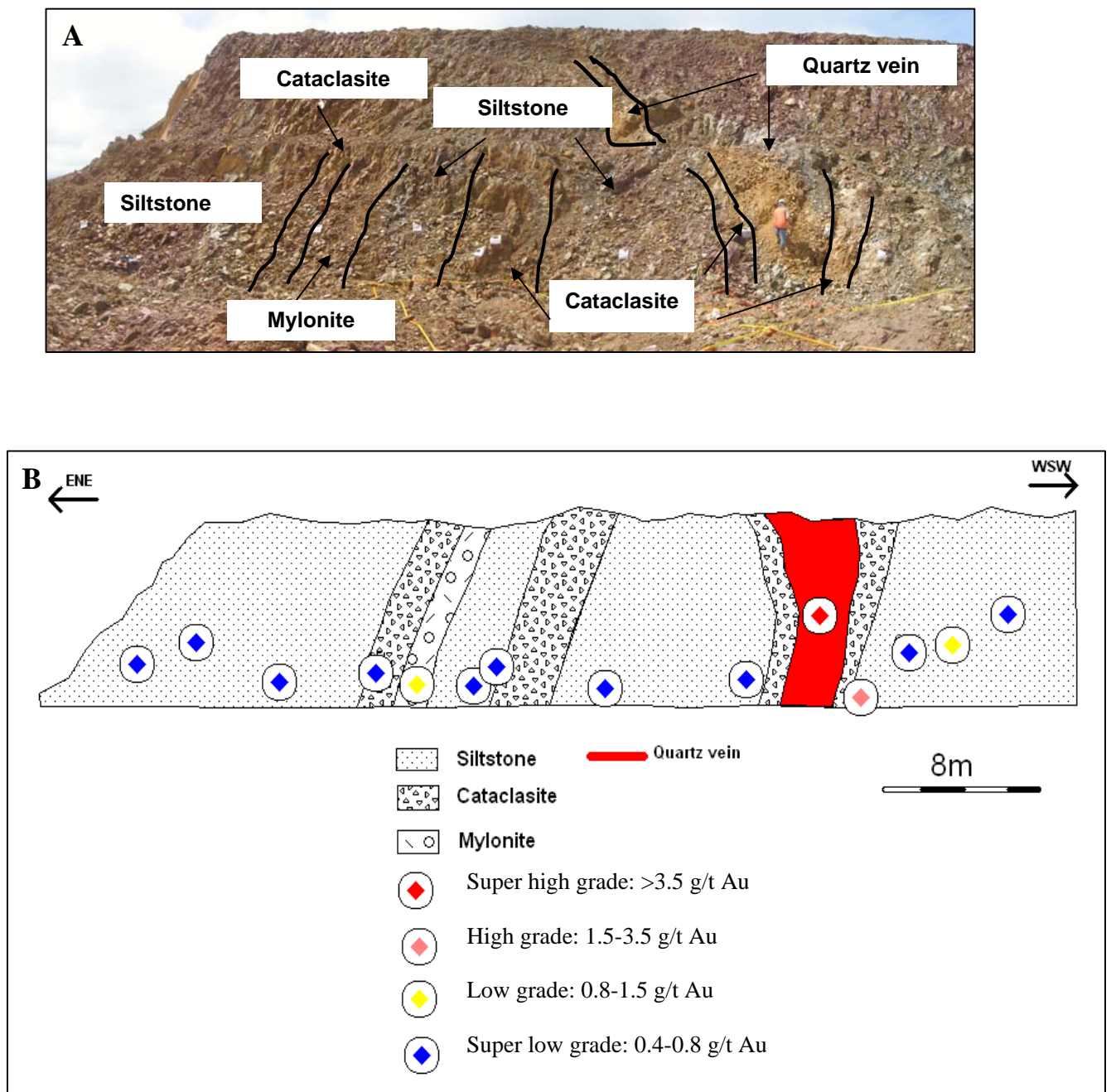


Fig. 4.10. Gold mineralisation at the Selinsing gold deposit. **A.** Outcrop photograph of pinch and swell structure associated with cataclasite, mylonite and the host siltstone at bench 547.5-545m reduced level. **B.** Cross-section across the bench showing higher concentration in gold close to the quartz vein that cross-cuts the cataclasite unit.

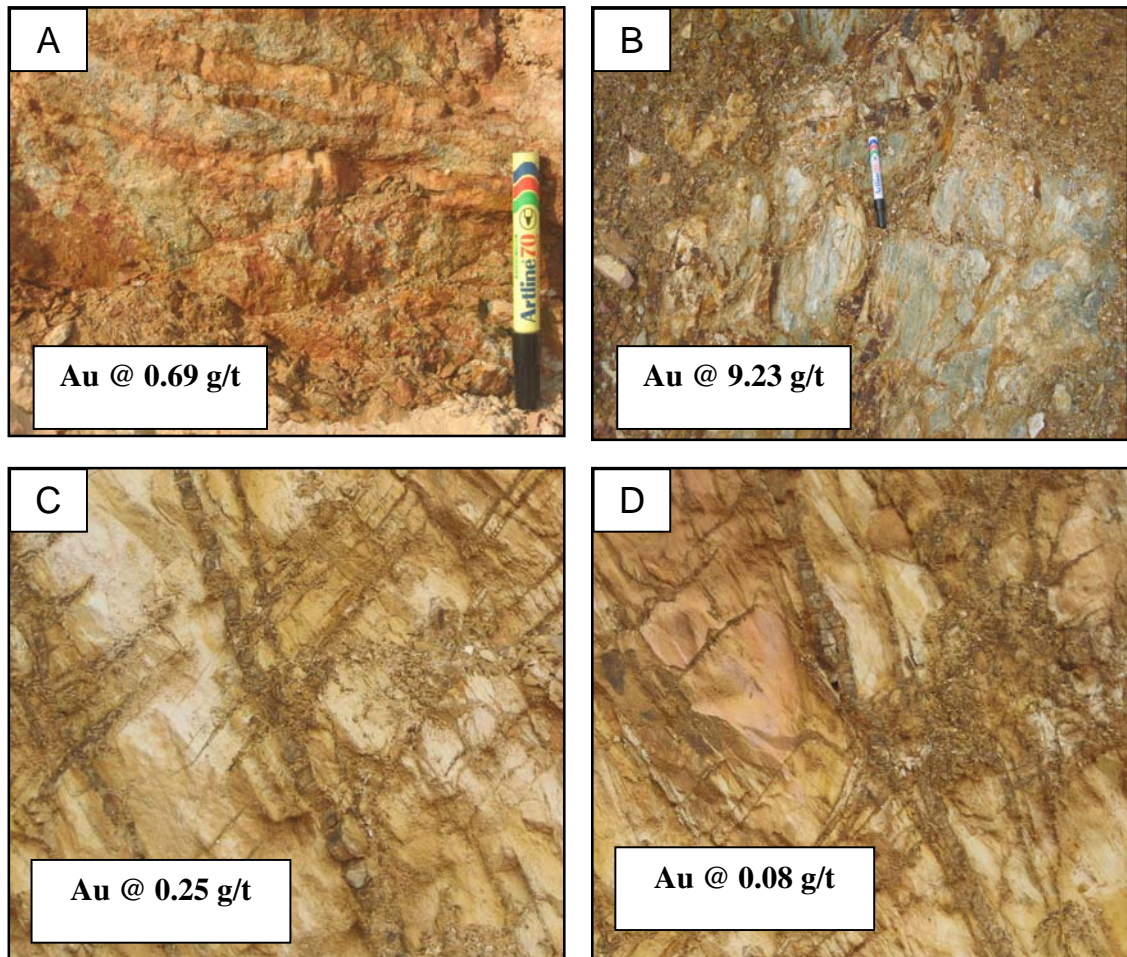


Fig. 4.11. Gold mineralisation at the Selinsing gold deposit. **A.** Gold bearing extension veins in mylonite. **A. B.** High grade quartz stockwork in phyllite. **C.** Barren to low grade quartz stockwork in argillite. **D.** Barren quartz stockwork in argillite, north of the orebody.

Multiple occurrence of cataclasite (Fig. 4.10) with lesser amount of mylonite suggests an evolving ductile deformation, which has been probably overprinted by brittle-ductile deformations.

CHAPTER 5 MINERALOGY, ALTERATION, PARAGENESIS AND METAL DISTRIBUTION

5.1. Introduction

This Chapter presents the nature of mineralisation at the Tersang and Selinsing gold deposits with an emphasis on alteration, mineral paragenesis, and distribution of pyrite and arsenopyrite within the zones of gold mineralisation. The Chapter finishes by describing metal distribution in drill holes at the Selinsing gold deposit.

5.2. Methods of study

Petrographic and textural studies were undertaken using Nikon and Olympus microscopes. Mineral paragenesis of the Tersang and Selinsing deposits were established by textural and cross-cutting relations of ore and gangue minerals. Alteration and clay mineral assemblages were determined by microscopy and Portable Infrared Mineral Analyzer (PIMA). First the samples are prepared by selecting the minerals for analysis using colour pencils. The samples must be dried in air or stove (<60°C). After sample preparation, the SWIR instrument is switched on and connected to a computer. Then the RS3 program is loaded to a computer for measuring purpose. In general, three measurements per samples were made. While measuring, the lights from other sources have to be avoided. The spectrum for each measurement is interpreted using the TSG (The Spectral Geologist) software.

Chapter 5: Mineralogy, alteration, paragenesis, and metal distribution

The scanning electron microscope (SEM) analysis was used to determine chemical composition and identification of ore and gangue minerals at the Central Science Laboratory (CSL), University of Tasmania. A total of 87 polished mounts were using Ladd 40,000 carbon evaporator with a 25 nm carbon layer. Voltage was set up at 25 kV and the spot calibrated at 6.0 (arbitrary unit) which corresponds to a beam current of around 1 nA. The back-scattered image comes with specific terms such as HFW which means horizontal field width (full width of image); WD means working distance (distance between final lens of SEM and sample surface) and SSD represents the solid state detector.

The Aqua Regia analysis was undertaken at the chemical laboratory of the Selinsing gold mine-site in Malaysia. The aim is to detect concentration of gold in drillcore samples. The results were used to discuss on gold distribution and metal zonation in drill holes. The procedure is to weigh 25 ± 0.01 g of pulverised sample in 500 ml beaker or conical flask. After weighing, add 30 ml HNO_3 (AR Grade). The measurement should proceed as the sample is totally wet and placed on hot plate and heated until vapour is colourless. After heating, the samples were removed and allowed to cool down. Later on 80 ml HCl and 30 ml HNO_3 were added and heating continued. Digestion followed for a minimum of 90 minutes until the sample reaches a pasty consistency (near dryness). If sample reaches dryness prior to 90 minutes, water was added and samples continued to digest. After that samples were removed from hotplate and rinsed from moisture on glass plates in beaker with tap water. In addition, 30 ml HCl and 10 ml of 0.05 % Magnafloc 333 solution were added and stirred up.

Afterwards, allow solids to settle to obtain clear liquor and decant 50 ml into test tube and extract 5 ml of 1 % Aliquat 336. Finally, shake for 1 minute, then remove clear liquor with vacuum device and add 50 ml 10% HNO_3 . Finally, the reading is made on AAS (atomic absorption spectrometry) for gold.

5.3. Alteration

This section describes alteration at the Tersang and Selinsing gold deposits in Central Malaysia.

5.3.1. Tersang deposit

At the Tersang gold deposit, argillic alteration is ubiquitous and characterised by occurrence of sericite, illite and montmorillonite as evidenced by PIMA. Illite and montmorillonite occur in the form of pinkish white patches infilling fissures that cross-cut quartz veins (Figs. 5.1A-D). Occurrence of these clay minerals may be due to supergene processes. In thin section, the sericitic alteration is pervasive in the sandstone unit within the Triassic Kaling Formation, and in some parts of the Triassic felsic intrusion (Figs. 5.1E-F).

Sericite is also found in the breccia where it replaced feldspar phenocrysts. The lack of core samples made it difficult to distinguish between proximal and distal alteration assemblage in and around the ore zone. However, illite-montmorillonite-hematite alteration seems to be distal from gold-bearing veins at about 40 m, and the sericite alteration appears to be proximal to the ore zone.

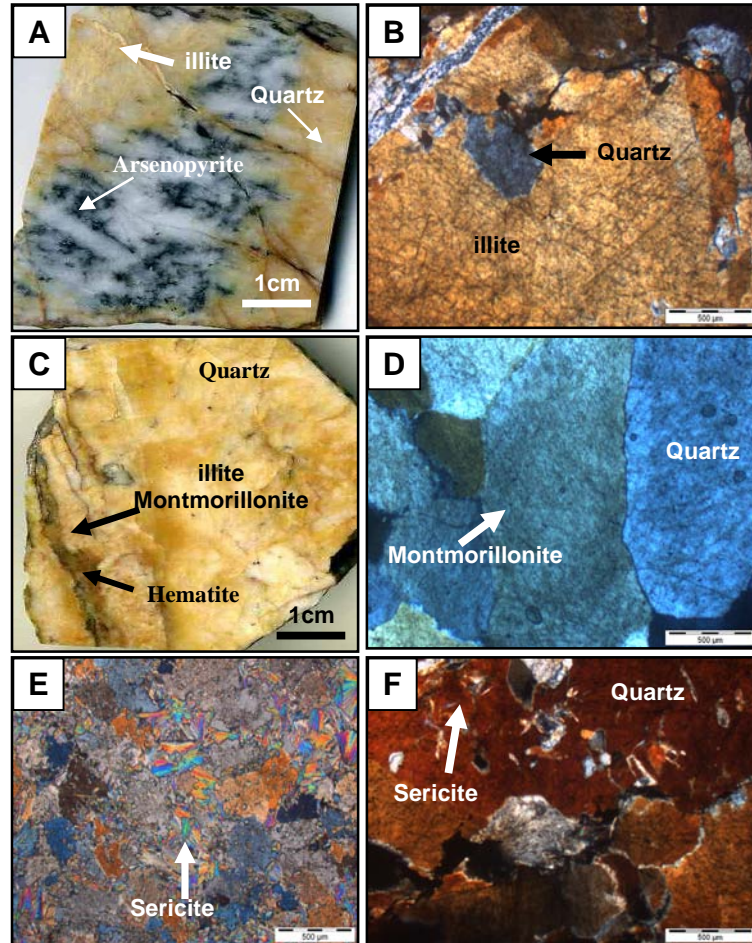


Fig. 5.1. Alteration mineral assemblages at the Tersang gold deposit. **A.** Quartz-illite-sulphide alteration (Sample No. TER-R029). **B.** Photomicrograph showing illite and quartz assemblage (Sample No. TER-R029). **C.** Quartz-illite-montmorillonite in hand specimen (Sample No. TER-R027). **D.** Photomicrograph of quartz-montmorillonite assemblage (Sample No. TER-R027). **E.** Photomicrograph of sericite alteration in the felsic intrusion (Sample No. TER-R033). **F.** Photomicrograph of quartz and sericite alteration in the host sandstone (Sample No. TER-R007). Photomicrographs were taken in transmitted light.

5.3.2. Selinsing deposit

At the Selinsing gold deposit, quartz-carbonate alteration is dominant in the host rock as well as in the veins (Fig. 5.2A). In interbedded black mudstone and siltstone,

1-3 mm thick, smoky quartz carbonate veinlets occur in core samples (Sample No. SEL-R009). At depth, ankerite alteration occurs in calcareous phyllite (Fig. 5.2B).

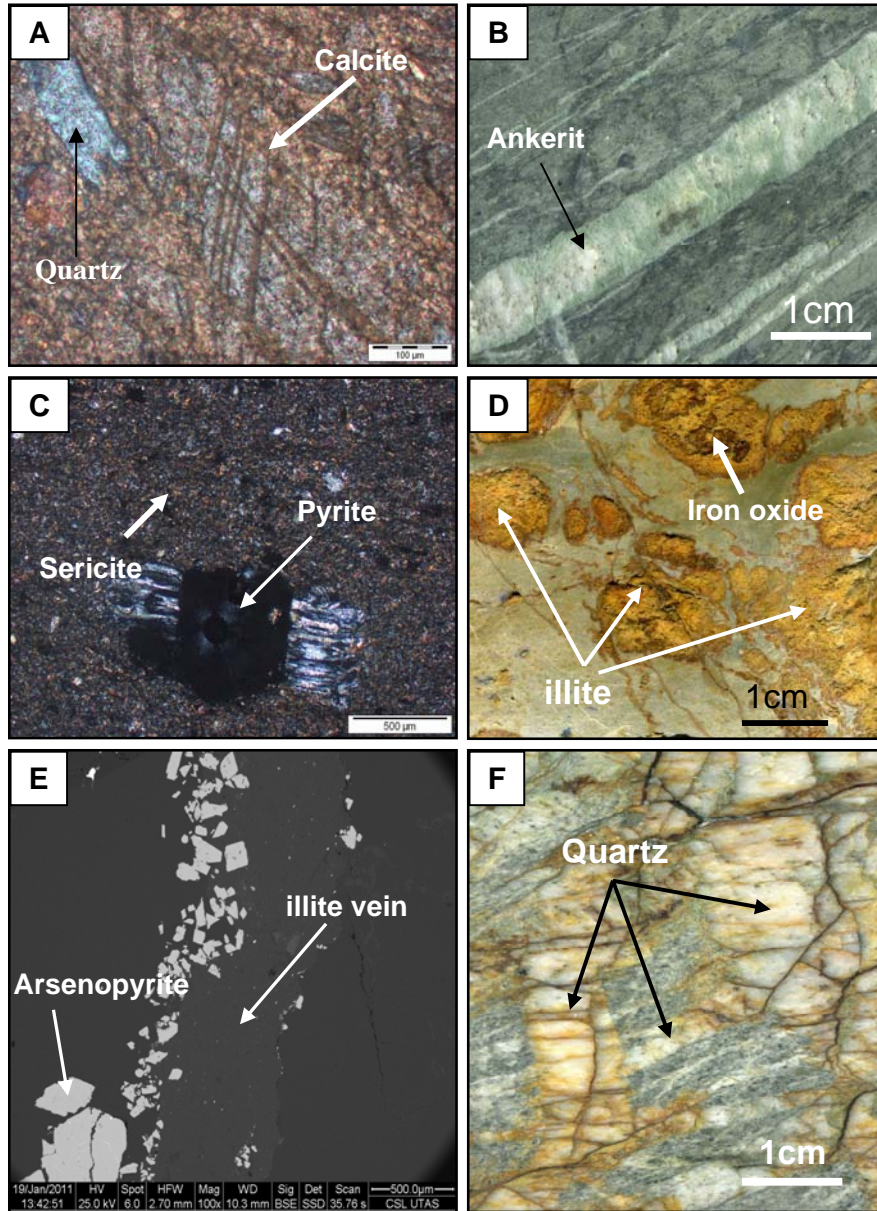


Fig. 5.2. Alteration assemblages at the Selinsing gold deposit. **A.** Quartz-calcite vein in mudstone (Sample No. SEL-R009). **B.** Quartz-ankerite vein (Sample No. SEL-R039). **C.** Sericite alteration in the host siltstone. **D.** Illite alteration in phyllite (Sample No. SEL-R094). **E.** Back-scattered image of illite vein associated with arsenopyrite (Sample No. SEL-R094). **F.** Quartz stockwork (Sample No. SEL-R001).

Quartz-ankerite alteration assemblage is close to the high-grade ore zone (Sample No. SEL-R041 @ 80.10 m) and mostly presents in pyritic cataclasite. Sericite alteration is present in the host siltstone and phyllite (Sample No. SM09-07) (Fig. 5.2C). Illite alteration occurs in a few samples (Sample No. SEL-R094@30m) (Fig. 5.2D) in strongly weathered phyllite and cataclasite as evidenced by electron probe microanalysis (Fig. 5.2E). The presence of illite associated with iron oxides could partially due to supergene processes. Silicification is characterised by the presence of quartz stockwork in shallow parts of the ore zone (Fig. 5.2F) and commonly in siltstone, cataclasite and breccia.

5.4. Ore mineralogy and paragenesis at Tersang deposit

The ore minerals found at the Tersang gold deposit are pyrite, arsenopyrite, sphalerite, galena, geocronite, covellite and gold with gangue minerals of ilmenite, rutile, hematite, illite and montmorillonite. The paragenesis of each mineral is summarised in Table 5.1.

5.4.1. Pyrite

Pyrite is the most common sulphide mineral at the Tersang deposit. Pyrite grains are white in colour in reflected light, sometimes show idiomorphic crystals but mostly the pyrite grains are brecciated or corroded in veins. They are often disseminated and angular together with carbonaceous materials in some veins. Detailed paragenetic studies at Tersang revealed four pyrite types as described below: (1) Euhedral to subhedral “spongy” pyrite with internal fracturing located in wallrock and quartz vein (pyrite 1).

Chapter 5: Mineralogy, alteration, paragenesis, and metal distribution

Table 5.1. Mineral paragenesis at the Tersang gold deposit, Central Malaysia

Stage		Stage 1	Stage 2
Ore minerals	Pyrite 1	██████████	
	Pyrite 2	██████████	
	Pyrite 3	██████████	
	Pyrite 4	██████████	
	Arsenopyrite	████████████████████	
	Galena	████████████████	
	Sphalerite	██████████████████	
	Gold	██	
	Geocronite		████████████████
	Covellite		██
Gangue	Ilmenite	-----	
	Rutile	-----	
	Sericite		██
	Hematite		██
	Illite		██
	Montmorillonite		██

██████████ Major ██████████ Minor ----- Trace

(2) euhedral clean pyrite found in wallrock and felsic rhyolite (pyrite 2) overgrown on pyrite 1, (3) amorphous pyrite with high As and high Au hosted in wall rock (pyrite 3) and (4) fracture-fill or vein pyrite with high As and low Au (pyrite 4).

5.4.1.1. Euhedral to subhedral “spongy” pyrite (pyrite 1)

This pyrite type has a variable size approximately up to 300 μm across. It represents the core zone of most pyrite grains found in the host sandstone (Fig. 5.3A). It contains tiny inclusions of sphalerite. Discontinuous microfractures are found in these pyrite grains. It also contains internal fractures when hosted in quartz veins.

5.4.1.2. Euhedral overgrown/clean pyrite (pyrite 2)

This pyrite type is characterised by the presence of internal fracturing, and the size ranges from 50 to 100 μm (Fig. 5.3B). This type of pyrite is mostly disseminated in the host rock with a discontinuous rim, and the thickness of which varies from 10 to 20 μm .

5.4.1.3. Vein and intrusion hosted pyrite (pyrite 1 and pyrite 2)

The vein-hosted pyrite is characterised by brecciated grains infilling fractures. They are euhedral to subhedral and up to 1 mm in width. These grains are also found in the form of cube-shaped grains in patches of oxidised geocronite in quartz veins (Fig. 5.3E). In addition, euhedral grains are found in silicate matrix trapped in the quartz veins. Intrusion-hosted pyrites are subhedral and clean pyrite, and disseminated. The pyrite grains are 0.5 to 1 mm in width (Fig. 5.3F).

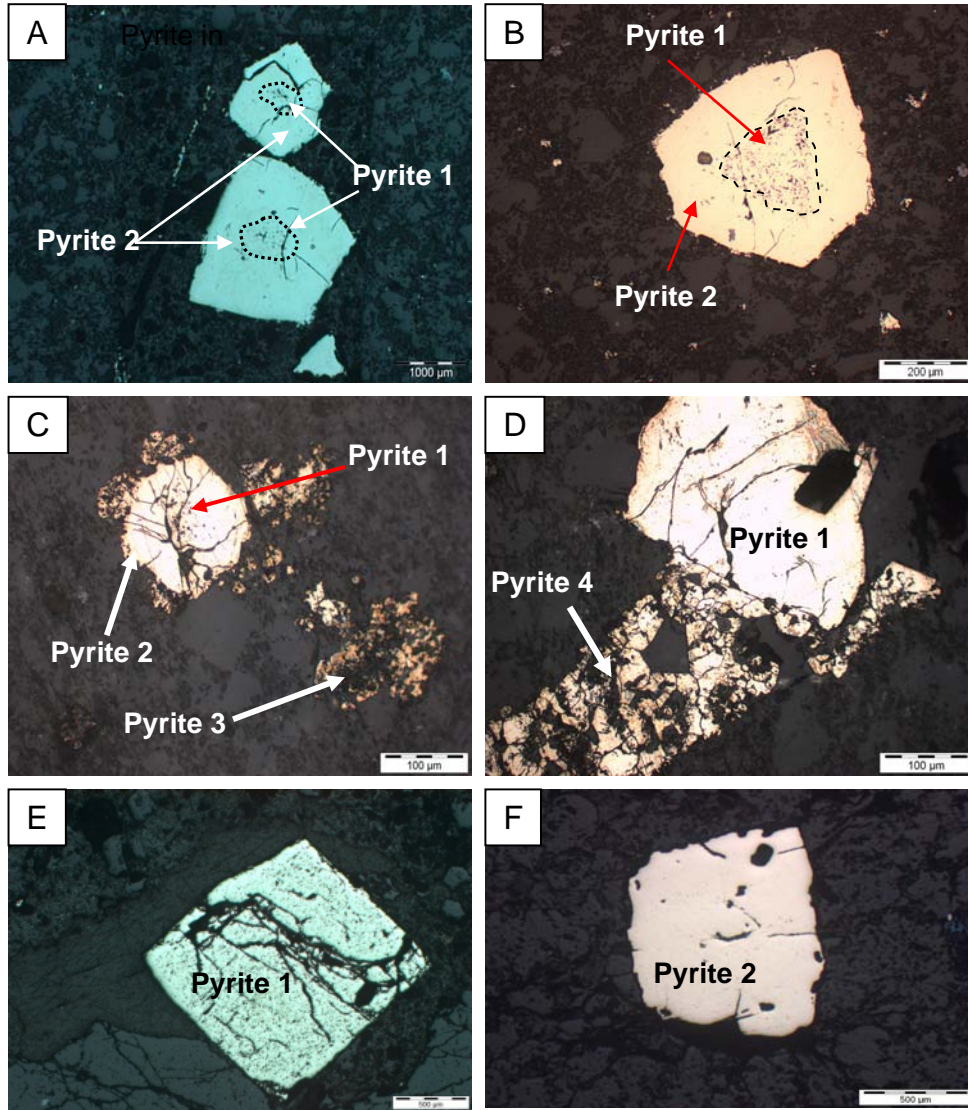


Fig. 5.3. Photomicrographs (reflected light) showing textural characteristics of different types of pyrite at the Tersang gold deposit. **A.** Spongy, subhedral pyrite (pyrite 1) and overgrown pyrite (pyrite 2) in host sandstone (Sample No. TER-R007). **B.** Euhedral clean pyrite (pyrite 2) and pyrite 1 (Sample No. TER-R007). **C.** Pyrite 1, pyrite 2 with internal fracturing and amorphous pyrite (pyrite 3) (Sample No. TER-R007). **D.** Pyrite 1 and vein pyrite (pyrite 4) (Sample No. TER-R007). **E.** Vein-hosted, euhedral pyrite (pyrite 1) (Sample No. TER-R039). **F.** Subhedral clean pyrite, intrusion-hosted pyrite (pyrite 2) (Sample No. TER-033).

5.4.1.4. Amorphous pyrite (pyrite 3) and fracture-filled (pyrite 4)

The amorphous pyrite grains (pyrite 3) are disseminated and their size ranges from 50 to 100 μm (Fig. 5.3C). They are found associated with pyrite 4 in the host sandstone. Some grains are sub-rounded and isolated in the sediment matrix. These grains are smaller than 50 μm . The host rock also contains a few microveins of grey-coloured quartz vein, which are filled with aggregates of pyrite (pyrite 4). The aggregates are mostly anhedral and form discontinuous bands of 250 – 500 μm in length within the veins (Fig. 5.3D).

5.4.2. Gold

5.4.2.1. Gold in vein

In quartz veins, gold is present in the following occurrences: (1) 20-30 μm grains isolated in the quartz matrix and 2-5 μm grains locked in arsenopyrite grains (Figs. 5.4 A-B); (2) up to 70 μm grains associated with geocronite (Figs. 5.5A-B); (3) up to 1mm grains sandwiched at fracture intersection, rimmed by pyrite and in contact with arsenopyrite, which in turn contains 20-50 μm gold inclusions. Arsenopyrite is cross-cut by tiny 2-5 μm gold veinlets (Figs. 5.6A-B). Scanning electron probe quantitative analysis of vein gold for Au, Ag, Pb, Sb, Te, Cu, Al, Fe, and Si is presented in Table 5.2. Result shows that gold grains (grain 1 to grain 4) found in quartz matrix have higher Ag content (4.07-22.99 wt %), whereas gold grains in fractures (grain 5 to grain 8) have lower Ag contents (3.46-3.92 wt %). This indicates that the Tersang ore veins contain two gold generations based on fineness: (1) high fineness (959-965) gold

associated with pyrite, arsenopyrite and geocronite; (2) low fineness (769-792) gold, which occurs with broken arsenopyrite grains.

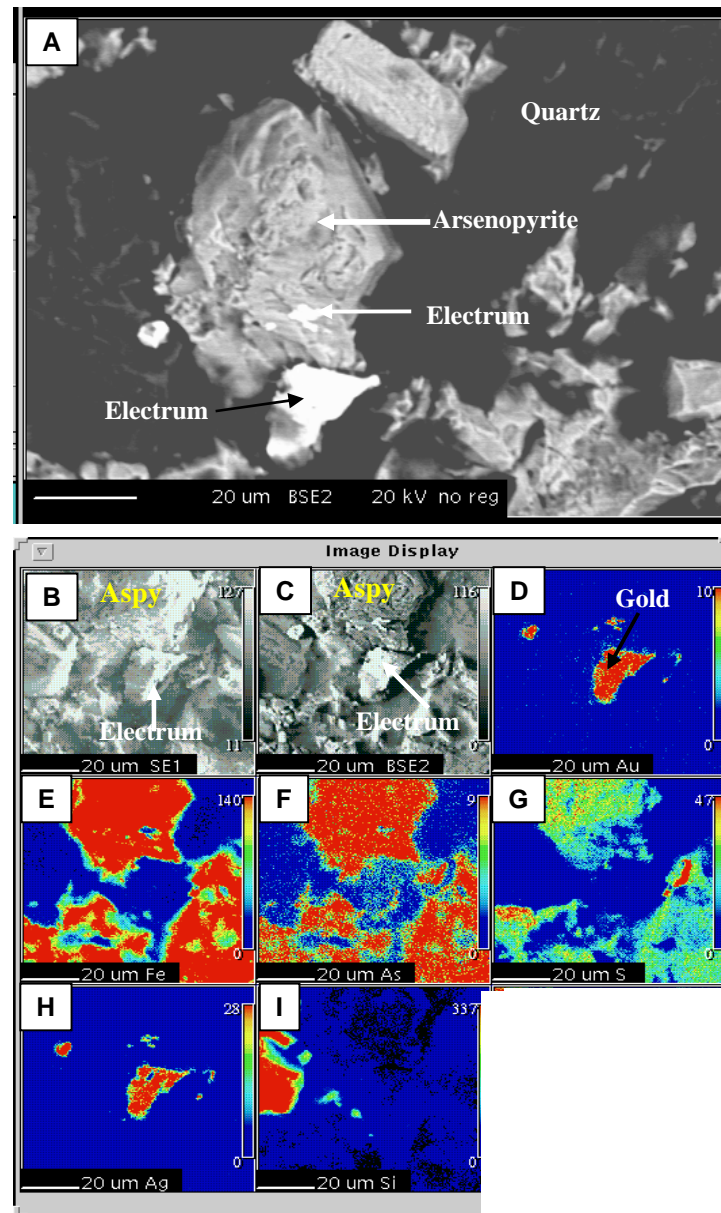


Fig.5.4. Back-scattered electron images of gold occurrence at the Tersang deposit. **A.** Gold associated with arsenopyrite (Aspy) in quartz vein (Sample No. TER-R030). **B.** Scanning electron map of the gold grain and arsenopyrite. **C.** Back-scattered image of electrum and arsenopyrite. **D.** Au inclusion in silica matrix. **E.** Fe. **F.** Arsenic. **G.** Sulphur. **H.** Ag. **I.** Silica.

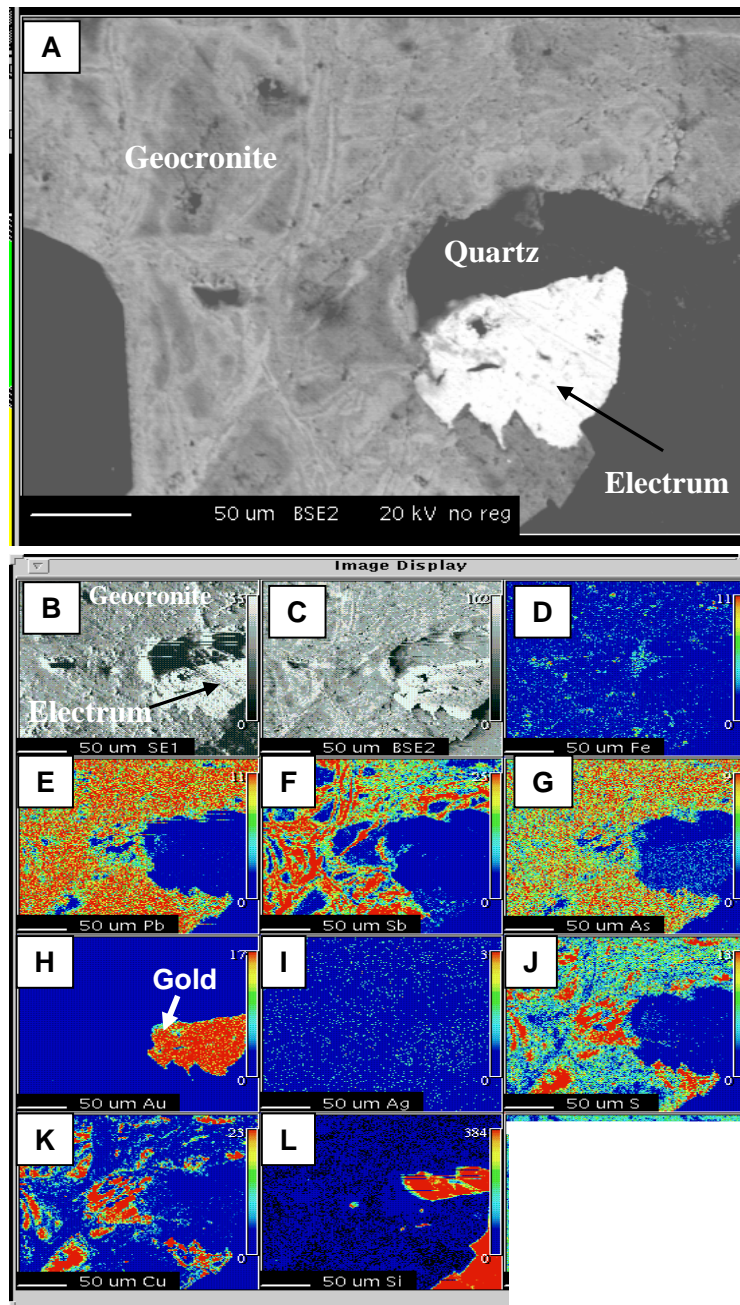


Fig. 5.5. Back-scattered electron images of gold occurrence at the Tersang deposit. **A.** Gold associated with geocronite in quartz vein (Sample No. TER-R010). **B.** Scanning electron map of the gold grain and geocronite. **C.** Back-scattered image of geocronite. **D.** Fe. **E.** Lead. **F.** Sb. **G.** As. **H.** Gold inclusion. **I.** Ag. **J.** Sulphur. **K.** Cu. **L.** Silica.

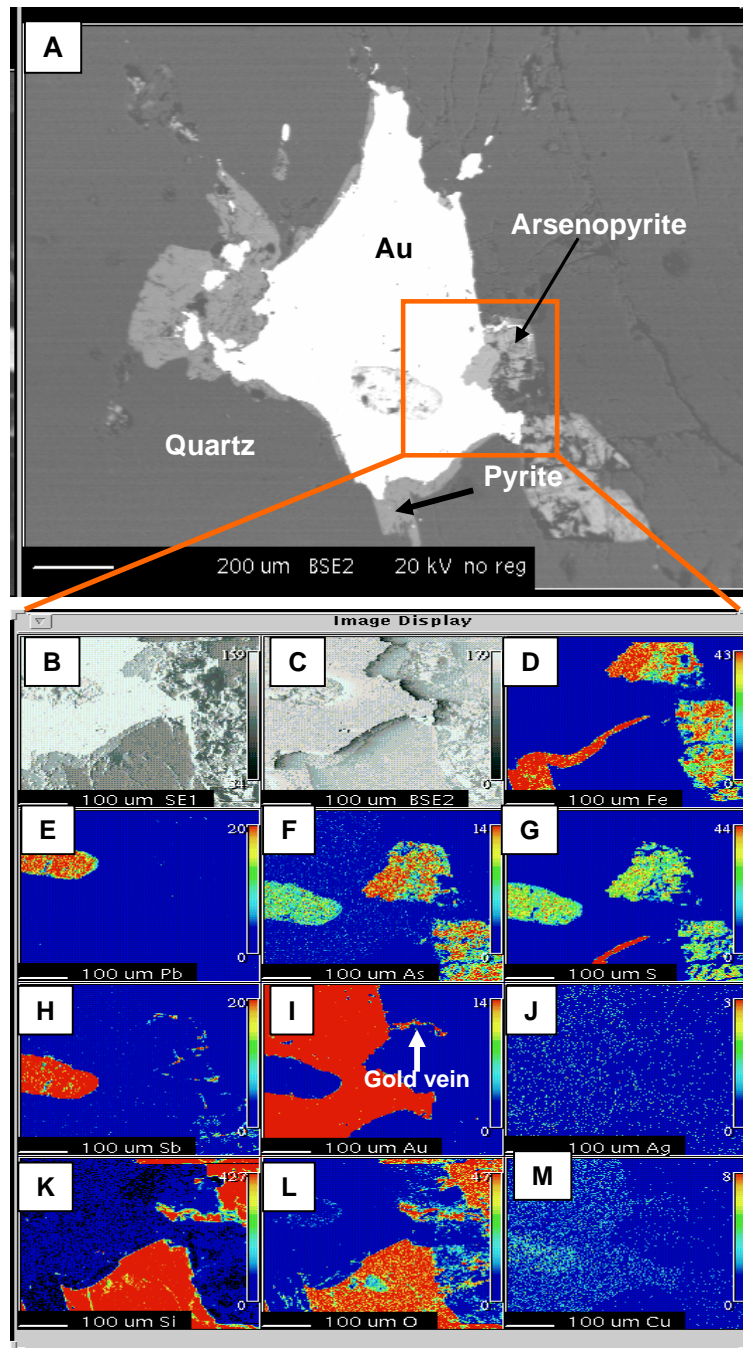


Fig. 5.6. Back-scattered electron images of gold occurrence at the Tersang deposit. **A.** Gold associated with arsenopyrite and pyrite (Sample No. TER-R035). **B.** Scanning electron map. **C.** Back-scattered image of square area in **A.** **D.** Fe. **E.** Low Pb in gold grain. **F.** As. **G.** Sulphur. **H.** Sb. **I.** Au as thin vein. **J.** Ag. **K.** Silica. **L.** Oxygen. **M.** Low copper in gold grain.

Table 5.2. Electron microprobe quantitative analysis (wt %) of selected trace elements of gold grains in vein at the Tersang deposit, Central Malaysia

	Au	Ag	Pb	Sb	Te	Cu	Fe	Si	Total	Fineness
Grain 1	77.69	21.52	0.00	0.06	0.00	0.66	0.02	0.06	100.00	783
Grain 2	76.36	22.99	0.08	0.00	0.00	0.51	0.00	0.04	100.00	769
Grain 3	78.22	20.45	0.06	0.00	0.00	1.15	0.03	0.07	100.00	792
Grain 4	95.41	4.07	0.00	0.00	0.36	0.09	0.03	0.04	100.00	959
Grain 5	95.94	3.92	0.00	0.05	0.00	0.03	0.01	0.04	100.00	961
Grain 6	96.24	3.47	0.17	0.03	0.01	0.00	0.01	0.06	100.00	965
Grain 7	96.07	3.63	0.18	0.00	0.00	0.04	0.02	0.06	100.00	963
Grain 8	95.95	3.72	0.11	0.08	0.04	0.00	0.04	0.06	100.00	962

5.4.2.2. Alluvial gold

Panned concentrate samples have been collected in streams draining downhill from the Tersang orebody. Textural characteristics of alluvial gold grains are presented in Fig. 5.7. Quantitative scanning electron microprobe analyses of alluvial gold grains for Au, Ag, Pb, As and Bi contents are presented in Table 5.3. Result shows that all alluvial grains are strongly depleted in Ag content from 1.26 to 5.22 wt % with no detectable Pb and Bi as well as negligible amount of As (0.01-0.02 wt %). All gold grains have high fineness which ranges from 948 to 981 (average fineness 968). The alluvial gold grains are strongly porous (pores are 1-5 μm in size) when found far from the deposit location.

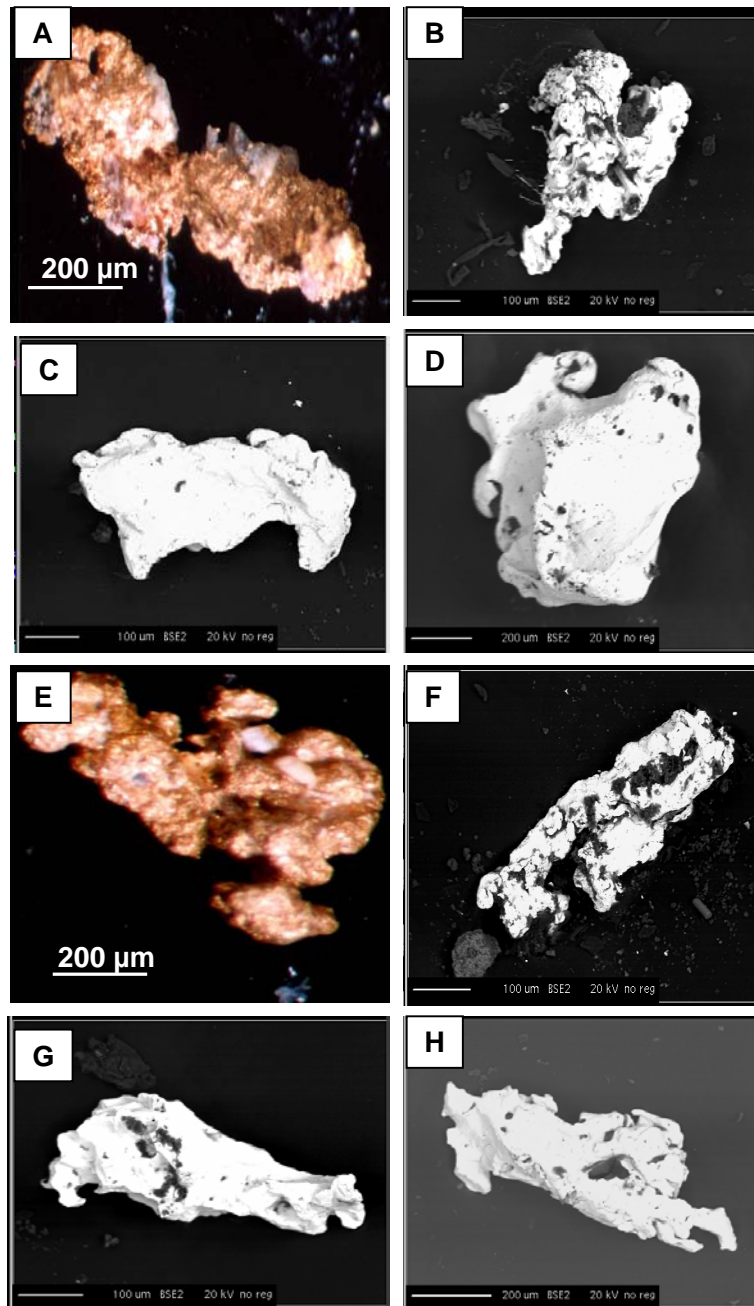


Fig. 5.7. SEM images showing morphology of alluvial gold grains at the Tersang deposit. **A.** Angular and prismatic. **B.** Subangular and subprismatic slightly arborescent. **C.** Subangular and subprismatic. **D.** Subrounded and subdiscoidal. **E.** Subangular and subdiscoidal. **F.** Subangular and prismatic. **G.** Angular and prismatic. **H.** Angular and prismatic.

Table 5.3. Electron microprobe quantitative analysis (wt %) of selected trace elements of alluvial gold grains from the Tersang area, Central Malaysia

Sample number	Ag	Au	Pb	As	Bi	Total	Fineness
PC02 grain 1	1.86	96.10	0.00	0.01	0.00	97.97	981
PC02 grain 1	2.93	94.94	0.00	0.01	0.00	97.88	970
PC02 grain 1	3.04	95.96	0.00	0.01	0.00	99.02	969
PC02 grain 2	3.34	95.93	0.00	0.00	0.00	99.27	966
PC02 grain 2	3.41	96.08	0.00	0.00	0.00	99.49	966
PC02 grain 2	3.31	95.46	0.00	0.00	0.00	98.78	966
PC02 grain 3	2.15	97.64	0.00	0.01	0.00	99.80	978
PC02 grain 3	2.12	97.10	0.00	0.02	0.00	99.24	979
PC02 grain 3	2.14	97.23	0.00	0.00	0.00	99.36	978
PC05 grain 1	5.22	94.92	0.00	0.00	0.00	100.14	948
PC05 grain 1	5.06	92.01	0.00	0.00	0.00	97.07	948
PC05 grain 1	5.13	94.90	0.00	0.00	0.00	100.03	949
PC05 grain 2	2.71	97.02	0.00	0.01	0.00	99.74	973
PC05 grain 2	2.75	97.47	0.00	0.01	0.00	100.23	973
PC05 grain 2	2.54	94.51	0.00	0.00	0.03	97.08	974

These grains are the Ag-leached grains due to weathering as shown in Figure 5.7.

5.4.3. Arsenopyrite

Arsenopyrite is present in the host rock in six forms (Fig. 5.8A-B): it is found as subhedral grains ranging from 200 to 300 μm and as rhomb-shaped grains ranging from 100 to 200 μm in size. In addition, it is abundant in the quartz veins where it occurs in the form of broken grains ranging from 50 to 100 μm in size (Sample No. TER-R025). Furthermore, it occurs as xenomorphic grains within patches of hematite, and carbonate in few areas. It rims pyrite grains in veins and sometimes occurs as isolated grains, which the size ranges from 200 to 400 μm in diameter. In the veins, it is mostly found associated with galena. Pitted arsenopyrite grains show infilling of secondary silica in quartz veins.

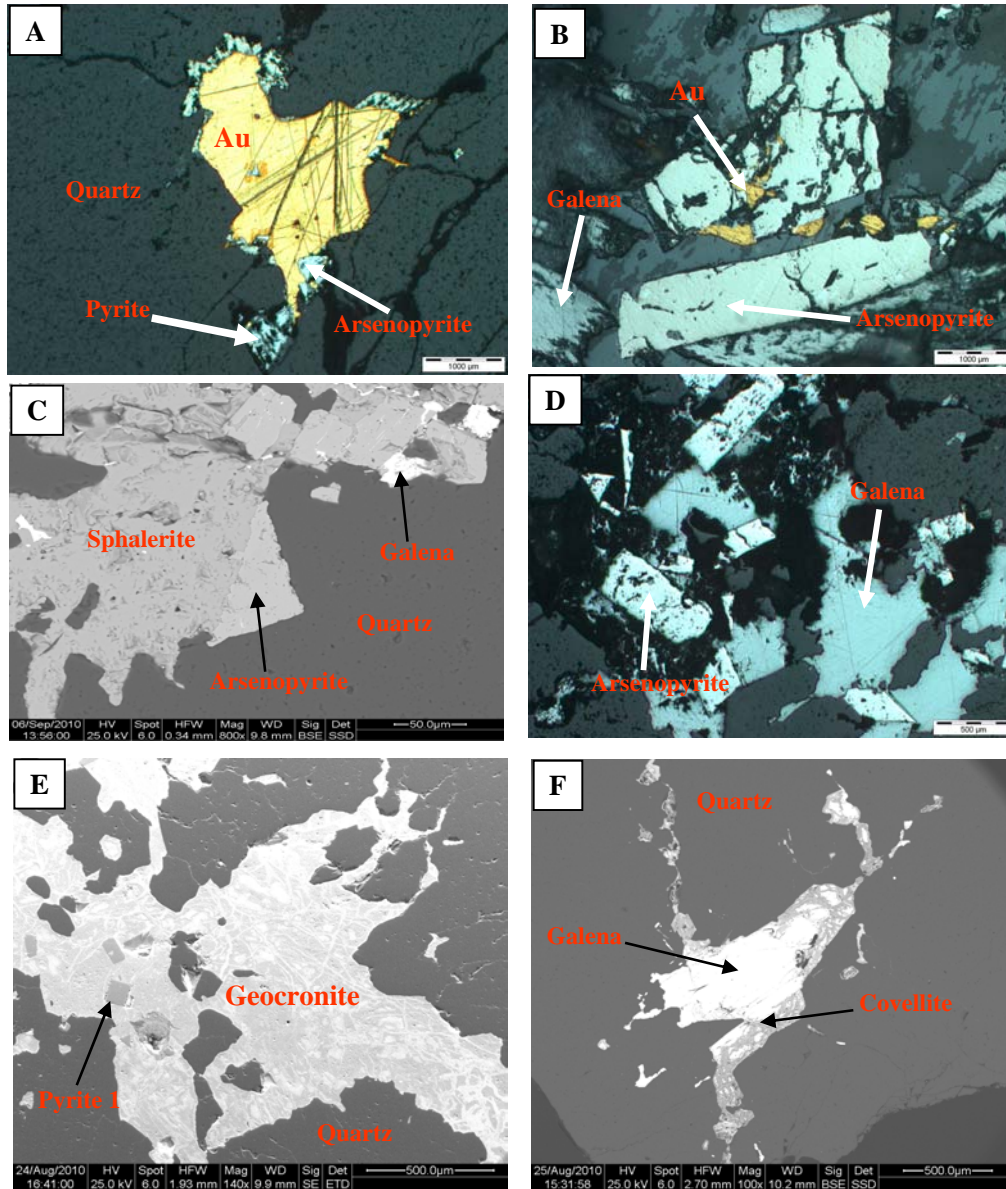


Fig. 5.8. Ore minerals at the Tersang deposit **A.** Free gold associated with pyrite and arsenopyrite in quartz-sulphide vein (Sample No. TER-R035). **B.** Free gold in quartz-sulphide vein (Sample No. TER-R042). **C.** Back-scattered electron image of sphalerite, arsenopyrite and galena (Sample No. TER-R008). **D.** Galena and arsenopyrite in quartz-sulphide vein (Sample No. TER-R029). **E.** Back-scattered electron image of supergene geocronite and euhedral pyrite 1 (Sample No. TER-R030). **F.** Back-scattered electron image of galena associated with supergene covellite (Sample No. TER-R041).

5.4.4. Sphalerite

Sphalerite occurs as large (up to 1 mm wide) patches in quartz veins in Sample TER-R008 together with arsenopyrite and galena (Fig. 5.8C). Galena forms tiny 10 µm inclusions in sphalerite (Fig. 5.8C).

5.4.5. Galena

Galena is present in most quartz veins. The grains are up to 1 mm across and are present in fractures of arsenopyrite and pyrite. In addition, galena rims brecciated grains of arsenopyrite and fills fractures in arsenopyrite. Galena is also present in larger patches around arsenopyrite, and as veinlets ranging in size from 5 to 10 µm wide, as well as inclusions in sphalerite grains (Fig. 5.8D).

5.4.6. Geocronite

Geocronite was identified by the help of electron probe microanalyser in Sample No. TER-R030. The chemical composition is made up of elements such as lead, antimony, arsenic and sulphur ($\text{Pb}_5\text{Sb}_2\text{As}_2\text{S}_8$). This mineral occurs as patches (up to 1 mm wide) sitting in microfractures in the quartz veins (Fig. 5.8E). It is commonly associated with euhedral pyrite (pyrite 1).

5.4.7. Covellite

This mineral was identified by using electron probe microanalyser in Sample No. TER-R041. It occurs in fractures as secondary mineral and replaces partly galena in

quartz veins (Fig. 5.8F). Chemical composition shows enrichment in copper and sulphur evidenced by electronprobe microanalyzer. The presence of covellite in fractures suggests a supergene or secondary origin.

5.4.8. Ilmenite and rutile

Ilmenite is rare at the Tersang gold deposit. However, in quartz veins, it occurs in inclusions with hematite, which is in the form of lenses, up to 5 μm wide and 20 μm long (Fig. 5.9A). Ilmenite is absent in the host siltstone. Rutile occurs either in the form of laths or patches in quartz veins. The patches of rutile are up to 500 μm in size and the laths are 10-30 μm wide and 30-40 μm long. Ilmenite and rutile are found embedded in the silica matrix (Figs. 5.9B and C), and are interpreted to be hydrothermal in origin.

5.4.9. Hematite

Hematite occurs in the form of disseminated patches in the silica matrix. It is abundant in fractures and rims a few sulphide minerals such as galena and arsenopyrite. It is also found veining pyrite grains (Figs. 5.10D-F). Chemical composition evidenced by electronprobe microanalyzer has shown the presence of low arsenic and molybdenum in hematite and its presence suggests a supergene origin.

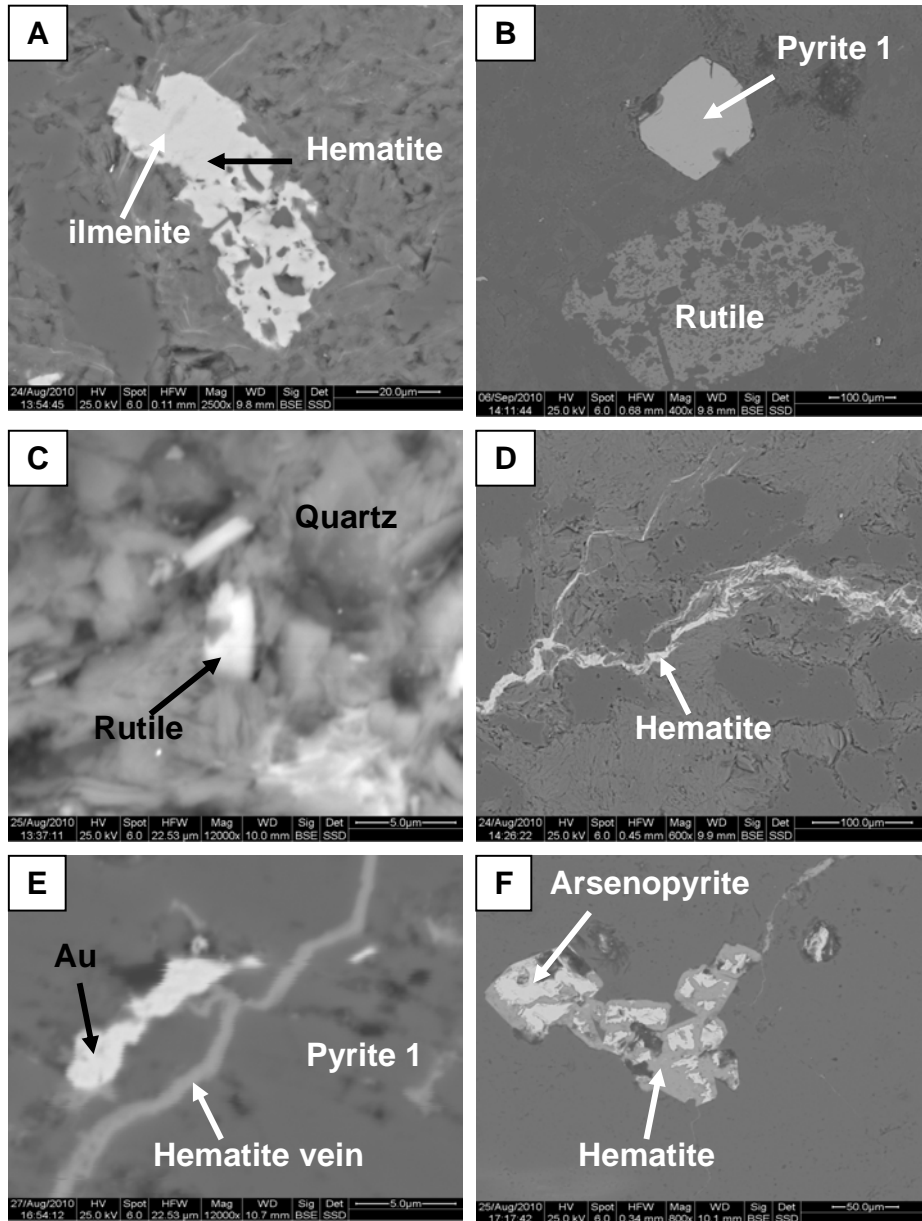


Fig. 5.9. Back-scattered electron images of ore and gangue minerals at the Tersang gold deposit. **A.** Ilmenite inclusion in hematite (Sample No. TER-R025). **B.** Rutile and pyrite 1 occurrence in quartz vein (Sample No. TER-R039). **C.** Lath-shaped rutile in silica matrix (Sample No. TER-R025). **D.** Hematite veins infilled fractures in felsic intrusion (Sample No. TER-R033). **E.** Gold associated with pyrite 1, which in turn is cross-cut by hematite vein (Sample No. TER-R035). **F.** Hematite associated with arsenopyrite broken grains (Sample No. TER-R022).

5.5. Ore mineralogy and paragenesis at the Selinsing deposit

The ore minerals found at the Selinsing gold deposit are pyrite, arsenopyrite, galena, sphalerite, chalcopyrite, pyrrhotite and gold. Gangue minerals are ankerite, rutile, sericite, hematite, calcite, illite and chlorite. The paragenesis of each mineral is summarised in Table 5.2.

5.5.1. Pyrite

Similar to the Tersang deposit, pyrite is the most abundant sulphide mineral at the Selinsing gold deposit. Detailed textural and chemical studies revealed seven pyrite types which include framboidal pyrite (pyrite 1), rounded recrystallised pyrite (pyrite 2), anhedral spongy with many inclusions (pyrite 3), euhedral to subhedral porous pyrite (pyrite 4), overgrown clean pyrite (pyrite 5), and euhedral to subhedral overgrown pyrite (pyrite 6) and euhedral overgrown on pyrite 6 (pyrite 7).




5.5.1.1. Framboidal pyrite (pyrite 1)

The framboidal pyrite occurs along the bedding plane in the host black mudstone. They are disseminated and occur as framboids and the size ranges up to 100 μm in diameter. Pyrite 1 is interpreted to have been formed during sedimentation or early diagenetic stage (Fig. 5.10A).

Chapter 5: Mineralogy, alteration, paragenesis, and metal distribution

Table 5.4. Mineral paragenesis at the Selinsing gold deposit, Central Malaysia.

Event		Diagenesis	Metamorphism	Supergene alteration
Ore minerals	Pyrite 1 and pyrite 2	Major		
	Pyrite 3		Major	
	Pyrite 4		Major	
	Pyrite 5		Major	
	Pyrite 6		Major	
	Pyrite 7		Major	
	Arsenopyrite		Major	
	Galena		Major	
	Sphalerite		Major	
	Chalcopyrite		Major	
	Gold		Major	
	Pyrrhotite		Major	
Gangue	Ankerite		Major	
	Rutile		Major	
	Sericite			Major
	Hematite			Major
	Calcite			Major
	Chlorite		Major	
	Illite			Major

 Major
  Minor
  Trace

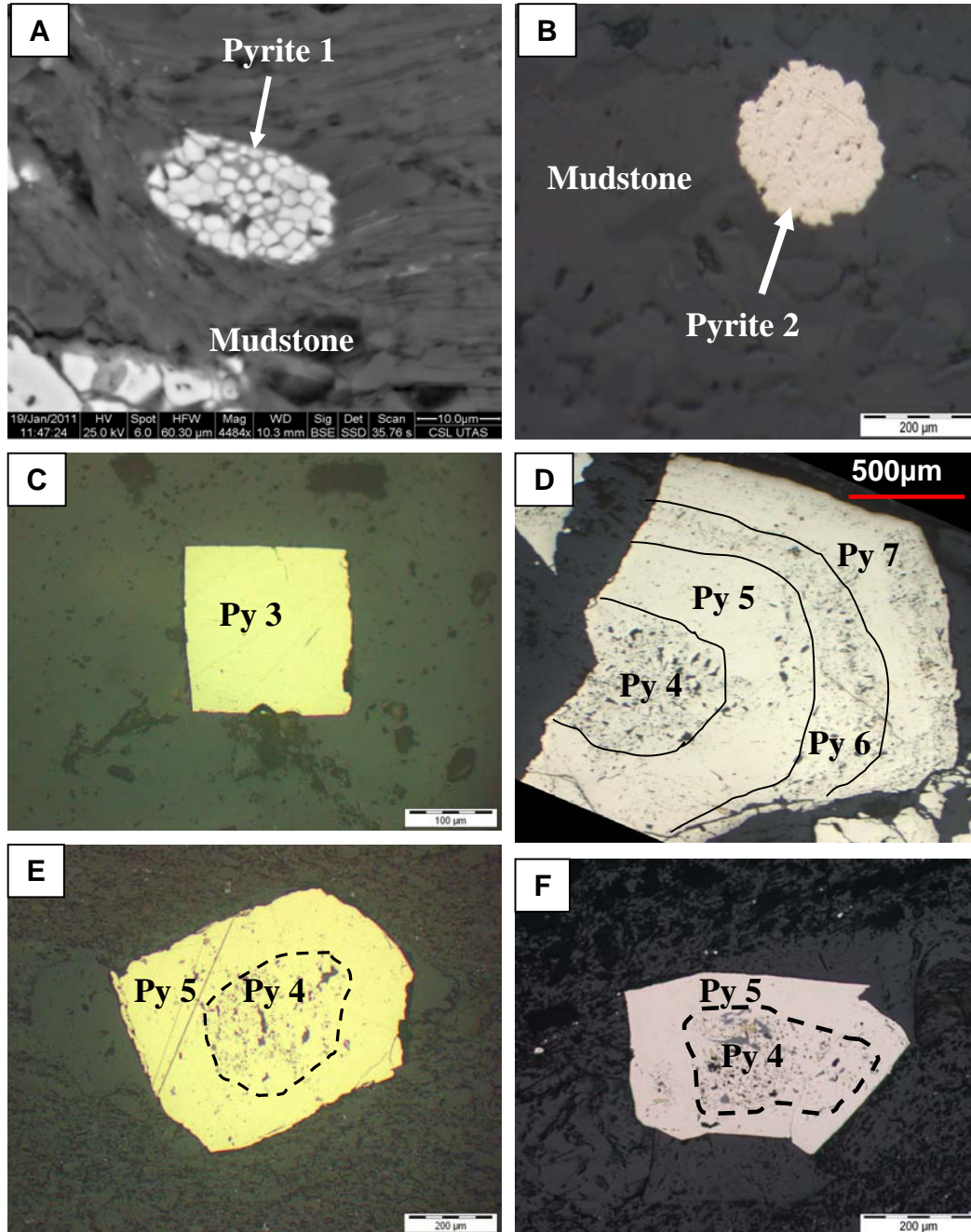


Fig. 5.10. Textural characteristics of pyrite at the Selinsing gold deposit. **A.** Framboidal pyrite (pyrite 1) (Sample No. SEL-R009). **B.** Recrystallised pyrite in mudstone (pyrite 2) (Sample No. SEL-R009). **C.** Spongy pyrite (pyrite 3), pyrite 4 and pyrite 5 (Sample No. SEL-R054). **D.** Growth zones of pyrite 4, pyrite 5, pyrite 6 and pyrite 7 (Sample No. SEL-R054). **E.** Euhedral pyrites 4 and 5 (Sample No. SEL-R025). **F.** Euhedral pyrites 4 and 5 (Sample No. SEL-R039).

5.5.1.2. Recrystallised pyrite (pyrite 2)

The recrystallised pyrite occurs in the host mudstone and shows aggregate of cemented framboids with a negligible amount of sediment infilling (Fig. 5.10B). The size of pyrite 2 is approximately up to 200 μm in diameter. This type of pyrite can be interpreted to be late diagenetic pyrite or having formed prior to metamorphism. The lack of pressure shadow around these pyrites may indicate post-metamorphic occurrence.

5.5.1.3. Euhedral clean pyrite (pyrite 3)

This pyrite is found in the host siltstone in the vicinity of narrow pressure shadow. It can be interpreted that this type of pyrite probably grew during late diagenesis or in the early stage of metamorphism (Fig. 5.10C). Large et al. (2007) interpreted this type of pyrite, which contains inclusions of chalcopyrite, sphalerite alongside with pyrrhotite as late diagenetic pyrite.

5.5.1.4. Composite pyrites (pyrite 4, pyrite 5, pyrite 6 and pyrite 7)

These euhedral to subhedral pyrites form growth zones in quartz veins. They contain inclusions of chalcopyrite, sphalerite and pyrrhotite. They also contain randomly oriented sediment matrix inclusions. This suggests that these pyrites were formed later than the earliest pyrites (pyrite 1 and pyrite 2). These composite pyrites are also hosted in fault-related rocks such as mylonite. This type of pyrite is surrounded by large pressure shadows.

Petrographic studies show that Pyrite 5 is commonly overgrown by pyrites 6 and 7. These pyrites are interpreted to have been formed during metamorphism and probably related to subsequent veining events (Fig. 5.10D).

Pyrite 4 and pyrite 5 also occur in the host siltstone, mylonite and cataclasite within areas of large pressure shadows (Figs. 5.10E-F). Pyrite 4 contains inclusions of silicate minerals either albite or chlorite, whereas pyrite 5 is clean and overgrown on pyrite core (pyrite 4). Similarly, this type of coarse-grained, zoned, euhedral pyrites is present in the turbidites at Bendigo gold deposit and was interpreted as metamorphic/hydrothermal pyrite (Thomas et al., 2011).

5.5.2. Arsenopyrite and galena

Arsenopyrite grains are brecciated and localised in pressure shadows in the host siltstone. The grains are also found in the wall rock. The grain size varies from 50 μm to 4mm. Arsenopyrite is sometimes associated with sphalerite which fills interstices. Arsenopyrite also contains inclusions of chalcopyrite and gold. In quartz veins, arsenopyrite grains are fractured (Fig. 5.11A). Galena is present in quartz veins with arsenopyrite and gold. The size of galena grains varies from 100 μm to 300 μm . In the grains of arsenopyrite, galena occurs as infilling in microfractures (Fig. 5.11B).

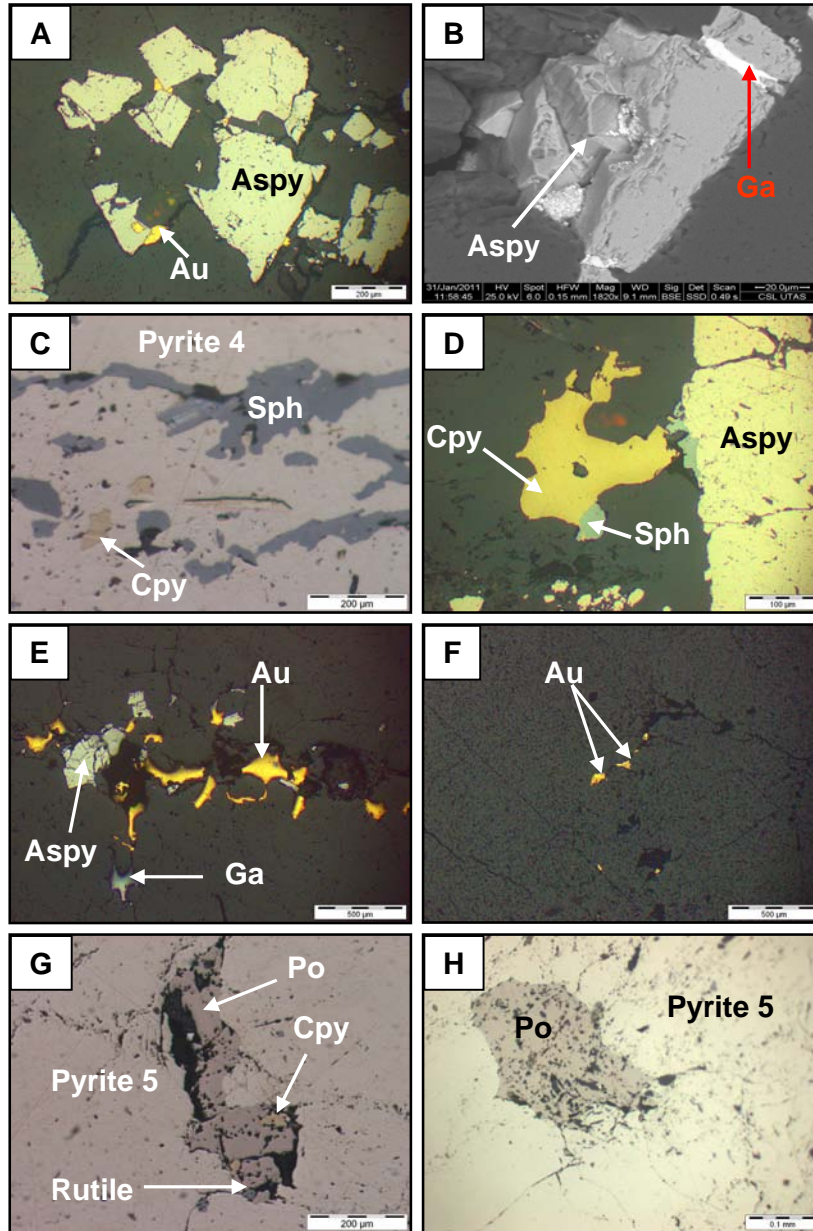


Fig. 5.11. Ore minerals at the Selinsing gold deposit. **A.** Arsenopyrite (Aspy) associated with gold (Sample No. SEL-R042). **B.** Back-scattered image of galena (Ga) and arsenopyrite (Sample No. SEL-R024). **C.** Sphalerite (Sph) replacement of the pyrite 4 with chalcopyrite (Cpy) inclusions (Sample No. SEL-R009). **D.** Chalcopyrite (Cpy), sphalerite (Sph) and arsenopyrite (Aspy) in pressure shadow (Sample No. SEL-R055). **E.** Gold mineralisation associated with galena and arsenopyrite in quartz vein (Sample No. SEL-R042). **F.** Gold mineralisation in quartz vein (Sample No. SEL-R024). **G.** Pyrrhotite (Po) replacement in the pyrite 5 with inclusions of rutile and chalcopyrite (Sample No. SEL-R025). **H.** Close-up view of pyrrhotite replacement of the pyrite 5 (Sample No. SEL-R006).

5.5.3. Sphalerite and chalcopyrite

Sphalerite forms inclusions in porous pyrite (pyrite 4) along laminations in interbedded mudstone and siltstone. It is present near or within chalcopyrite and arsenopyrite in pressure shadows in the host siltstone. In addition, chalcopyrite is present as infilling in brecciated arsenopyrite and forms 100 μm long and 50 μm wide elongated shapes. In quartz vein, sphalerite is associated with chalcopyrite (Fig. 5.11C).

Chalcopyrite also occurs as inclusions in arsenopyrite and the pyrite 4. The size of inclusions ranges from 40 μm to 200 μm . The inclusions are abundant in the pyrite 4. Some inclusions are associated with pyrrhotite in the pyrite (Fig. 5.11D).

5.5.4. Pyrrhotite

Pyrrhotite forms as inclusion in pyrite 5, which are present in pressure shadows in mylonite. The inclusions are up to 200 μm across. Pyrrhotite contains inclusions of chalcopyrite and it is associated with rutile (Figs. 5.11G-H). In this study, pyrrhotite occurs in metamorphic pyrite generations. Pyrrhotite is interpreted to have formed by the replacement of pyrite 5 during metamorphism. Large et al. (2007) also interpreted the presence of pyrrhotite in pyrite within the ore body as replacement texture at the Sukhoi Log deposit. Similarly, Thomas et al. (2011) reported that diagenetic pyrite in carbonaceous shale has been replaced by pyrrhotite during metamorphism.

5.5.5. Gold

Gold is present as 1-2 mm nuggets in quartz veins. Within sulphide minerals, gold is within or proximal to arsenopyrite and galena, and forms 20µm wide sub-rounded inclusions. Sometimes, gold appears as microveinlets with thickness ranging from 50 to 100 µm in arsenopyrite (Fig. 5.11E). In some quartz veins, gold is disseminated and displays 100 to 200µm size patches in fractures (Fig. 5.11F). Gold also is present as rare discontinuous rims on pyrite grains with length ranging from 20 to 50 µm long. Moreover, it is also present in the form of patchy inclusions. In addition, scanning electron microscope reveals the presence of gold in the form of tiny grains (100 to 250 µm) along the boundaries of arsenopyrite and also as inclusions in pyrite (Figs. 5.12A-B).

5.5.6 Hematite and rutile

Hematite occurs associated with chalcopyrite mostly in quartz veins. Sometimes, it forms discontinuous bands and the thickness varies from 250 to 450 µm (Figs. 5.13A-B). Rutile occurs as intermittent rims and inclusions in the pyrite 4 along the bedding in interbedded mudstone and siltstone. The rim thickness varies from 10 to 20 µm. Patches of rutile have also replaced partly the pyrite 4 (Figs. 5.13C-D). This replacement texture may suggest that rutile was formed during hydrothermal activity.

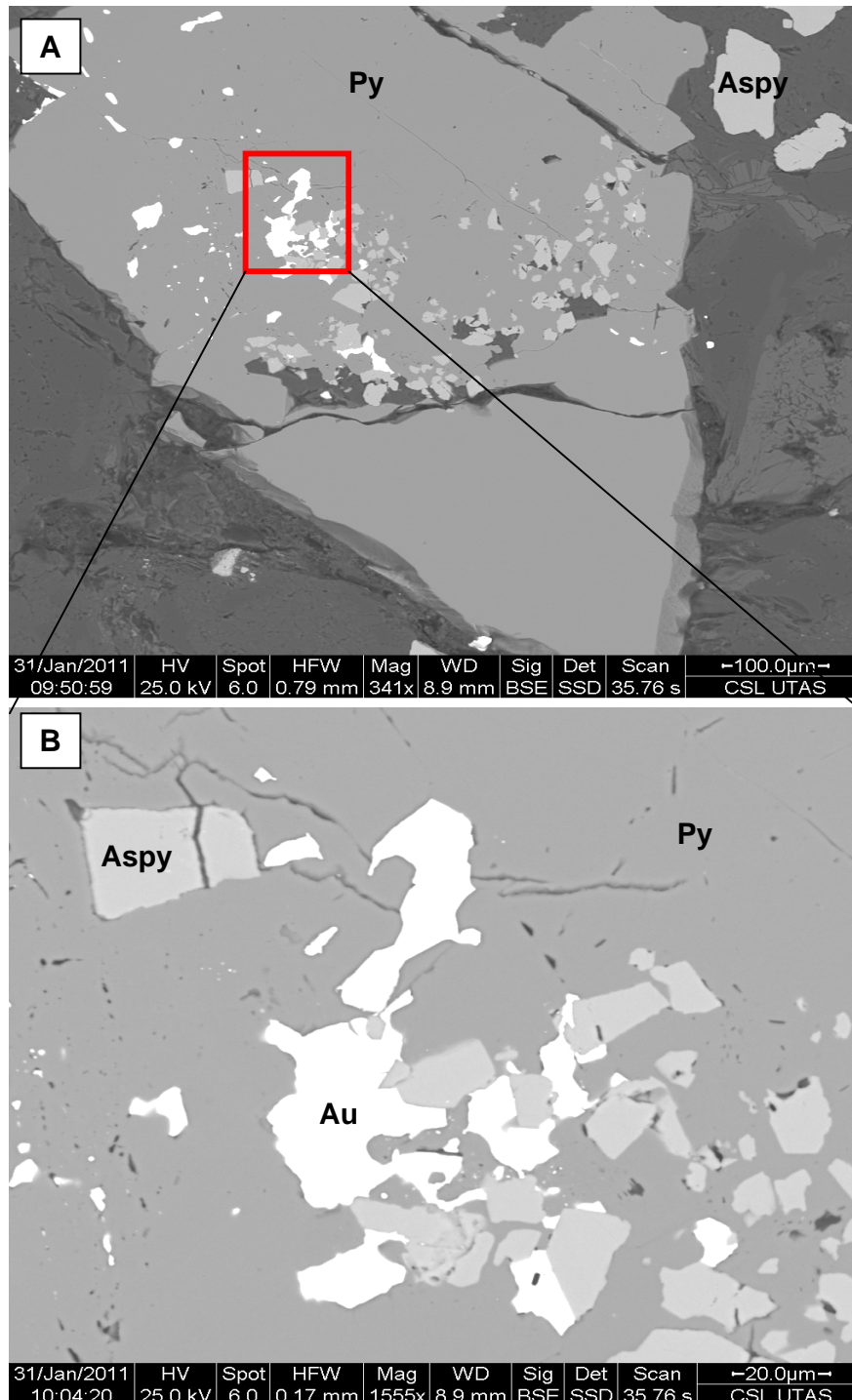


Fig. 5.12. Gold occurrence at the Selinsing deposit, Central Malaysia. **A.** Gold inclusion in pyrite associated with arsenopyrite (Sample No. SEL-R024). **B.** Close-up view of the gold inclusions.

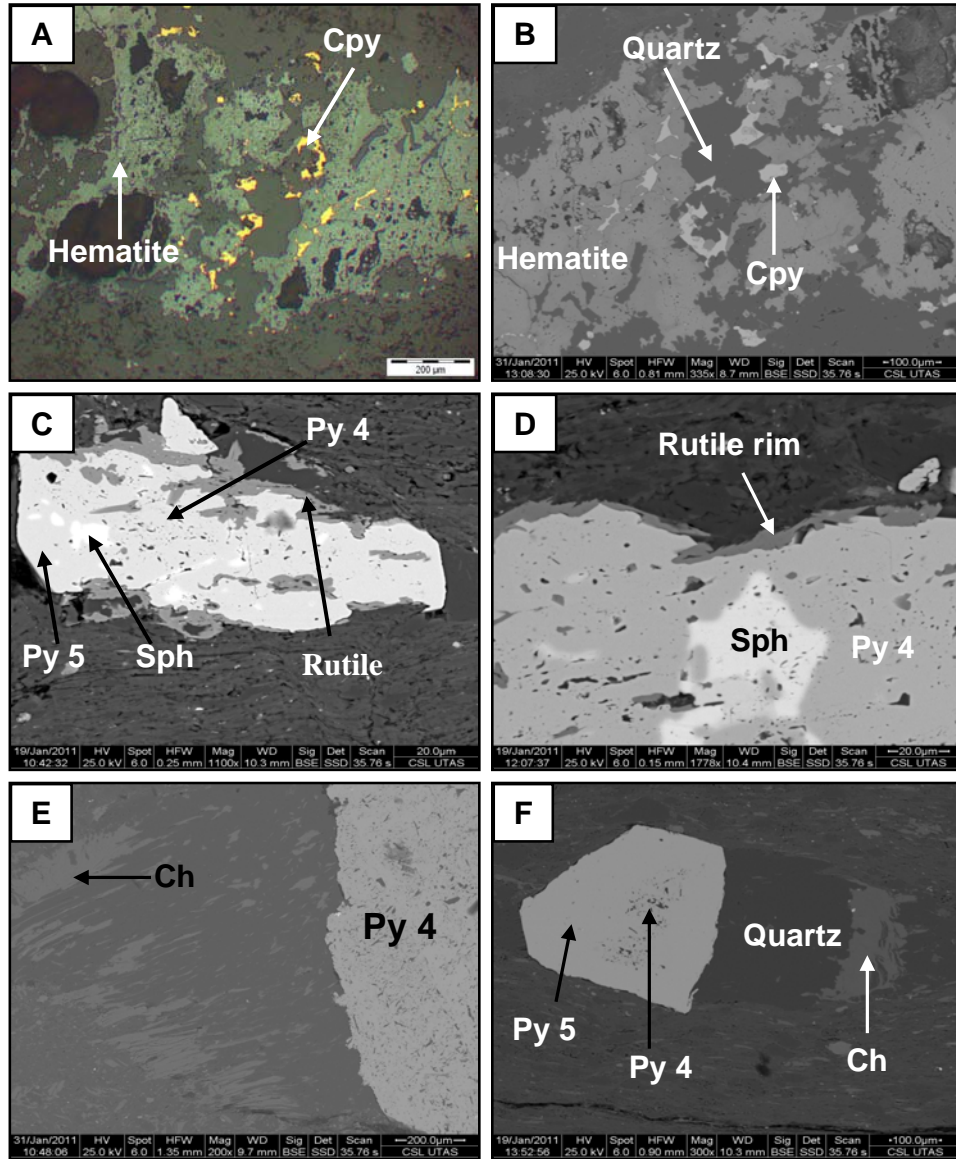


Fig. 5.13. Ore and gangue minerals at the Selinsing deposit. **A.** Chalcopyrite (Cpy) and hematite in quartz vein (Sample No. SEL-R026). **B.** Back scattered image of chalcopyrite and hematite. **C.** Rutile replacement of the pyrite 5 and inclusions of sphalerite (Sph) in the pyrite 4 (Sample No. TER-R009). **D.** Close-up view of rutile by electron probe microanalyser (Sample No. SEL-R009). **E.** Close-up view of chlorite (Ch) in pressure shadow and pyrite 4 (Sample No. SEL-R054). **F.** Late precipitation of chlorite in pressure shadow. Note pyrite 5 overgrown on pyrite 4 (Sample No. SEL-R054).

5.5.7. Chlorite

Chlorite and illite form 50 μm wide, 200 μm long patches in pressure shadows. Electron probe microanalysis shows that chemistry in the pressure shadow is variable with magnesium and potassium rich zones suggesting presence of illite associated with chlorite. Occurrence of chlorite may indicate low grade metamorphic conditions or may be related to propylitic alteration. The evidence seems to suggest that the pyrite 4 precipitated during metamorphism (Figs. 5.13E-F).

5.6. Metal distribution

In this section, metal distribution only at Selinsing gold deposit is presented as no metal assay data are available for the Tersang and Penjom gold deposits. Lithology and concentration of gold as well as pyrite, arsenopyrite and quartz data are put together in order to discuss the distribution of Au mineralisation in selected drill holes. Five drill holes have been logged with a total of 700 m. Concentration of Au is plotted against the estimated volumes of pyrite and arsenopyrite in each zone. The distribution of lithology, quartz veins, sulphide and gold concentrations are presented in Figs. 5.15-5.19.

The drill hole SEL-DD0001 shows that gold mineralisation varies from less than 1 ppm to 99.05 ppm (Fig. 5.14). This elevated concentration is found in quartz-vein rich zone within the host siltstone and can be interpreted as high nugget effect. Gold mineralisation has no correlation with the pyrite and arsenopyrite suggesting that gold may be located in the quartz matrix as free gold. This hypothesis supports previous observation of free gold in quartz veins found

during mapping at mine-site. Gold mineralisation varies from 1 ppm to 1.84 ppm in arsenopyrite rich zones probably relating to the presence of gold blebs in arsenopyrite as inclusions. The gold plot shows correlation with the pyrite and arsenopyrite contents in the host siltstone. Gold concentration drops in ores significantly in carbonaceous shales at depth with Au content less than 0.01 ppm. In drill hole SEL-DD0002, gold content correlates with pyrite and arsenopyrite concentrations (Fig. 5.15). Gold concentration varies from detection limit (0.01 ppm) up to 44.6 ppm. High grade mineralisation is associated with occurrence of quartz veins and cataclasite. There is no sulphide mineralisation at depth below 83.43 m and gold mineralisation does not occur, although some quartz veins have been found at 84.98 m, 90.60 m and 95.36 m.

In drill hole SEL-DD0003, gold mineralisation varies from 0.01 to 48.2 g/t (Fig. 5.16). The high grade zone is present in quartz sulphide veins in the host siltstone. In addition, the highest grade occurs in the breccia units suggesting that the gold mineralisation could be related to multiple deformation. The drill hole SEL-DD0007 is characterised by two major lithologic units: calcareous phyllite and fault-related rocks such as cataclasite (Fig. 5.17). In the calcareous phyllite, gold mineralisation is low with grades at 0.01 ppm. However, in the cataclasites, gold grade is higher and varies from 0.89 to 17.55 g/t. This observation shows that gold mineralisation was structurally controlled. In drill hole SEL-DD0009, gold mineralisation is confined within brecciated zones. Gold grade varies from 1 to 10 ppm. In these zones, pyrite is present in the wall rock and quartz veins (Fig. 5.18). The evidence suggests that gold mineralisation may have occurred during brecciation.

Chapter 5: Mineralogy, alteration, paragenesis, and metal distribution

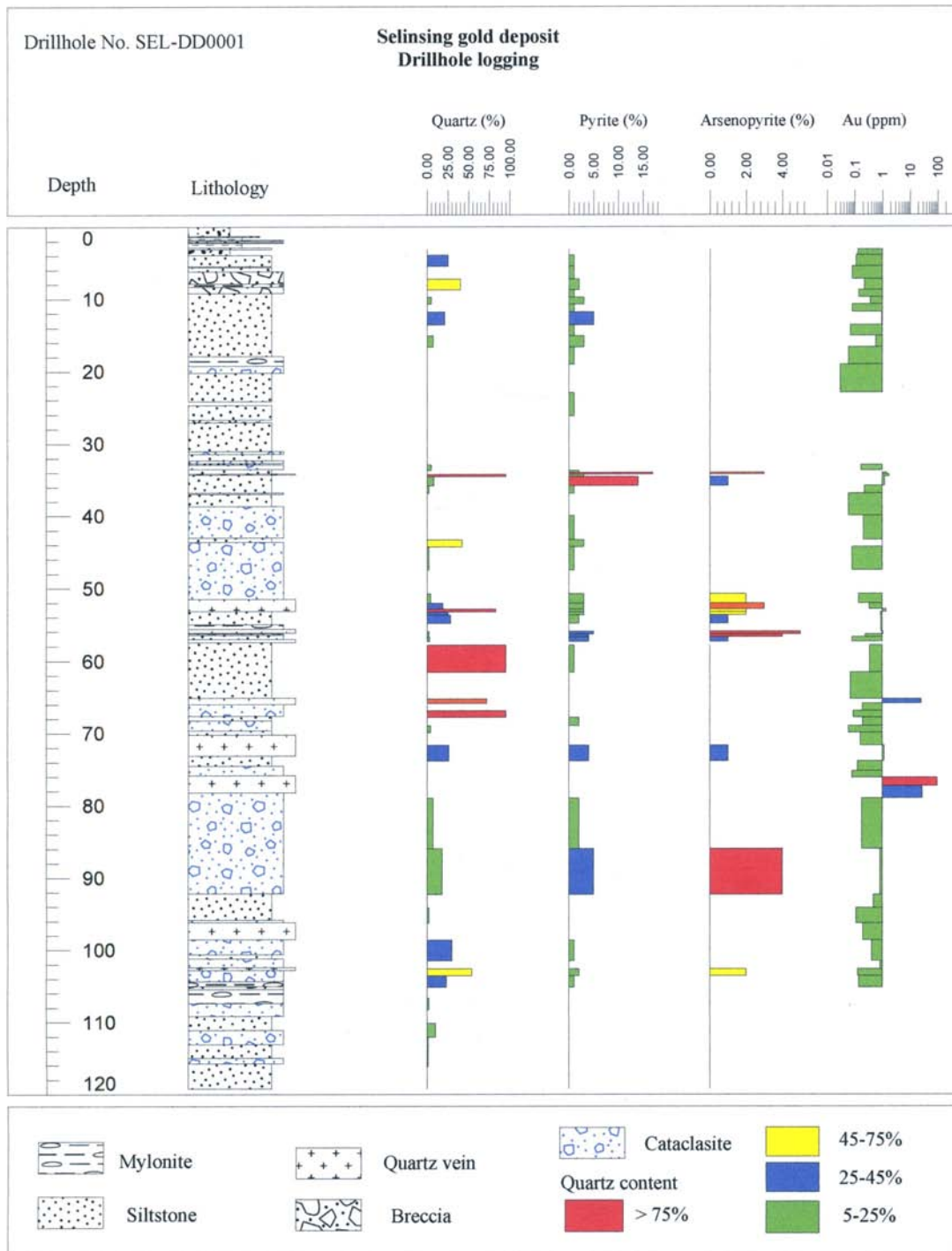


Fig. 5.14. Lithologic log of the drill hole SEL-DD0001 showing distribution of the gold, pyrite and arsenopyrite at the Selinsing gold deposit, Central Malaysia.

Chapter 5: Mineralogy, alteration, paragenesis, and metal distribution

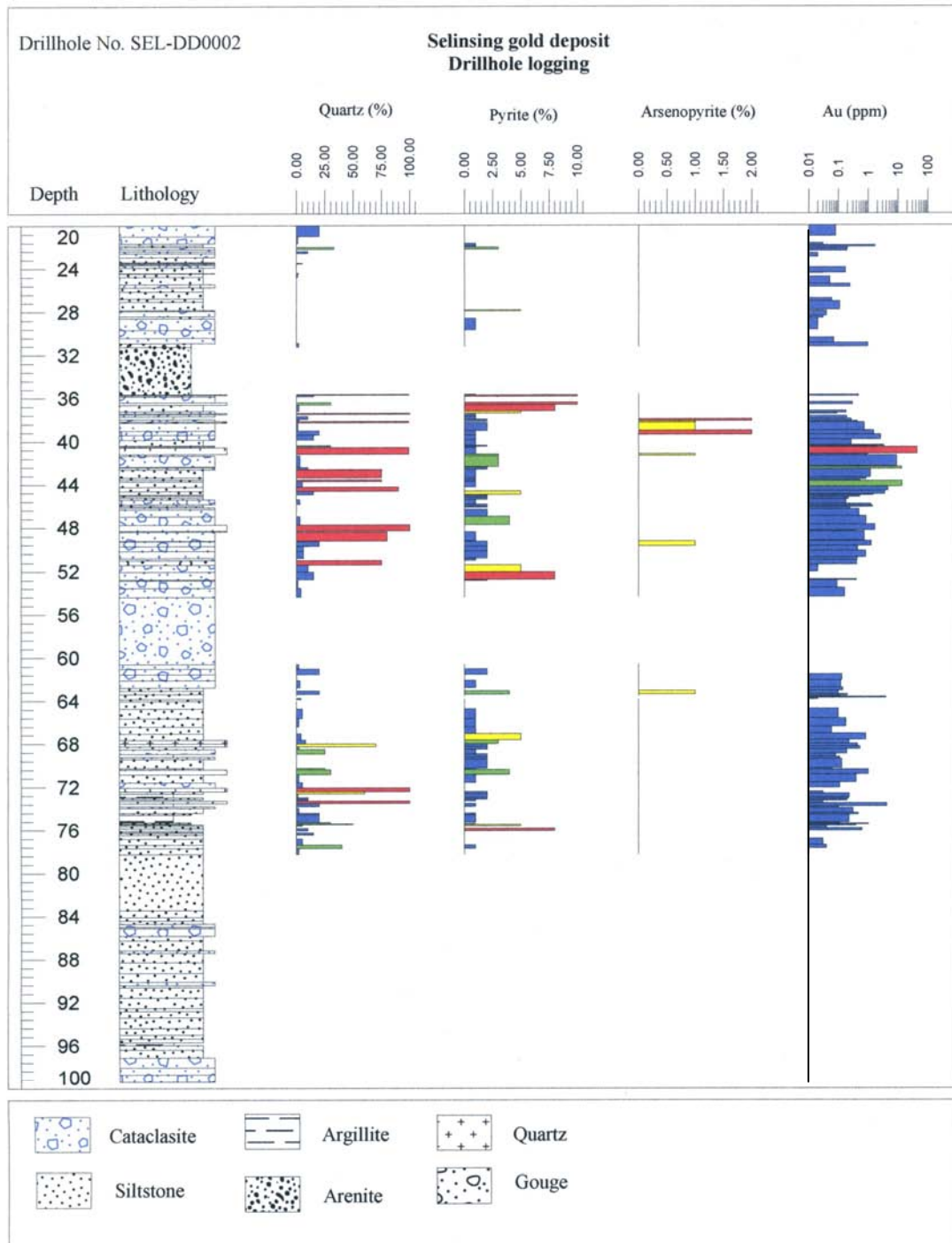


Fig. 5.15. Lithologic log of the drill hole SEL-DD0002 showing distribution of the gold, pyrite and arsenopyrite at the Selinsing gold deposit, Central Malaysia. The colour legend for quartz content is the same as on Fig. 5.14.

Chapter 5: Mineralogy, alteration, paragenesis, and metal distribution

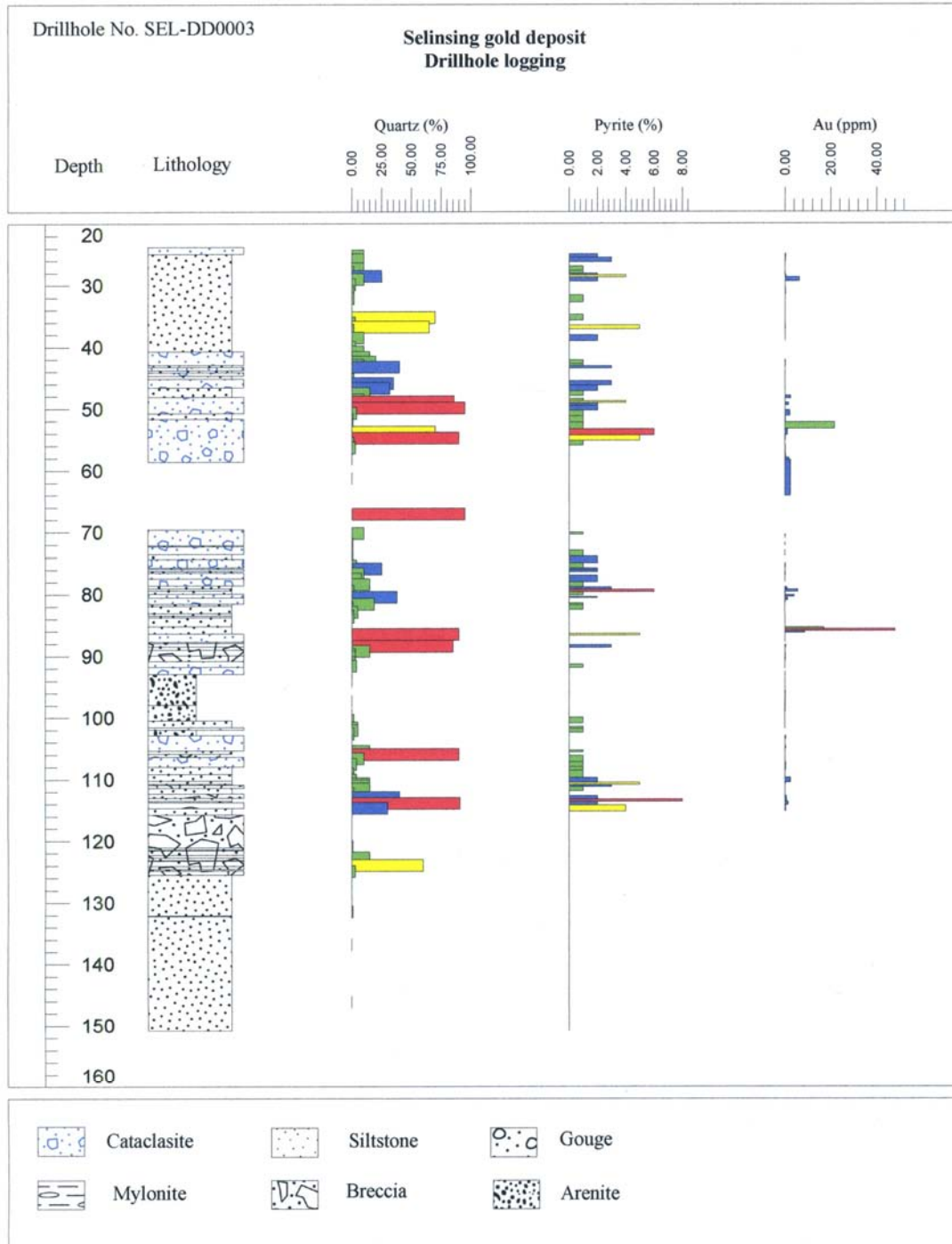


Fig. 5.16. Lithologic log of the drill hole SEL-DD0003 showing distribution of the gold, pyrite and arsenopyrite at the Selinsing gold deposit, Central Malaysia. The colour legend for quartz content is the same as on Fig. 5.15.

Chapter 5: Mineralogy, alteration, paragenesis, and metal distribution

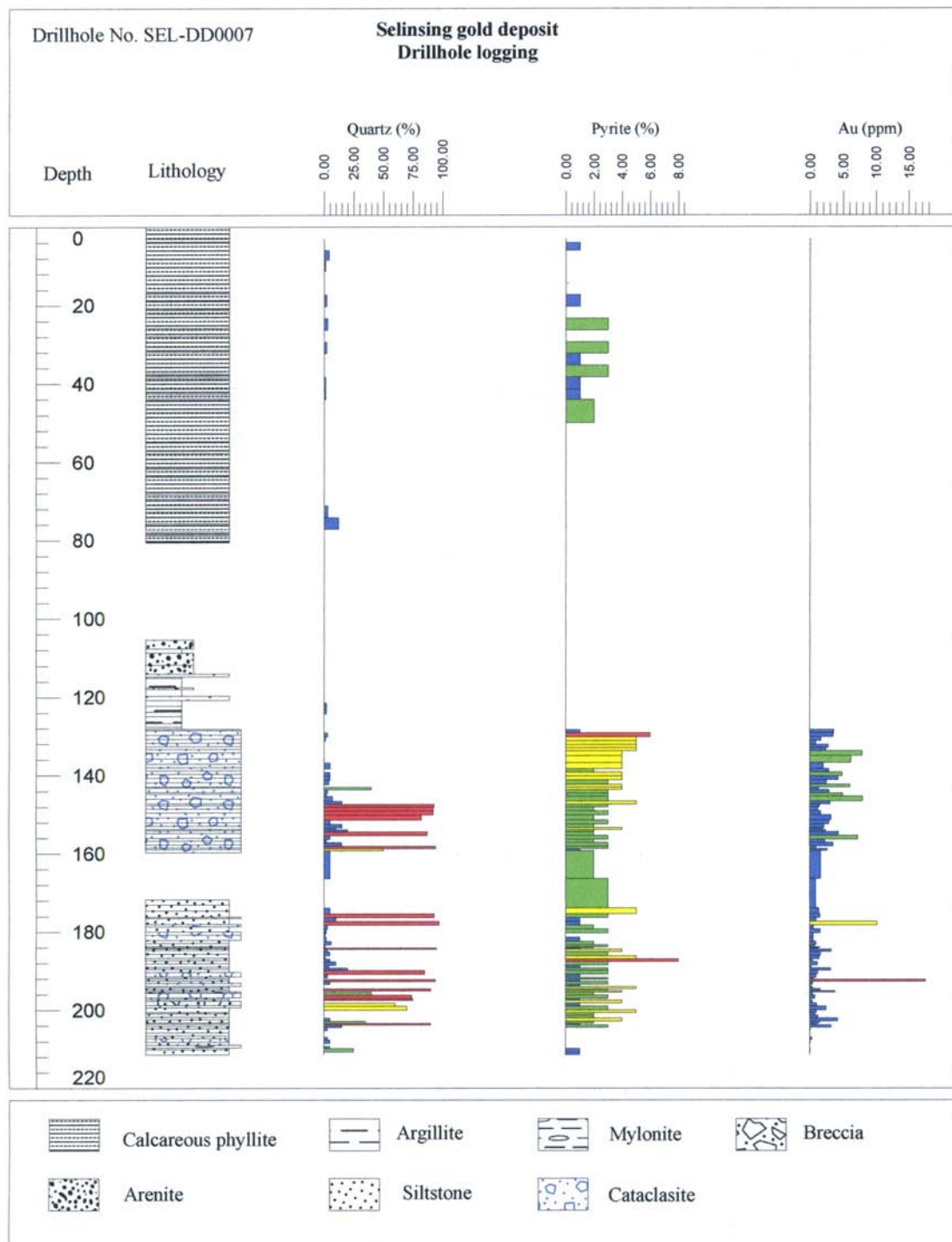


Fig. 5.17. Lithologic log of the drill hole SEL-DD0007 showing distribution of the gold, pyrite and arsenopyrite at the Selinsing gold deposit, Central Malaysia. The colour legend for quartz content is the same as on Fig. 5.16.

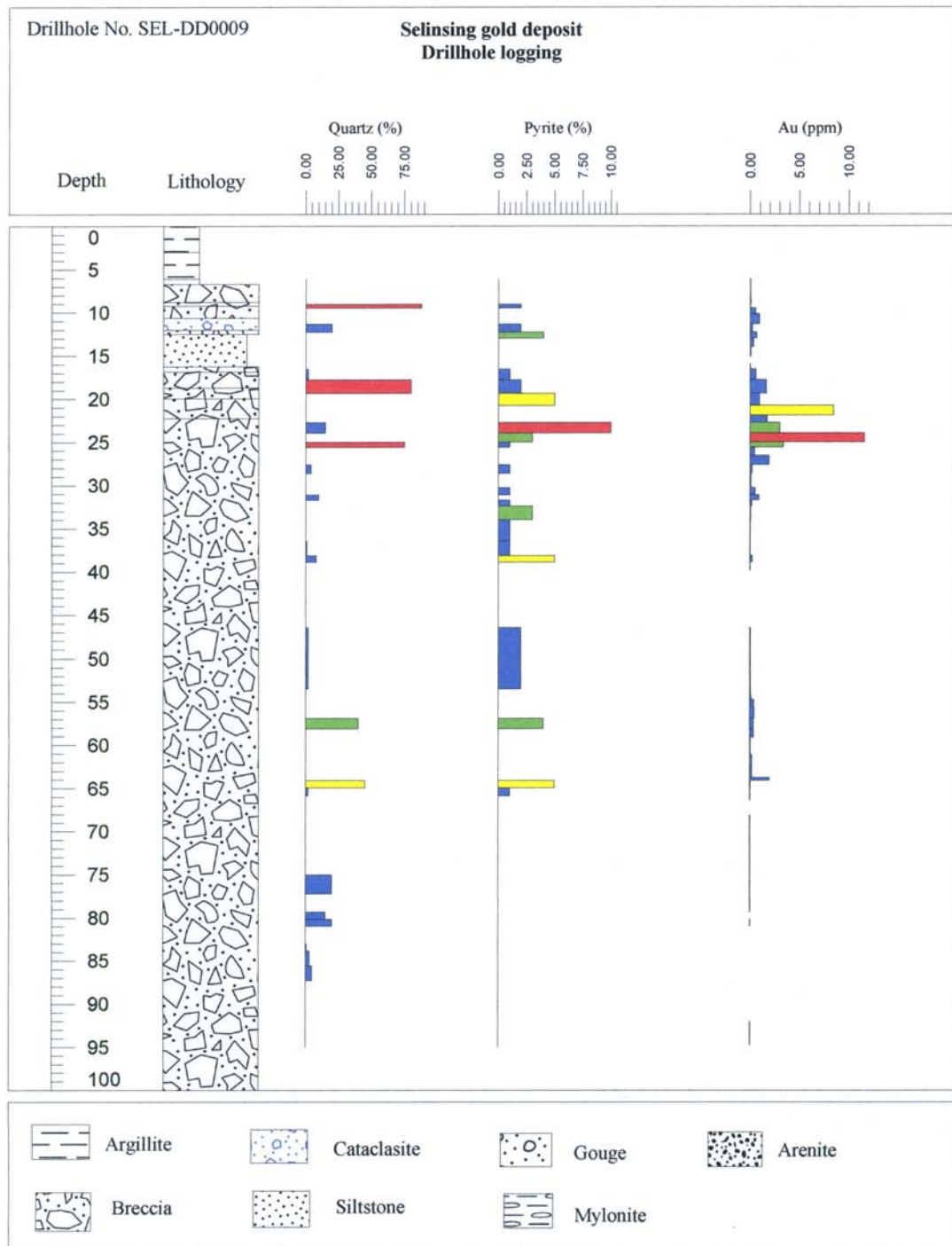


Fig. 5.18. Lithologic log of the drill hole SEL-DD0009 showing distribution of the gold, pyrite and arsenopyrite at the Selinsing gold deposit, Central Malaysia. The colour legend for quartz content is the same as on Fig. 5.17.

5.7. Discussion

Metal distribution at the Selinsing gold deposit shows that gold mineralisation is mostly hosted by cataclasite and breccia zones. This observation matches with the repetitive sequences of cataclasite and breccia that are exposed along the faults zones at mine-site. The structural control of the gold can also be explained by the play of the three main deformation events as discussed in Chapter 4. Within the argillite and siltstone layers, gold content is mostly low and characterised by the absence of quartz veins and sulphide minerals.

Gold mineralisation also shows sharp variation in Au concentration in cataclasite and mylonite rocks. Gold content is higher ($\text{Au} > 1 \text{ ppm}$) in cataclasite, whereas Au content is lower ($\text{Au} < 1 \text{ ppm}$) in mylonite. This change in Au content is probably due to remobilisation and variation of shearing and faulting in different host rocks. Higher Au in cataclasite may be related to grain size as cataclasites are coarse-grained than mylonites and therefore more permeable allowing more fluid circulation. Research by Wan Fuad and Heru (2002) also indicate that gold-bearing quartz veins have been found in the shear zones where cataclasite and breccia outcrop. The density of quartz occurrence changes from one drill hole to the other suggests multiple episode of veining. For instance, the drill hole SEL-DD007 shows high amount of quartz associated with gold mineralisation (Au content: 0-10 ppm) below 150 m downhole; however, the drill hole SEL-DD009 exhibits high amount of quartz associated with pyrite at shallow depth between 5 and 25 m downhole. The hypothesis of multiple

veining was also reported by Jasmi (2007). The Au vs Ag variation both alluvial and in gold vein grains from the Tersang deposit is shown in Figure 5.19. The high fineness in alluvial gold grains at the Tersang gold deposit is probably related to surficial supergene effect (Fig. 5.19). Similarly, Bahna and Chovan (1999) reported that at the Pukanec deposit, Central Slovakia, high fineness in alluvial gold resulted from the transport in supergene conditions. Therefore Ag was dissolved from the surface of the Au-Ag alloy resulting in an increase of fineness. The evidence also indicates that gold grains infilling fractures in some quartz veins within the orebody and those in nearby streams show similarity in low Ag and Pb contents. This chemical signature may be also related to a supergene origin of the gold. However, gold grains in non-brecciated quartz veins, which have higher Ag contents are interpreted to be of primary origin.

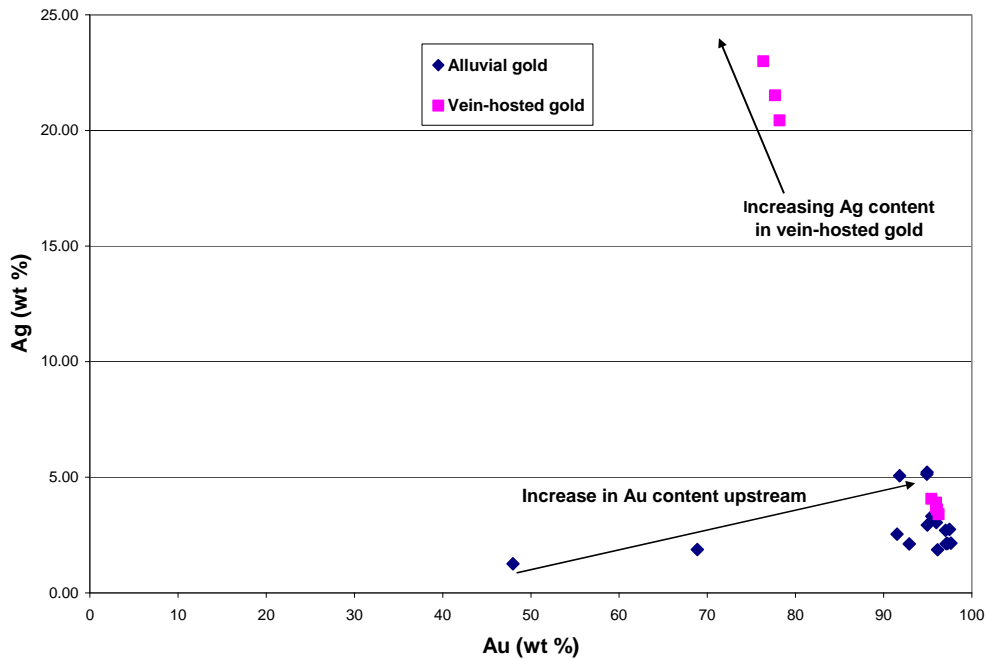


Fig. 5.19. Binary plot of Au and Ag contents in vein and alluvial gold grains at the Tersang deposit.

At Tersang, limited analyses from electrum showed two ranges of fineness: (1) high fineness (959-965) gold associated with pyrite, arsenopyrite and geocronite and (2) low fineness (769-792) gold which occurs with broken arsenopyrite grains. The gold grains found in quartz matrix have higher Ag content (4.07-22.99 wt %) as shown in Fig. 5.19, whereas the gold grains in fractured arsenopyrite (Fig. 5.8B) are depleted in Ag content (3.46-3.92 wt %). This high Ag content also occurs together with As and Sb in the quartz veins. Similarly, the high Ag with As and Sb was recorded in the ore zone at the Hellyer VHMS deposit in the Mount Read Volcanics of Tasmania, Australia (Huston et al., 1992). The evidence seems to suggest that at Tersang the ore zone is probably located where gold and silver are associated with As and Sb.

Khin Zaw (1991) reported that the electrum found together with pyrite has elevated fineness which varies from 430 to 970 for the South Hercules deposit and the high fineness is related to remobilisation of Au. Similarly, at Tersang the electrum associated with pyrite grains have high fineness values (up to 965) suggesting remobilisation of Au. Such occurrences were also observed at the Balcooma Prospect in Queensland, Australia (Huston et al., 1992). At Terang, the high fineness (769-792) of gold are also recorded within broken arsenopyrite also suggesting that Au was remobilized and recrystallised during later events. It can be concluded that as pyrite or arsenopyrite fractured during deformation, gold migrated through the processes of solution-precipitation to cracks and grain edges to form electrum by mixing with silver which is sourced from sulphide minerals. This interpretation was also given by previous authors (e.g., Huston et al., 1992).

5.8. Conclusions

At Tersang, sericite alteration is pervasive within the ore zone where ore minerals are pyrite, arsenopyrite, galena, sphalerite, gold, geocronite and covellite. Gangue minerals include ilmenite, sericite, hematite, illite, and montmorillonite. Among the gangue minerals, sericite, hematite, illite and montmorillonite are dominant. Gold mineralisation in veins shows two generations on the basis of fineness probably suggesting multiple gold depositions. At least one of these generations of gold occurred during brittle deformation as free gold was both found in cracks within quartz matrix and fissures of arsenopyrite.

At Selinsing, illite alteration probably occurred during brittle deformation as evidenced by the presence of illite veins along fracture-filled broken arsenopyrite. In addition, ore mineral assemblage includes pyrite, arsenopyrite, galena, gold, sphalerite, chalcopyrite and pyrrhotite. Gangue minerals are ankerite, rutile, sericite, hematite, calcite, chlorite and illite. Furthermore, gold mineralisation at Selinsing is structurally controlled by the occurrence of cataclasite and breccia units. Moreover, gold mineralisation mostly occurred during brittle deformation at different times.

CHAPTER 6 PYRITE GEOCHEMISTRY

6.1. Introduction

Pyrite is the most abundant and pervasive sulphide mineral in the earth's crust, forming in diverse geological settings as well as modern sedimentary basins (Mann et al., 1990). It is also a common sulphide mineral in numerous ore deposits and can host a great number of trace elements (Huston et al., 1995; Large et al., 2009). This Chapter presents the results of the composition of pyrites to characterise their geochemical signatures and zonation at the Tersang and Selinsing deposits. The aim of this study is to constrain the source of fluids and metals that are responsible for the formation of the deposits. The Chapter will also place an emphasis on the location and distribution of Au within the pyrite grains as this has important implications for timing of gold, as well as mineral processing and extraction. In this Chapter, all gold values plotted above the Au saturation line are interpreted as free gold inclusions (Reich et al., 2005; Large et al., 2007). The trace elements such as V, As, Mo, Se, Ni, Ag and Zn, which are termed the VAMSNZ suite were used as a proxy to suggest a syngenetic origin of gold for the sediment-hosted deposits (Large et al., 2010).

6.2. Method of study

Trace element geochemistry and imaging of the trace element zonation were undertaken using LA ICP-MS facilities at CODES ARC Centre of Excellence in Ore Deposits, University of Tasmania. Analyses were done using a Newwave UP213 laser ablation microprobe coupled with

an Agilent 7500 or 7700 ICP-MS. Samples were ablated in He and mixed with Ar before reaching the ICP-MS. Calibration was carried out with the in-house standard (STDGL2b2), which is a lithium borate fused glass disk, with known concentrations of trace elements (Danyvshevsky et al., 2011). The standard was analysed at regular intervals during analysis to correct for drift and mass bias. To minimize surface contamination, sulphides were pre-ablated with laser pulses. The background gas levels were monitored for 30 s before analysis. The laser shutter was then opened and the sulphides were ablated for about 60-70 s at a firing rate of 5 Hz with laser energy of 3.5 J/cm^2 . The spot sizes used were 10, 15, 20 and 22 μm . Line analyses were done with laser spot sizes of 15 and 25 μm and a firing rate of 5 Hz, with laser energy of 3.5 J/cm^2 . For imaging, the laser was rastered across the sample in a series of parallel lines. The spot size used was 22 μm and each line was pre-ablated before analysis. The backgrounds were recorded before each image and subtracted from each analysis line (Large et al., 2009). The standard STGDL2b2 was set up at the beginning and the end of each analysis (Danyvshevsky et al., 2011).

6.3. Processing of trace element maps

A total of twenty-nine elements were analysed by LA ICP-MS from pyrites including: Na, Mg, Al, Si, K, Ca, Ti, V, Cr, Mn, Fe, Co, Ni, Cu, Zn, As, Se, Mo, Ag, Sb, Te, W, Pt, Au, Hg, Tl, Pb, Bi and U. First, the trace element maps were converted from count per second into part per millions (ppm) in order to get a robust representation of element concentration for each pyrite type. Second, the csv files were imported into ioGAS which is an advanced geochemical

exploratory data analysis software package. Third, each pyrite types for each gold deposit were classified and examined in x and y coordinates for visualization and presentation. Fourth, statistical analysis of all trace elements within each pyrite type were exported into excel for further data processing and interpretation. All results comprising mean, median, and standard deviation are presented in Appendix C.

6.4. Pyrite geochemistry at the Tersang gold deposit

The pyrite trace elements analysis and mapping were undertaken for the four pyrite types that were identified earlier on the basis of their textures including euhedral to subhedral “spongy” pyrite with internal fracturing (pyrite 1), euhedral clean pyrite (pyrite 2) overgrown on pyrite 1, amorphous pyrite with high As and high Au (pyrite 3), and crack-fill or vein pyrite with high As and low Au (pyrite 4). Eight pyrite maps and sixty two spot analyses were done in this study.

6.4.1. Pyrite trace element mapping at Tersang

The LA ICP-MS trace element maps of pyrites are shown in Figs. 6.1-6.6. The LA-ICPMS images of trace elements in pyrite 1 and pyrite 2 are shown in Figs. 6.1-6.4. Mapping of pyrite 1 shows enrichment in Au (mean: 3.4 ppm), As (mean: 8,496 ppm), Sb, and Bi and depletion in Pb, Cu, Se, Tl, and Pt (Fig. 6.1) compared with typical Tersang pyrite (average). Pyrite 2 is enriched in Co and Ni which display oscillatory zoning. In addition, pyrite 1 when hosted in veins has a core which is depleted in gold with slight enrichment of Au in the outer core zone (Fig. 6.2). Pyrite 2 was also found overgrown on pyrite 1 in the wall rock and shows enrichment in As, Au, Sb, Tl and Pb and depletion in Cu, Zn, and Ag (Fig. 6.3).

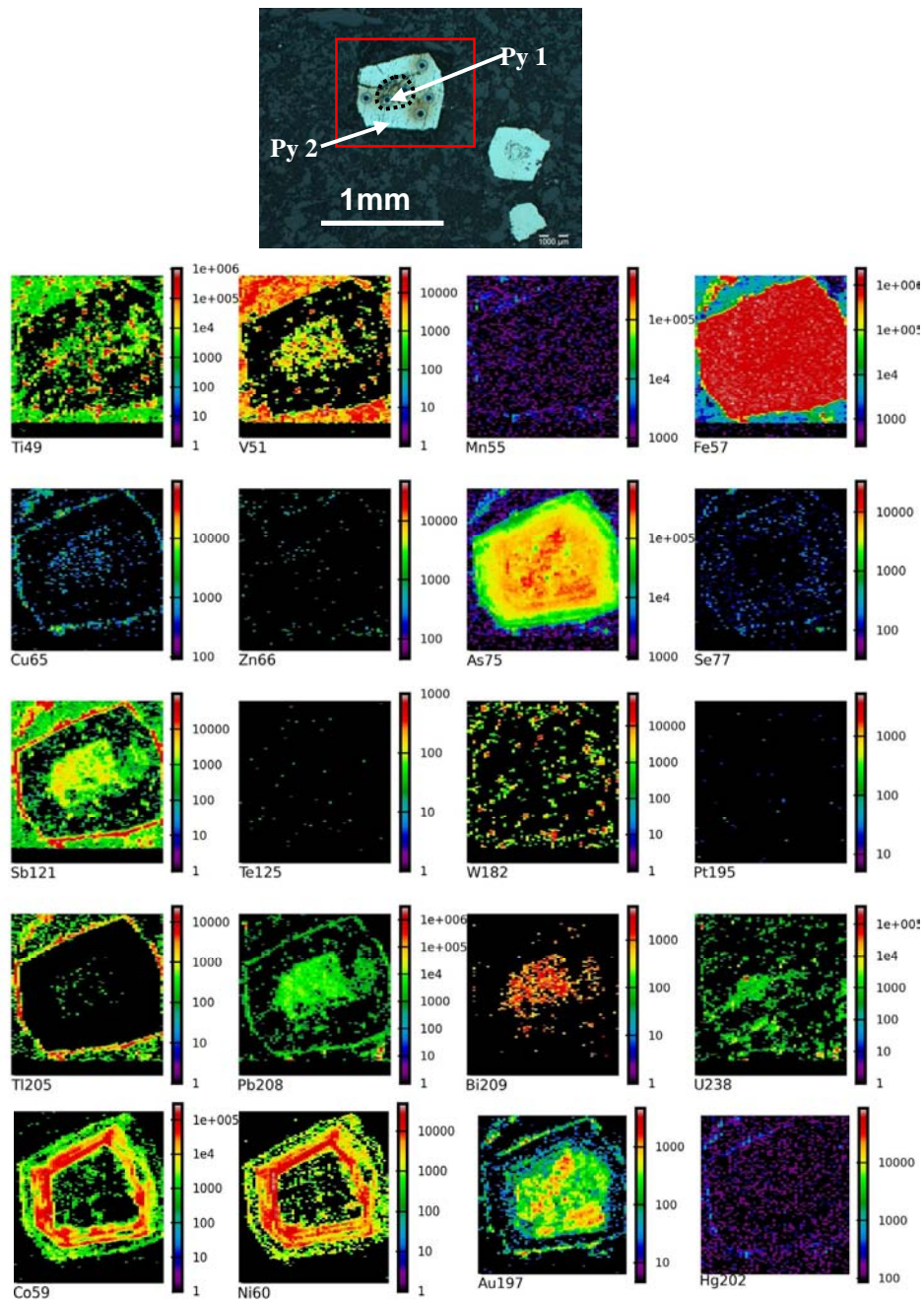


Fig. 6.1. LA-ICPMS images of trace elements in pyrite 1 and pyrite 2 (Sample No. TER-R007) at the Tersang gold deposit. The core part which is pyrite 1 is enriched in Au, Bi, Sb, As, V and Ti. The red spots in the Ti image of pyrite 1 suggest micro-inclusions of rutile. The outer zone shows Co-Ni rings in the pyrite 2. The outermost rim shows enrichment in Au, Ti, Pb and Sb. Values are in ppm.

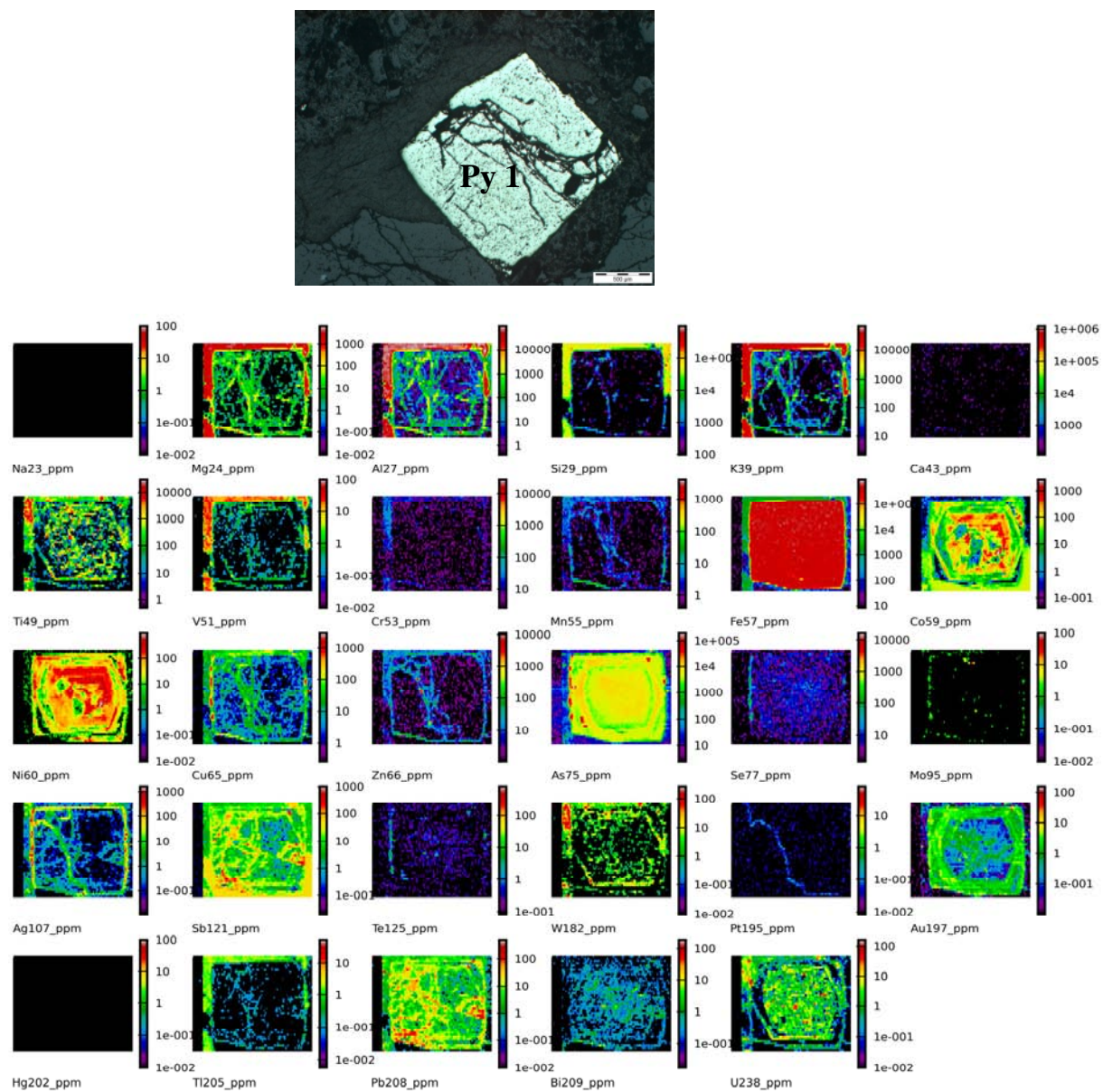


Fig. 6.2. LA-ICPMS images of trace elements in vein-hosted pyrite 1 (Sample No. TER-R039) at the Tersang gold deposit. Pyrite 1 is enriched in Pb, Sb, Co, Ni and U. Co, Ni and As show cyclic zonation. Au > 1ppm is in the outer As-rich zone. The outermost rim is enriched in Cu, Ag, As. The dotted texture of Ti suggests presence of micro-inclusions of rutile.

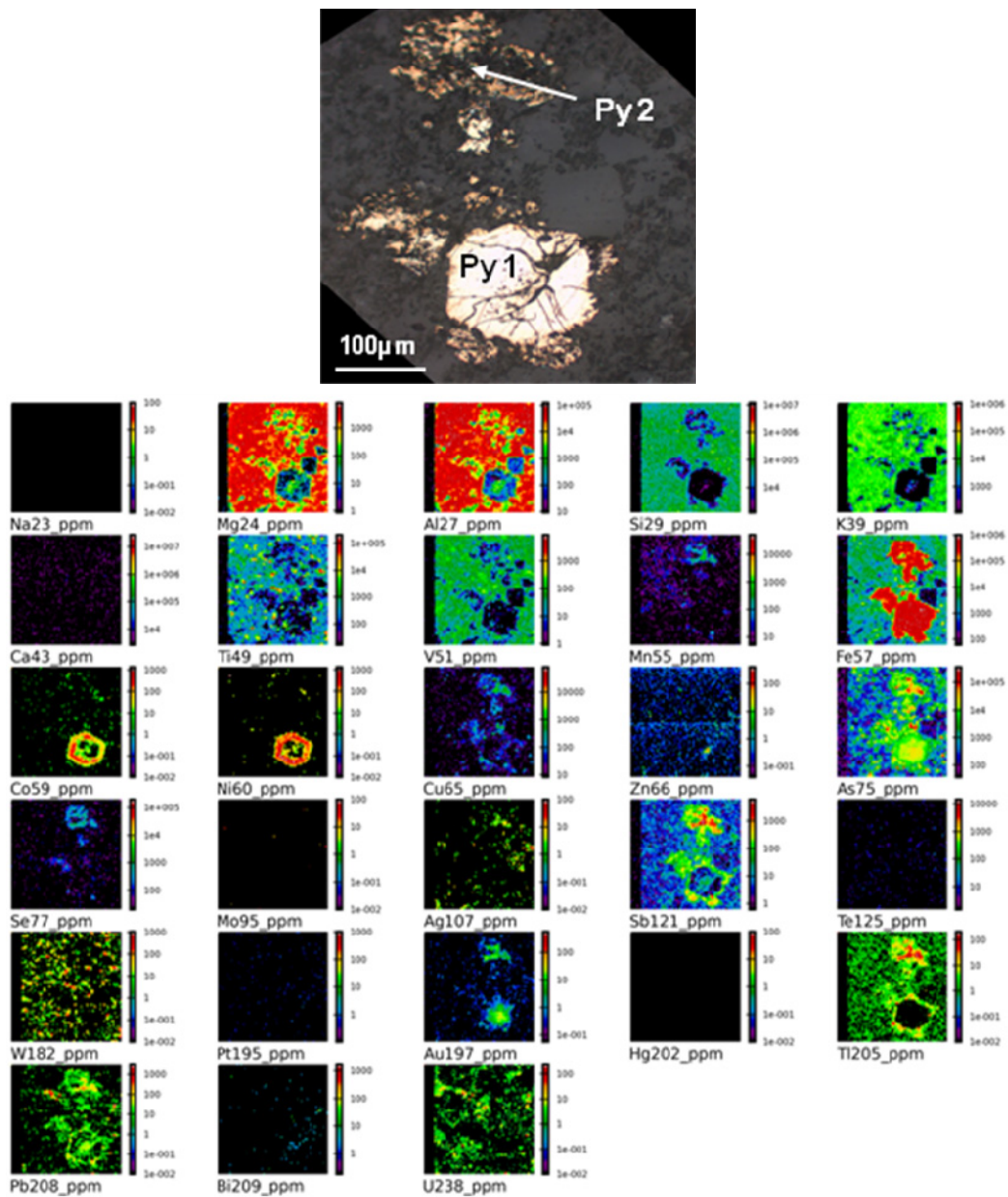


Fig. 6.3. LA-ICPMS images of trace elements in wallrock-hosted pyrite 1 and pyrite 2 (Sample No. TER-R007B) at the Tersang gold deposit. Pyrite 1 shows Co-Ni zoning patterns and it is enriched in Au, As in the core with lesser enrichment in Pb. The rim of Pyrite 1 is enriched in Tl, Sb and Pb. Both pyrite 1 and pyrite 2 show low V.

Chapter 6: Pyrite geochemistry

Intrusion-hosted pyrite 2 is mostly depleted in trace elements but it shows a core enriched in Se and Te and an outer core with high As (Fig. 6.4). Mapping of pyrite 4 shows enrichment in As and depletion in Au (mean: 0.3 ppm) as in Fig. 6.5. Furthermore, pyrite 4 is enriched in Te, Se, Tl, and Pt and depleted in Au, Ag, and Bi. All maps show the presence of Co and Ni oscillatory zoning pattern in pyrites 1 and 2 (Fig. 6.5).

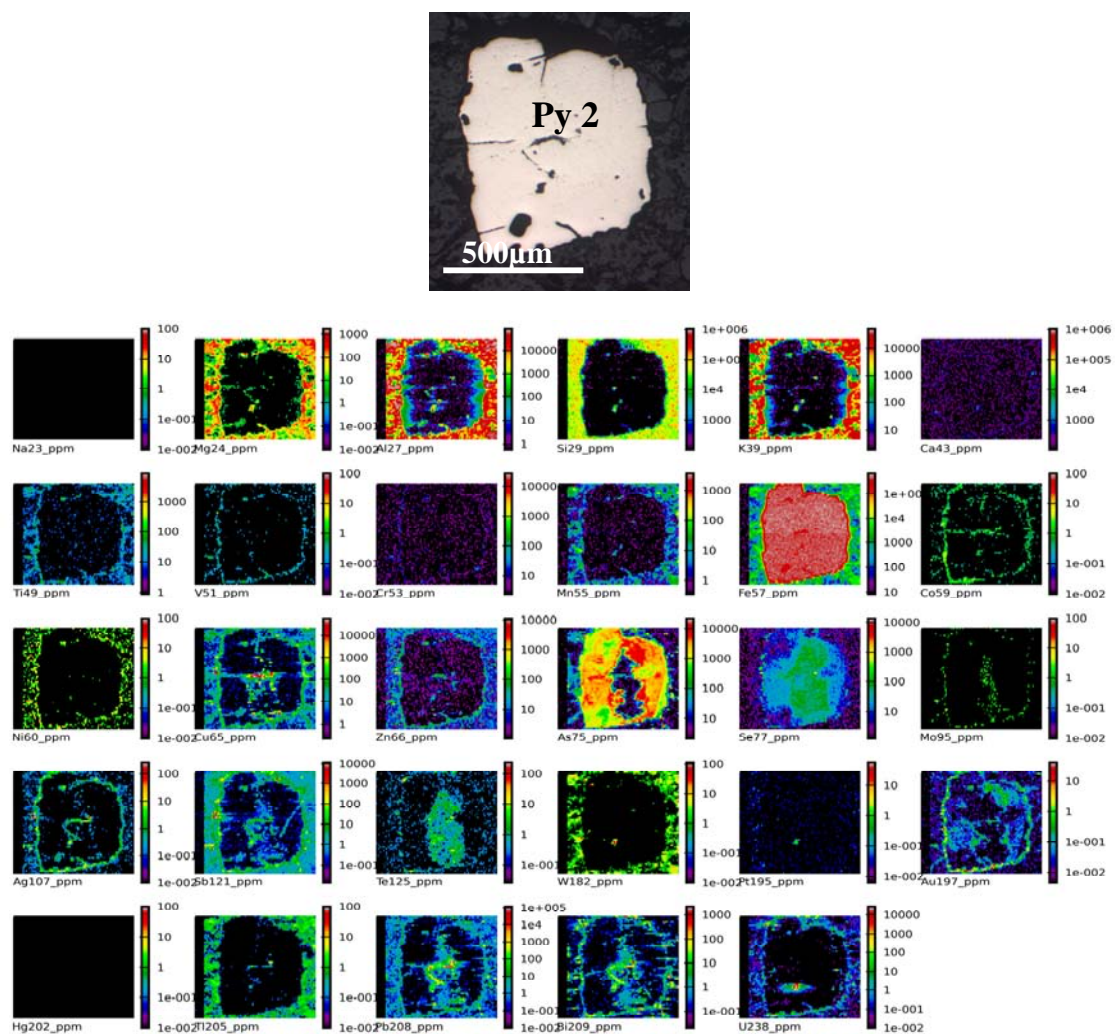


Fig. 6.4. LA-ICPMS images of trace elements intrusion-hosted pyrite (pyrite 2) (Sample No. TER-R033) at the Tersang deposit. The core of py2 is enriched in Te, Se, with lesser Cu, Sb and Pb. The outer part of pyrite 2 is enriched in As and patchy very minor (<1 ppm) Au. There is a lack of Co and Ni in py2 except for a narrow outer rim.

Chapter 6: Pyrite geochemistry

The LA ICP-MS trace element mapping of pyrite 3 shows enrichment in As, Se, Sb, Tl, and Mn and depletion in elements such as Co, Ni, Zn, Ag, Te, Bi, Ti, V, W, and Pt (Fig. 6.5). Importantly, pyrite 3 is highly enriched in Au (mean: 16 ppm). Overall, higher gold concentrations were found in pyrite 3.

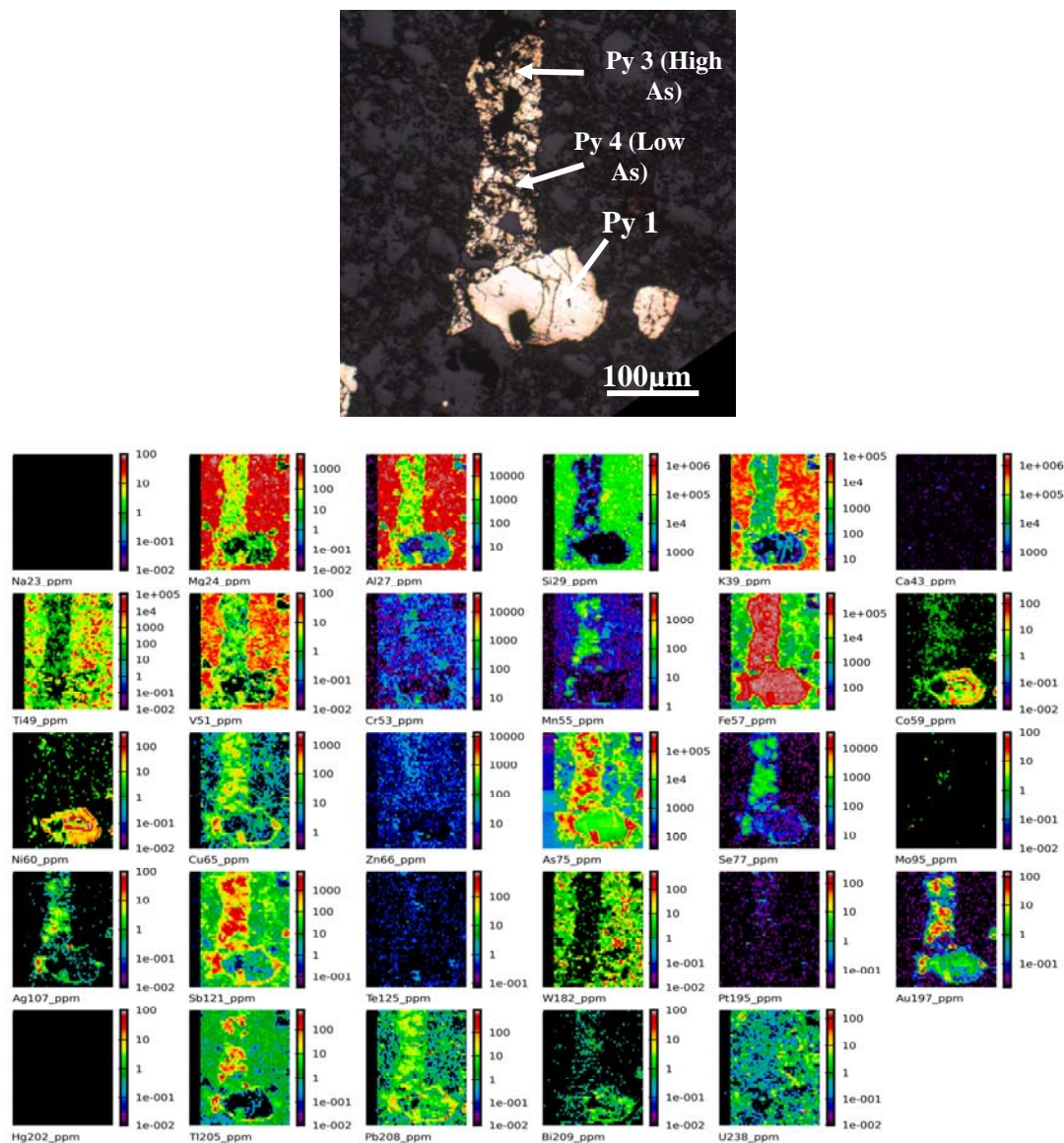


Fig. 6.5. LA-ICPMS images of trace elements in pyrite 1, pyrite 3 and pyrite 4 (Sample No. TER-R007B) at the Tersang gold deposit. Pyrite 1 shows Co-Ni zoning pattern and enrichment in Bi. There is depletion in As, Au, Sb in the inner core. Pyrite 4 is enriched in Au, As, Tl, Sb with a decrease in concentration in Se, Pb, Bi, Hg and V. Note some gold inclusions in the rim of the pyrite 1.

Chapter 6: Pyrite geochemistry

The pyrite attribute map (Fig. 6.6A) comprises all pyrite types and Sample numbers. Construction of this map involves two stages: (1) upload all pyrite ppm (part per million) data into ioGAS software; (2) group pixels into each pyrite type on the basis of As, Au and other trace elements. Some pyrite grains are similar in chemistry with different texture. The data for each pixel in the images are presented in the gold solubility diagram of Reich et al. (2005) in Fig. 6.6B. This diagram indicates the presence of gold inclusions (above the saturation line) mostly in silicate minerals or along the edges of pyrite.

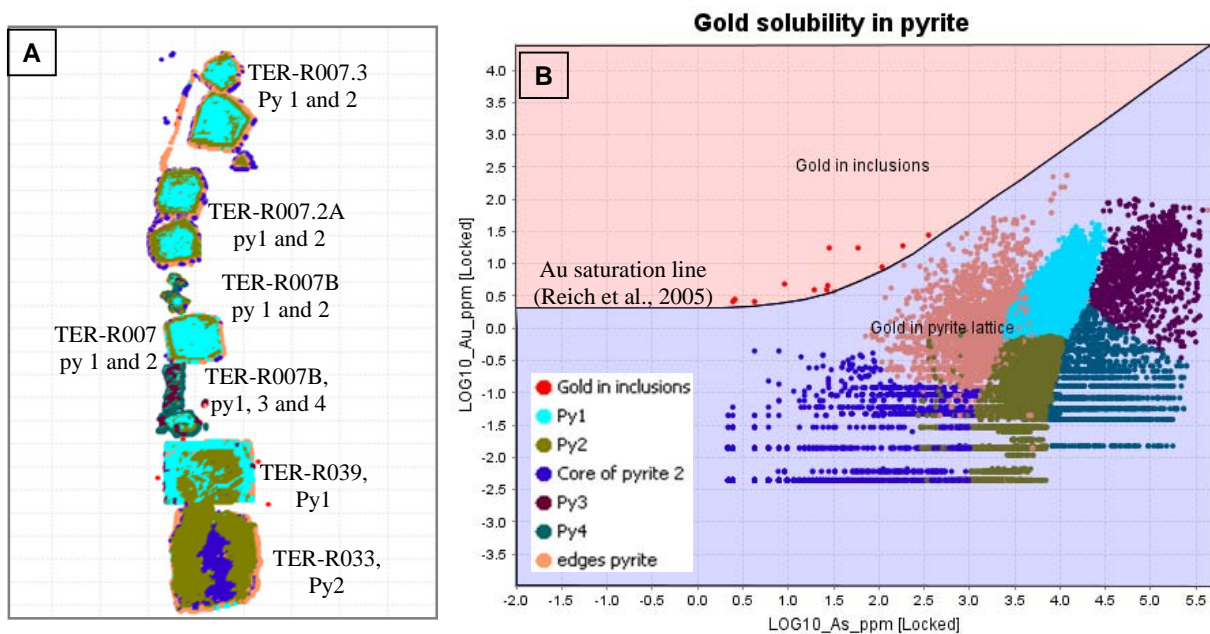


Fig. 6.6. Attribute map of pyrite grains and gold solubility diagram at Tersang. **A.** Attribute map of all pyrite types (pyrite 1, pyrite 2, pyrite 3 and pyrite 4) at the Tersang gold deposit. **B.** Gold solubility plot of As against Au for all the pyrite types at the Tersang deposit, Central Malaysia. Legend refers to euhedral to subhedral “spongy” pyrite with internal fracturing (pyrite 1), euhedral clean pyrite (pyrite 2), amorphous pyrite with high As and high Au (pyrite 3), and crack-fill or vein pyrite with high As and low Au (pyrite 4). Note the presence of gold inclusions (red colour points) above the Au saturation line (curved black line).

6.4.2. Trace element distribution at Tersang

This section examines trace element distribution in all pyrite grains and focuses on concentrations and trends of certain trace elements within the pyrite types. Trace elements have been plotted according to their order of increasing atomic number and valence from left to right as shown in the periodic table of chemical elements (Fig. 6.7). The average compositions of each pyrite types were then normalised to the average of the Tersang pyrites in order to highlight their differences (Fig. 6.8).

Group #	1	2	3	4	5	6	7	8	9	10	11	12	13	14	15	16	17	18
Period 1	1 H																	2 He
Period 2	3 Li	4 Be											5 B	6 C	7 N	8 O	9 F	10 Ne
Period 3	11 Na	12 Mg											13 Al	14 Si	15 P	16 S	17 Cl	18 Ar
Period 4	19 K	20 Ca	21 Sc	22 Ti	23 V	24 Cr	25 Mn	26 Fe	27 Co	28 Ni	29 Cu	30 Zn	31 Ga	32 Ge	33 As	34 Se	35 Br	36 Kr
Period 5	37 Rb	38 Sr	39 Y	40 Zr	41 Nb	42 Mo	43 Tc	44 Ru	45 Rh	46 Pd	47 Ag	48 Cd	49 In	50 Sn	51 Sb	52 Te	53 I	54 Xe
Period 6	55 Cs	56 Ba	*	72 Hf	73 Ta	74 W	75 Re	76 Os	77 Ir	78 Pt	79 Au	80 Hg	81 Tl	82 Pb	83 Bi	84 Po	85 At	86 Rn
Period 7	87 Fr	88 Ra	**	104 Rf	105 Db	106 Sg	107 Bh	108 Hs	109 Mt	110 Ds	111 Rg	112 Cn	113 Uut	114 Uuq	115 Uup	116 Uuh	117 Uus	118 Uuo
* Lanthanides (Lanthanoids)			57 La	58 Ce	59 Pr	60 Nd	61 Pm	62 Sm	63 Eu	64 Gd	65 Tb	66 Dy	67 Ho	68 Er	69 Tm	70 Yb	71 Lu	
** Actinides (Actinoids)			89 Ac	90 Th	91 Pa	92 U	93 Np	94 Pu	95 Am	96 Cm	97 Bk	98 Cf	99 Es	100 Fm	101 Md	102 No	103 Lr	

Fig. 6.7. Periodic table of chemical elements. Note the red zones comprising the elements mapped using LA ICP-MS at CODES Centre of Excellence in Ore Deposit Research, University of Tasmania.

Chapter 6: Pyrite geochemistry

Normalised quantification of trace element contents shows that pyrite 1 and pyrite 2 are enriched in the elements such as Co, Ni and Ti. In contrast, pyrite 3 and pyrite 4 show low Co, Ni, Ag, Tl and Cu. Normalised quantitative analysis of elements expected to be enriched in diagenetic pyrite, the VAMSNZ (V, As, Mo, Se, Ni, Ag, Zn) trace elements suite of Large et al. (2010) is also shown in Fig. 6.8. Correlations of Ag-Au and Ni-Co for all pyrite types are shown in Fig. 6.9.

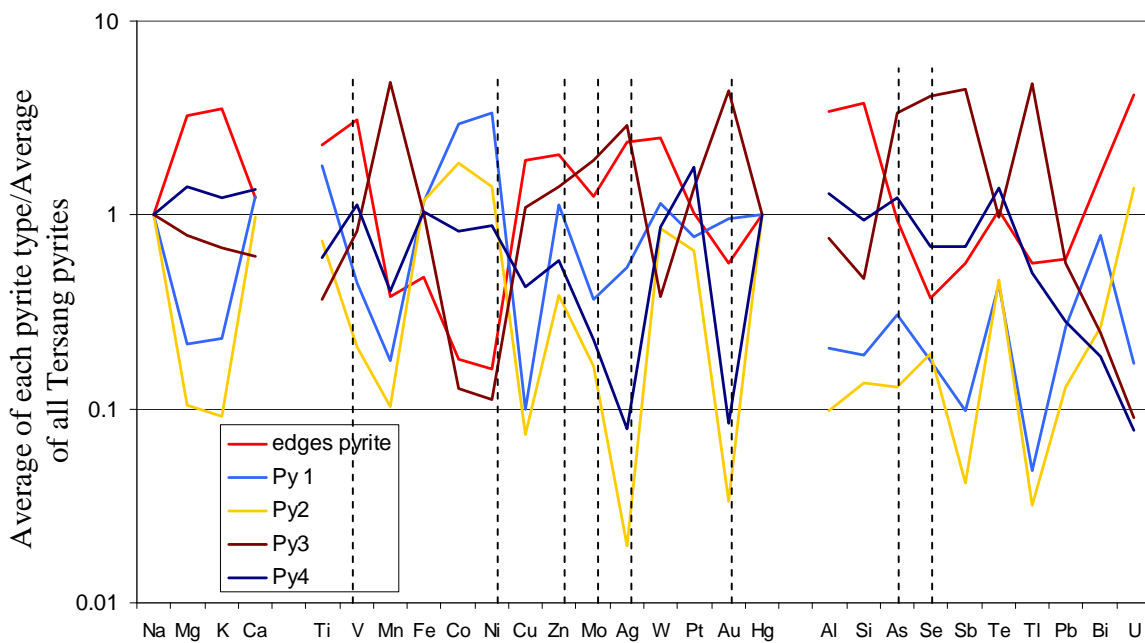


Fig. 6.8. A normalised quantitative analysis of trace elements for all pyrite types at the Tersang gold deposit, Central Malaysia. Pyrite 1 and pyrite 2 has the highest Co and Ni content compared to pyrite 3 and pyrite 4. Pyrite 3 has the highest Au content and also enriched in Zn, Mo, As, Se, Sb, Tl and Ag. Edges of pyrite contain about 2 ppm Au with higher contents in silicates (Na, Mg, K, Ca). Pyrite 1, pyrite 2 and pyrite 4 have the lowest Au concentration. Pyrite 1, pyrite 2 and pyrite 3 have low silicates content whereas pyrite 4 has higher silicate contents. Dotted lines indicate all VAMSNZ trace elements and Au.

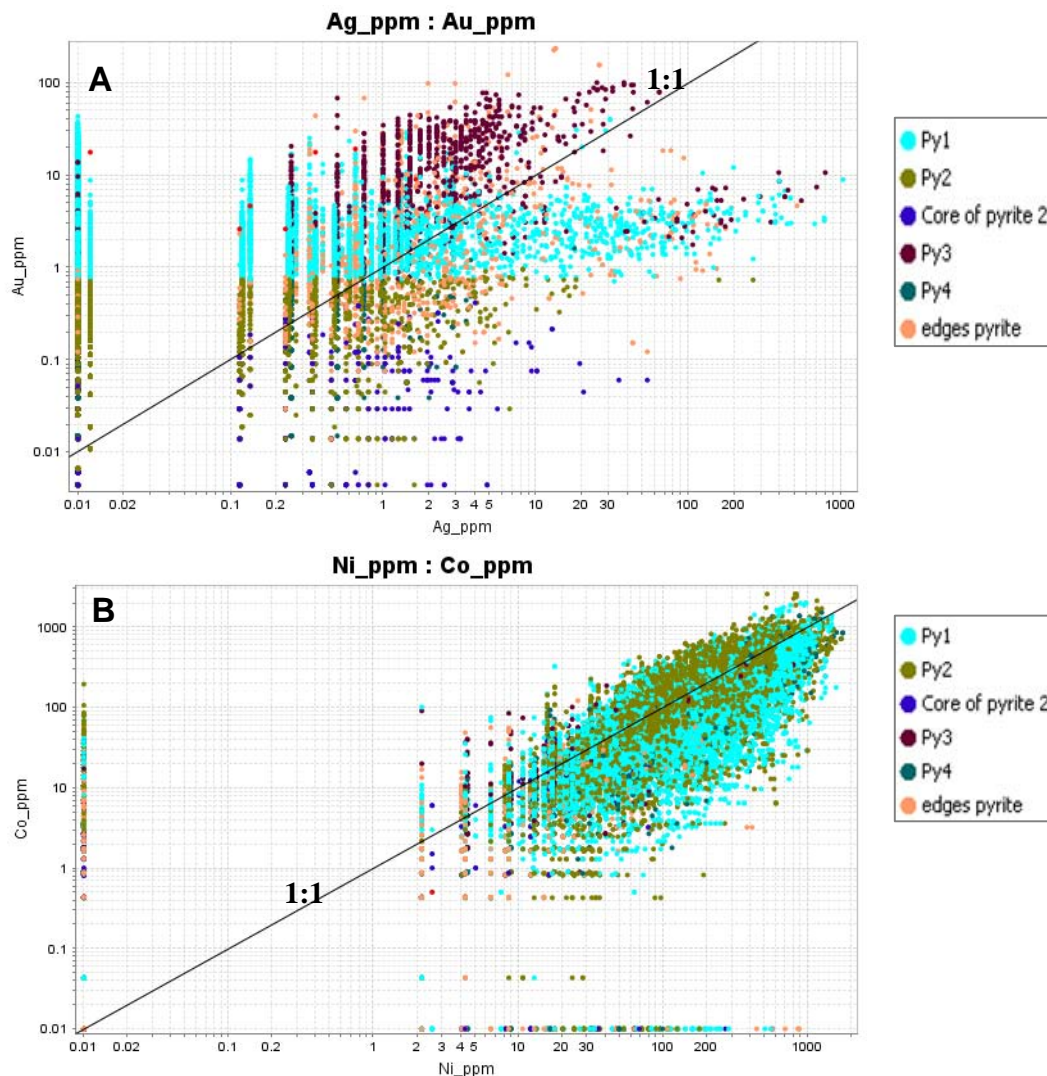


Fig. 6.9. Trace element ratios at the Tersang gold deposit. **A.** Ag-Au ratio of all pyrite types. **B.** Ni-Co through pyrite paragenesis showing good correlation from pyrite 1 to pyrite 4.

Figure 6.9A shows that the main gold-bearing pyrite (Py3) has a high Au/Ag ratio which is typical of hydrothermal (orogenic) gold (Large et al., 2007; 2009). The ratio Co/Ni shows a linear trend for all Tersang pyrite types.

6.5. Pyrite geochemistry at the Selinsing gold deposit

Six pyrite maps and sixty-four spot analyses were done at the LA ICP-MS Laboratory, CODES ARC Centre of Excellence in Ore Deposits, University of Tasmania. Pyrite 1 and pyrite 2 were not mapped using LA ICP-MS due to their small size. Therefore, only the spot analysis data are available for pyrites from the early generation at Selinsing. The same analytical procedure for Tersang was also employed at Selinsing. Pyrite trace element mapping and spot analyses were undertaken for all seven pyrite types. Spot analysis indicates that pyrite 1 and 2 are enriched in Ti, Co, V, Cu and Sb and depleted in As, Ni, Au and Bi relative to the other pyrite types at Selinsing. Mean concentrations of V, As, Mo, Se, Te, Ni, Ag, Zn (VAMSNAZ), Au and pyrite morphology are shown in Fig. 6.10.

The LA ICP-MS trace element map of pyrite 3 shows that the core of pyrite 3 is enriched in As (mean: 22101 ppm), Au (mean: 41.20 ppm), Co, and Ni and depleted in Cu, Bi, and Pb (Fig. 6.11). LA ICP-MS trace element map of pyrite 4, pyrite 5, and pyrite 6 shows that pyrite 4 is enriched in As (mean: 2524 ppm), Co, Ni, and Sb and depleted in Au (mean: 0.6 ppm), Cu, Ag, Te, and V. Similarly, pyrite 5 is enriched in As (mean: 3,188 ppm), Co and Ni but strongly depleted in Au (mean: 0.4 ppm), Sb, Ag, Te, Zn (Fig. 6.12). The LA ICP-MS trace element map of pyrite 6 shows enrichment in As (mean: 6,928 ppm), Au (mean: 8 ppm), Co, Ni, Pb and Bi and depletion in Ag, Te, Se, Mo, Sb, Tl and U. However, pyrite 7 is enriched only in Co and Ni and depleted in As (mean: 627 ppm), Au (mean: 0.8 ppm), Te and Se compared to pyrite 6 (Fig. 6.13). The LA ICP-MS trace element map of composite pyrite (pyrite 4, pyrite 5, pyrite 6, and pyrite 7) shows variation in trace elements concentration of each pyrite type as they grew on one another through time (Fig. 6.14).

Chapter 6: Pyrite geochemistry

The map shows enrichment in As within pyrite 4, pyrite 5 and pyrite 6. Gold oscillates through time reaching the highest concentrations in pyrite 3 and pyrite 6.

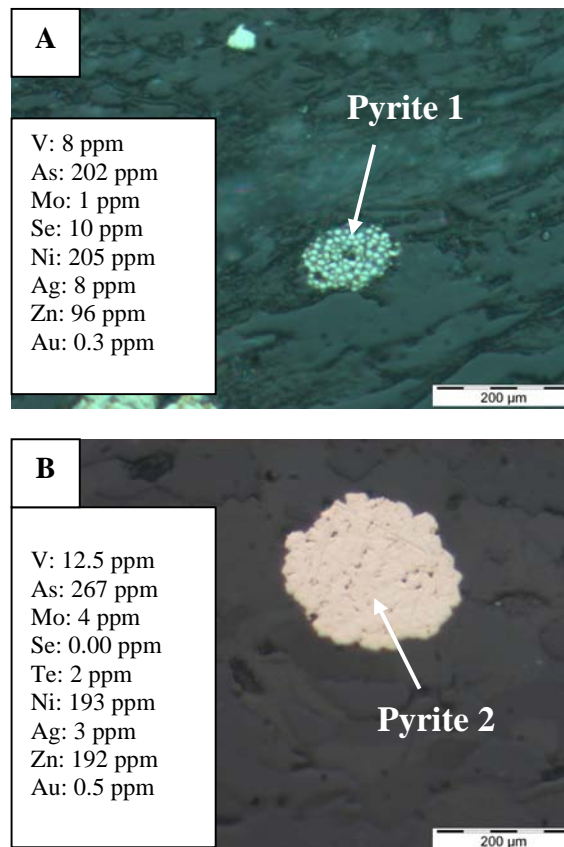


Fig. 6.10. Framboidal pyrite textures and LA ICP-MS spot analysis at Selinsing (Sample No. SEL-R009). **A.** Framboidal pyrite (pyrite 1) with mean concentration of VAMSNZ (V, As, Mo, Se, Ni, Ag, and Zn) trace elements. **B.** Recrystallised pyrite (pyrite 2) with results of VAMSNZ trace element contents.

The LA ICP-MS trace element map of pyrite 4 and pyrite 5 shows enrichment in As (mean: 5618 ppm), Ni and Bi within the core and rim. However, the core (pyrite 4) is particularly enriched in silicates and rutile inclusions (Fig. 6.15). Another LA ICP-MS trace element map of pyrite 4 and pyrite 5 revealed very low Au content (mean: 0.01 ppm) for both pyrite types and higher contents in As (mean: 278 ppm) in pyrite 5 (Fig. 6.16). High Ni is in both pyrite types.

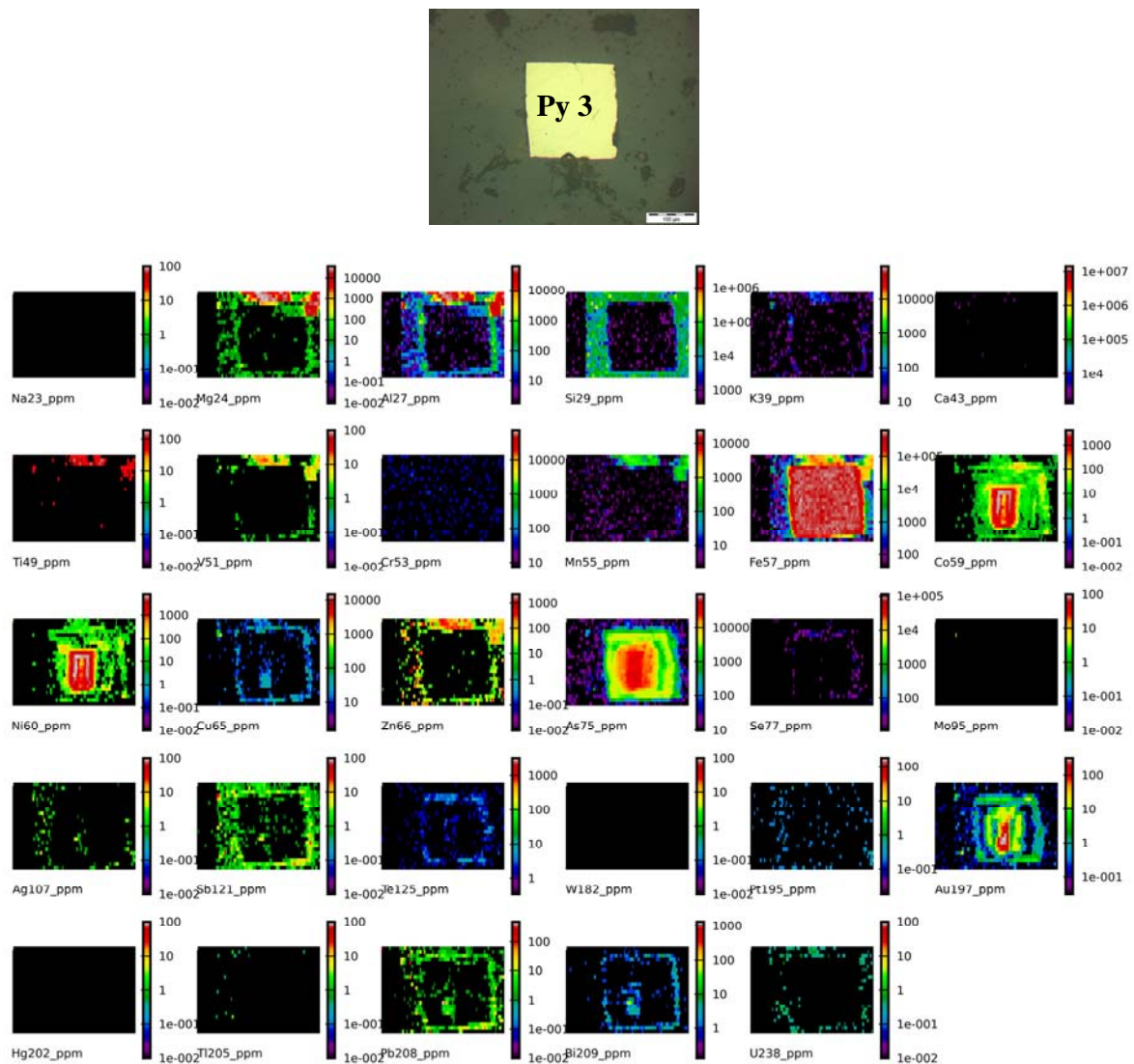


Fig. 6.11. LA-ICPMS images of trace elements in early metamorphic, vein-hosted pyrite 3 (Sample No. SEL-R039) at the Selinsing gold deposit. There is enrichment in As, Au, Co and Ni in the core and lesser enrichment in the rim in Zn, Cu, Sb, Bi and Pb.

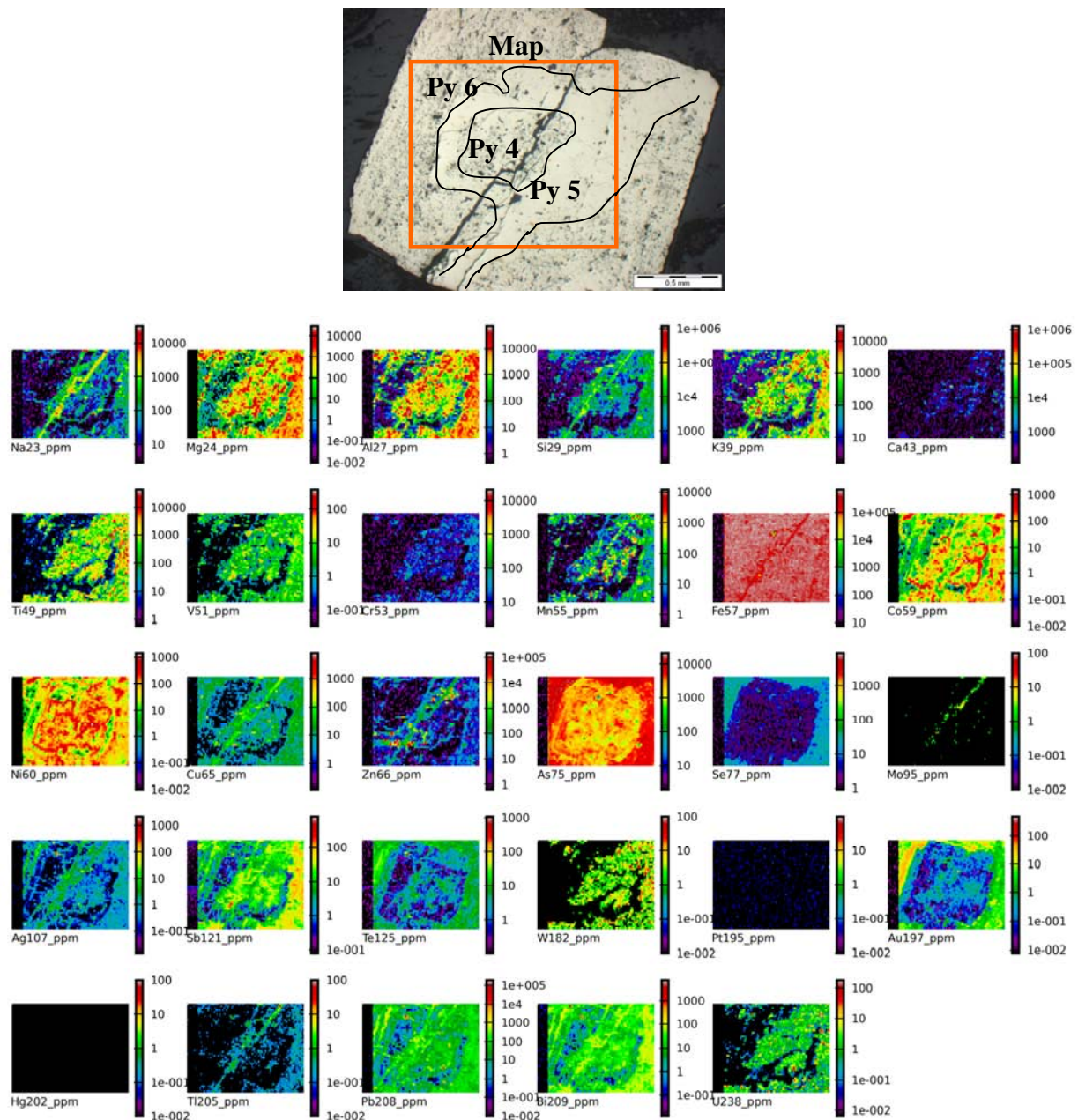


Fig. 6.12. LA-ICPMS images of trace elements in pyrite 4, pyrite 5, and pyrite 6 (Sample No. SEL-R006) at the Selinsing gold deposit, Central Malaysia. Pyrite 4 is enriched in Sb, Co, Ni, W and U. However, pyrite 5 and pyrite 6 are enriched in As, Au, Pb, Bi, and also contain relatively high concentration of Co and Ni. Pyrite 6 contains the highest Au and As concentrations (1-20 ppm Au). Pyrite 4 contains inclusions of sphalerite, sericite, chlorite and albite.

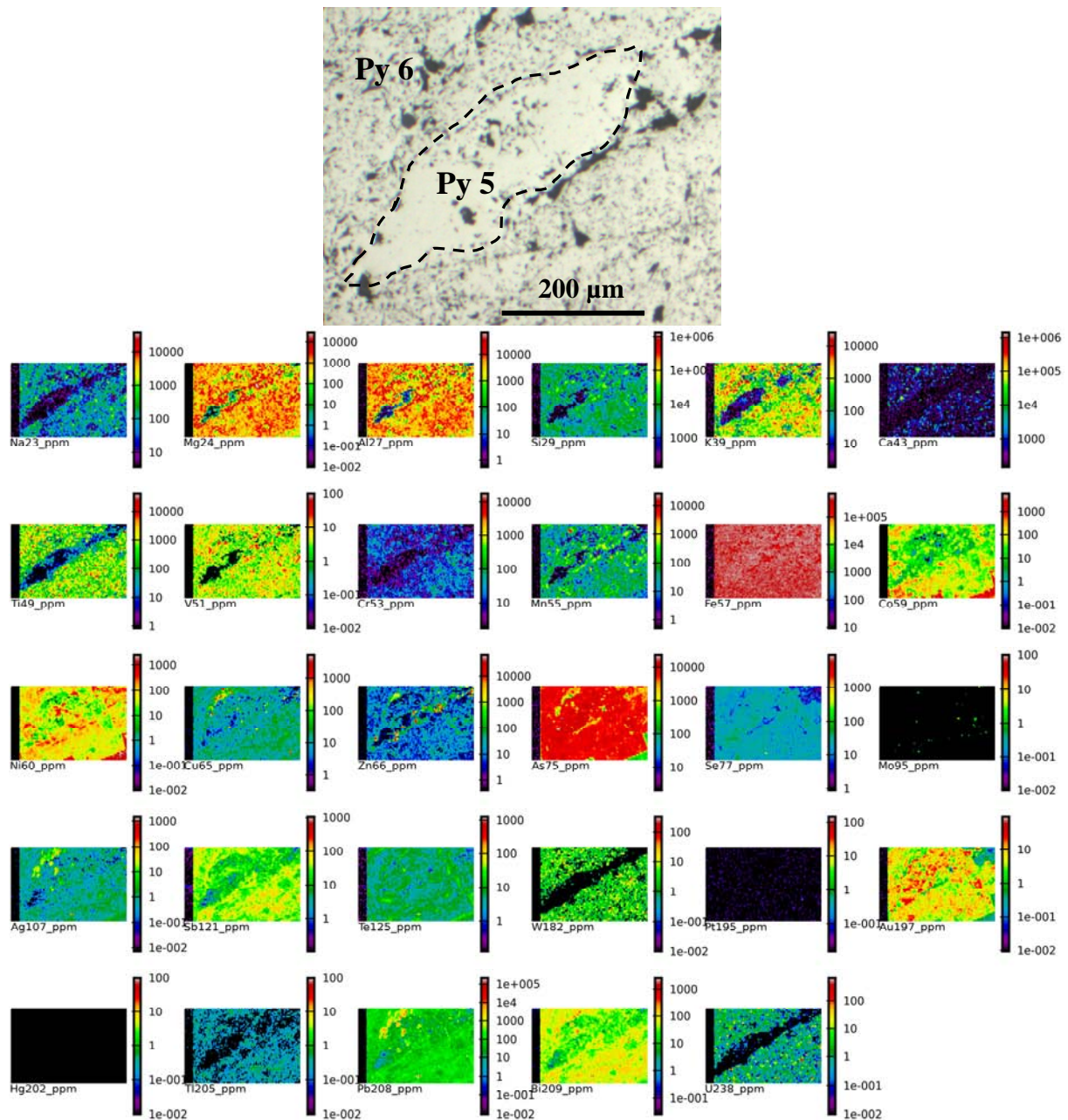


Fig. 6.13. LA-ICPMS images of trace elements in pyrite 5, pyrite 6 (Sample No. SEL-R006) at the Selinsing gold deposit, Central Malaysia. Pyrite 5 is enriched in chlorite, sericite and calcite with high As and low Se content. Pyrite 5 has high As, Au with low Pb and Bi contents. Pyrite 5 also contains inclusions of sphalerite, chalcopyrite and galena. Pyrite 6 is enriched in Co, Ni and Au.

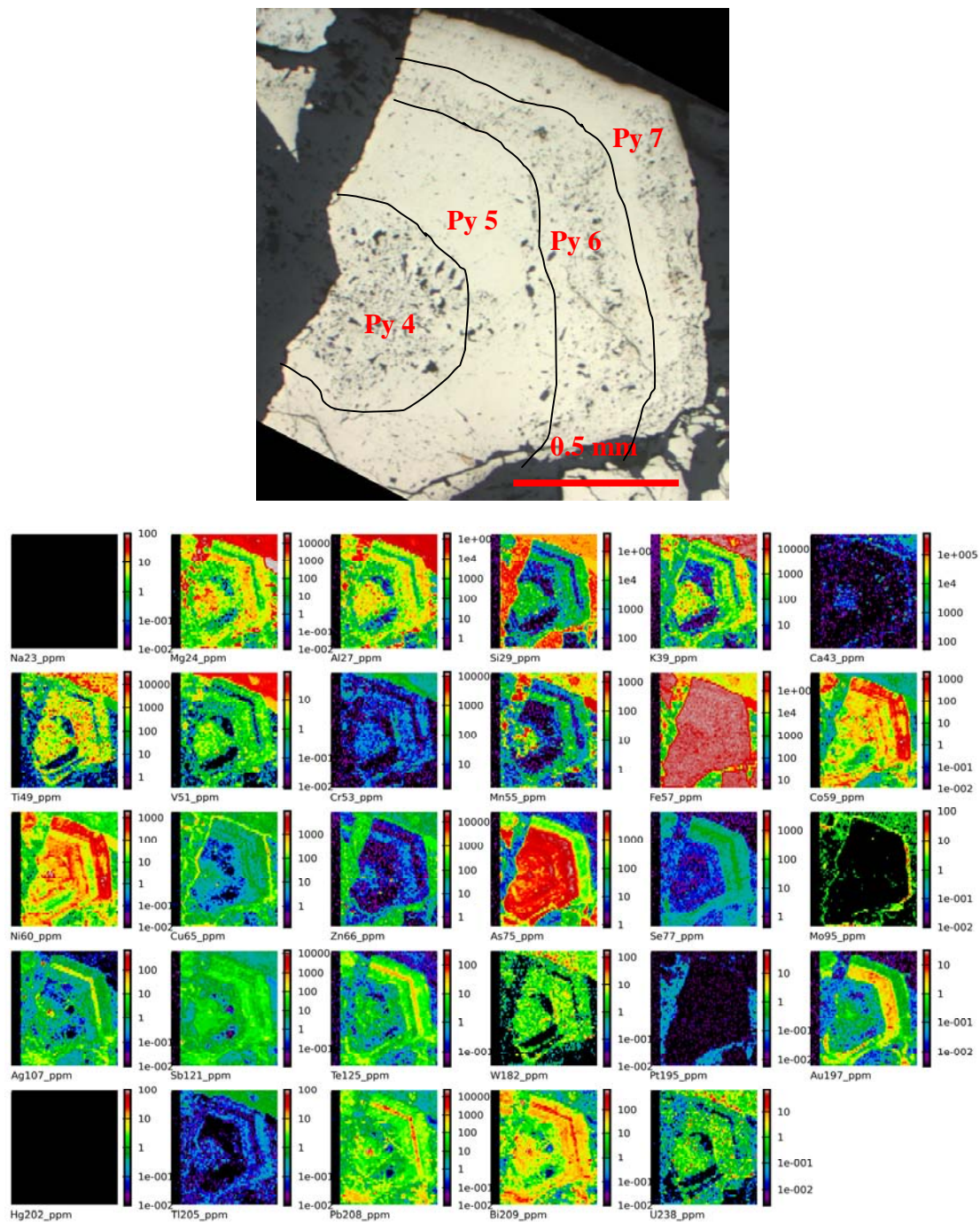


Fig. 6.14. LA-ICPMS images of trace element of zone hydrothermal pyrites (pyrite 4, pyrite 5, pyrite 6, and pyrite 7) at the Selinsing gold deposit (Sample No. SEL-R006). The core (pyrite 4) is enriched in As, Bi, Ti, Pb and depleted in Au, Te, V, Sb and Cu. There are also inclusions of galena in pyrite 4. Hydrothermal pyrites (pyrite 5, pyrite 6 and pyrite 7) are characterised by Co-Ni zoning. Pyrite 6 has elevated Au, As, Pb, Te, and Ag contents. Pyrite 7 has high Co and Ni contents with some inclusions of chalcopyrite in the rim. Abundant rutile inclusions in pyrite 4, pyrite 6 and pyrite 7.

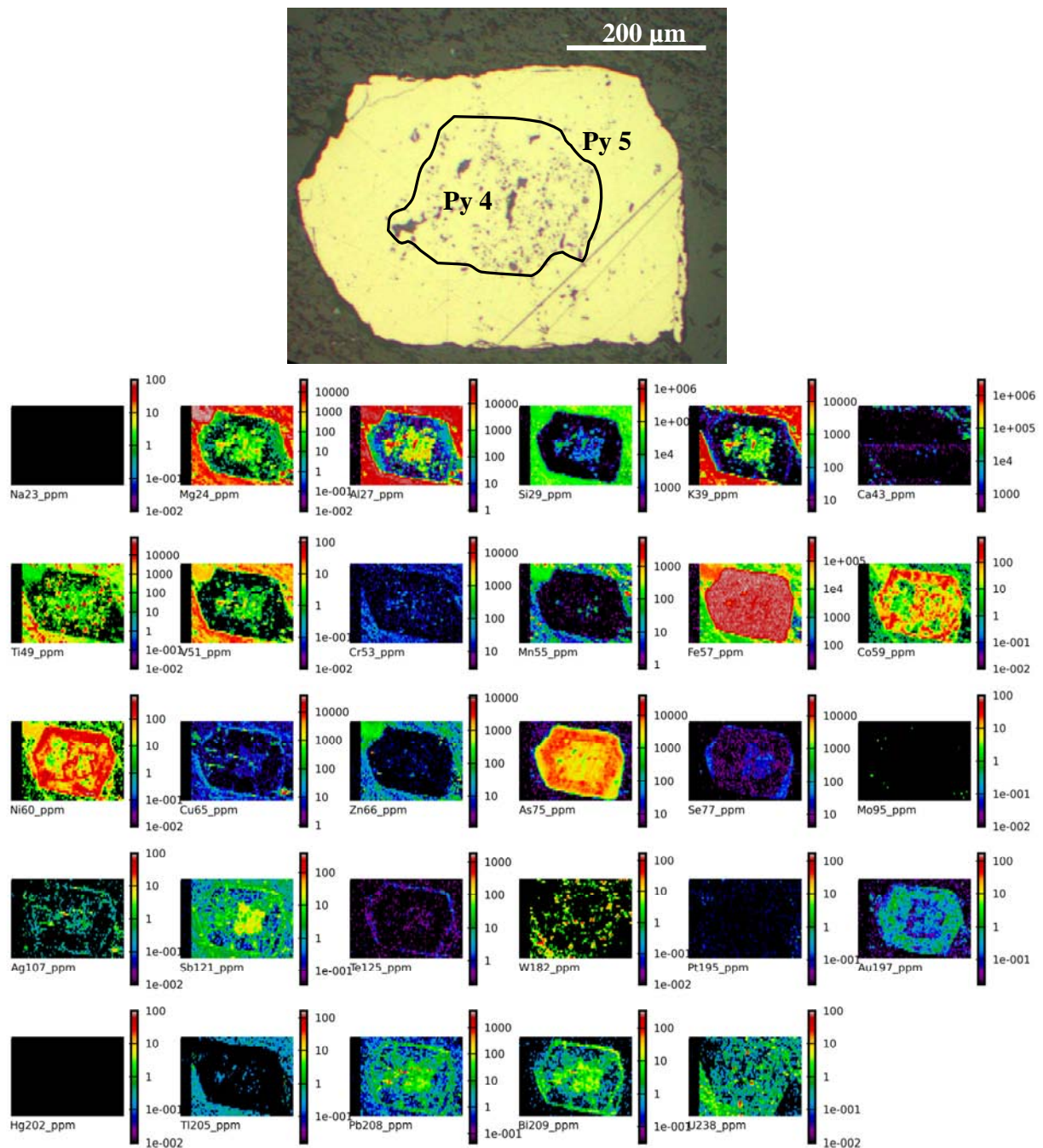


Fig. 6.15. LA-ICPMS images of trace elements in pyrite 4 and pyrite 5 (Sample No. SEL-R054C) at the Selinsing gold deposit, Central Malaysia. Pyrite 4 core is enriched in Sb, Bi, Pb and V in the core and depleted in Zn, Tl, Te, Se, Mo and Au. There is occurrence of galena, silicate, and rutile inclusions in the core of pyrite 4. Outer zone (py 5) is enriched in As, Ni, Co and Au.

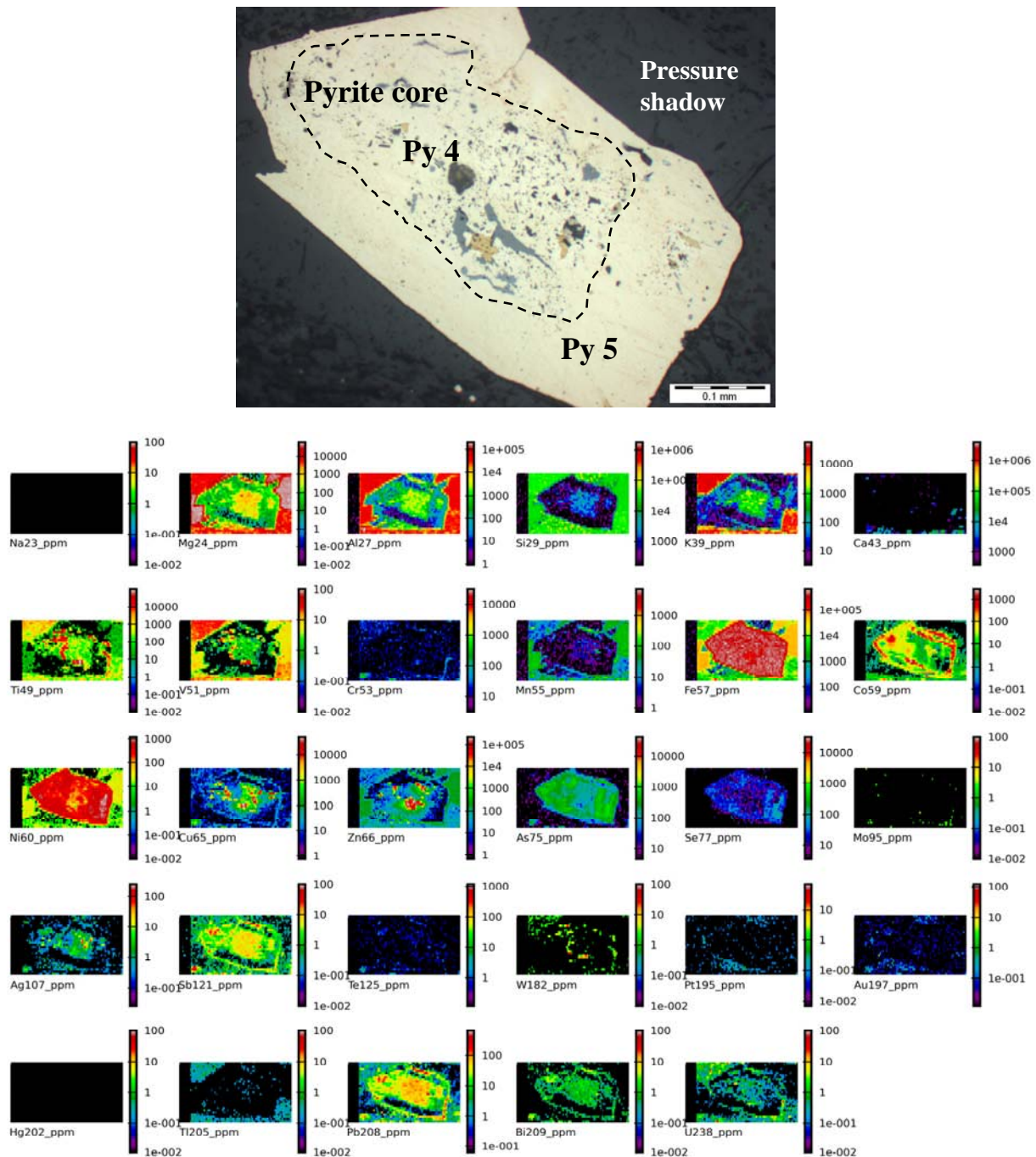


Fig. 6.16. LA-ICPMS images of trace elements in pyrite 4 and pyrite 5 (Sample No. SEL-R009) in black shale at the Selinsing gold deposit. Pyrite 4 shows dotted texture suggesting presence of micro-inclusions of chalcopyrite, rutile and sphalerite. Bi, Pb and Sb show zonation as they appear enriched in the core zone (pyrite 4) and in the outer rim (pyrite 5). Gold is lacking in pyrite 5 and pyrite 6. There are also inclusions of galena in the rim of pyrite 5. Pyrite 5 is enriched in Co and Ni and depleted in As.

6.5.1. Trace element distribution at Selinsing

This section focuses on trace element distribution with an emphasis on enrichment and depletion through pyrite paragenesis at Selinsing. Similar to the Tersang pyrite attribute map, the Selinsing pyrite attribute map was also constructed using ioGAS software (Fig. 6.17A). The gold solubility diagram indicates the presence of two free gold inclusions in pyrite and all other gold is in the structure of the pyrite (Fig. 6.17B). The As and Au contents of framboidal pyrites (pyrite 1 and pyrite 2) are plotted in the vicinity of pyrite 7.

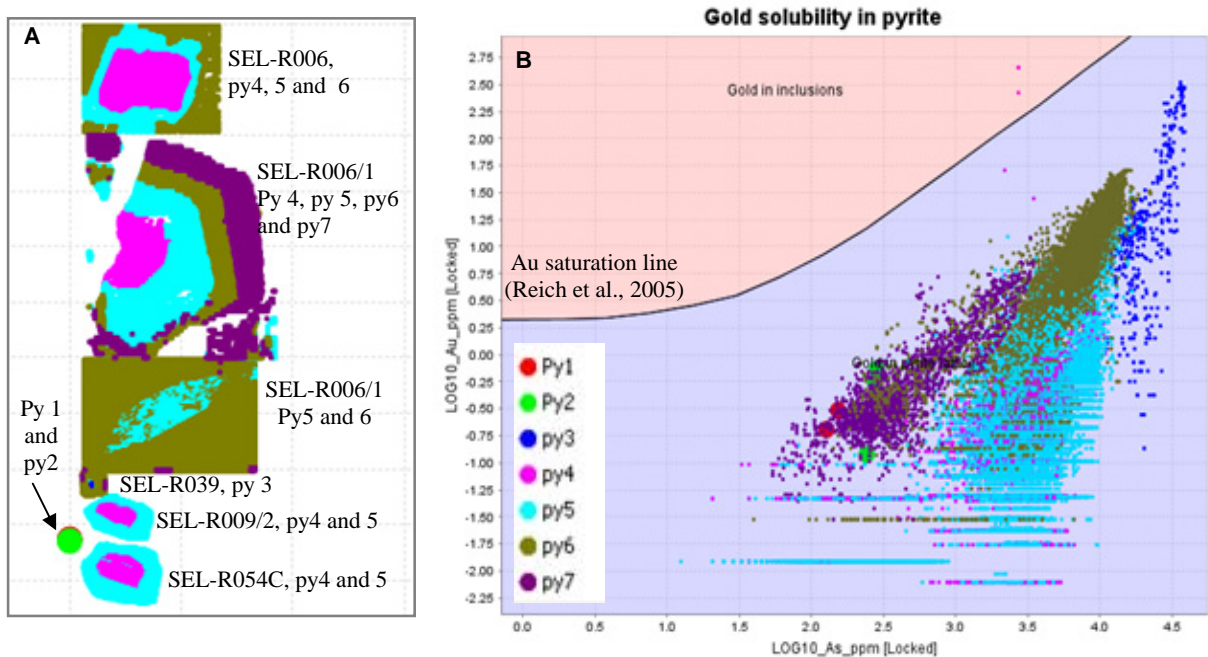


Fig. 6.17. Attribute map of pyrite grains and gold solubility diagram at Selinsing. **A.** Attribute pyrite map of all pyrite types at Selinsing. **B.** Gold solubility plot of As against Au for all the pyrite types at the Selinsing deposit, Central Malaysia. Note the presence of two free gold inclusions in pyrite.

Chapter 6: Pyrite geochemistry

Concentrations of all trace elements in each pyrite type have been normalised to the average Selinsing pyrite in order to evaluate on trace element enrichment patterns through the pyrite paragenesis as shown in Fig. 6.18. Mean of trace elements in framboidal pyrites were plotted (Fig. 6.19).

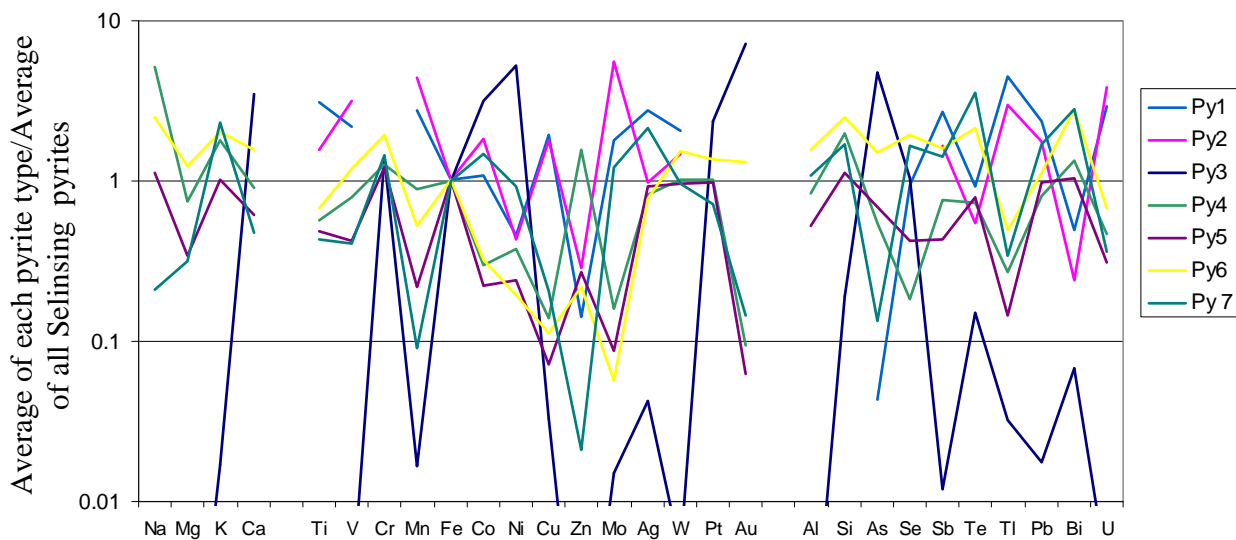


Fig. 6.18. Normalised quantitative analysis of trace elements for all pyrite types at the Selinsing gold deposit, Central Malaysia. This figure also shows multiple stages of gold enrichment and a complex trace element patterns. Trace elements associated with Au (in mean of abundance) are Zn, Mo, Ni, As, Cu, Tl, U, Te, V, Co, Ti, Bi, Ag, Sb and Cr.

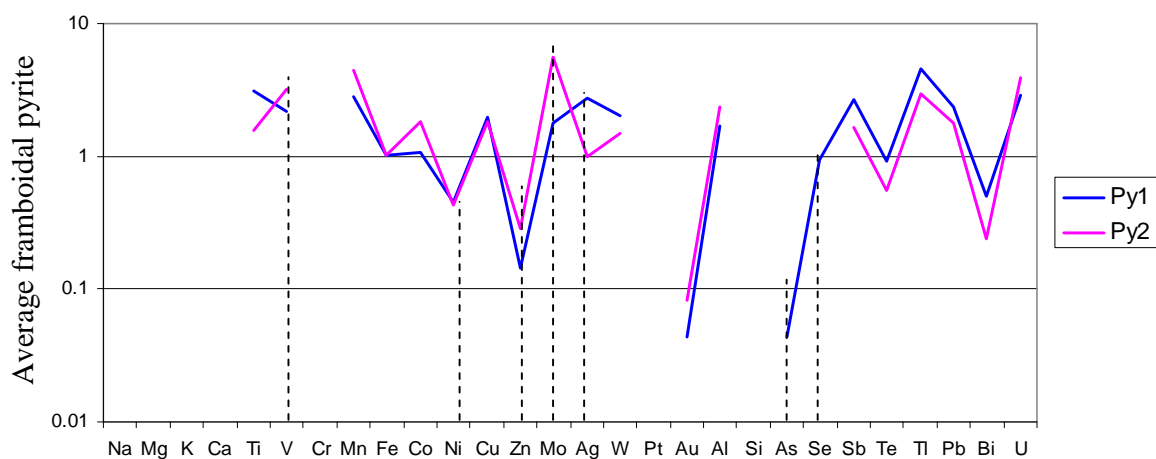


Fig. 6.19. Normalised quantitative analysis of framboidal pyrites (pyrite 1 and pyrite 2) at the Selinsing gold deposit, Central Malaysia. Pyrite 1 is enriched in Tl, Mo, Cu, Co, Sb, Pb and depleted in Ni, Zn, Au, Se, and Te. In contrast, pyrite 2 is enriched in Co, Cu, Mo, Sb, Tl, Pb, and U and depleted in Ni, Zn, Ag, Au, Te, and Bi.

Binary plots of Au against Bi and Te are shown in Fig. 6.20. The plot shows a weak correlation between Au and Bi (Fig. 6.20A) as well as Au and Te (Fig. 6.20B) in the Selinsing pyrites. In addition, ratios of Ag/Au and Ni/Co were also plotted. The Ag/Au ratio for the hydrothermal pyrites is complex to interpret but that of framboidal pyrite shows $\text{Ag/Au} > 1$ (Fig. 6.21). In Figure 6.21, the round and green points represent the framboidal pyrites (pyrites 1 and 2).

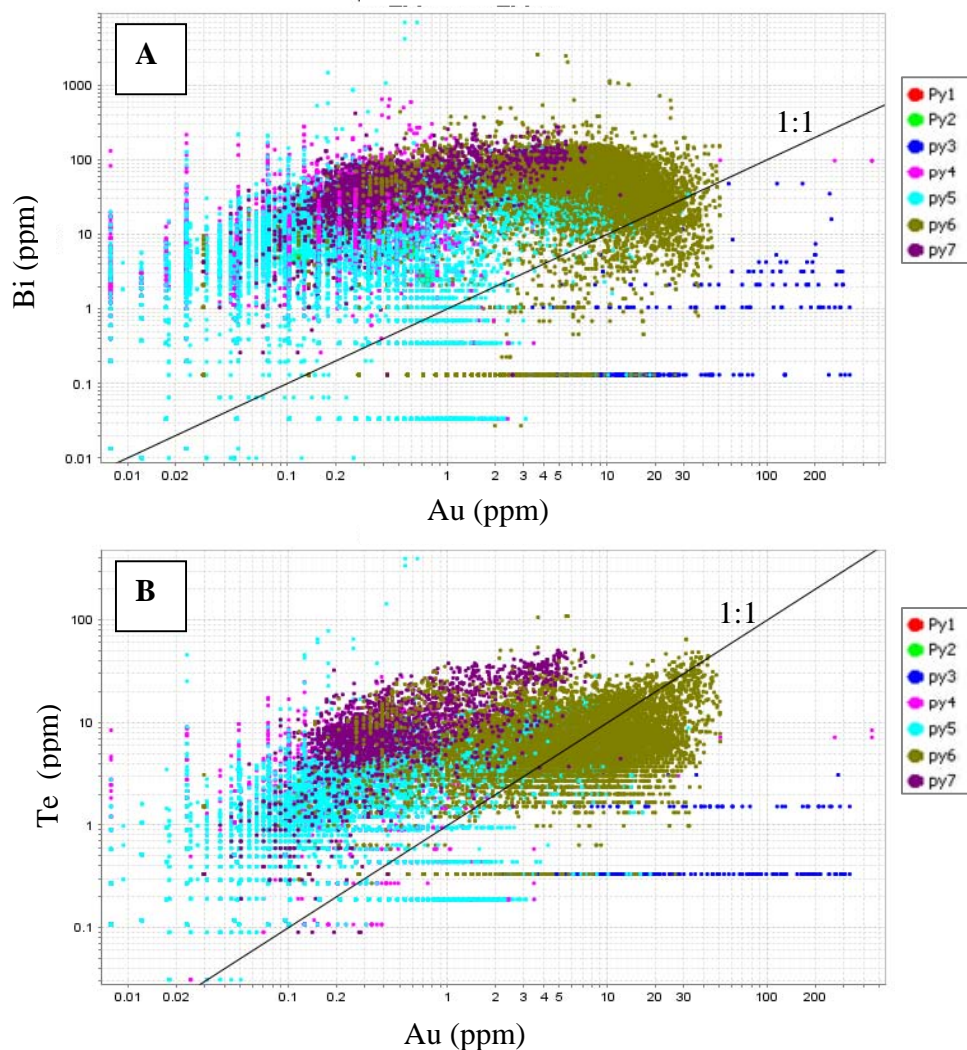


Fig. 6.20. Binary plot of Au against Bi (A) and Te (B) showing a weak correlation in all pyrite types at the Selinsing gold deposit, Central Malaysia.

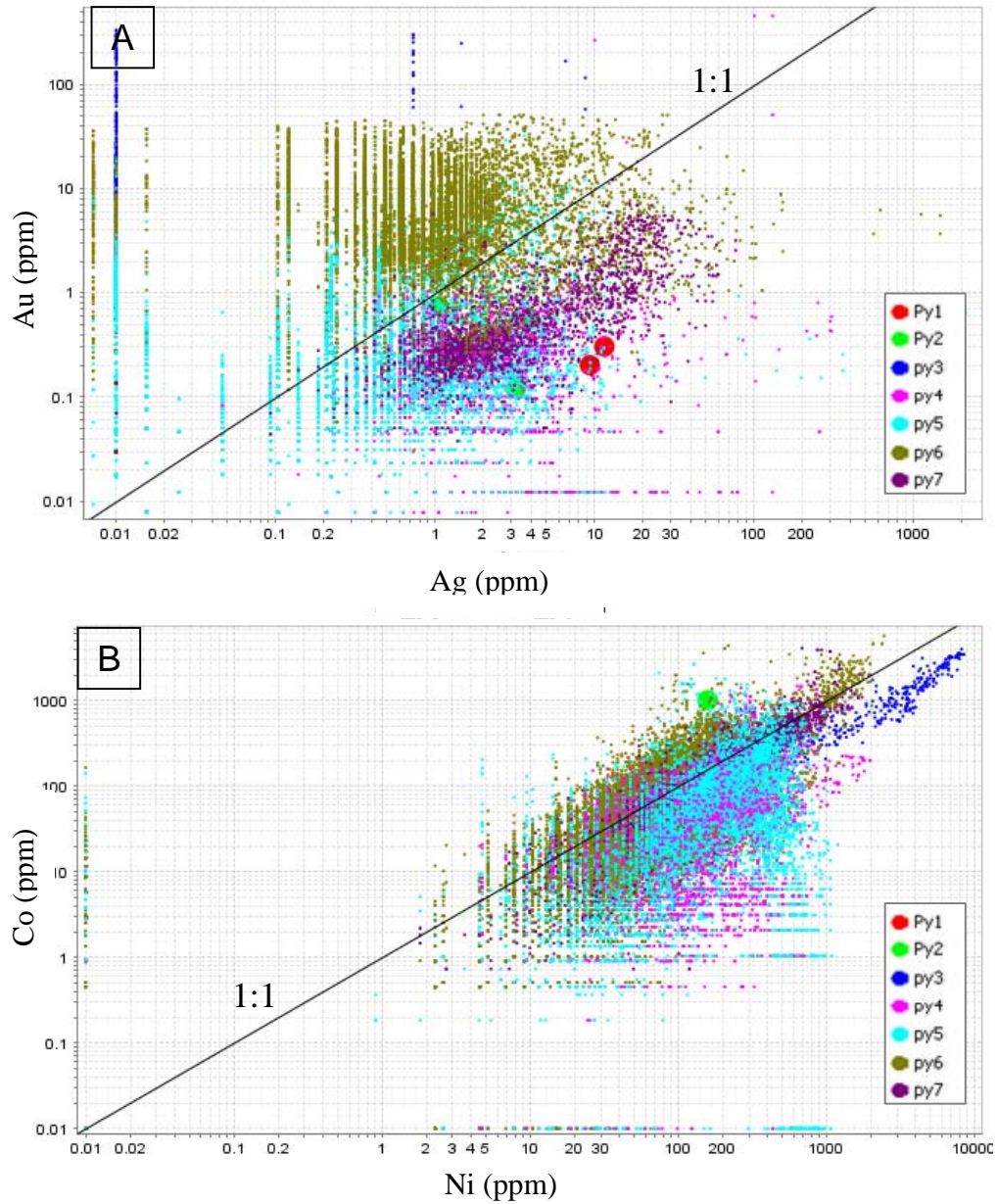


Fig. 6.21. Ratio of trace elements at the Selinsing gold deposit, Central Malaysia. **A.** Ag/Au ratio for all pyrite types at Selinsing. **B.** Ni/Co ratio for the Selinsing pyrites showing a linear trend through the Selinsing pyrite paragenesis.

Chapter 6: Pyrite geochemistry

Line ablation across a pyrite crystal (pyrites 4 and 5) illustrates the presence of invisible inclusions in pyrite. Invisible inclusions of galena, sphalerite and chalcopyrite have been also detected in the hydrothermal pyrites (pyrites 4 and 5) as shown in Fig. 6.22.

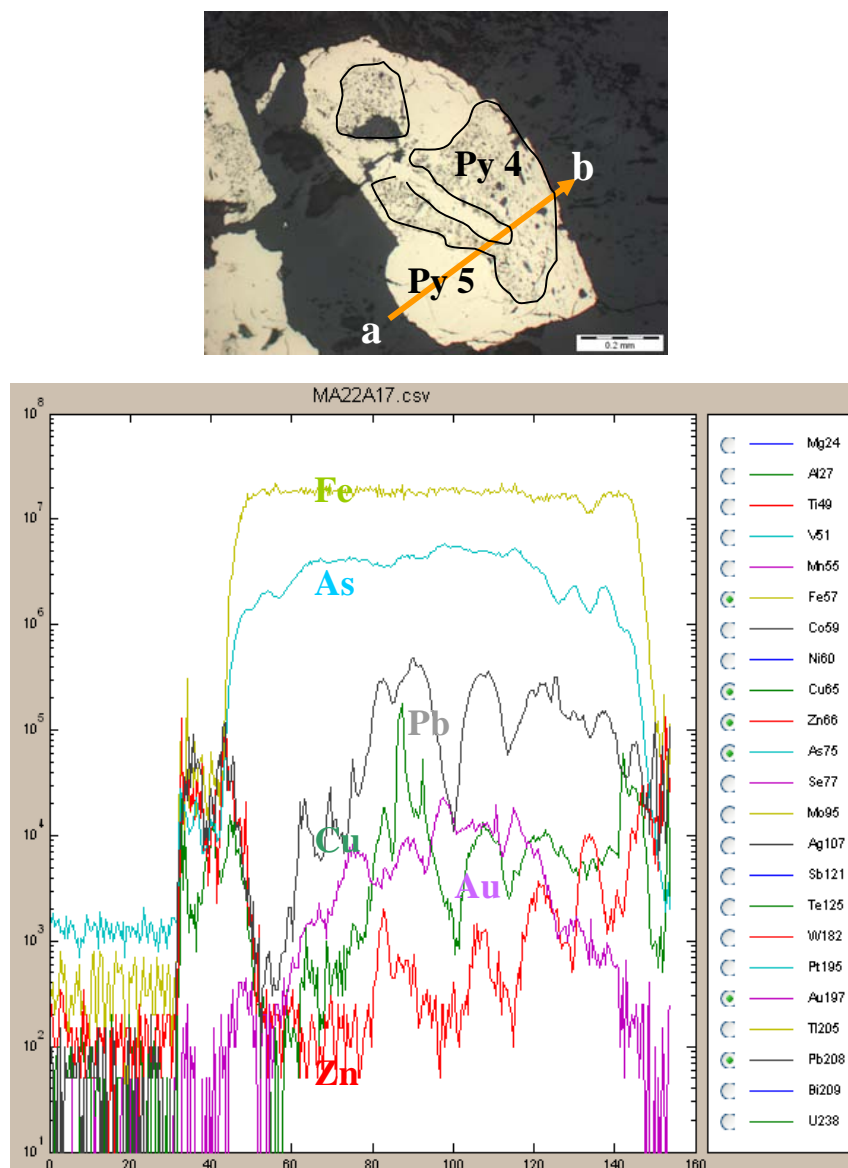


Fig. 6.22. Line ablation (ab) showing spatial relationship between the concentration of As and Au in pyrite 4 and pyrite 5 at the Selinsing gold deposit. The line also shows clear trace element enrichment in pyrite 4 and strong depletion in trace elements in pyrite 5. Pb content is high and correlates with Cu and Zn contents suggesting presence of chalcopyrite, galena and sphalerite inclusions.

6.6. Comparative trace element distribution at Tersang and Selinsing

Trace element distributions of different pyrite types from both the Tersang and Selinsing deposits are shown in Figs. 6.23-6.26.

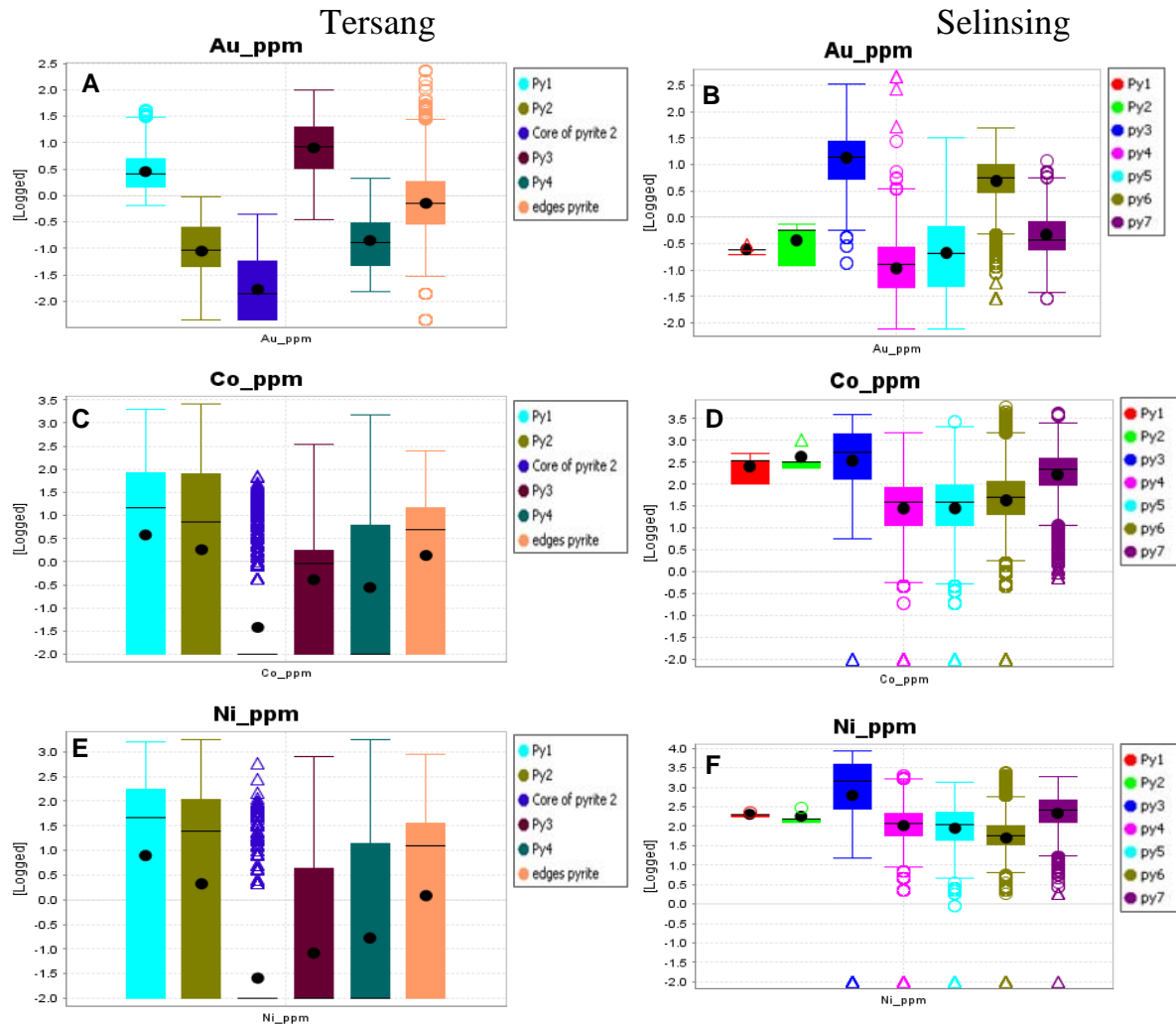


Fig. 6.23. Box plots showing mean concentrations of Au, Co, and Ni in pyrite for both the Tersang and Selinsing gold deposits. Y axis values are in log units as follows: -1.0 is 0.1 ppm; 0.0 corresponds to 1 ppm; 1.0 is 10 ppm; 2 is 100 ppm and 3 is 1000 ppm. **A.** Tersang wallrock-hosted pyrite 3 is enriched in Au (mean= 15 ppm) compared to pyrite 1, pyrite 2 and pyrite 4, which are depleted in Au. **B.** Selinsing vein-hosted pyrite 3 contains high Au (mean= 41ppm) compared to other pyrite types. **C.** Tersang pyrite 1 is enriched in Co (mean= 58 ppm) compared to pyrite 2, pyrite 3 and pyrite 4. **D.** Selinsing pyrite 1, pyrite 2, pyrite 3 and pyrite 7 contain high Co contents (mean: 311-907 ppm). **E.** Tersang pyrite 1 is enriched in Ni (mean=149 ppm), whereas pyrite 2, pyrite 3 and pyrite 4 are depleted in Ni. **F.** Selinsing pyrite 3 has high Ni content (mean: 2,352 ppm) while other pyrites are depleted in Ni. In every box plot, the open circle represents an outlier, which is the top and bottom 5% of the data. The triangular is a far outlier that indicates a highly anomalous value.

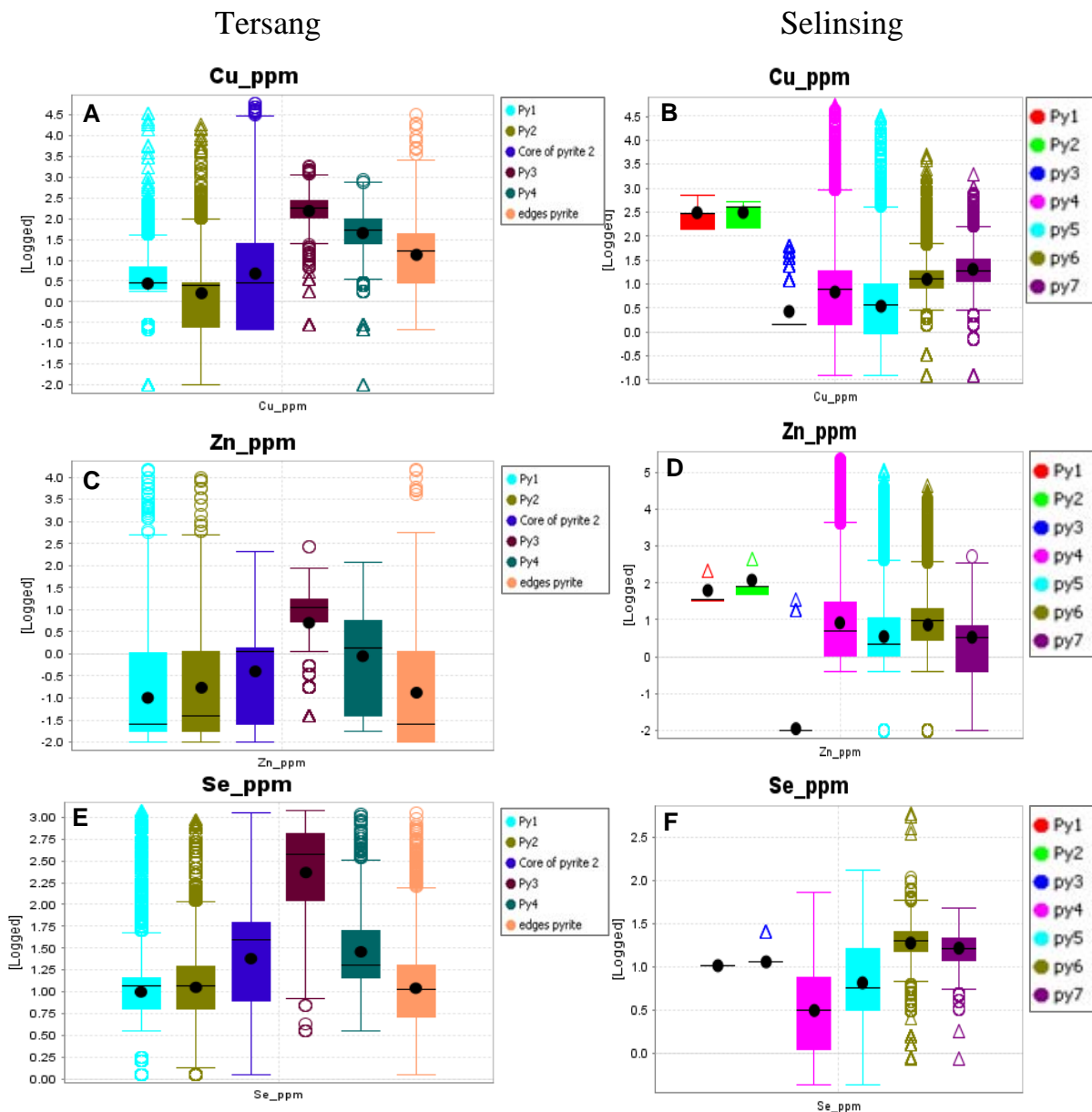


Fig. 6.24. Box plots showing mean concentrations of Cu, Zn, and Se in pyrite for both the Tersang and Selinsing gold deposits. Y axis values are in log units as follows: -1.0 is 0.1 ppm; 0.0 corresponds to 1 ppm; 1.0 is 10 ppm; 2 is 100 ppm and 3 is 1000 ppm. **A.** Tersang pyrite 3 has high Cu (mean= 240 ppm), whereas other pyrite are depleted. **B.** Selinsing framboidal pyrites 1 and 2 have high Cu (mean= 352-382 ppm), and other pyrite types are depleted in Cu. **C.** Tersang all pyrites showing low Zn content (mean= 3.41-12.60 ppm). **D.** Selinsing pyrite 4 has the highest Zn content (mean= 4350 ppm) compared to other pyrite types. **E.** Tersang pyrite 3 has high Se content (mean= 447 ppm) while other types contain low Se. **F.** Selinsing pyrites have low Se (mean= 0-21 ppm).

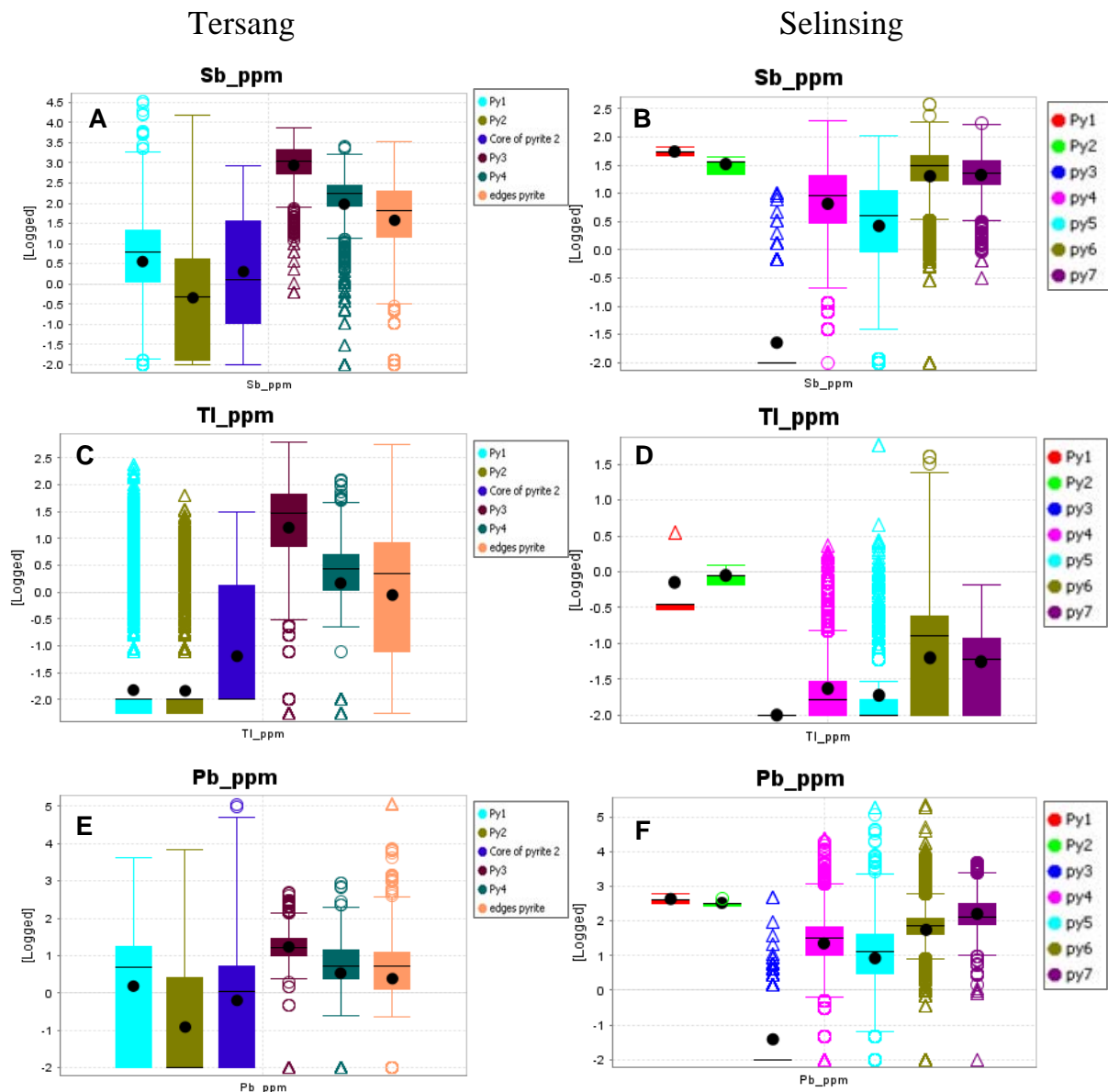


Fig. 6.25. Box plots showing mean concentrations of Sb, Tl, and Pb in pyrite for both the Tersang and Selinsing gold deposits. Y axis values are in log units as follows: -1.0 is 0.1 ppm; 0.0 corresponds to 1 ppm; 1.0 is 10 ppm; 2 is 100 ppm and 3 is 1,000 ppm. **A.** Tersang pyrite 3 enriched in Sb (mean= 1,598 ppm) and other pyrites are depleted in Sb. **B.** Selinsing pyrites have low Sb (mean= 0.24-56 ppm). **C.** Tersang pyrite 3 has highest Tl content (mean= 56 ppm) while other pyrites have Tl concentration below 6 ppm. **D.** Selinsing pyrites are all depleted in Tl (mean= 0.01-1.4 ppm). **E.** Tersang pyrites have low Pb content (mean= 7-30 ppm). **F.** Selinsing framboidal pyrites (pyrite 1 and pyrite 2) have highest Pb contents (mean= 338-449 ppm) compared to other pyrite types.

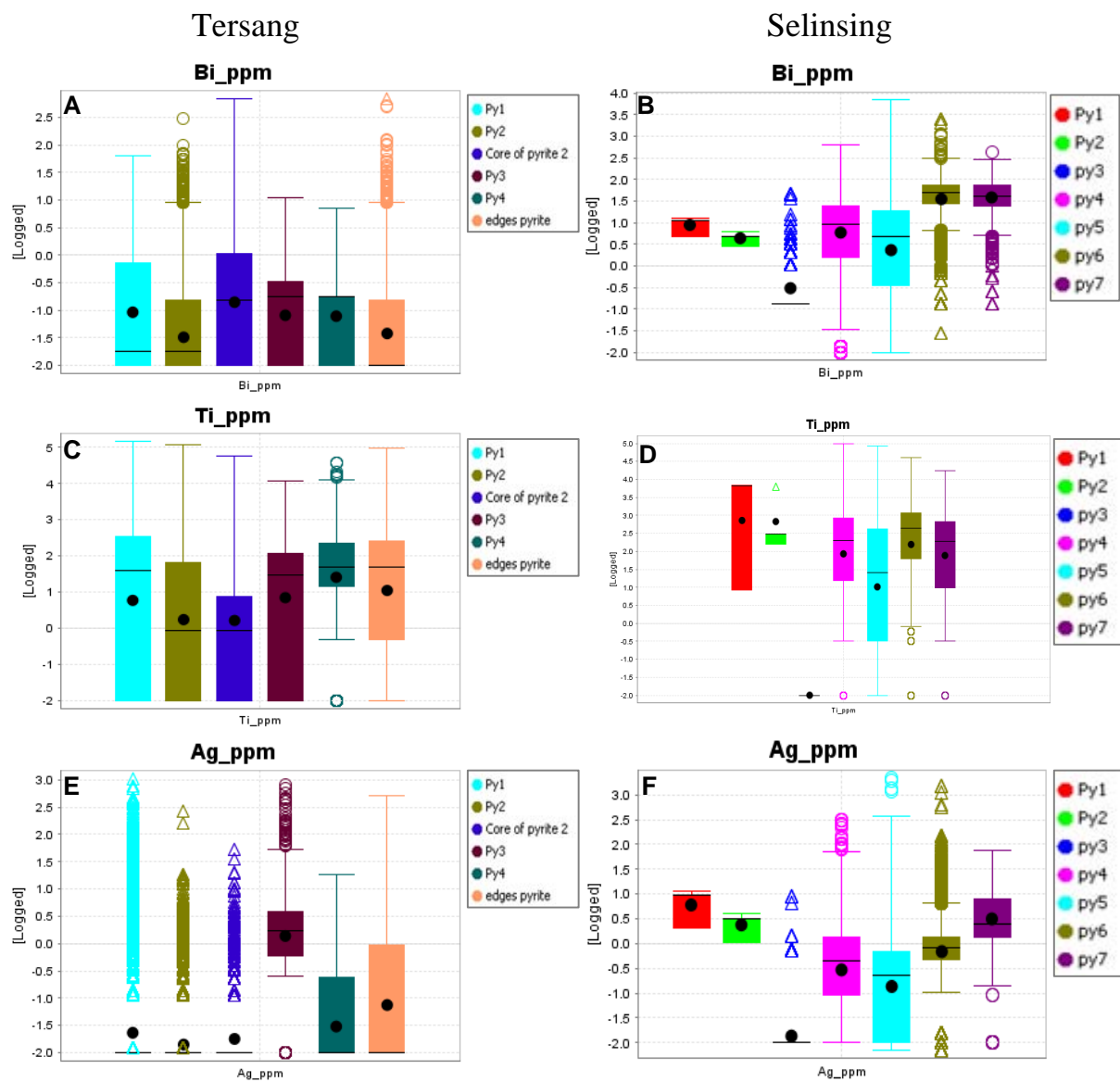


Fig. 6.26. Box plots showing mean concentrations of Bi, Ti, and Ag in pyrite for both the Tersang and Selinsing gold deposits. Y axis values are in log units as follows: -1.0 is 0.1 ppm; 0.0 corresponds to 1 ppm; 1.0 is 10 ppm; 2 is 100 ppm and 3 is 1,000 ppm **A.** Tersang pyrites show low Bi (mean= 0.2-1.1 ppm). **B.** Selinsing pyrite 4, pyrite 5, pyrite 6, and pyrite 7 have elevated Bi contents (mean: 20.4 – 55 ppm). **C.** Ti content in Tersang pyrite (mean= 260-1,268). **D.** Most Selinsing pyrites are enriched in Ti except pyrite 3 which has low Ti content. **E.** Ag content in Tersang pyrite (mean= 0.05-9 ppm). **F.** Ag content in Selinsing pyrite (mean= 0.1-8 ppm).

Chapter 6: Pyrite geochemistry

The point density maps of main Au and As deposition events are presented in Fig. 6.27. The red oval zones contain the maximum of Au and As values in pyrite 1 and pyrite 3 for the Tersang deposit (Fig. 6.27A). Similarly, the high Au and As values in pyrite 3 and pyrite 6 are also plotted for the Selinsing deposit (Fig. 6.27B).

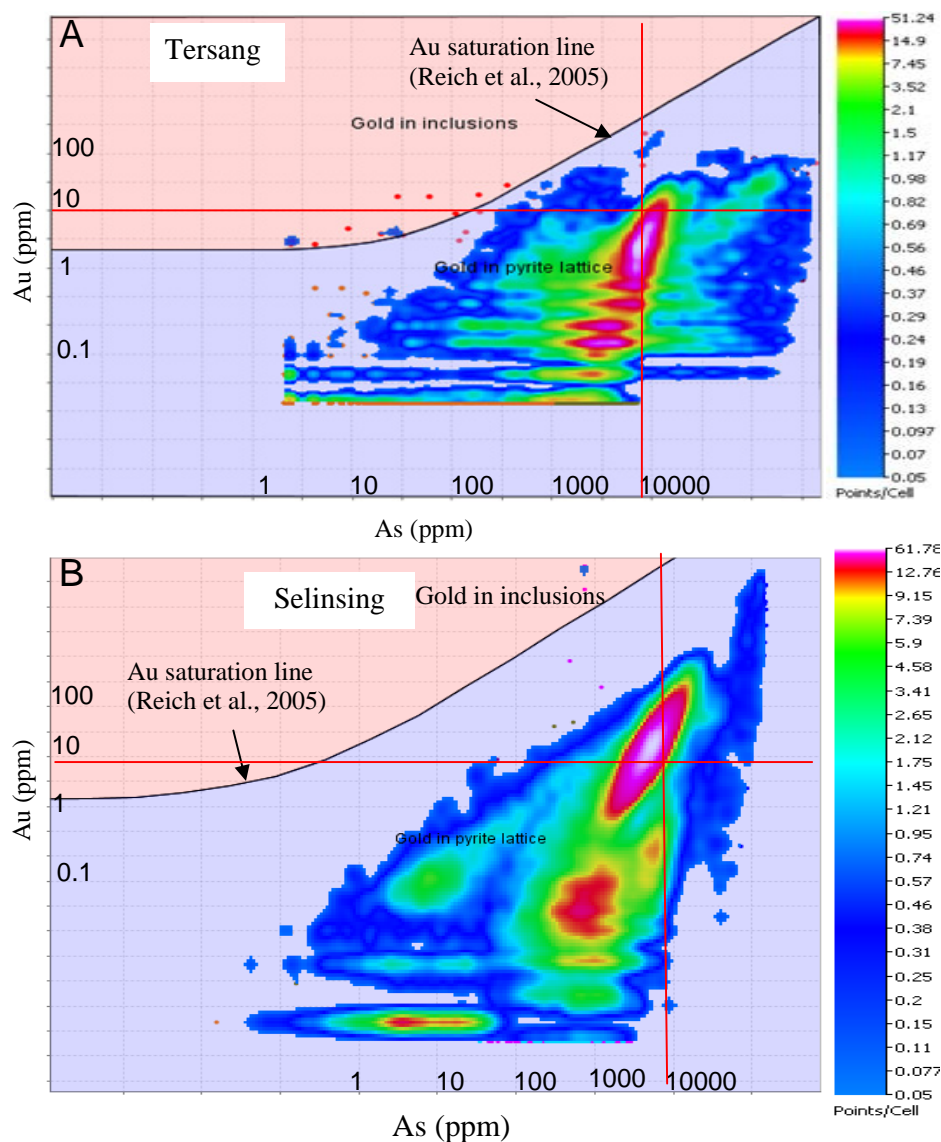


Fig. 6.27. Point density maps of main Au-As concentration. **A.** Density map of Au-As deposition event of the Tersang deposit. **B.** Density map of Au-As deposition event of the Selinsing deposit. The plots show that the Selinsing As-Au event has higher Au concentration than the Tersang As-Au event.

6.7. Discussion

In this study, chemistry of the four pyrite types at Tersang and seven pyrite types at Selinsing were analysed and trace element patterns are discussed below. At the Tersang gold deposit, gold mineralisation shows two main stages of Au enrichment: an early stage within the core of pyrite 1 and a late stage in pyrite 3. Gold in the first stage is associated with elevated values of Co, Ni and Ti. However, gold deposition in the late stage is accompanied with high values of As, Ag, Cu, Sb, Se, Tl, and Mn. The elements such as Ni, Co and As as in Figs. 6.1-6.3 show zoning patterns which indicate that their host pyrites (pyrite 1 and pyrite 2) are likely of metamorphic and/or hydrothermal origin similar to the hydrothermal/metamorphic pyrites from the giant Sukhoi Log deposit in Russia (Large et al., 2007). It is also reported that in the Carlin-style deposits, the trace elements such as Ni, Co, and As also exhibit zoning patterns and were also interpreted as having a hydrothermal origin (Large et al., 2007).

Large et al. (2009) reported that at Sukhoi Log, Bendigo, and Spanish Mountain, the early hydrothermal pyrites were rich in Co, and followed by Co-poor pyrite. Similarly, at Tersang, there is a progressive drop in Co content from pyrite 1 to pyrite 4. Large et al. (2009) also argued that diagenetic pyrite commonly displays high Ag/Au, and Ni/Co ratios. At Tersang, there is low Ag/Au, with linear trend for the Co and Ni data suggesting that pyrite 1, pyrite 2 and pyrite 3 are not diagenetic in origin. None of the four types of pyrite (pyrite 1, pyrite 2 pyrite 3, and pyrite 4) are diagenetic in origin. The Tersang gold solubility diagram shows the presence of free gold in silicates with minor amount in pyrite rims.

At Selinsing, normalised quantitative analysis has shown multiple Au enrichment and two main stages of high Au accumulation (Fig. 6.18). The first stage (pyrite 3) is associated with elevated contents in Mo, Tl, Sb and Co with minor concentrations of Zn, Te, and Bi. Later Au enrichment in pyrite 6 is characterised by high contents of As, Cu, Co, Zn, Te, Bi, Sb, Se, Mo, and Ag. The evidence shows that the Selinsing gold mineralisation occurred in two main events as at Tersang. The framboidal pyrites (pyrite 1 and pyrite 2) show enrichment in the VAMSNZ (V, As, Mo, Se, Ni, Ag, Zn) trace element suite. Therefore, a syngenetic origin of gold is supported by the pyrite chemistry at Selinsing (Large et al., 2010) as these framboidal pyrites carry low gold. Gold may have been leached from early pyrites and remobilized and reconcentrated in later pyrites. In addition, framboidal pyrite (pyrite 1 and 2) is of diagenetic origin as indicated by the texture and high Ag/Au ratio with elevated Zn, Pb and Ni. At Selinsing, pyrite 4 and pyrite 5 have high Ag/Au indicating a metamorphic origin. Furthermore, pyrite 3 and pyrite 6 have a low Ag/Au <1 and high Co suggesting a metamorphic-hydrothermal origin. Based on the Ag/Au ratios and Co concentrations, the position of pyrite 3 in the paragenesis is difficult to establish.

By comparing trace element distribution at Tersang and Selinsing, it is found that both deposits are characterised by multiple high Au episodes during pyrite growth. The Tersang pyrite is also characterised by high Se mainly in fracture-filled pyrite (pyrite 3). This may be due to the arrival of Se-rich hydrothermal fluids, probably contributed by proximal emplacement of igneous rocks. Compared to Tersang, the Selinsing pyrites have low Se. The Selinsing pyrites are more enriched in Co and Ni than the Tersang pyrites. The Tersang pyrites show Co and Ni concentrations, which decrease through time before plummeting within the core of pyrite 2

followed by a significant increase from pyrite 3 to the edges. However, the Selinsing pyrites show Co and Ni concentrations which fluctuate through time. Both deposits show also low Cu and Zn. The Tersang pyrite shows a similar pattern for the elements including Sb, Tl and Pb and their concentrations are the highest in the hydrothermal pyrite 3. In contrast, at Selinsing, pyrite has low Sb, Tl, and Pb. Most Tersang pyrite has low Bi and Ag, whereas the Selinsing pyrites have high Bi but low Ag similar at Tersang. The point density maps show a remarkably similar pattern on both Au and As (Figs. 6.27A and B). At Tersang, statistical analysis of gold shows that pyrite 3 contains approximately 63.4 % of the gold measured, whereas pyrite 4 has 15.7 % Au. Pyrite edges contain an estimate of 3.8 % of the Au and the silicates have 5.5 % of the Au. At Selinsing, pyrite 3 yields 8.45 % of the total Au; however pyrite 6 contains 58.2 % of the Au. Other pyrite types are mostly depleted in Au. Table of statistical analysis of gold in pyrite and silicates for both the Tersang and Selinsing deposits is shown in Appendix D.

6.8. Conclusions

Pyrite geochemistry indicates that both the Tersang and Selinsing gold deposits record several episodes of Au enrichment. At Tersang, the Au event is associated with significant amounts of trace elements such as Co, Ni, Cu, Zn, Mo, As, Se, Sb and Tl; however at Selinsing, high Au occurrence is accompanied by trace elements including Co, Ni, Cu, Zn, Mo, As, Te, Sb, Tl, Bi, Ti and Pb. At both Tersang and Selinsing, gold has introduced during growth of metamorphic-hydrothermal pyrite. At Tersang the most invisible gold is found in pyrite 3, whereas at Selinsing the most gold is present in pyrite 6.

CHAPTER 7 SULPHUR AND LEAD ISOTOPES

7.1. Introduction

In this Chapter, the results of sulphur and lead isotopic studies of the Tersang, Selinsing and Penjom deposits are documented. The main aim is to discuss the possible source of sulphur and lead in relation to the formation of ore deposits at Tersang, Selinsing and Penjom in Central Malaysia.

7.2. Sulphur isotopes

It is known that gold is commonly transported as bisulfide complexes in orogenic deposits (Groves et al., 2003; Goldfarb et al., 2005). For this reason, the source of sulphur is critical to the understanding of the source of gold, the source of ore-forming fluids and the genesis of a given deposit. Sulphur comprises of the following four stable isotopes: S^{32} (95.02 %), S^{33} (0.75 %), S^{34} (4.21 %), and S^{36} (0.02 %). S^{32} and S^{34} differ in mass by 6% with a precision ratio of 0.02 % (Rye and Ohmoto, 1974). The isotopic ratio in any reservoir is determined by the heavy isotope over the light isotope, which is the ratio of S^{34}/S^{32} . The isotopic composition is calculated by the measurement of the S^{34}/S^{32} with data given in parts per thousand or per mil and expressed in the following equation formulated from Rollinson (1996): $\delta^{34}S = [(R_{\text{sample}} - R_{\text{standard}}) / R_{\text{standard}}] \times 10^3$; here $R = S^{34}/S^{32}$. The Canon Diablo Troilite (CDT) is the standard for $\delta^{34}S$ which has an isotopic ratio of $S^{34}/S^{32} = 0.0450045$ (Ault and Kulp, 1960) and an attributed value of 0.00 ‰

Chapter 7: Sulphur and Lead isotopes

(Ohmoto and Rye, 1979). Positive per mil deviations point to enrichments of S^{34} relative to the standard (CDT); however negative per mil deviations indicate depletions.

7.2.1. Previous studies

Khin Zaw et al. (2008) undertook limited sulphur isotope studies at Penjom using in-situ Laser ablation method on vein-hosted arsenopyrite and pyrite from host rocks. Analysis returned sulphur isotope values which range from -8.4 to -4.0 per mil.

7.2.2. Methods

In this study, twenty samples from the Tersang and Selinsing deposits were analysed by the conventional method at the Central Science Laboratory (CSL), University of Tasmania. Results of this analysis were combined with those of previous data from the Penjom deposit (Khin Zaw et al., 2008). For the conventional technique, sulphides such as pyrite, galena and arsenopyrite from the Tersang and Selinsing deposits were drilled out of the samples using a dentist's drill to produce a powdered sample of about 10-25 mg. The powdered sulphide samples (n=20) were submitted to the Central Science Laboratory. The isotopic compositions for S^{34}/S^{32} were obtained by combustion with cuprous oxide method (Robinson and Kasakabe, 1975). The Canon Diablo Troilite (CDT) international standard was used to monitor the raw sulphur isotopic data. An accuracy of ± 0.15 ‰ is obtained by the conventional method at the CSL.

7.2.3. Sulphur isotope compositions

This section describes the sulphur isotopic composition for both the Tersang, Selinsing, and Penjom gold deposits in Central Malaysia. Results of the sulphur isotope analysis with those from the Penjom gold deposit (Khin Zaw et al., 2008) are presented in Table 7.1. Histograms for the $\delta^{34}\text{S}$ values for the Tersang, Selinsing, and Penjom deposits are presented in Figs. 7.1A-C.

7.2.3.1. Tersang

All sulphide grains analysed by the conventional method come from the quartz veins and the host sandstone (Table 7.1, Fig. 7.1A). The Tersang gold deposit has a relatively narrow range of $\delta^{34}\text{S}$ values from -8.3 to 2.5 ‰. The $\delta^{34}\text{S}$ values from the host sandstone range from -5.2 to -3.7 ‰, whereas the vein pyrites have $\delta^{34}\text{S}$ values from -4.5 to 2.5 ‰. The sulphur isotopic composition of arsenopyrite values vary from -8.3 to -6.0 ‰ and sulphur isotopic composition of one galena sample is at -2.6 ‰. The results show that the $\delta^{34}\text{S}$ values from host rocks and veins overlap but vein pyrite tend to be heavier (up to + 2.5 ‰).

7.2.3.2. Selinsing

The sulphur isotope composition of pyrite from the Selinsing deposit ranges from 1.5 to 9.2 ‰. Within this range, the $\delta^{34}\text{S}$ values from vein-hosted pyrite sit between 2.8 and 9.2 ‰, whereas the $\delta^{34}\text{S}$ values of wall rock hosted-pyrite vary from 1.2 to 6.1 ‰ (Table 7.1, Fig. 7.1B). The result also shows that vein pyrites are heavier than wall rock-hosted pyrites.

Chapter 7: Sulphur and Lead isotopes

Table 7.1. Sulphur isotope compositions for the Tersang, Selinsing and Penjom gold deposits, Central Malaysia.

CSL No.	Deposit	Sample No.	Occurrence	Ore mineral	$\delta^{34}\text{S}$ values (permil)
12387	Tersang gold deposit	TER-S007a	Host rock	Pyrite	-5.2 (This study)
12388	Tersang gold deposit	TER-S007b	Host rock	Pyrite	-3.7
12389	Tersang gold deposit	TER-S008	Vein	Arsenopyrite	-8.3
12390	Tersang gold deposit	TER-S009	Vein	Arsenopyrite	-6.0
12391	Tersang gold deposit	TER-S025a	Vein	Pyrite	2.5
12392	Tersang gold deposit	TER-S025b	Vein	Pyrite	1.5
12393	Tersang gold deposit	TER-S029	Vein	Galena	-2.6
12394	Tersang gold deposit	TER-S030	Vein	Pyrite	-4.5
12395	Tersang gold deposit	TER-S039	Vein	Pyrite	1.6
12376	Selinsing gold deposit	SEL-S001	Vein	Pyrite	3.6
12377	Selinsing gold deposit	SEL-S017	Vein	Pyrite	2.9
12378	Selinsing gold deposit	SEL-S018	Vein	Pyrite	6.5
12379	Selinsing gold deposit	SEL-S025	Host rock	Pyrite	3.3
12380	Selinsing gold deposit	SEL-S026	Vein	Pyrite	9.2
12381	Selinsing gold deposit	SEL-S039	Vein	Pyrite	7.2
12382	Selinsing gold deposit	SEL-S041	Host rock	Pyrite	6.1
12383	Selinsing gold deposit	SEL-S051	Vein	Pyrite	6.0
12384	Selinsing gold deposit	SEL-S078	Host rock	Pyrite	1.6
12385	Selinsing gold deposit	SEL-S090	Host rock	Pyrite	1.2
12386	Selinsing gold deposit	SEL-S091	Host rock	Pyrite	1.5
123A	Penjom gold deposit	M12.3A	Vein	Arsenopyrite	-6.2*
123B	Penjom gold deposit	M12.3B	Vein	Arsenopyrite	-8.4*
124A	Penjom gold deposit	M12.4A	Vein	Arsenopyrite	-7.5*
124B	Penjom gold deposit	M12.4B	Vein	Arsenopyrite	-7.7*
124C	Penjom gold deposit	M12.4C	Vein	Arsenopyrite	-4.9*
124D	Penjom gold deposit	M12.4D	Vein	Arsenopyrite	-7.3*
1-22A	Penjom gold deposit	M1-22A	Host rock	Pyrite	-4.0*
1-22A	Penjom gold deposit	M1-22A	Host rock	Pyrite	-6.8*

* Data from Khin Zaw et al. (2008)

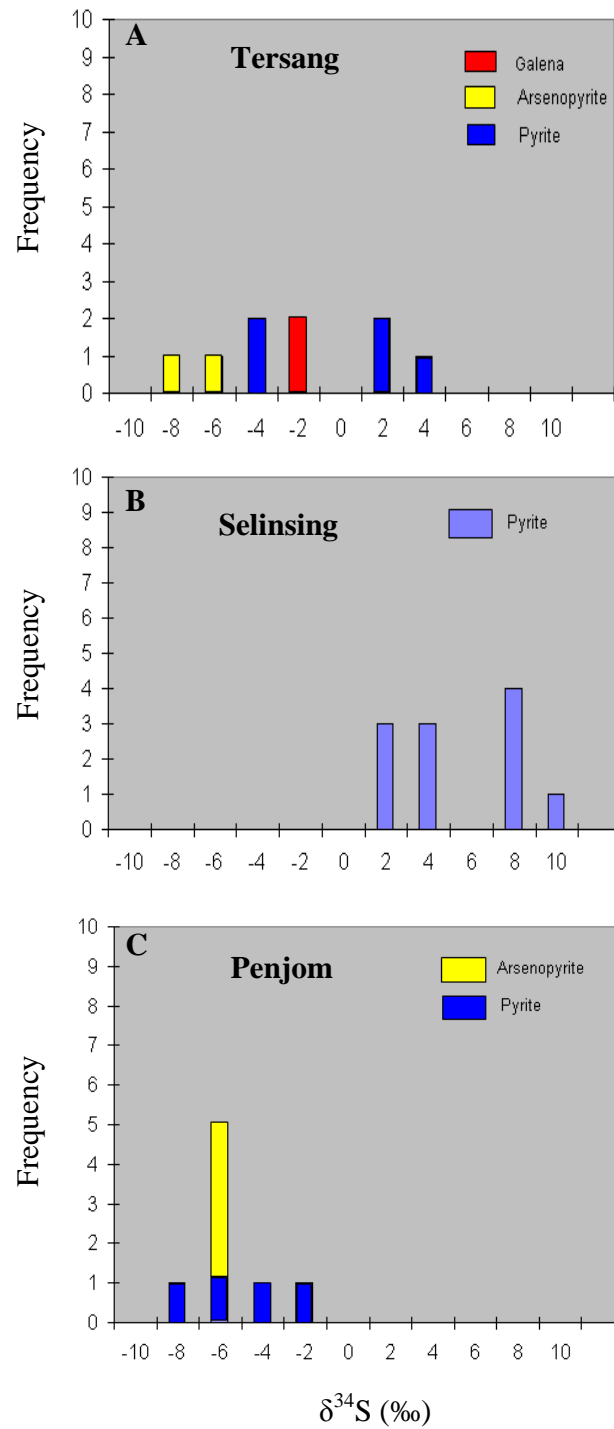


Fig. 7.1. Histograms showing the $\delta^{34}\text{S}$ (‰) compositions of sulphides from the Tersang, Selinsing and Penjom deposits, Central Malaysia. **A.** Tersang. **B.** Selinsing. **C.** Penjom (after Khin Zaw et al., 2008).

7.2.3.3. Penjom

Khin Zaw et al. (2008) recorded that the sulphur isotopic composition of pyrite from the host rock ranges from -4.0 to -6.8 ‰ and sulphur isotopic values of vein-hosted arsenopyrite are between -4.9 and -8.4 ‰ (Fig. 7.1C).

7.2.4. Discussion

Sources and isotopic composition of sulphur vary from magmatic, metamorphic to biogenic origin. Rye and Ohmoto (1974) reported that sulphur of mantle and magmatic origin is considered to have a $\delta^{34}\text{S}$ value close to zero comparable to the standard (CDT). In contrast, $\delta^{34}\text{S}$ values of approximately +20 per mil imply that marine evaporates or seawater is likely to be the source of the sulphur. Seawater sulphates can yield variable heavy $\delta^{34}\text{S}$ isotopic values ranging from +10 to +35 ‰ from the Cambrian to the present (Rollinson, 1996).

Modern seawater sulphates have $\delta^{34}\text{S}$ values which range from +18 to 20 ‰ (Rollinson, 1996), whereas sedimentary environments can have variable $\delta^{34}\text{S}$ values ranging from -70 to >+20 ‰ (Ohmoto and Rye, 1979). Furthermore, sulphides in hydrothermal systems mostly yield $\delta^{34}\text{S}$ values clustered around 0.0 ‰ with values ranging up to 10‰ when certain conditions of temperature and pH are met and the primary isotopic compositions are preserved (Ohmoto and Rye, 1979). Sulphur can be also introduced by metamorphic fluids from wall rocks (Sangster, 1992; Goldfarb et al., 1997) or from the deep crust during amphibolite-grade and granulite-grade metamorphism (Kerrick and Fryer, 1979; Phillips et al., 1987).

Chapter 7: Sulphur and Lead isotopes

Sometimes, sulphur can also be sourced from the mantle depths (Perring et al., 1987). Sulphur can be also sourced from metamorphic fluids (Groves et al., 1998; Kerrich et al., 2000). Most $\delta^{34}\text{S}$ values of sulphides from skarn deposits are between -5 per mil and +8 per mil implying a magmatic origin of the sulphur (Bowman, 1998).

In this study, sulphur isotopic compositions of the Tersang, Selinsing, and Penjom deposits show a relatively wide range of $\delta^{34}\text{S}$ values from -8 to 10 ‰. The sulphur isotope values of vein-hosted sulphide minerals from the adjacent host rocks in these deposits are largely similar (Table 7.1) suggesting that there was no significant interaction between the wall rocks and the ore fluids or indicating that the fluid had equilibrated with the wall rock.

Three possible sources of sulphur including magmatic/metamorphic, biogenic or seawater are discussed as follows. At Tersang, the $\delta^{34}\text{S}$ values are made up of heavier (1.6 ‰ to 2.5 ‰) and lighter sulphur (-8.3 ‰ to -2.6 ‰). Scanning electron microscope studies show the presence of primary hematite associated with brecciated vein-hosted pyrite and arsenopyrite in felsic intrusion (Chapter 5, Fig. 5.10). Therefore, the lighter $\delta^{34}\text{S}$ values may be derived from the oxidation of the sulphur at Tersang. Cooke and Simmons (2000) and Wilson et al. (2007) argued that negative $\delta^{34}\text{S}$ values in porphyry-related magmatic hydrothermal fluids can also occur under redox controlled oxidising conditions. The Tersang $\delta^{34}\text{S}$ values are also comparable to the Carlin-type Au deposits and skarn at Sepon, Laos that yielded a range from -6 to + 4 ‰ (Cromie, 2010). This type of range is similar to magmatic systems implying that at Tersang there may have been dominantly magmatic sulphur. However, mixing with metamorphic sulphur is also possible as evidenced by the presence of CO_2 - rich fluid inclusions.

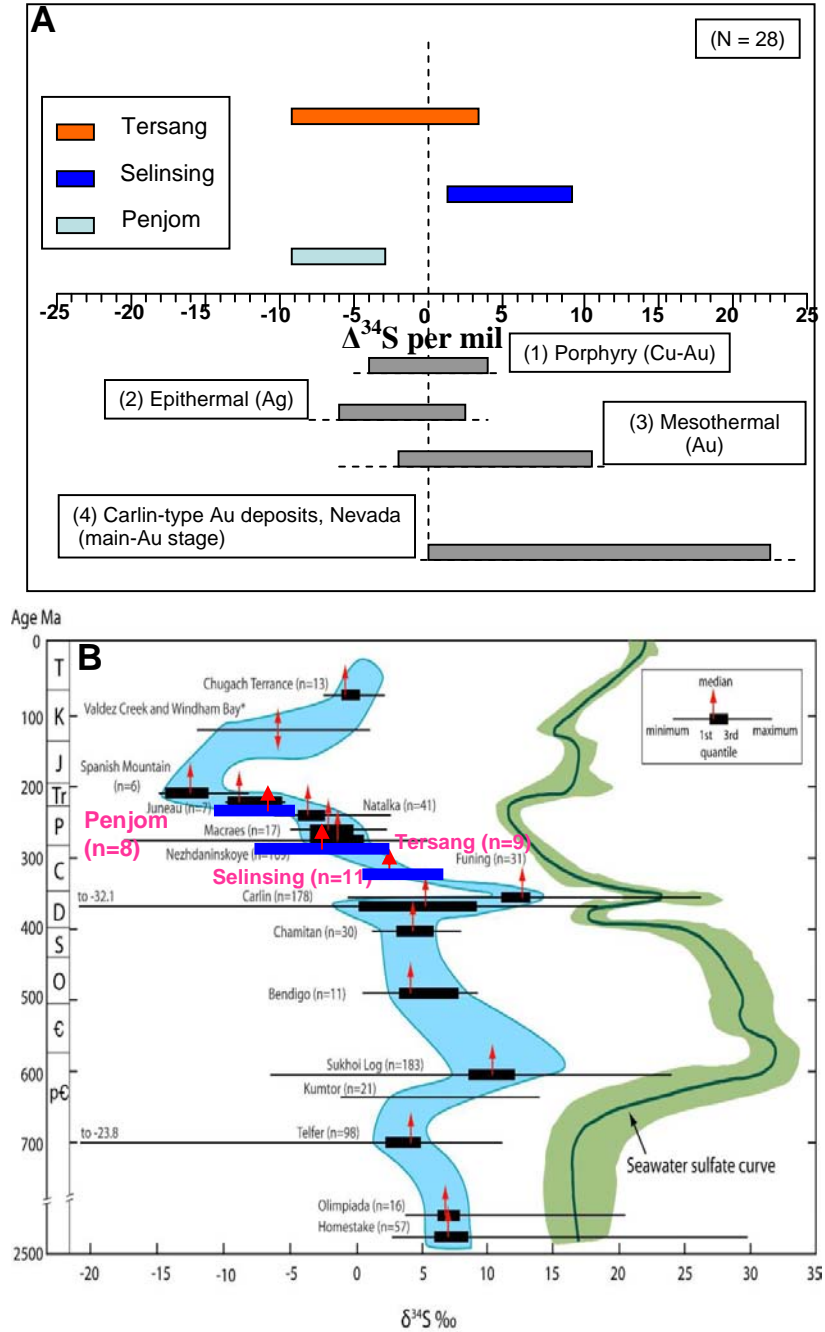


Fig. 7.2. Sulphur isotope composition at the Tersang, Selinsing and Penjom deposits, Central Malaysia. **A.** Diagram showing sulphur isotope comparison of $\delta^{34}\text{S}$ per mil for these deposits and other known deposit types studied by previous workers (Modified after Cromie, 2010). Note Hofstra and Cline (2000) for deposit types (1), (3) and (4); Cooke and Simmons (2000) for epithermal type (2). **B.** Variation of sulphide S isotopic composition in Selinsing, Tersang and Penjom deposits with other known sediment-hosted orogenic gold deposits through geologic time and seawater sulfate curve (Modified after Chang et al., 2000).

Chapter 7: Sulphur and Lead isotopes

At Selinsing, $\delta^{34}\text{S}$ values are above 0.0 ‰ (from 1.2 ‰ to 9.2 ‰). These values are consistent with magmatic or a mixture of metamorphic and magmatic origin. The metamorphic source of sulphur is also supported by the presence of fluid inclusions rich in CO_2 and CH_4 as detected by Laser Raman analysis (Chapter 8). Mernagh et al. (2007) argued that the metamorphic fluids that are associated with gold deposition commonly contain CO_2 and CH_4 gases. At Penjom, $\delta^{34}\text{S}$ values are all lighter (-8.4 ‰ to -4.0 ‰). These lighter isotopic compositions of sulphide minerals at Penjom suggest a biogenic origin of the sulphur, and possibly implying redox reactions were present (Ohmoto, 1986).

The comparison of the variation of the $\delta^{34}\text{S}$ values of these deposits through time with those of the seawater sulphate curve indicates that the sulphur isotopic compositions of the deposits vary in a parallel fashion to the seawater sulphate curve through geologic time. Additionally, their sulphur values are within the ranges of the Carboniferous and Permian sulphur sources ((Fig. 7.2B). The Tersang and Selinsing deposits are hosted in Carboniferous sediments, whereas the Penjom deposit is hosted in the Permian shale sequence. Therefore, the hypothesis of the source of sulphur from seawater cannot be ruled out.

Goldfarb et al. (1997) also reported that $\delta^{34}\text{S}$ values of sulphide minerals in orogenic gold deposits in Alaska have a timing variation pattern, which is similar to that of seawater sulphate. Large et al. (2008) discussed that the S isotopic composition of sulphide through the pyrite paragenesis in the giant Sukhoi Log Au deposit in Russia show a pattern, which is parallel to the seawater sulphate curve, indicating that the sulphur was probably originated from the reduction of seawater sulphate. The above

Chapter 7: Sulphur and Lead isotopes

interpretation cannot be ruled out for the Tersang, Selinsing and Penjom deposits. This hypothesis is consistent with the presence of framboidal pyrites at the Selinsing gold deposit and their occurrence in black mudstone interbedded with siltstone indicating reduction of seawater sulphate during the growth of pyrite onto layers of organic matter complexed with metals. In comparison, none of the deposits studied fall within the Carlin-type $\delta^{34}\text{S}$ value range which is between -1 and 17 ‰ (Hofstra and Cline, 2000).

7.3. Lead isotopes

This part of the study focuses on discussing the source of lead for the Tersang, Selinsing, and Penjom gold deposits, Central Malaysia. Lead isotope studies are useful to (a) determine the age of rocks and minerals, and (b) examine geological processes that constrain the source of the metals (Zartman and Stacey, 1971; Zartman and Doe, 1981; Gulson, 1986; Carr et al., 1995; Rollinson, 1996), and (c) provide insights into the ore genesis (Large et al., 2007; Meffre et al., 2008; Large et al., 2009). Isotopic concentrations of Pb^{204} , Pb^{206} , Pb^{207} and Pb^{208} in sulphide minerals such as pyrite, galena, and arsenopyrite can provide metallogenic signatures to support lead isotopic studies. Isotopic ratios vary through time for $\text{Pb}^{206}/\text{Pb}^{204}$, $\text{Pb}^{207}/\text{Pb}^{204}$ and $\text{Pb}^{208}/\text{Pb}^{204}$. These isotopes are also helpful for calculating the isotopic concentration of minerals and fluids.

7.3.1. Methods

All analyses were conducted at the University of Tasmania using LA ICP-MS method. The analyses were performed on an Agilent 4500 ICPMS coupled to a New Wave 213 nm solid state laser in a custom made, low volume (3.4 cm^3), barrel-shaped

Chapter 7: Sulphur and Lead isotopes

chamber in a He atmosphere. The laser was operated at 5 or 10 Hz using spot sizes between 15 and 110 μm . Data were collected in time-resolved mode with 30s gas blank measurement followed by 60s analysis time typically drilling at around $\sim 1 \mu\text{m s}^{-1}$. Data deconvolution was performed using custom made excel-based spreadsheets.

7.3.2. Lead isotope compositions

This section discusses the results of lead isotope composition from the Tersang Selinsing, and Penjom deposits in Central Malaysia. Results are presented in Table 7.2.

Table 7.2. Lead isotope data from the Tersang, Selinsing, and Penjom gold deposits, Central Malaysia.

Sample No. and deposit	Ore mineral	Lead isotope ratios				
		Abbreviation: Se= Standard error				
		$\text{Pb}^{207}/\text{Pb}^{206}$	$\text{Pb}^{208}/\text{Pb}^{206}$	$\text{Pb}^{206}/\text{Pb}^{204}$	$\text{Pb}^{207}/\text{Pb}^{204}$	$\text{Pb}^{208}/\text{Pb}^{204}$
SM09-17	Pyrite	0.84	2.09	18.59	15.75	38.91
Tersang	Se	0.001	0.002	0.039	0.026	0.090
SEL-DD1-102	Pyrite	0.82	2.07	19.10	15.72	39.58
Selinsing	Se	0.001	0.002	0.040	0.026	0.091
SELR091-16	Pyrite	0.83	2.07	18.94	15.73	39.26
Selinsing	Se	0.001	0.002	0.040	0.026	0.091
PENR16A	Galena	0.84	2.09	18.54	15.70	38.78
Penjom	Se	0.001	0.002	0.039	0.026	0.090
PENR16-B	Galena	0.84	2.09	18.57	15.70	38.84
Penjom	Se	0.001	0.002	0.039	0.026	0.090

Chapter 7: Sulphur and Lead isotopes

Surface contamination was eliminated by pre-ablating all spots at the same spot size as used for analysis but a lower repetition rate (typically 5s at 1 Hz). Hg interferences were stripped using the same techniques as described above for the multicollector instrument. Where necessary, corrections for radiogenic Pb growth resulting from in-situ decay of U and Th within the pyrite or included minerals were undertaken using measured U/Pb, Th/Pb and Pb isotope ratios and the known or estimated age of the deposit.

The results show that Selinsing pyrite Pb isotope values range from 18.94 to 19.10 ($\text{Pb}^{206}/\text{Pb}^{204}$) and from 15.72 to 15.73 for $\text{Pb}^{207}/\text{Pb}^{204}$. The Penjom galena isotope values range from 18.54 to 18.57 ($\text{Pb}^{206}/\text{Pb}^{204}$) and with a constant 15.70 ($\text{Pb}^{207}/\text{Pb}^{204}$). In comparison, the Tersang pyrite isotope values are at 18.59 for $\text{Pb}^{206}/\text{Pb}^{204}$ and 15.75 for $\text{Pb}^{207}/\text{Pb}^{204}$. Overall, the Selinsing pyrite has higher radiogenic Pb isotope values compared to the Penjom galena and Tersang pyrites. This isotopic signature stands out in the plot where the Tersang pyrite and Penjom galena are less radiogenic than the Selinsing pyrite (Fig. 7.3).

In addition, the results also show that the Pb isotopic ratios for $\text{Pb}^{208}/\text{Pb}^{204}$ versus $\text{Pb}^{206}/\text{Pb}^{204}$ differ at Selinsing, Tersang and Penjom deposits in Central Malaysia (Fig. 7.4). The Selinsing pyrite is more radiogenic, whereas the Tersang pyrite and Penjom galena are less radiogenic. Lead isotopic data distribution for the Tersang, Selinsing, and Penjom gold deposits with established growth curves are shown in Fig. 7.5.

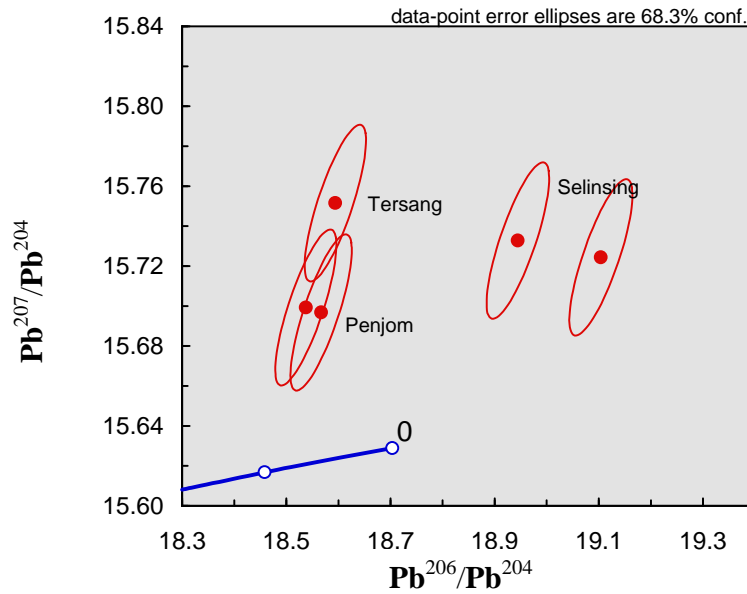


Fig 7.3. Pb isotope ratio for pyrites from the Selinsing, Tersang and Penjom gold deposits, Central Malaysia. The blue line represents the Pb growth curve of Stacey and Kramer (1975). Ellipses are errors approx. 2σ .

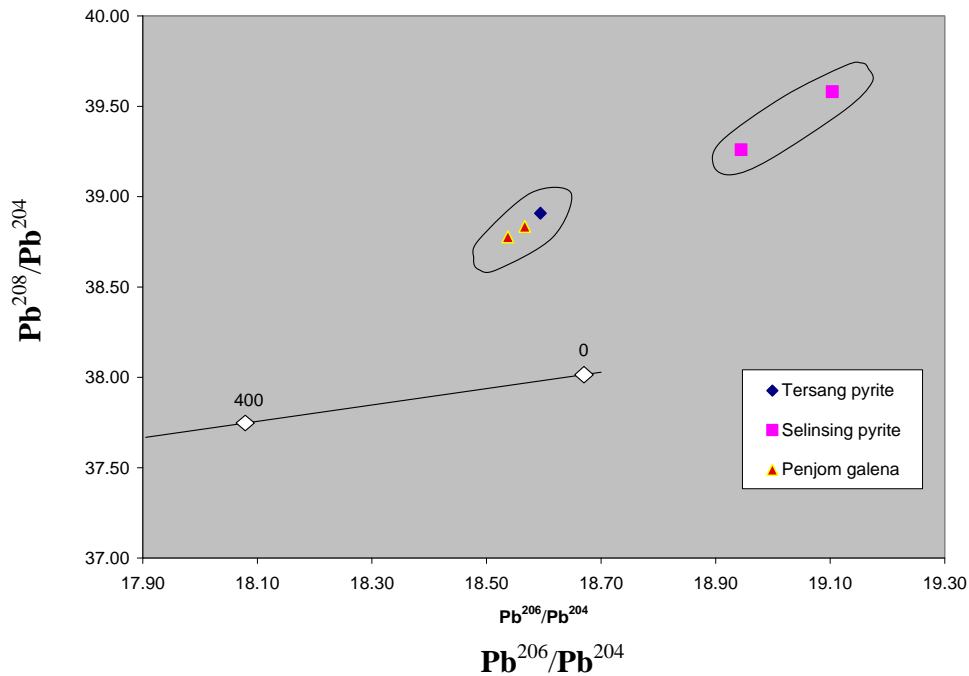


Fig. 7.4. Plot of lead isotopic compositions for Pb^{208}/Pb^{204} versus Pb^{206}/Pb^{204} from the Tersang, Selinsing, and Penjom deposit. The black line represents the Pb growth curve of Stacey and Kramer (1975) for the age interval between 400 Ma and 0 Ma. Ellipses are errors approx. 2σ .

7.3.3. Discussion

The Pb isotope data from the Tersang, Selinsing, and Penjom deposits plots below the upper crust line suggesting that the lead was derived from the bulk crust probably related to subduction-related magmatism. The Tersang and Penjom gold deposits show Pb isotopic data that cluster below the upper crust line indicating that lead may have been derived from the bulk crust and probably in relation to magmatism during collision of the Sibumasu and Indochina terranes (Fig. 7.5).

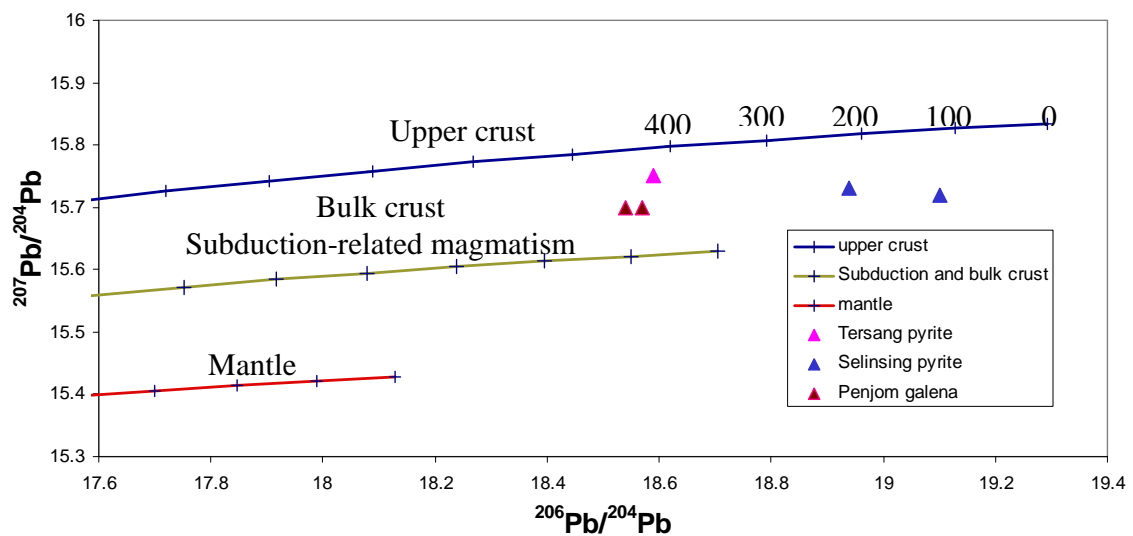


Fig 7.5. Pb isotope compositions for $\text{Pb}^{207}/\text{Pb}^{204}$ versus $\text{Pb}^{206}/\text{Pb}^{204}$ for the Tersang, Selinsing, and Penjom deposits, Central Malaysia. Crosses indicate ages (Zatman and Doe, 1981).

Some authors suggested that Pb in these deposits were probably concentrated by Late Triassic/Early Jurassic fluids or may be related to upper crustal melting during metamorphic and igneous activities in Central Malaysia. The interpretation is supported

Chapter 7: Sulphur and Lead isotopes

by the fact that multiple magmatic events occurred in Peninsular Malaysia (Mitchell 1981; Chung, 1982; Sengor 1984; Metcalfe 2000; Khin Zaw et al., 2010) and were evidenced by Rb/Sr radiometric dating of granitoids (mainly granite). Recent regional geochronological work using LA ICP-MS U-Pb zircon yielded ages ranging from Late Carboniferous (300 to 285 Ma), through Triassic (210 to 240 Ma), to Late Cretaceous (75 ± 1 Ma) (Khin Zaw et al., 2010).

CHAPTER 8 FLUID INCLUSIONS

8.1. Introduction

Fluid inclusions may provide clues to (a) the nature and origin of ore-forming fluids, and (b) the physical and chemical processes of fluid evolution such as mixing, boiling and conductive cooling (e.g., Roedder, 1984; Shepherd et al., 1985 and Khin Zaw et al., 1999). Microthermometric analysis comprises determining homogenisation temperatures and salinities of the ore fluids. Roedder (1984) described primary fluid inclusions as those trapped during the time of mineral growth and occur as separated clusters or as single inclusions or along the mineral growth planes. Pseudosecondary fluid inclusions are similar to primary fluid inclusions because they have the same origin. But they are commonly trapped during deformation or before completion of mineral growth (Goldstein, 2003). Secondary fluid inclusions occur along healed fractures and provide information into the later phases of ore formation or post-mineralisation process (Roedder, 1984).

This Chapter examines petrography of fluid inclusions at the Tersang, Selinsing and Penjom gold deposits and presents the results of microthermometry and Laser Raman Spectrometry for these deposits. In addition, the Chapter discusses fluid processes that evolved during the formation of the deposits.

8.2. Methodology

Two methods were used to characterise the ore fluids at the Tersang, Selinsing, and Penjom gold deposits in Peninsular Malaysia: Microthermometric analysis was used

to determine the homogenisation temperatures and salinities. Laser Raman Spectroscopy was undertaken to determine gas composition of the fluid inclusions.

8.2.1. Microthermometric methods

The samples for fluid inclusion analysis were prepared at CODES, University of Tasmania. Before microthermometry, the samples were examined under the microscope to document the textural characteristics of fluid inclusions, recording their different types such as primary, secondary and pseudosecondary. Prior to microthermometric analysis, cathodoluminescence (CL) imaging was also undertaken on selected samples to portray growth zones in quartz veins. The growth zones are particularly useful because they contain primary fluid inclusions. In addition, CL quartz imaging also helps record the secondary fluid inclusions as they are present in healed cracks or damaged zones. At a later stage, the samples were marked in the areas of fluid inclusion assemblages and then cut into chips to a size of <1 cm in diameter, before proceeding to heating and freezing experiments.

A Linkam TH600 heating-freezing stage was utilized at 1 atm for all microthermometric analyses at CODES, University of Tasmania. Microthermometric measurements were undertaken using the analytical method detailed by Roedder (1984). Temperature measurements have an accuracy of about $\pm 1^{\circ}\text{C}$ for heating and $\pm 0.3^{\circ}\text{C}$ for freezing. The accuracy was insured by the triple point of CO_2 (-56.6°C), the freezing point of water (0.0°C) and the critical point of water (374.1°C). Freezing point depressions (T_m) were measured prior to heating experiments and salinity values were

calculated using equation from Bodnar (1983): Salinity (wt% NaCl equiv.) = $1.78 \times \theta - 0.0442 \times \theta^2 + 0.000557 \times \theta^3$, where θ is the depression temperature in °C.

8.2.2. Laser Raman Spectrometry method

Laser Raman Spectrometric analysis was undertaken on unopened fluid inclusions. It is an in-situ non-destructive method to examine components such as CO, CO₂, CH₄, H₂, H₂S, N₂, NH₃, and SO₂ (Khin Zaw et al., 1999; Mernagh et al., 2007). The fluid inclusion samples from Tersang, Selinsing, and Penjom were analysed using a Laser Raman Spectrometry (LRS) at Geoscience Australia, Canberra. Laser Raman spectra of fluid inclusion were recorded on a Dilor® SuperLabram spectrometer comprising a holographic notch filter, 600 and 1,800 g/mm gratings and a liquid N₂ cooled, 2000 x 450 pixel CCD detector. The inclusions were hit with 514.5 nm laser excitation from a Melles Griot 543 Series argon ion laser, using 5mW power at the samples, and a single 30 seconds accumulation.

A 100x Olympus microscope objective served to focus the laser beam and collect the scattered light. The laser spot on the samples was about 1 µm in diameter. Wave numbers are accurate to $\pm 1 \text{ cm}^{-1}$ as indicated by plasma and neon emission lines. Analysis of gas components such as CO₂, O₂, N₂, H₂S and CH₄ was undertaken by recording spectra from 1,000 to 3,800 cm^{-1} using a single 20 second integration time per spectrum. Laser Raman detection limits were estimated around 0.1 mole % for CO₂, O₂ and N₂. For H₂S and CH₄ the detection limit was around 0.03 mole % and errors in gas ratios was less than 1 mole %.

8.3. Inclusion Petrography

Fluid inclusions have been examined under a petrographic microscope for the Tersang, Selinsing, and Penjom gold deposits. The characteristics of fluid inclusions from the Tersang gold deposit in Central Malaysia are shown in Fig. 8.1. Cathodoluminescence images of quartz are shown in Figs. 8.1A and B. Fluid inclusion petrography has shown two types under the microscope:

Type I: Primary, liquid-rich two-phase inclusions and the size of these inclusions is between 8-10 μm (Fig. 8.1C).

Type II: Primary, vapour-rich two-phase inclusions and the size of these inclusions ranges from 5 to 10 μm and they homogenised into liquid phase. In addition, the both types of fluid inclusions are found within the growth zones in quartz veins (Fig. 8.1D).

The characteristics of the fluid inclusions from the Selinsing gold deposit in Central Malaysia are shown in Fig. 8.2. The fluid inclusions were identified based on phases and paragenesis. The elongated primary inclusions were found in the direction of the quartz growth. Some fluid inclusions are also called Pseudosecondary (PS). At the Selinsing gold deposit, quartz veins are characterised by the presence of growth zones, which are represented by the cloudy zones rich in fluid inclusions and the clear zones poor in fluid inclusions. Cathodoluminescence image of quartz is shown in Fig. 8.2A. The following fluid inclusion types are recorded at Selinsing:

Type I: Primary, liquid-rich two-phase (L + V) inclusions, abundant found in quartz veins. Most inclusions show variable size ranging from 10 to 40 μm (Fig. 8.2B).

Type II: Primary, vapour-rich two-phase (L + V) inclusions, less abundant. The inclusion size ranges from 4 to 8 μm and homogenised into liquid phase (Fig. 8.2C).

Chapter 8: Fluid inclusions

Type III: Secondary, liquid-rich 2-phase (L + V) inclusions, which are found along healed cracks. The size of these inclusions is less than 20 μm . These inclusions are found along sealed cracks and cross-cut early generation (Fig. 8.2D).

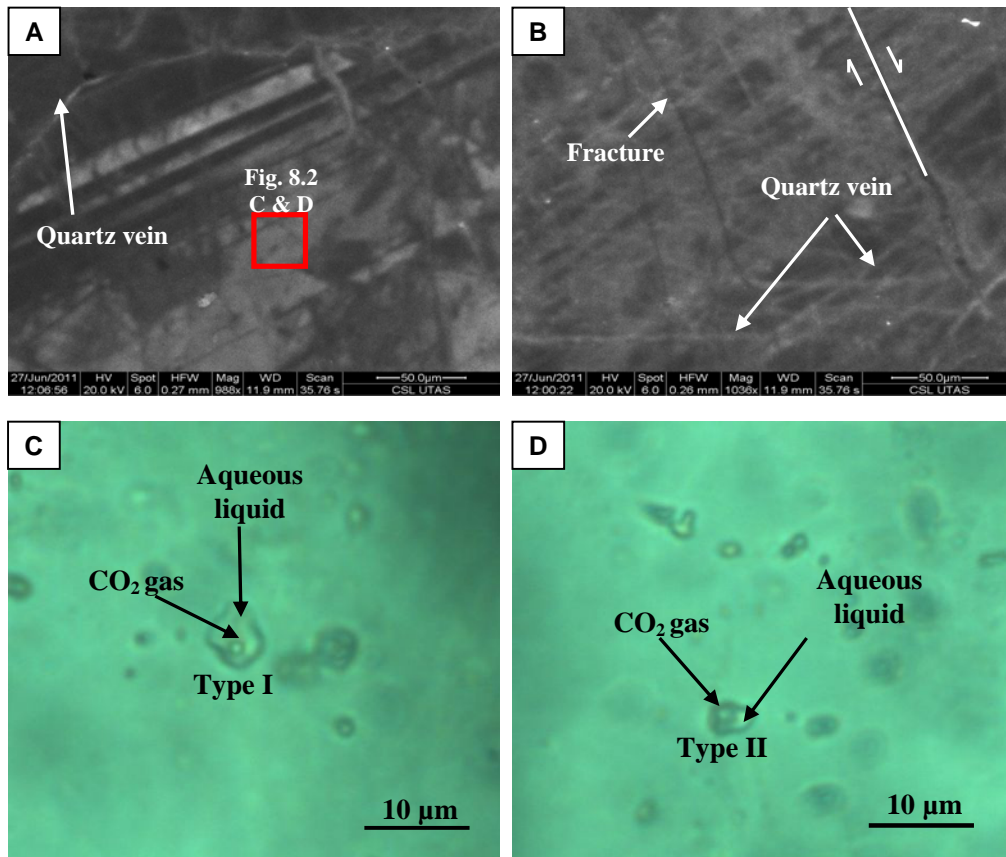


Fig. 8.1. Photomicrographs of fluid inclusions in quartz veins at the Tersang gold deposit, Central Malaysia. **A.** Cathodoluminescence (CL) image showing growth zones crosscut by quartz veinlets. **B.** CSL image of growth zones disrupted by intense fracturation. **C.** Liquid-rich, two-phase fluid inclusion (Type I) (Sample No. TER-R029). **D.** Vapour-rich two-phase inclusion (Type II) (Sample No. TER-R029).

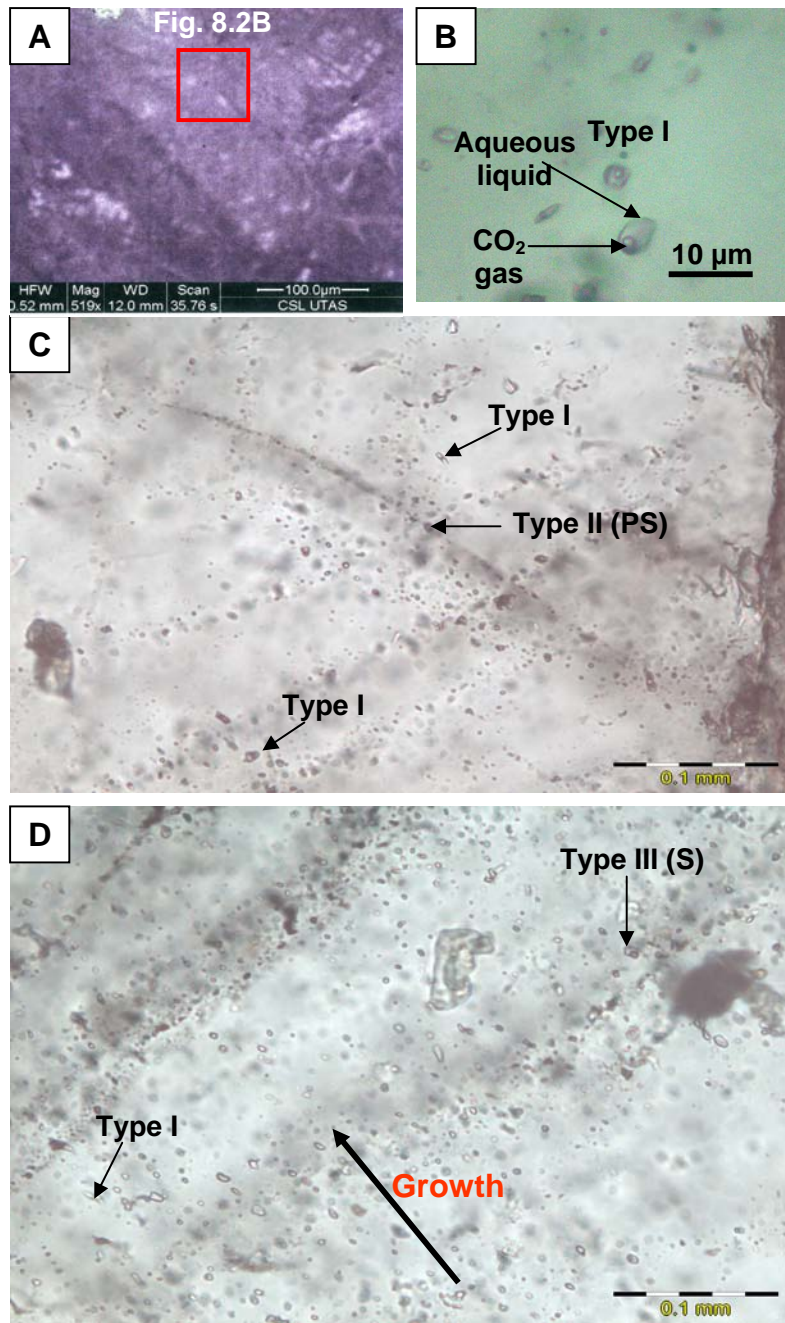


Fig. 8.2. Photomicrographs of fluid inclusions in quartz veins at the Selinsing gold deposit. **A.** Cathodoluminescence image of quartz (Sample No. SEL-DD7@173m). **B.** Primary, two-phase inclusion with liquid and gas phase (Sample No. SEL-DD7@173). **C.** Primary and pseudosecondary inclusions (P and PS) with liquid and vapour phase (Sample No. SEL-R032). **D.** Secondary, two-phase (liquid + vapour) and vapour inclusions (Sample No. SEL-R032).

Chapter 8: Fluid inclusions

The characteristics of the fluid inclusions from the Penjom gold deposit in Central Malaysia are shown in Fig. 8.3.

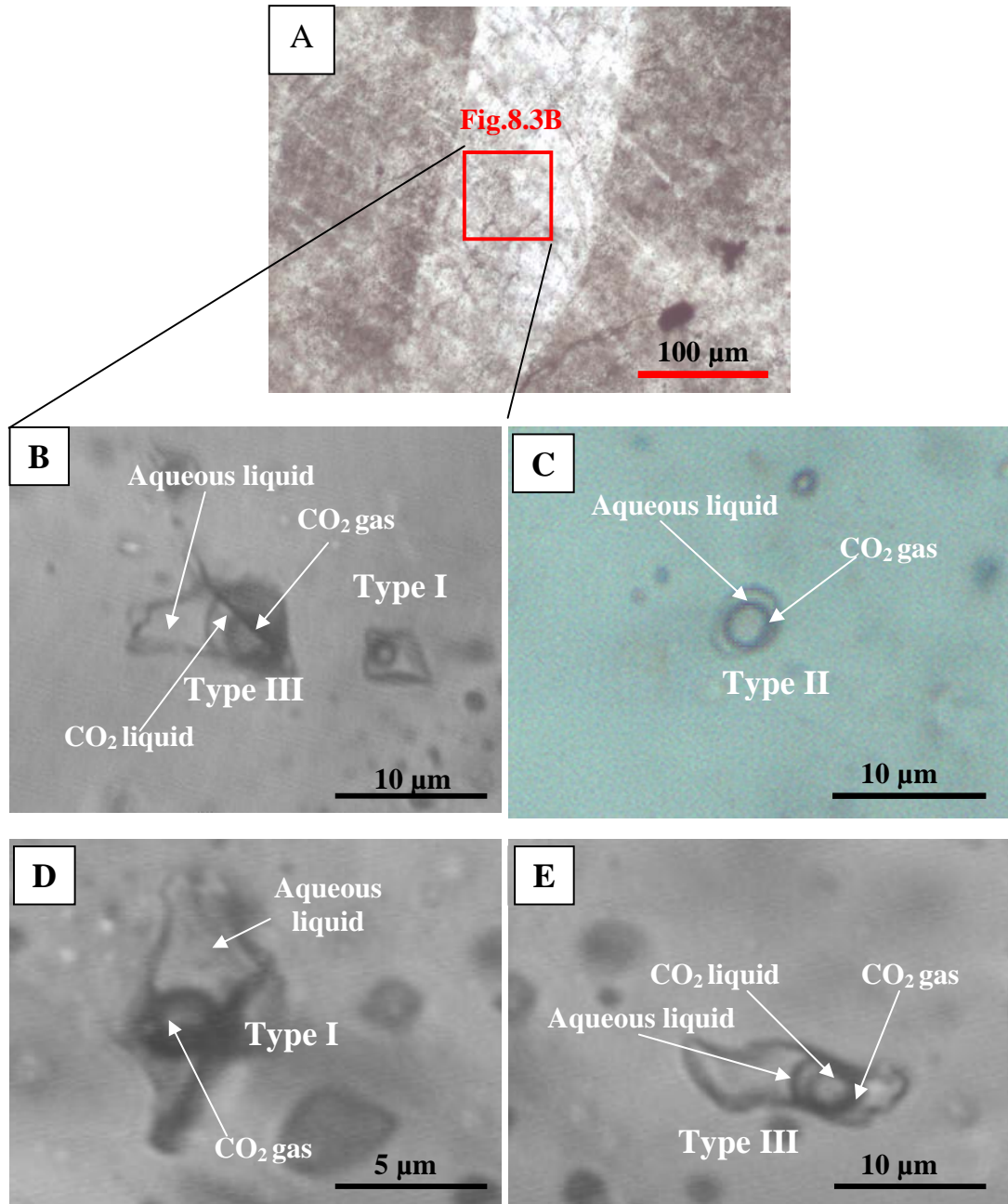


Fig. 8.3. Photomicrographs of fluid inclusions in mineralised quartz at the Penjom gold deposit, Central Malaysia. **A.** Cathodoluminescence image of quartz showing growth zones (Sample No. Penjom 4). **B.** Two and three-phase fluid inclusions (Type I and Type III). **C.** Vapour-rich, two-phase inclusion (Type II). **D.** Two-phase fluid inclusion (Type I). **E.** Three-phase fluid inclusion (Type III).

Chapter 8: Fluid inclusions

Cathodoluminescence image of quartz is shown in Fig. 8.3A. Fluid inclusions at Penjom have shown three types under the microscope:

Type I: Primary, two-phase inclusions, liquid-rich, abundant with size ranging from 8 to 20 μm (Fig. 8.3B).

Type II: Primary, two-phase, vapour-rich inclusions occur together with liquid-rich inclusions and homogenised into liquid phase. The size varies from 5 to 8 μm (Figs. 8.3D and C).

Type III: Primary, three-phase, CO_2 -liquid bearing inclusions, less abundant and their size ranges from 10 to 15 μm (Figs. 8.3A and 8.3E).

8.4. Microthermometric results

Microthermometric measurements were undertaken for the Selinsing, Tersang, and Penjom gold deposits and a summary of homogenisation temperatures and salinities data are presented in Table 8.1.

At the Tersang gold deposit, heating experiments indicated that the homogenisation temperatures are between 210 and 348 $^{\circ}\text{C}$ for liquid-rich (Type I) inclusions (Fig. 8.1). Vapour-rich two-phase (Type II) inclusions are rare and no data were collected due to their smaller size for heating and freezing experiments. The salinities range from 2.41 to 8.95 wt % NaCl equiv. Histograms of homogenisation temperatures and salinities are shown in Figs. 8.4-8.5. Similarly, at the Selinsing gold deposit, microthermometry was performed only for the Type I inclusions, which are liquid-rich inclusions and larger enough in size to do heating and freezing measurements

Chapter 8: Fluid inclusions

(Fig. 8.2). Other types such as Type II, and III are excluded in this study because of their smaller size and difficulty in doing the heating and cooling experiments.

Table 8.1. Summary of homogenisation temperature and salinity at the Tersang, Selinsing gold deposits, Central Malaysia.

Location	Tf (°C)	Tm (°C)	Th (°C)	Salinity* Wt % NaCl equiv.
Tersang deposit (Type I)	nd	nd	237.5	nd
	nd	nd	269.6	nd
	nd	nd	246.4	nd
	nd	nd	263.2	nd
	nd	nd	276.1	nd
	nd	nd	232.2	nd
	nd	nd	247.5	nd
	nd	nd	250.1	nd
	nd	nd	290.7	nd
	nd	nd	261	nd
	nd	nd	237.5	nd
	nd	nd	269.6	nd
	nd	nd	246.4	nd
	nd	nd	263.2	nd
	nd	nd	276.1	nd
	-32.8	-2.1	232.2	3.55
	-35.3	-1.5	247.5	2.57
	-38.8	-6	250.1	9.21
	-36	-1.4	290.7	2.41
	-36.3	-5.8	261	8.95
	nd	nd	284.2	nd
	nd	nd	270.4	nd
	nd	nd	294.6	nd
	nd	nd	348	nd
	nd	nd	283.6	nd
Selinsing deposit (Type I)	-37	-5	203.5	7.86
	-33	-0.7	193.9	1.23
	-37.7	-6.5	213	9.86
	-34.1	-1.4	347.5	2.41
	Nd	nd	301	nd
	-31.7	-6.6	337	9.98
	-40.1	nd	343.7	nd
	-36.7	-3.4	200.5	5.56
	-37.3	-5.7	216.6	8.81
	-37.3	-6	244.9	9.21

Note: Tf: first melting temperature; Tm: last ice melting temperature; Th: homogenisation temperature; nd: no data available. * Salinities were calculated using the equation of Bodnar (1983).

Chapter 8: Fluid inclusions

Table 8.1 (Continued). Summary of homogenisation temperature and salinity at the Penjom gold deposits, Central Malaysia.

Location	Tf (°C)	Tm (°C)	Th (°C)	Salinity* wt% NaCl equiv.
Penjom deposit (Type I)	nd	-49	236.5	nd
	nd	nd	277.3	nd
	nd	nd	330.6	nd
	nd	nd	220.8	nd
	nd	nd	293.8	nd
	nd	nd	260.4	nd
	nd	nd	295.8	nd
	nd	nd	268.5	nd
	nd	nd	345.2	nd
	nd	nd	302.1	nd
Penjom deposit (Type II)	nd	nd	345.7	nd
	nd	nd	282.3	nd
	nd	nd	332.4	nd
	nd	nd	316.7	nd
Penjom deposit (Type III)	-29	-5.4	256	8.41
	nd	-5.6	280	8.68
	-44	-4	259.5	6.45
	-28.9	-4.3	256	6.88
	-49	-2.6	236.5	4.30
	-28.1	-3.9	276	6.30
	-28.7	-4.2	302	6.74
	-29.4	-4.5	289	7.17
	-28.8	-4.8	271.6	7.59

Note: Tf: first melting temperature; Tm: last ice melting temperature; Th: homogenisation temperature; nd: no data available. * Salinities were calculated using the equation of Bodnar (1983).

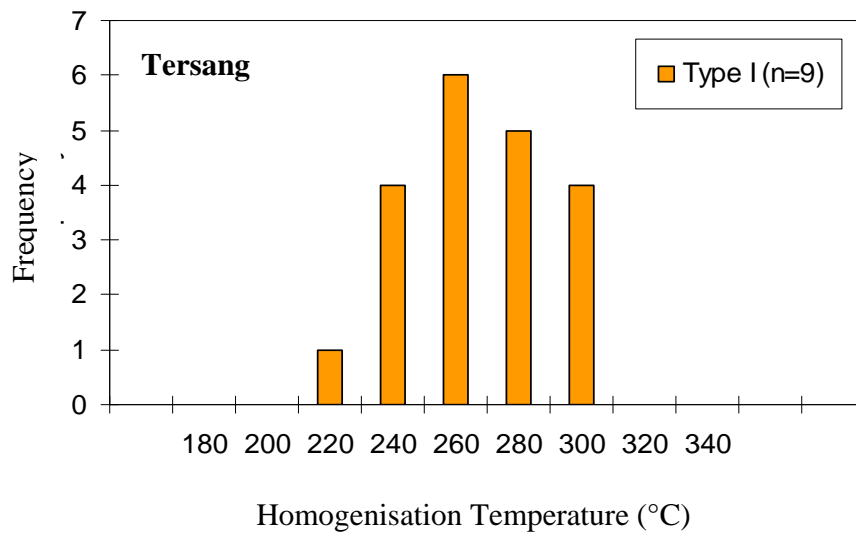


Fig. 8.4. Histogram of homogenisation temperature (°C) of Type I inclusions in mineralised quartz veins at the Tersang gold deposit, Central Malaysia.

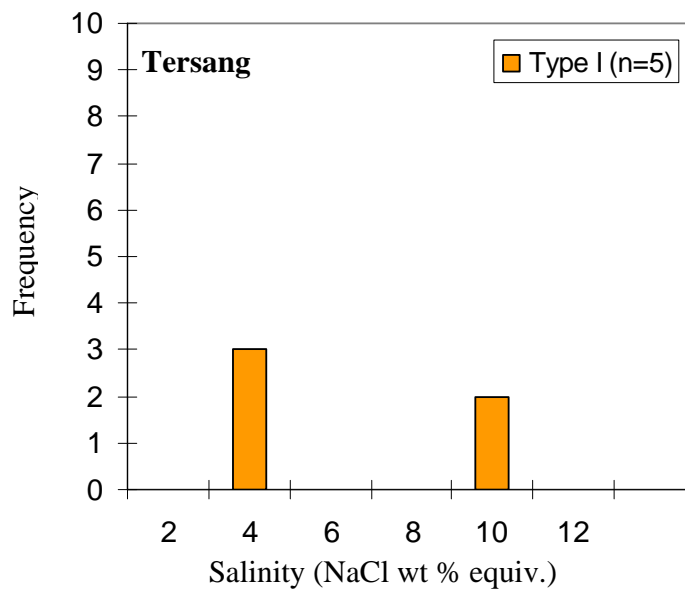


Fig. 8.5. Histogram of salinities of Type I inclusions in mineralised quartz veins at the Tersang gold deposit, Central Malaysia.

At Selinsing, the Type I inclusions yielded the homogenisation temperature range from 194 to 348 °C and salinities between 1.23 and 9.98 wt % NaCl equiv. Histograms of homogenisation temperatures and salinities are shown in Figs. 8.6-8.7.

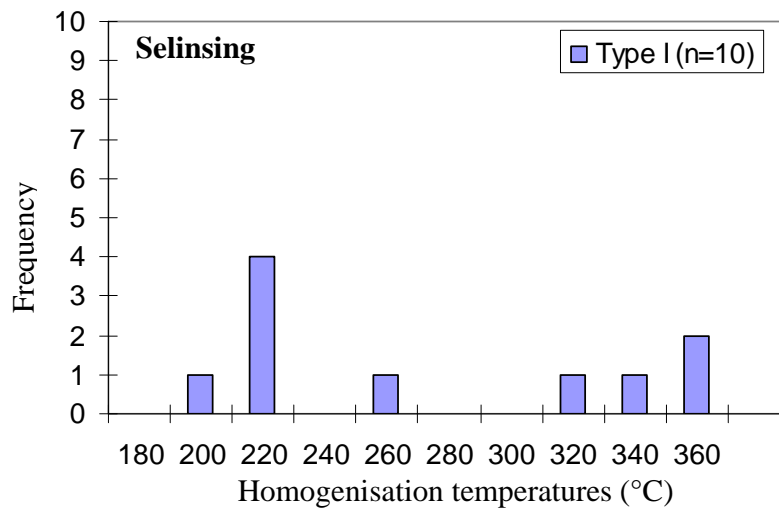


Fig. 8.6. Histogram of homogenisation temperature (°C) of Type I inclusions in mineralised quartz veins at the Selinsing gold deposit, Central Malaysia

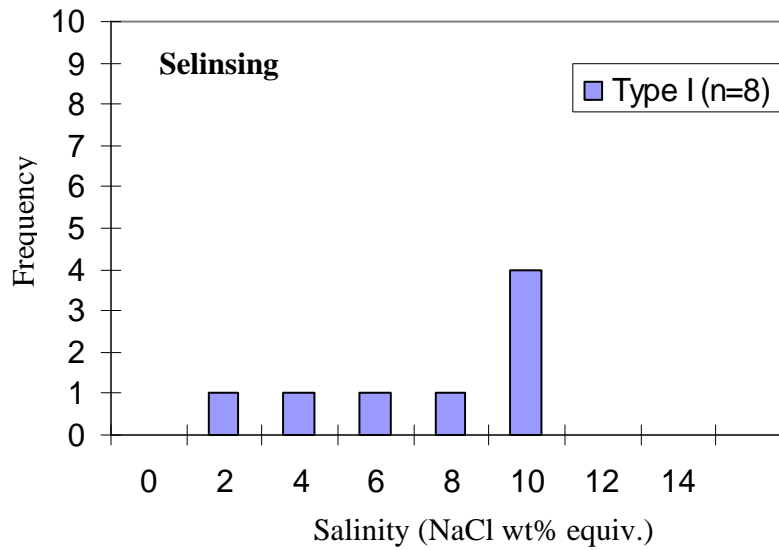


Fig. 8.7. Histogram of salinities of Type I inclusions in mineralised quartz veins at the Selinsing gold deposit, Central Malaysia.

At Penjom, heating and freezing results indicated that homogenisation temperatures are between 221 and 346 °C and the salinities range from 4.34 to 9.34 wt% NaCl equiv. Histograms of homogenisation temperatures and salinities are presented in Figs. 8.8-8.9.

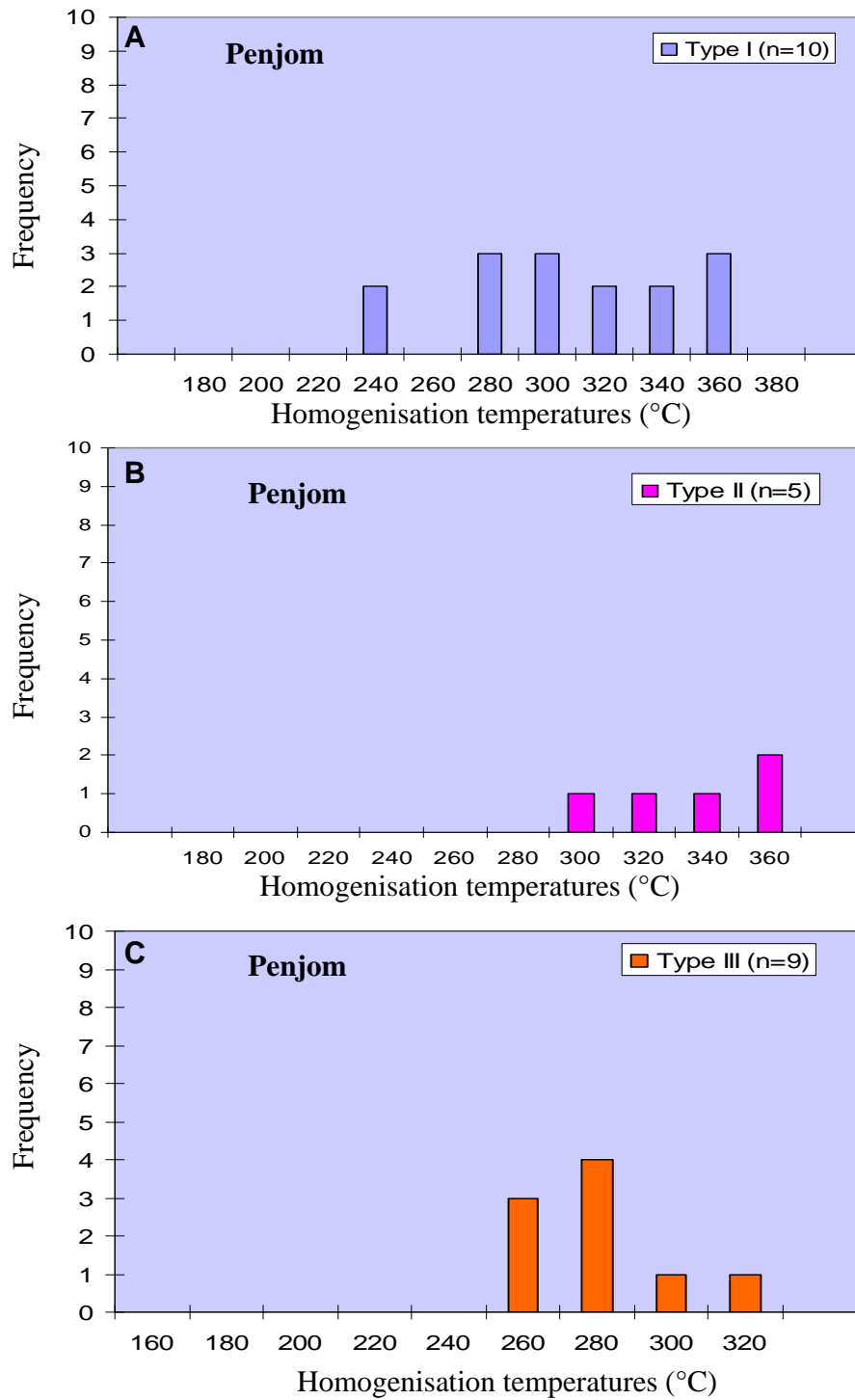


Fig. 8.8. Histograms of homogenisation temperature (°C) of different fluid inclusion types in quartz at the Penjom gold deposit, Central Malaysia. **A.** Type I two-phase, liquid-rich inclusions. **B** Type II two-phase, vapour-rich inclusions. **C.** Type III three- phase, CO₂-liquid bearing inclusions.

Chapter 8: Fluid inclusions

For the Penjom gold deposit, heating experiments were conducted for Type I, Type II and Type III inclusions but the freezing measurements were only undertaken for the Type III because other inclusion types were too small to determine their salinities.

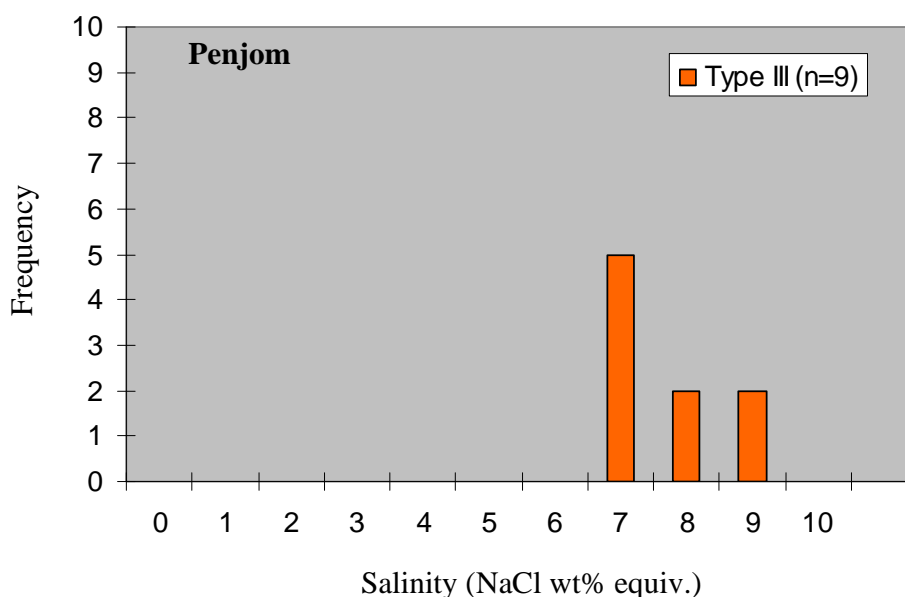


Fig. 8.9. Histogram of salinities for the Type III fluid inclusions from the Penjom gold deposit, Central Malaysia.

8.5. Laser Raman results

This section presents the results of Laser Raman Spectrometry analysis for the Tersang, Selinsing, and Penjom deposits, Central Malaysia. At the Tersang gold deposit, most inclusions contain pure or nearly pure CO₂ (98.13-100 mole %), and one inclusion has a small amount of CH₄ (0-1.9 mole %) as shown in Table 8.2. At Selinsing, most inclusions are CO₂-rich (100 mol %). However, an inclusion was found containing CO₂ (95 mol %) and N₂ (5 mol %) as shown in Table 8.3. At the Penjom gold deposit, the

Chapter 8: Fluid inclusions

majority of fluid inclusions are CO₂- rich (100 mol %), whereas one fluid inclusion is N₂-rich (100 mol %) as shown in Table 8.4.

Table 8.2. Laser Raman Spectrometry results of fluid inclusion Type I in mineralised quartz veins at the Tersang gold deposit, Central Malaysia.

Sample number	SO ₂	CO ₂	N ₂	H ₂ S	C ₃ H ₈	CH ₄	C ₂ H ₆	NH ₃	H ₂
	mol %	mol %	mol %	mol%	mol %	mol %	mol %	mol %	mol %
TER-029B2	0	100	0	0	0	0	0	0	0
TER-030_1	0	100	0	0	0	0	0	0	0
TER-030_2	0	100	0	0	0	0	0	0	0
TER-030_3	0	100	0	0	0	0	0	0	0
TER-030_4	0	100	0	0	0	0	0	0	0
TER-030_5	0	98.13	0	0	0	1.9	0	0	0

Table 8.3. Laser Raman Spectrometry results of fluid inclusion Type I in mineralised quartz veins at the Selinsing gold deposit, Central, Malaysia.

Sample number	SO ₂	CO ₂	N ₂	H ₂ S	C ₃ H ₈	CH ₄	C ₂ H ₆	NH ₃	H ₂
	mol %	mol %	mol %	mol%	mol %	mol %	mol %	mol %	mol %
SEL-R32_1	0	100	0	0	0	0	0	0	0
SEL-R32_2	0	100	0	0	0	0	0	0	0
SEL-R32_3	0	100	0	0	0	0	0	0	0
SEL-R32_4	0	100	0	0	0	0	0	0	0
SEL-R32_5	0	100	0	0	0	0	0	0	0
SEL-90_1	0	100	0	0	0	0	0	0	0
SEL-90_2	0	100	0	0	0	0	0	0	0
SEL-90_3	0	100	0	0	0	0	0	0	0
SEL-90_4	0	100	0	0	0	0	0	0	0
SEL-90_5	0	95	5	0	0	0	0	0	0

Chapter 8: Fluid inclusions

Table 8.4. Laser Raman Spectrometry results of fluid inclusion Type I in mineralised quartz veins at the Penjom gold deposit, Central, Malaysia.

Sample number	SO ₂	CO ₂	N ₂	H ₂ S	C ₃ H ₈	CH ₄	C ₂ H ₆	NH ₃	H ₂
	mol %	mol %	mol %	mol%	mol %	mol %	mol %	mol %	mol %
PEN-1	0	0	100	0	0	0	0	0	0
PEN-2	0	100	0	0	0	0	0	0	0
PEN-3	0	100	0	0	0	0	0	0	0
PEN-4	0	100	0	0	0	0	0	0	0
PEN-5	0	100	0	0	0	0	0	0	0
PEN-6	0	100	0	0	0	0	0	0	0
PEN-7	0	100	0	0	0	0	0	0	0
PEN-8	0	100	0	0	0	0	0	0	0
PEN-9	0	100	0	0	0	0	0	0	0

8.6. Discussion

Microthermometric analysis has shown that the Tersang fluid inclusions have homogenisation temperatures ranging from 232 to 348 °C and low salinities (2.41 – 9.21 wt % NaCl equiv.). In addition, the Tersang fluid inclusions mostly contain CO₂ (98-100 mol %) and a trace amount of CH₄. The presence of CO₂-rich inclusions suggests that these fluids were probably trapped during metamorphism. Evidence of metamorphism is also supported by the presence of graphite by scanning electron back-scattered imaging of quartz veins. This can also imply involvement of metamorphic fluids during the formation of the Tersang gold deposit.

In comparison, at Selinsing, homogenisation temperatures are between 200 and 340 °C and salinities range from 2.41 to 9.86 wt % NaCl equiv. Fluid inclusions have

Chapter 8: Fluid inclusions

considerable amounts of CO₂ (95-100 mol %), with a minor proportion of N₂ (5 mol %). The results in this study are comparable to a previous study on fluid inclusions in quartz-carbonate veins done by Gunn et al. (1993) who reported high temperature (270-280 °C), low salinity and CO₂-rich fluids for the Selinsing gold deposit. The authors also suggested that these results showed similarity with other orogenic gold deposits where fluids were introduced into the shear zone carrying gold and other trace elements.

At Penjom, homogenisation temperatures range from 230 to 300 °C and salinities between 4.30 and 8.68 wt % NaCl equiv. Most fluid inclusions are typically CO₂-rich (100 mol %) but one inclusion is N₂-rich (100 mol %). Ridley and Diamond (2000) argued that the typical conditions of mineralisation formation in orogenic gold deposits include temperatures of 300-350 °C at pressures of 1-2.5 Kb. This thermal signature is similar to the Tersang, Selinsing, and Penjom deposits which are found in this thermal range as evidenced in this study.

The depth of entrapment of fluid inclusions has been estimated using the FLINCOR software (Brown, 1989) for the Tersang, Selinsing and Penjom deposits, Central Malaysia. The plot shows two populations: one population along the line constrained by Hendel and Hollister (1981) which is characterised by salinity values of 6 NaCl wt % equiv. and pressure of 1 Kb and another population clustered in the blue polygon found on the line H₂O-CO₂ liquid with negligible salinity at a pressure of 1 Kb as well. The molar percentages of H₂O together with homogenisation temperatures for each measurement were plotted as shown in Figures. 8.10-12.

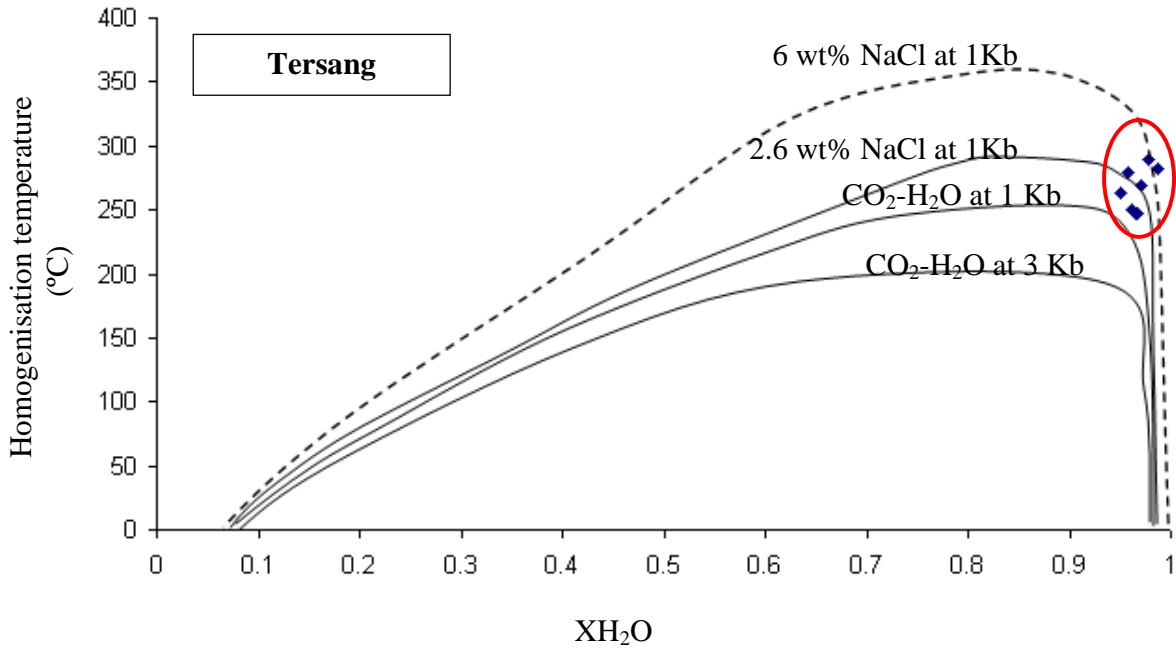


Fig. 8.10 Plot of molar percent of H₂O against homogenisation temperature at the Tersang gold deposit, Type I inclusions plotting on Hendel and Hollister (1981) (Red polygon). XH₂O is the molar composition of water.

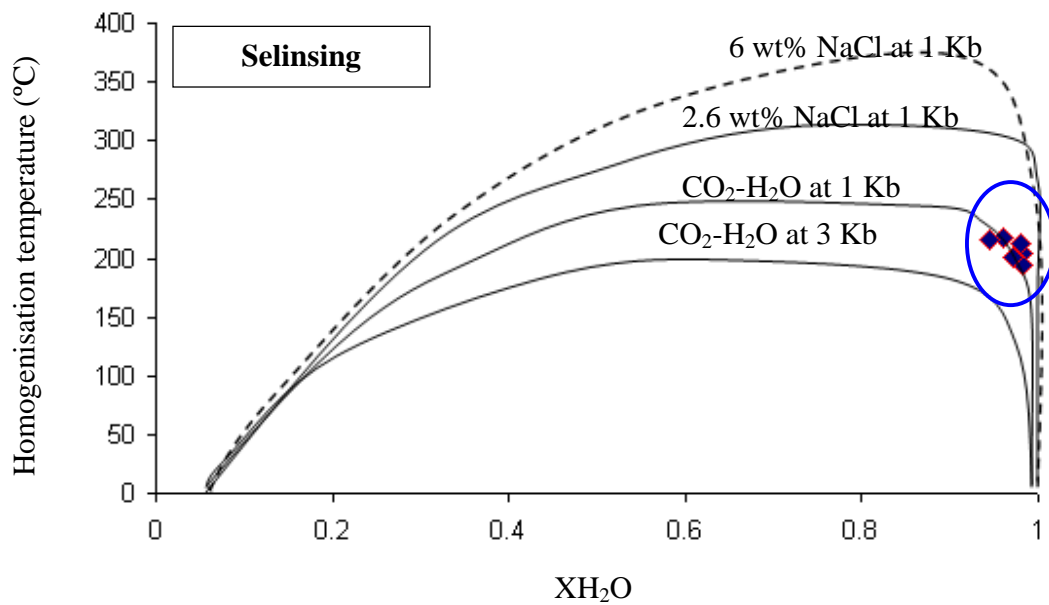


Fig. 8.11. Plot of molar percent of H₂O against homogenisation temperature at the Selinsing gold deposit, Type I inclusions plotting on Todheide and Franck (1963) (Blue polygon). XH₂O is the molar composition of water.

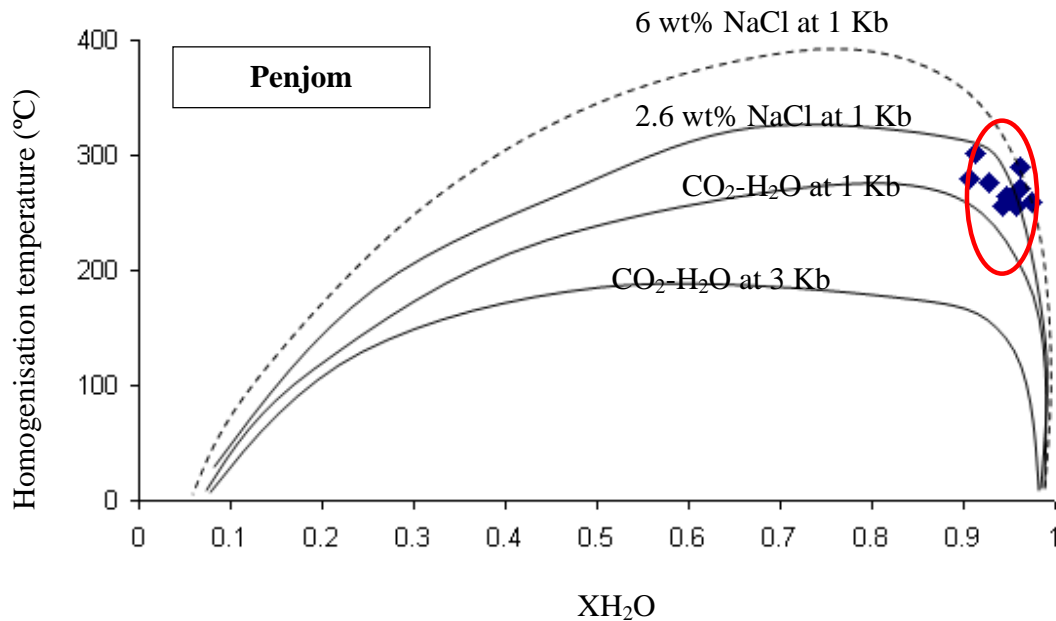


Fig. 8.12. Plot of molar percent of H_2O against homogenisation temperature at the Penjom gold deposit, Type III inclusions plotting on Hendel and Hollister (1981) (Red polygon). XH_2O is the molar composition of water.

At Tersang, the plot of molar percentage of H_2O against homogenisation temperature indicates an estimate of pressure of entrapment of 1 Kb (Fig. 8.10). The plots of molar percentage of H_2O against homogenisation temperature also indicate an approximate pressure of entrapment of 1 Kb for the Selinsing and Penjom gold deposits. The pressure of 1 Kb is equivalent to 2.6 km assuming density of rock is about 2.6 g/cm^3 .

As a whole, the homogenisation temperatures of the Tersang, Selinsing, and Penjom range from 200 to 350 °C. This temperature range has been interpreted to be typical of epizonal orogenic gold deposits in metamorphic terranes (Goldfarb et al., 2005). These authors also suggested that these deposits formed at a depth ranging from 2 to 5 km. The calculation of depth in this study supports this interpretation as estimated around 2.6 km for the deposits in this study (Figs. 8.10-8.12). This interpretation was also given by Hofstra and Cline (2000) who reported that higher contents of CO_2 in ore fluid

Chapter 8: Fluid inclusions

occurred at greater depths at about 5-8 km. The evidences indicate that these deposits are characterized by homogenisation temperatures ranging from 200 to 348 °C, low salinity (<10 wt % NaCl equiv.) and $\text{H}_2\text{O}-\text{CO}_2 \pm \text{CH}_4 \pm \text{N}_2$ fluids with depth < 10 km making them comparable to orogenic Au deposits (Colvine, 1989; Groves, 1993). The plot of salinity against homogenisation temperature data for the Type I fluid inclusions from Selinsing and Tersang, and Type III from Penjom is shown in Fig. 8.13A. This plot can be interpreted using the Shepherd et al. (1985) model as follows:

(i) Isothermal mixing

The isothermal mixing of fluid of contrasting salinity produces the trends 1 and 2 (Figs. 8.13B1 and B2). The trend shows fluid of contrasting salinities with no significant variation in homogenisation temperature (Figs. 8.13B1 and 2).

(ii) Surface fluid dilution

This process is characterised by mixing with cooler less saline fluids (Fig. 8.13B3).

(iii) Cooling

In this fluid process, there is significant decrease in temperature while salinity almost remains unchanged (Fig. 8.13B4).

(iv) Boiling

Boiling involves separation of liquid and vapour is shown by the trend 5. During boiling, there is a decrease of temperatures with increase of salinity (Fig. 8.13B5).

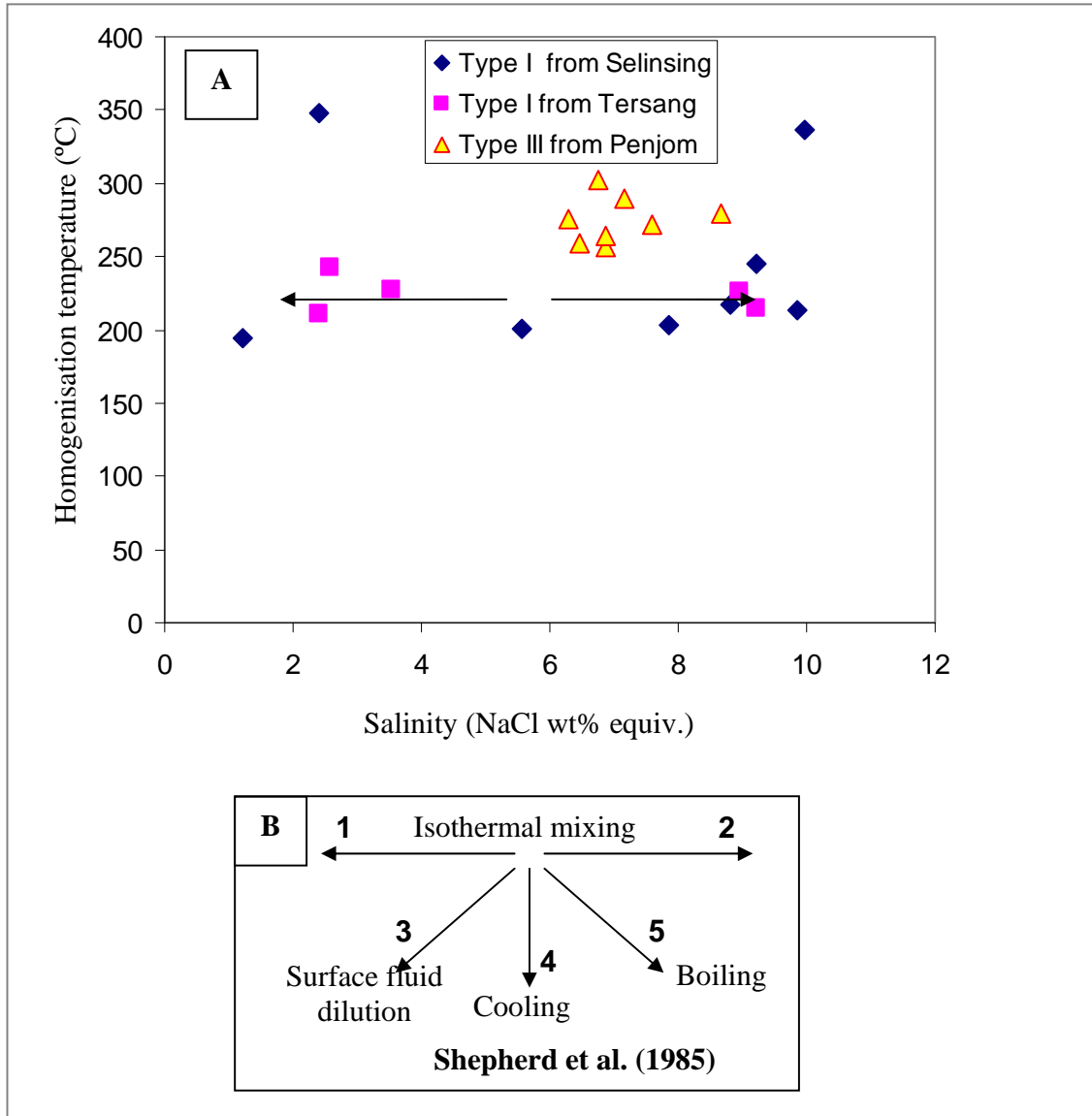


Fig. 8.13. Plot of homogenisation temperatures and salinities for the Tersang, Selinsing and Penjom deposit, Central Malaysia. **A.** Plot of salinity against homogenisation temperature for inclusion Type I from the Selinsing, Tersang, and Type III from the Penjom gold deposit. **B.** Shepherd et al. (1985) model of fluid processing trends.

At a regional scale, the homogenisation temperatures against salinity plot for the Tersang, Selinsing, and Penjom gold deposits probably indicate an isothermal mixing of magmatic/metamorphic (salinities as high as 10 wt % NaCl equiv.) and/or meteoric fluids is invoked as evidenced by salinities as low as 0.5 wt % NaCl equiv. The plot also shows a lack of evidence for fluid boiling probably due to the ranges of depth of formation for these gold deposits between 1.7 and 6.5 km (Hofstra and Cline, 2000).

CHAPTER 9

DISCUSSION, GENETIC MODELS AND EXPLORATION IMPLICATIONS

9.1. Introduction

This Chapter combines geological and geochemical data obtained from the Selinsing, Tersang, and Penjom deposits and establishes genetic models for these deposits. The Chapter also proposes some exploration implications based on pyrite chemistry and other results obtained in this study. The characteristics of these three deposits are also summarised in this Chapter.

9.2. Summary of results

9.2.1. Geological setting

The Tersang gold deposit lies in Central Malaysia at the east of the Bentong-Raub Suture Zone. This deposit is found in sandstone and breccia units possibly Carboniferous in age, which are cross-cut by Late Triassic alkali rhyolite and rhyodacite intrusive rocks. To the north, the Selinsing gold deposit is also located at the east of the Bentong-Raub Suture Zone. This deposit is hosted in phyllite, siltstone, and argillite units probably Carboniferous in age, which are associated with fault-related rocks such as mylonite and cataclasite. No intrusive phases were recorded in the Selinsing area. Further east from the Tersang deposit, there is the Penjom gold deposit, which is hosted in Permian sequence of carbonaceous shale, tuffaceous conglomerate, tuffaceous siltstone and felsic sills and dykes of trachyandesite and trachyte/phonolite compositions. The age of these intrusive rocks has not been determined due to lack of zircon in all the analysed samples.

9.2.2. Structural setting

At Tersang, two sets of mineralised veins were recognised including NNW-SSE trending veins (set 1) and the ESE-WNW orientated veins (set 2): the set 1 veins are characterised by quartz, pyrite, arsenopyrite, sphalerite and minor rutile. The earliest vein-fill materials contain up to 90% of quartz. These veins also contain a large number of fractured pyrite, arsenopyrite and sphalerite grains suggesting multiple episodes of brittle deformation. The set 2 veins are probably the main event of gold deposition with pyrite, galena, geochronite, covellite, ilmenite, quartz and some silicates, amounting from 1 to 5 % of the vein filling.

Similarly, the Selinsing gold deposit comprises of two generations of mineralised veins based on their mineral assemblage and paragenesis as described from drill core samples: an early vein set 1, trending NNW-SSE, is composed of milky white quartz, carbonate, chlorite, and sulphide and later vein set 2, trending ESE-WNW, consists of quartz, sulphide, and chlorite. The earlier veins exhibit deformed pinch and swell structures at depth and contain pyrite, arsenopyrite and ankerite. The earlier veins are thought to have formed during a ductile deformation. The later veins contain several fractures filled with sulphides and free gold which have overprinted the earlier veins. The sulphides are pyrite, arsenopyrite and galena. These veins occur as extensional veins (1-4 mm wide).

At Penjom, the major structures are aligned in the N-S and NE-SW directions. These main trends were intercepted by many faults zones interpreted as shear or lateral fault zones. Most of the high angle faults are striking in the direction of N355°-005°E or N-S and N300°-310°E or WNW-ESE show right lateral movement or slip. Faults in the

direction of N035°-045°E or NE-SW indicate left lateral movement or slip (Heru et al., 2000).

9.2.3. Alteration and ore minerals

The ore mineral assemblage at Tersang consists of gold, pyrite, arsenopyrite, galena, sphalerite, geochronite, and covellite. Gold is particularly associated with pyrite, arsenopyrite and geochronite. The ore zone is characterised by a ubiquitous alteration assemblage of sericite, illite and montmorillonite. The sericite alteration is proximal to the high grade zone. In contrast, the ore minerals at Selinsing include gold, pyrite, arsenopyrite, galena, sphalerite, chalcopyrite and pyrrhotite. Moreover, occurrence of phyllite and mylonite in the host sequence suggests that low-grade metamorphism occurred during D1 thrusting event at the Selinsing gold deposit. The quartz-ankerite alteration is pervasive in high grade ore zones at the Selinsing gold deposit.

In comparison, at the Penjom gold deposit, the ore minerals are gold, pyrite, galena, sphalerite, and arsenopyrite. Gold is associated with pyrite and arsenopyrite in quartz-carbonate veins within the shear zones. Three dominant types of alteration were recognised including silicification, argillic alteration (illite) and chloritisation, marked by a development of secondary minerals over the primary minerals (Wan Fuad and Heru Sigit, 2001). Limonitic iron staining is also present. In addition, carbonate minerals (mostly ankerite) are associated with tonalite intrusion and sedimentary rock adjacent to dacitic and rhyodacitic rocks. At the Tersang gold deposit, scanning electron probe quantitative analysis of vein gold shows that electrum is associated with higher Ag content (4.07-22.99 wt %), whereas gold grains in fractures within arsenopyrite are depleted in Ag content (3.46-3.92 wt %). The result also shows that the Tersang ore

Chapter 9: Discussion, genetic models and exploration implications

veins have two types of fineness: 1) high fineness (959-965) gold associated with pyrite, arsenopyrite and geochronite; 2) low fineness (769-792) gold which occurs with broken arsenopyrite grains. In contrast, alluvial grains are significantly depleted in Ag content from 1.26 to 5.22 wt % with no Pb and Bi contents as well as negligible amount of As content (0.01-0.02 wt %). All gold grains have high fineness which ranges from 948 to 981 (average fineness 968). In addition, the grains have lower Au content in porous cores (2.12-5.06 wt %), whereas the rims which thickness varies from 10 to 30 μm have higher Au content (1.86-5.22 wt %).

9.2.4. Pyrite chemistry

At the Tersang gold deposit, gold mineralisation shows two main stages of Au enrichments: an early stage within the core of pyrite 1 and a late stage in pyrite 3. Gold in the first stage is associated with elevated values of Co, Ni and Ti. In comparison, gold deposition in the late stage is accompanied with high values of As, Ag, Cu, Sb, Se, Tl, and Mn. At Tersang, there is low Ag/Au, with linear trend for the Co and Ni data suggesting that pyrite 1, pyrite 2, pyrite 3 and pyrite 4 are not diagenetic in origin. The Tersang gold solubility diagram shows the presence of free gold in silicates with minor amount in pyrite rims.

At Selinsing, LA ICP-MS mapping of pyrite has shown multiple Au enrichment and two main stages of high Au accumulation. The first stage (pyrite 3) is associated with high contents in Mo, Tl, Sb and Co with minor concentrations of Zn, Te, and Bi. Later Au enrichment in pyrite 6 characterised by high contents of As, Cu, Co, Zn, Te, Bi, Sb, Se, Mo, and Ag. The framboidal pyrites (pyrite 1 and pyrite 2) show enrichment in the

Chapter 9: Discussion, genetic models and exploration implications

VAMSNZ (V, As, Mo, Se, Ni, Ag, Zn) trace element suite suggesting a syngenetic origin of gold. In addition, the framboidal pyrites (pyrite 1 and 2) have high Ag/Au ratio with elevated Zn, Pb and Ni. At Selinsing, pyrite 4 and pyrite 5 have high Ag/Au indicating a late diagenetic origin. Furthermore, pyrite 3 and pyrite 6 have a low Ag/Au <1 and high Co suggesting a metamorphic-hydrothermal origin. Overall, both the Tersang and Selinsing gold deposits record several episodes of high Au enrichment. At Tersang, the high Au event is associated with significant amounts of trace elements such as Co, Ni, Cu, Zn, Mo, As, Se, Sb and Tl. In comparison, at Selinsing, high Au occurrence is accompanied by trace elements including Co, Ni, Cu, Zn, Mo, As, Te, Sb, Tl, Bi, Ti and Pb.

9.2.5. Sulphur isotopes

The sulphur isotope data indicate that three possible sources of sulphur were involved during the formation of the Tersang, Selinsing and Penjom deposits. At Tersang, the $\delta^{34}\text{S}$ values (-8.3 – 2.5 ‰) combined with pyrite chemistry suggest derivation from a magmatic/metamorphic source. The hypothesis of a metamorphic source is consistent with the occurrence of metamorphic-hydrothermal pyrites (pyrites 1 and 2) and presence of CO₂-bearing fluid inclusions in ore zone at the Tersang gold deposit. These values are also comparable to the seawater sulphate curve indicating a possible additional source of sulphur from reduction of seawater sulphate. This interpretation cannot be ruled out.

Similarly, at the Selinsing deposit, the heavier $\delta^{34}\text{S}$ values (1.2 – 9.2 ‰) suggest that sulphur was likely derived from magmatic or a mixture of magmatic and

Chapter 9: Discussion, genetic models and exploration implications

metamorphic fluids. Additionally, these $\delta^{34}\text{S}$ values plotted against the seawater sulphate curve show a parallel pattern through geological times suggesting that additional sulphur was probably derived from reduction of seawater sulphate. At Penjom, the lighter $\delta^{34}\text{S}$ values (-8.4 – 4.0 ‰) indicate a biogenic source of the sulphur; however these $\delta^{34}\text{S}$ values may have derived from the reduction of seawater sulphate.

9.2.6. Pb isotopes

The Tersang pyrite isotope values are at 18.59 for $\text{Pb}^{206}/\text{Pb}^{204}$ and 15.75 for $\text{Pb}^{207}/\text{Pb}^{204}$. The Selinsing pyrite Pb isotope values range from 18.94 to 19.10 ($\text{Pb}^{206}/\text{Pb}^{204}$) and from 15.72 to 15.73 for $\text{Pb}^{207}/\text{Pb}^{204}$. The Penjom galena isotope values range from 18.54 to 18.57 ($\text{Pb}^{206}/\text{Pb}^{204}$) and remain at 15.70 ($\text{Pb}^{207}/\text{Pb}^{204}$). Overall, the Selinsing pyrite has higher radiogenic Pb isotope values compared to the Penjom galena and Tersang pyrites. This isotopic signature indicates that the Tersang pyrite and Penjom galena are less radiogenic than the Selinsing pyrite (Fig. 7.3). The Pb isotope data from the Tersang, Selinsing and Penjom gold deposits plots below the upper crust line suggesting that the lead was derived from the bulk crust probably related to subduction-related magmatism.

9.2.7. Fluid characteristics

At the Tersang gold deposit, heating experiments indicated that the homogenisation temperatures are between 210 and 348 °C for liquid-rich (Type I) inclusions in mineralised quartz veins. The salinities range from 2.41 to 8.95 wt % NaCl equiv. Additionally, most inclusions contain pure or nearly pure CO_2 (98.13-100 mol %),

Chapter 9: Discussion, genetic models and exploration implications

and one inclusion has a small amount of CH₄ (0-1.9 mol %). At Selinsing, the Type I inclusions in quartz veins yielded the homogenisation temperature range from 194 to 348 °C and salinities between 1.23 and 9.98 wt % NaCl equiv. In addition, most inclusions are CO₂-rich (100 mol %) and one inclusion was found containing CO₂ (95 mol %) and N₂ (5 mol %). At Penjom, heating and freezing results indicated that homogenisation temperatures are between 221 and 346 °C and the salinities range from 4.34 to 9.34 wt % NaCl equiv. Furthermore, the majority of fluid inclusions are CO₂-rich (100 mol %), whereas one fluid inclusion is N₂-rich (100 mol %).

9.3. Ore deposit models

Geological and geochemical characteristics of the Tersang, Selinsing, and Penjom gold deposits with other better known orogenic gold deposits are summarised in Tables 9.1 and 9.2.

9.3.1. Tersang deposit model

A simplified genetic model at Tersang is proposed based on field investigation combined with structural and geochemical data (Fig. 9.1). The absence of framboidal pyrites with VAMSNZ trace element suite points to a lack of pre-Au enrichment in diagenetic environment. Broken arsenopyrite grains which contain gold in its cracks may indicate that fluid have circulated through the fissures of arsenopyrite during brittle deformation and deposited gold. This fact may also point to an epigenetic origin of the gold at Tersang.

Chapter 9: Discussion, genetic models and exploration implications

Fluid inclusions studies showed the presence of CO₂-rich fluid (98 – 100 mol %) inclusions with minor proportions of CH₄ (2 mol %) implying involvement of metamorphic fluids acting as transport agents of metals. Furthermore, lead isotope composition suggests derivation from the lower crust.

Table 9.1: Comparison of the Tersang, Selinsing, and Penjom Au deposits, Central Malaysia.

Characteristics	Tersang gold deposit	Selinsing gold deposit	Penjom gold deposit
Host Rock Stratigraphy	Sandstone, breccia (Upper Triassic) (This study)	Siltstone, phyllite, black mudstone, argillite (Triassic) (This study)	Carbonaceous shale, tuffaceous conglomerate, tuffaceous siltstone, tuffaceous breccia (Permian) (This study)
Intrusions	Alkali rhyolite (Late Triassic) (This study)	Felsic dykes (Age unknown)	Rhyodacite, trachyte, trachyandesite (Age unknown)
Structural controls	Low angle, hybrid extensional faults (This study)	NNW-SSE and NS faults, thrust faults, listric normal faults (This study)	Thrust fault, high angle faults orientated WNW-ESE, NS, NE- SW faults (Heru et al., 2000 ; Flinder, 2003)
Gold - Ore minerals	Pyrite, arsenopyrite (Au inclusions), galena, sphalerite, geochronite, covellite (This study)	Free gold in veins, pyrite, arsenopyrite, galena, sphalerite, chalcopryrite, pyrrhotite (This study)	Pyrite, galena (Au inclusions), sphalerite, arsenopyrite, chalcopryrite (Kamar shah and Hewson, 2007)
Trace element associations	Au, As, Co, Ni, Pb, Cu, Sb, Tl ± Bi, Se, Ag, Te (This study)	Au, As, Co, Ni, W, U, Zn, Cu, Te, Mo ± Sb, Bi, Pb, TL (This study)	Au, Cu, As, Pb, Zn ± Te (Jasmi, 2007)
Sulphur isotope ($\delta^{34}\text{S}$: per mil)	-8.26 to 2.49 ‰ (This study)	1.18 – 9.22 ‰ (This study)	-8.43 to -3.99 ‰ (This study)
Fluid inclusions	210 – 290 °C 2 – 9 wt% NaCl. equiv. (This study)	190 – 340 °C 1 – 9 wt% NaCl. equiv. (This study)	250 – 300 °C 6 – 8 wt% NaCl. equiv. (This study)

Chapter 9: Discussion, genetic models and exploration implications

Table 9.2: Comparison of gold deposits in Central Malaysia with other better known deposits.

Characteristics	Bentong-Raub Suture Zone, gold deposits, Malaysia (This study)	Victoria gold deposits, Australia (Phillips and Hughes, 1998)	Southern China (Carlin-like) (Peters et al., 2007)	Nevada, USA (Carlin-type) (Hofstra and Cline, 2000; Emsbo et al., 2003)
Host Rock Stratigraphy	Sandstone, siltstone, phyllite, black mudstone and volcanics (Permian - Triassic)	Metasediments Flysch, mafic volcanics (Cambrian to Early Permian)	Mudstone, silty-carbonates, dolomite, siliciclastics (Ordovician-Triassic)	Siltstone, silty carbonates, dolomite, siliciclastics (Silurian – Devonian)
Intrusions	Alkali rhyolite (Late Triassic) Rhyodacite, trachyte, and trachyandesite (Age unknown)	Mafic diorite (Middle Devonian) Rare dolerite	Gabbro and diorite (Triassic)	Granite (Jurassic) Felsic dykes (Eocene)
Structural control	NS, NE-SW trending structures; pinch and swell quartz veins and felsic sill and dyke	Strike fault of moderate to steep dip near major reverse faults	High angle extensional Faults, low angle faults, unconformities	High angle extensional faults, low angle faults, bedding, fold noses/flanks
Gold-ore minerals	Pyrite, arsenopyrite, galena, sphalerite, geochronite. Free Au inclusions in pyrite.	Pyrite, arsenopyrite, galena, chalcopyrite, and pyrrhotite	Pyrite, arsenian-pyrite (Au on rims) arsenopyrite, stibnite, realgar orpiment, cinnabar	Pyrite, arsenian pyrite (Au on py rim), arsenopyrite, stibnite, realgar, orpiment, cinnabar
Trace element associations	Au, As, Co, Ni, Pb, Cu, Sb, Tl ± Bi, Se, Ag, Te	As, Sb, Cu, Pb, Zn, Bi, W, Mo, Te associated with granite occurrences	Au, As, Hg, Sb, Tl ± Ag, Cu, Pb, W, Mo, Ba (Zhang et al., 2005)	Au, As, Hg, Sb, Tl ± Ag, Zn, Pb, Cu (Hofstra and Cline, 2000)
Sulphur isotopes	- 8.43 – 9.22 ‰	0 – 2 ‰	-10 to +15 ‰ (Triassic) -30 to +12 ‰ (Permian) (Zhang et al., 2005)	+1 to +28 ‰ (Main-Au stage); -30 to -2 ‰ (Late-Au stage)
Fluid inclusions (Homogenisation temperature and salinities)	190 – 340 °C; 1 – 9 wt % NaCl equiv.	Approximately around 250 °C Low salinity: <5 wt % NaCl equiv.	165 - 290 °C Low salinity: <5 wt % NaCl equiv. (Liu et al., 1991; Zhang et al., 2005)	140 – 280 °C; 3 - 8 wt % NaCl. equiv. (Hofstra and Cline, 2000)

Chapter 9: Discussion, genetic models and exploration implications

The Tersang fluids show moderate temperature range (210 – 242 °C) with low salinities (2.41 - 9.21 wt % NaCl equiv). The salinity range up to 9.21 wt % NaCl equiv. suggests some magmatic input of fluids in the ore-forming system as was also supported by sulphur isotope data.

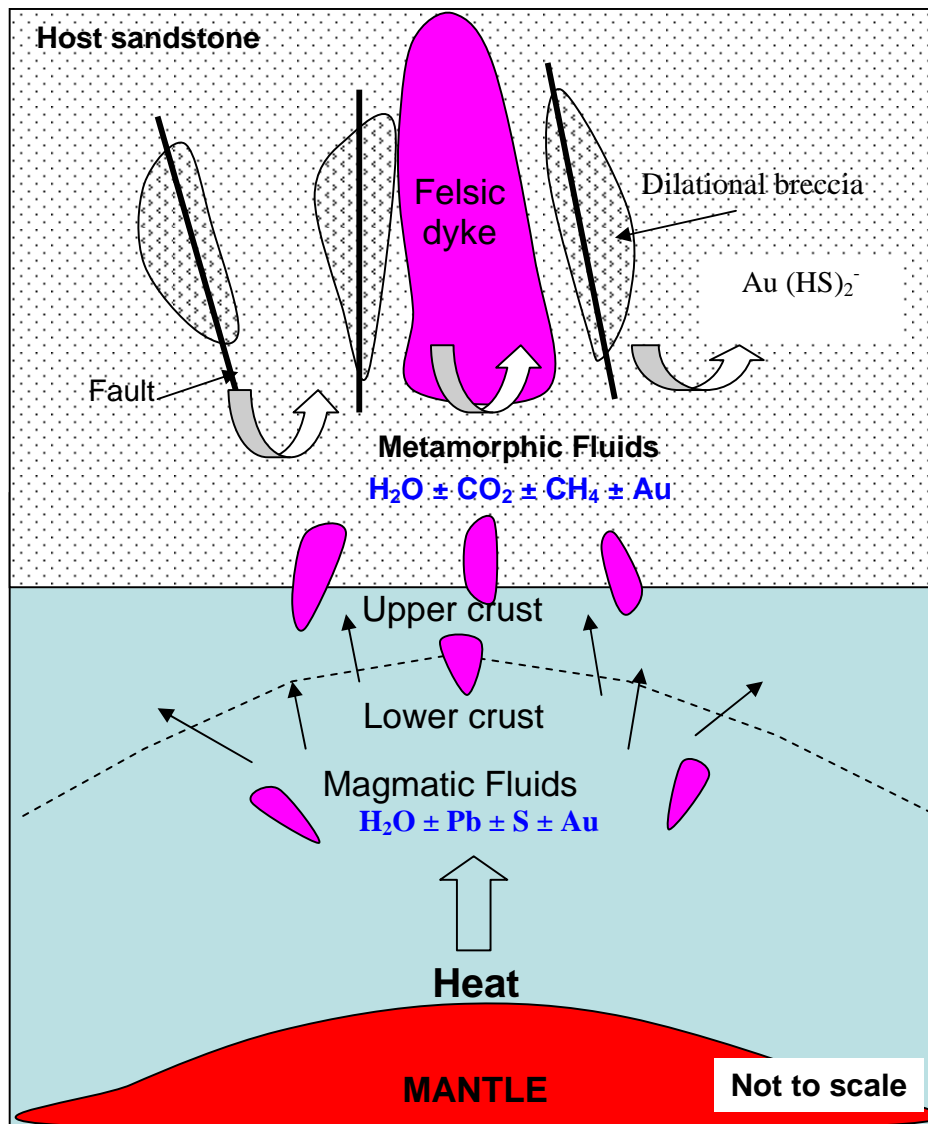


Fig. 9.1. Cartoon showing a simplified ore deposit model of the Tersang gold deposit, Malaysia.

Seward and Barnes (1997) reported that for the fluids at low salinities and moderate temperatures, gold is likely to be transported as bisulphide complex ($\text{Au}(\text{HS})_2$). This deposit model also takes into account the intensity of fracturing that affected the host sequence as evidenced by numerous sheeted quartz veins and breccia units at the mine-site. The ore fluids would have ascended and exploited these fracture system and deposited Au and other mineralising materials.

9.3.2. Selinsing deposit model

In this study, the author suggested a two-phase model for the formation of the gold deposit at Selinsing (Fig. 9.2). Phase 1 (Fig. 9.2A): Pyrite chemistry indicates early enrichment of Au and VAMSNZ (V, As, Mo, Se, Ni, Ag, and Zn) metals implying a syngenetic origin of the gold. The low level of gold (up to 0.5 ppm) in VAMSNZ sediments can be interpreted as a result of trace element leaching from diagenetic pyrites and precipitation in later pyrites. Phase 2 (Fig. 9.2B): Repetitive occurrences of mylonite and cataclasite units mixed with siltstone, phyllite and argillite in the ore zone suggest multiple phases of post-diagenetic deformation (D_1 , D_2 and D_3), which favored the development of several fluid pathways and remobilisation of Au.

During the three deformation phases at Selinsing, several enrichment of gold occurred due to fluid flow and circulation through faults during intense shearing and faulting suggesting that early structures have been overprinted by later structures. Laser Raman Spectrometry analysis revealed the presence of CO_2 -rich fluid (mol 95 – 100 %) inclusions with minor quantity of N_2 (mol 5 %) implying involvement of metamorphic fluids that served as carriers of metals.

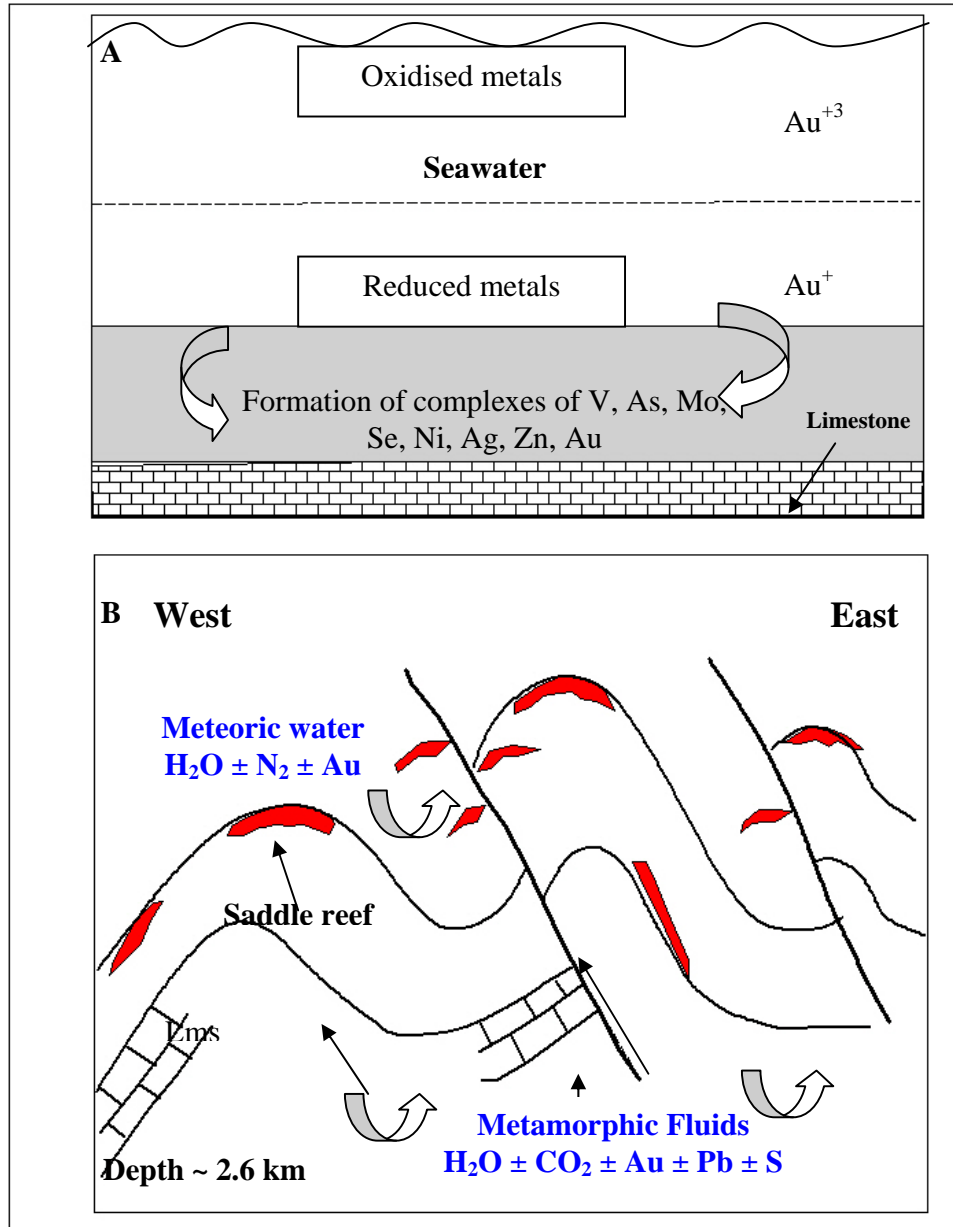


Fig. 9.2. A two-phase genetic model of the Selinsing gold deposit, Central Malaysia. **A.** Early enrichment in VAMSNZ (V, As, Mo, Se, Ni, Ag, Zn) metals in sediments suggesting a syngenetic origin of the gold. **B.** Remobilisation and redeposition of gold in structural traps with growth of metamorphic-hydrothermal pyrites containing invisible gold. Lms = limestone. Note occurrence of high grade quartz veins as extensional veins, pinch and swell veins (D_2 deformation), saddle reefs and or ribbons along bedding (D_3 deformation).

Chapter 9: Discussion, genetic models and exploration implications

According to Hofstra and Cline (2000) metamorphism produces ore fluids that transport metals. Fluid inclusions indicated homogenisation temperatures ranging from 200 to 347 °C with salinities between 1.23 and 9.98 wt % NaCl equiv. The heavier $\delta^{34}\text{S}$ values (1.2 – 9.2 ‰) suggest that sulphur was probably sourced from a mixture of magmatic and metamorphic fluids. The lower salinity (near 0 wt % NaCl equiv.) suggests the presence of meteoric water that probably leached early gold in diagenetic pyrites from black mudstones and released Au to metamorphic fluids. It is also argued that the shallow and deeply circulating meteoric water mostly removed and remobilised Au and other metals from the host sequences (Emsbo et al., 2003). As deformation evolved, fluids moved in the system remobilising and accumulating gold and other metals during the formation of saddle reefs in the shear zone (Large et al., 2011). The ore mineral assemblage, salinity and homogenisation temperature of the Selinsing deposit shows remarkable similarity to the Hodgkinson type deposit in Queensland, Australia (Peters et al. 1990).

9.3.3. Penjom deposit model

The Penjom deposit model is proposed based on geological and geochemical data gathered in this study and other previous authors (Fig. 9.3). At Penjom, shearing and faulting played an important role in the formation of the deposit. Gold mineralisation is associated with NS and NE trending shears (Jasmi, 2007). Kidd and Fauzi (2000) argued that the NS shear zones are probably the main weak zones at depth that facilitated the flow of ore fluids at Penjom. It is also reported that the Penjom thrust dips to the east and cut by sub-vertical NS trending faults (Teh et al., 2001).

Gold mineralisation occurs within quartz-ankerite stockwork in the felsic intrusion. Sulphur isotope gave values range from -4.0 to -8.4 per mil suggesting a

Chapter 9: Discussion, genetic models and exploration implications

biogenic source of the sulphur. The presence of felsic sills and dykes in the host stratigraphy indicates the possibility of a magmatic input of sulphur in the Penjom gold system. The alteration minerals in the felsic intrusion include sericite, carbonates and chlorite suggesting circulation of hydrothermal fluids that triggered chemical changes in the host rocks. It has been found a graphitic blanket above the Penjom thrust suggesting involvement of metamorphic fluids (Jasmi, 2007). The graphitic cover probably played a role of a seal rock that favored the trapping and deposition of Au and other metals. Fluid inclusion studies indicate homogenisation temperatures from 250 to 300°C and low salinity (4.30 to 8.68 wt % NaCl equiv).

Laser Raman analysis revealed that most fluid inclusions are CO₂-rich (100 mole %) and one inclusion was found N₂-rich (100 mole %). These evidences further indicate that metamorphic fluids were involved in the deposition of Au at Penjom. The presence of carbonaceous shales suggests that hydrothermal fluids and organic matter in the shales reacted and produced CO₂-rich fluids as evidenced by Laser Raman Spectrometry that mixed with gold-bearing fluids to precipitate gold by reduction of gold bisulfide complex (Cox et al., 1991).

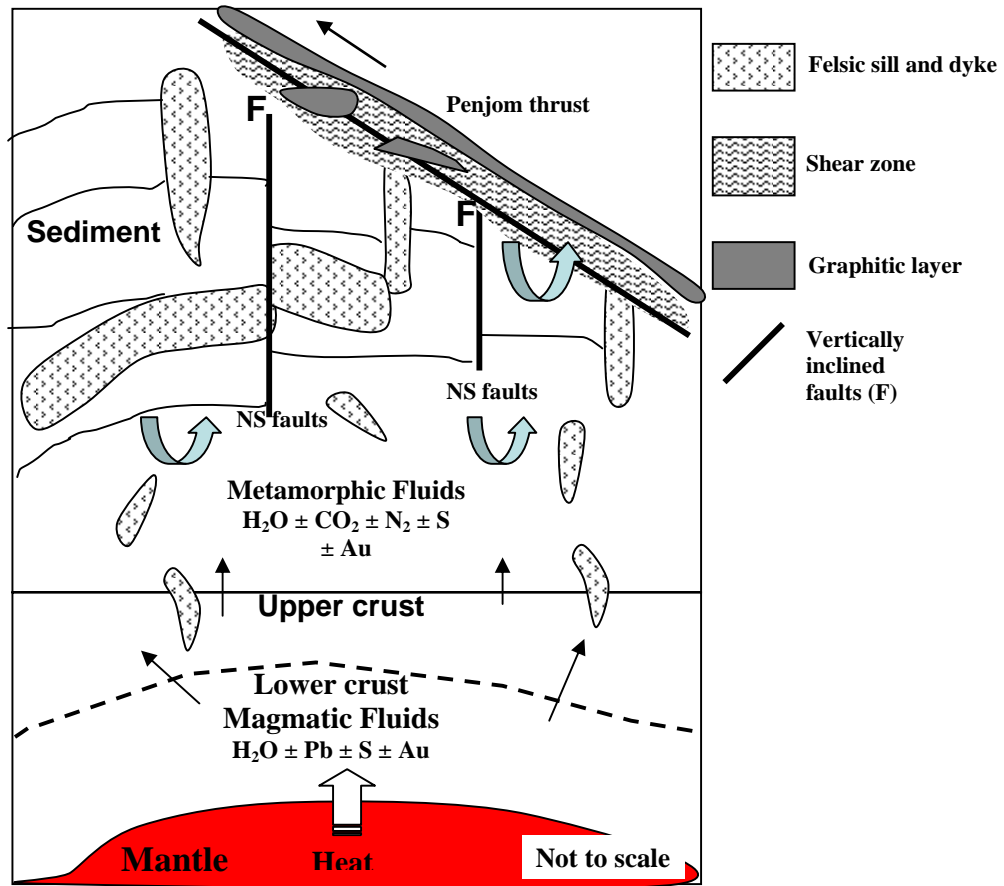


Fig. 9.3. Deposit model of the Penjom gold deposit, Central Malaysia.

9.4. Exploration implications

Pyrite chemistry, alteration, Pb isotopes and structural data at the Tersang, Selinsing and Penjom gold deposits provide exploration tools in discovering new potentially economic gold deposits along the Bentong-Raub Suture Zone, Central Malaysia.

Chapter 9: Discussion, genetic models and exploration implications

1. In the Tersang area, elements such as As, Sb, Pb, Ag, Co, Ni, Tl, Te and Se occurring together with Au can be used as vectoring tools in exploration. Much attention should be paid in areas where sericitic alteration is ubiquitous.
2. In the Selinsing area, elements such as V, As, Mo, Se, Ni, Ag, Zn, Co, Ni, U, Bi, and Pb which are accompanied with elevated Au contents may be utilized as pathfinders in searching for gold.
3. At Selinsing, another criterion is quartz-ankerite alteration which is the most common alteration assemblage that is proximal to high-grade ore zones.
4. In the Penjom area, gold is mostly found associated with trace elements such as Cu, As, Pb, Zn, and Te (Kamar Shah Ariffin, 1994). In addition, exploration should also target zones of alteration types such as silicification, argillic alteration (illite), chloritisation, and carbonate (ankerite).
5. Most potentially economic goldfields along the Bentong-Raub Suture Zone are those with pyrite and galena Pb isotope values that range from 18.54 to 19.10 ($\text{Pb}^{206}/\text{Pb}^{204}$) and from 15.70 to 15.73 ($\text{Pb}^{207}/\text{Pb}^{204}$). These Pb isotope compositions can be used to discriminate other ore deposit types in Malaysia, as well as in SE Asia region.
6. Shear zones that show the presence of mylonite, cataclasite and felsic intrusives should be given more attention to narrow down mineralised haloes and zones.

REFERENCES

- Alexander, J.B., 1959, The Geology and mineral resources of Bentong, Pahang and adjoining portions of Selangor and Negeri Sembilan, Geological Society of Malaysia, Memoir 8, 250p.
- Ault, W.V., and Kulp, J.L., 1960, Sulphur isotopes and ore deposits: Economic Geology, v. 55, pp. 73 -100.
- Bahna, B., and Chovan, M., 1999, Morphology and chemical composition of gold from Pukanec. Mineralia Slov, 31, pp. 259 -262.
- Baker, J., Peate, D., Waight, T., and Meyzen, C., 2004, Pb isotopic analysis of standards and samples using a $\text{Pb}^{207}/\text{Pb}^{204}$ double spike and thallium to correct for mass bias with a double-focusing MC-ICP-MS. Chemical Geology, 211, pp. 275 - 303.
- Barber, A.J., Crow, M.J., 2003, Evaluation of plate tectonic models for the development of Sumatra, Gondwana Research, 20, pp. 1 - 28.
- Barber, A.J., Crow, M.J., 2007, The structure of Sumatra and its implications for the tectonics assembly of Southeast Asia and the destruction of Palaeotethys, Southeast Asia Research Group, pp. 1 - 35.
- Barber, A.J., Crow, M.J., and Milsom, J.S. (Eds.), 2005, Sumatra: Geology, Resources and Tectonics. Geological Society, London, Memoir 31, 289p.
- Bignell, J.D., and Snelling, N.J., 1977, K-Ar ages on some basic igneous rocks from Peninsular Malaysia and Thailand, Bulletin of the Geological Society of Malaysia, v. 8, pp. 89 - 93.
- Black, L.P., and Gulson B.L., 1978, The age of the Mud tank Carbonatite, Strangways Range, Northern Territory. BMR Journal of Australian Geology and Geophysics 3, pp. 227 - 232.
- Black, L.P., Kamos, L., Allen., C.M., Aleinikoff, J.N., Davis, D.W., Korsch, R.J., Foudoulis, C., 2003, TEMORA 1: a new zircon standard for Phanerozoic U–Pb geochronology. Chemical Geology 200, pp. 155 – 170.
- Black, L.P., Kamo, S.L., Allen, C.M., Davis, D.W., Aleninikoff, J.N., Valley, J.W., Mundil, R., Campbell, I. H., Korsch, R. J., Williams, I. S., and Foudoulis, C., 2004, Improved $^{206}\text{Pb}/^{238}\text{U}$ microprobe geochronology by the monitoring of a trace-element related matrix effect; SHRIMP, ID-TIMS, ELA-ICP-MS, and oxygen isotope documentation for a series of zircon standards. Chemical Geology 205, pp. 115 -140.

- Bodnar, R.J., 1983, A method of calculating fluid inclusion volumes based on vapour bubble diameters and P-V-T-X properties of inclusion fluids. *Economic Geology*, 78, pp. 535 - 542.
- Bowman, J.R., 1998, Stable-isotope systematics of skarns, in Lentz, D. R (Eds), *Mineralised intrusion-related skarn systems: Mineralogical Association of Canada Short Course Series*, v. 26, pp. 359 - 414.
- Carr, G.R., Dean, J.A., Suppel, D.W., and Heithersay, P.S., 1995, Precise lead isotope fingerprinting of hydrothermal activity associated with Ordovician to Carboniferous metallogenetic events in the Lachlan Foldbelt of New South Wales: *Economic Geology*, v. 90, pp. 1467-1505.
- Carter, A., Roques, D., Bristow, C., and Kinny, P., 2001, Understanding Mesozoic accretion in Southeast Asia: significance of Triassic thermotectonism (Indosinian orogeny) in Vietnam: *Geology*, v. 29, pp. 211 - 214.
- Curry, J.R., 2005, Tectonics and history of the Andaman Sea region: *Journal of Asian Earth Sciences*, 25, pp. 187 - 232.
- Chang, Z., Large R.R. and Maslennikov V., 2000, Sulphur isotope in sediment-hosted orogenic gold deposits: Evidence for an early timing and a seawater sulphur source. *Geology*, v. 36, pp. 971 - 974.
- Chung, S.C., (Ed), 1982, Regional geology of Peninsular Malaysia, Annual report. Geological Society of Malaysia, pp. 72 - 79.
- Cook, D.R., and Simmons, S.F., 2000, Characteristics and genesis of epithermal gold deposits: *Reviews in Economic Geology*, v. 13, pp. 221 - 244.
- Colvine, A.C., 1989, An empirical model for the formation of Archean gold deposit-products of final cratonisation of the Superior province, Canada: *Economic Geology Monograph* 6, pp. 37 - 53.
- Cox, S.F., Wall, V.J., Etheridge, M.A., and Potter, T.F., 1991, Deformational and metamorphic processes in the formation of mesothermal vein hosted gold deposits—examples from the Lachlan Fold Belt in central Victoria, Australia: *Ore Geology Reviews*, v. 6, pp. 391 - 423.
- Cromie, P.W., 2010, Geological setting, geochemistry and genesis of the Sepon gold and copper deposits, Laos, Ph.D thesis University of Tasmania, 395p.

- Danyushevsky, L.V., Robinson, P., Gilbert, S., Norman, M., Large, R.R., McGoldrick, P., and Shelley, J. M. G., 2011, Routine quantitative multi-element analysis of sulphide minerals by laser ablation ICP-MS: Standard development and consideration of matrix effects. *Geochemistry: Exploration, Environment, Analysis*, 11, pp. 51 - 60.
- Emsbo, P., Hofstra, A.H., Lauha, E.A., Griffin, G.L., and Hutchinson, R.W., 2003, Origin of high-grade gold ore, source of ore fluid components, and genesis of the Meikle and neighboring carlin-type deposits, northern carlin Trend, Nevada: *Economic Geology*, v. 98, pp. 1069 - 1105.
- Flindell, P., 2003. Avocet Mining – Exploration and Development across Central and Southeast Asia. Australian Institute of Geoscientists (AIG), Mineral Exploration Discussion Group (SMEDG). 10 October, Sydney, 8p.
- Gobbett, D.J. and Hutchison, C.S. (Eds) 1973. *Geology of the Malay Peninsula: West Malaysia and Singapore*. New York: Wiley – Interscience, 438p.
- Goldstein, R., 2003, Petrographic analysis of fluid inclusions. In: Samson, A. I., Anderson, and Marshall, D (Eds). *Fluid inclusions: Analysis and interpretation*. Mineral. Assoc. Can., Short Course Ser. 32, pp. 9 - 53.
- Goldfarb, R.J., Baker, T., Dube, B., Groves, D.I., Hart, C.J.R., and Gosselin, P., 2005, Distribution, character and genesis of gold deposits in metamorphic terranes: *Economic Geology 100th Anniversary Volume*, pp. 407 - 450.
- Goldfarb, R.J., Miller, L.D., Leach, D.L., and Snee, L.W., 1997, Gold deposits in metamorphic rocks of Alaska: *Economic Geology Monograph* 9, pp. 151 - 190.
- Gulson, B.L., 1986, Lead isotopes in mineral exploration: Development in *Economic Geology*, v. 23, pp. 1 - 245.
- Gunn, A.G., Halim Hamzah, AB., Sinjeng, P.P., Wan Zawawie, W.A., Dzazali, A, and Chow, C., 1993, Gold mineralisation at Penjom, Kuala Lipis, Pahang, Malaysia. Geological Survey of Malaysia – British Geological Survey, Report 93/1, 78p.
- Groves, D.I., Goldfarb, R.J., Gebre-Mariam, M., Hagemann, S.G., and Robert, F., 1998, Orogenetic gold deposits: A proposed classification in the context of their crustal distribution and relationship to other gold deposit types: *Ore Geology Reviews*, v. 13, pp. 7 - 27.
- Groves, D.I., Goldfarb, R.J., Robert, F., and Hart, C.J.R., 2003, Gold deposits in metamorphic belts: overview of current understanding, outstanding problems, future research, and significance: *Economic Geology*, v. 98, pp. 1 - 29.

- Heru, S.G., Wan Fuad, W.H., and Ibrahim, A., 2000, Palaeostress influence in controlling the gold mineralisation in Penjom area, Peninsular Malaysia, *Geoscience Journal*, 4, pp. 85-90.
- Hirsch, F., Ishida, K., Kozai, T., Meesook, A., 2006, The welding of Shan-Thai. *Geosci. J.* 10, pp. 195–204.
- Hofstra, A.H., and Cline, J.S., 2000, Characteristics and models for Carlin-type deposits: *Reviews in Economic Geology*, v. 13, pp. 162-221.
- Hutchison, C.S., 1994, Gondwana and Cathaysian blocks, Palaeotethys sutures and Cenozoic tectonics in Southeast Asia. *Geologische Rundschau* 82, pp. 388 - 405.
- Hutchinson, R.W., 1993, A multi-stage, multi-process genetic hypothesis for greenstone-hosted gold lodes: *Ore Geology Review*, v. 8, pp. 349 - 382.
- Huston, D.L., Bottrill, R.S., Creelman, R.A., Khin Zaw., Ramsden, T.R., Rand., S.W., Gemmel, J.B., Jablonski, W., Sie, S.H., Large, R.R., 1992, Geologic and geochemical controls on the mineralogy and grain size of gold-bearing phases, Eastern Australian volcanic-hosted massive sulphides deposits, v. 87, pp. 542-563.
- Huston, D.L., Power, M., Gemmel, J.B., and Large, R.R., 1995, Design, calibration and geological application of the first operational Australian laser ablation sulphur isotope microprobe: *Australian Journal of Earth Sciences*, v. 42, pp. 549 - 555.
- Jaafar, B.A., 1976, Geology and mineral resources of the Karak and Temerloh areas, Pahang, *Geological Society of Malaysia, Memoir* 15, 138p.
- Jackson, S.E., Pearson, N.J., Griffin, W.L., Belousova, E.A., 2004, The application of laser ablation-inductively coupled plasma-mass spectrometry to in situ U–Pb zircon geochronology: *Chemical Geology* 211, pp. 47 - 69.
- Jasmi Hafiz, B.A.A., 2007, Geochemistry and EPMA characterisation of Gold in the Central Belt Area, Peninsular Malaysia, *MSc Thesis University of Malaya*, 183p.
- Kamar Shah, A. and Hewson, J.N., 2007, Gold-related sulfide mineralisation and ore genesis of the Penjom gold deposit, Pahang, Malaysia, v. 57, No. 2, *The Society of Resource Geology*, pp. 149 - 169.
- Kamar Shah, A., 2007, Low grade mesothermal gold deposit, characteristics of the Penjom gold deposit, Kuala Lipis, Pahang, Malaysia: *Warta Geologi*, v. 33, No. 3, pp. 102 - 110.

- Kerrick, R., and Fryer, B.J., 1979, Archean precious metals hydrothermal systems, Dome mine, Abitibi greenstone belt: Pt. II. REE and oxygen isotope relations: Canada Journal of Earth Sciences, v. 16, pp. 440 - 458.
- Kerrick, R., Goldfarb, R., Groves, D.L., and Gravin, S.L., 2000, The geodynamics of World-class gold deposits: characteristics, space-time distribution and origins: Reviews in Economic Geology, v. 13, pp. 501-551.
- Kidd, R.P., and Fauzi Zainuddin, 2000, Geology of the Penjom gold deposit, Pahang, Malaysia. Conference Proceeding Asia Pacific Mining and Quarrying 2000. The 6th International Mining and Mineral Conference 2000, 16-18 November 2000.
- Khin Zaw, 1991, The effect of Devonian metamorphism and metasomatism on the mineralogy and geochemistry of the Cambrian VHMS deposits in the Rosebery-Hercules district, western Tasmania: Unpub. Ph.D. thesis, Univ. Tasmania, 302 p.
- Khin Zaw, Cooke, D.R, and Kamenatsky, D., 1999, Fluid and melt inclusions. In Exploration geochemistry and hydrothermal geochemistry, Master of Economic geology Course Work Manual 12: Centre for Ore Deposit Research, University of Tasmania, pp. D1-D120.
- Khin Zaw, Meffre, S., and Khositantont, S., 2008, Sulphur Isotope at Penjom gold deposit. Ore Deposit of SE Asia. Annual Progress Report, No. 4, pp. 4 - 5.
- Khin Zaw, Meffre, S., and higher degree students., 2010, Final report "Ore deposit of Southeast Asia" Project, ARC Centre of Excellence in Ore Deposits, University of Tasmania.
- Kobayashi, T., and Tamura, M., 1968, Myophoria in Malaya with a note on the Triassic Trigonicea. In: Kobayashi, T and Toriyama, R (Eds), Geology and palaeontology of Southeast Asia, v. 5, Tokyo: University of Tokyo Press, pp. 88 - 137.
- Kosler, J., 2001, Laser-ablation ICPMS study of metamorphic minerals and processes. In: Sylvester, P. J. (Ed). Laser-ablation-ICPMS in the earth sciences; principles and applications: Mineralogical Association of Canada Short Course Handbook 29, pp. 185 - 202.
- Large, R.R., Maslennikov, V., Robert, F., Danyushevsky, L.V., Scott, R.J., and Chang, Z., 2007, Multi-stage sedimentary and metamorphic origin of pyrite and gold in the giant Sukhoi Log deposit, Lena Goldfield, Russia: Economic Geology and the Bulletin of the Society of Economic Geologists, v. 102, pp. 1,233 - 1,267.

- Large, R.R., Danyushevsky, L., Hollit, C., Maslennikov, V., Meffre, S., Gilbert, S., Bull, S., Bull, S., Scott, R., Embsbo, P., Thomas, H., Singh, B., and Foster, J., 2009, Gold and Trace element zonation in pyrite using a laser imaging technique: Implications for the timing of gold in orogenic and Carlin-style sediment-hosted deposits: *Economic Geology*, v. 104, pp. 635 - 668.
- Large, R.R., Bull, S.W., Scott, R and Meffre, S., 2010, Stratiform organic-rich V-As-Mo-Se-Ni-Ag-Zn-Au horizons in the Popovich and Roberts Mountain Formations, Carlin district, Nevada (abs): Geological Society of Nevada, 2010 Symposium , Reno, program with Abstract, pp. 59 - 60.
- Large, R.R., Bull, S.W., Maslennikov, V.V., 2011, A carbonaceous sedimentary source-rock model for Carlin-type and orogenic gold deposits: *Society of Economic Geologists*, v. 106, pp. 331 - 358.
- Leman, M.S., 1994, The significance of Upper Permian Brachiopods from Merapoh area, northwest Pahang. *Geological Society of Malaysia. Bulletin* 35, pp.113 -121.
- Liew, T.C., McCulloch, M.T., 1985, Genesis of granitoid batholiths of Peninsular Malaysia and implications for models of crustal evolution: Evidence from a Nd-Sr isotopic zircon study. *Geochimica et Cosmochimica Acta*, 49, pp. 587-600.
- Liu, D.S., Tan, Y.J., Wang, J., and Lui, L.L., 1991, Carlin-type gold deposits in China. In Laderia, E. A (Eds): *Brazil Gold '91*, pp. 89 - 93.
- Makoundi, C., 2004, Facies analysis of the Triassic Jelai Formation in the Central Basin of Peninsular Malaysia: Implications on Paleogeography and Tectonics. M.Sc Thesis, University of Malaya, 140p.
- Mann, S., Sparks, N.H.C., Frankel, R.B., Bazylnski, D.A., and Jannasch, H.W., 1990, Biomineralisation of ferromagnetic greigite (Fe_3S_4) and iron pyrite (FeS_2) in a magnetotactic bacterium: *Nature*, v. 343, pp. 258 - 242.
- Meffre, S., Large, R.R., Scott, R., Woodhead, J., Chang, Z., Gilbert, S.E., Danyushevsky, L. V., Maslennikov, V., and Hergt, J., 2008, Age and pyrite Pb-isotopic composition of the giant Sukhoi Log sediment-hosted gold deposit, Russia: *Geochimica et Cosmochimica Acta*, v. 72, pp. 2,377 – 2,391.
- Mernargh, T.P., Bastrakov, E.N., Khin Zaw, Wygralak, A.S., and Wyborn, L.A.I., 2007, Comparison of fluid inclusion data and mineralisation processes for Australian orogenic gold and intrusion-related gold systems: *Acta Petrologica Sinica*, v. 23, pp. 21 - 32.

- Metcalf, I., 1996, Pre-Cretaceous evolution of SE Asian terranes. *Tectonic Evolution of Southeast Asia*, Hall, R., Blundell, D (Eds.). Geological Society of London, Special Publication 106, pp. 97–122.
- Metcalf, I., 1988, Origin and Assembly of Southeast Asian Continental Terranes. In: Audley-Charles, M.G & A. Hallam (Eds). *Gondwana and Tethys*. Geological Society Special Publication, London, 37, pp.79-100.
- Metcalf, I., 2000, The Bentong-Raub Suture Zone. *Journal of Asian Earth Sciences*, 18, Barber, A.J (Ed). Maxwell Pergamon Macmillan plc, pp.691-712.
- Metcalf, I., 2002, Permian Tectonic Framework and Paleogeography of SE Asia: *Journal of Asian Earth Science*, 20, pp.551-566.
- Metcalf, I., 2005, Asia: South-East. In: Selley, R.C., Cocks, L.R.M., and Plimer, I.R., (Eds) *Encyclopedia of Geology*, Elsevier, pp. 169 - 196.
- Mustaffa, K., and Abdul Hadi Abdul Rahman, 1999, A five fold stratigraphic and tectonic subdivision of Peninsular Malaysia. In: *Dynamic stratigraphy and tectonics of Peninsular Malaysia – Problems and Issues*. Geological Society of Malaysia (1999), a thematic publication, pp. 38 - 63.
- Mitchell, A.H.G., 1981, Phanerozoic plate boundaries in mainland SE Asia, the Hymalayas and Tibet: *Journal of the Geological Society of London* 138, pp. 109 - 122.
- Ohmoto, H., and Rye, R.O., 1979, Isotopes of sulphur and carbon. In: Barnes H.L. (Ed) *Geochemistry of hydrothermal ore deposits*. Wiley, New York, pp. 509-567.
- Ohmoto, H., 1986, Stable isotope geochemistry of ore deposits: *Reviews in Mineralogy*, v. 16, pp. 491 - 559.
- Oliver, G., Khin Zaw, Hoston, M., 2011, Dating rocks in Singapore: Plate tectonics between 280 and 200 million years ago, *National University of Singapore, The Singapore Magazine of Research*, v. 10, No. 2, pp. 23-25.
- Paton, C., Woodhead, J.D., Hellstrom, J.C., Hergt, J.M., Greig, A., and Maas, R., 2010, Improved laser ablation U-Pb zircon geochronology through robust down-hole fractionation correction. *Geochemistry, Geophysics, Geosystems* 11, pp.1,525 – 2,027.
- Pearce, J.A., 1996, A user's guide to basalt discrimination diagrams, in Wyman, D.A (Ed), *Trace element geochemistry of volcanic rocks: Applications for massive sulphide exploration*, Geological Association of Canada Short Course Notes, v.12, pp. 79 -113.

- Perring, C.S., Groves, D.I., and Ho, S.E., 1987, Constraints on the source of auriferous fluids for Archean gold deposits: Geology Department and Extension Service, University of Western Australia Publication 11, pp. 287 -306.
- Peters, S.G., Golding, S.D., and Dowling Kim, 1990, Melange and sediment-hosted gold-bearing quartz veins, Hodgkinson gold field, Queensland, Australia. *Economic Geology*, 85: 312-327
- Peters, S.G., Huang Jianzhau, Li Zhiping, and Jing Chenggui, 2007, Sedimentary rock-hosted Au deposits of the Dian-Qian-Gui area, Guizhou, and Yunnan Provinces and Guangxi district, China. In: Khin Zaw, Peters, S. G., Cook, N. G., Zengqian Hou (Eds), *Ore Geology Reviews, Journal for Comprehensive Studies of Ore Genesis and Ore Exploration*, v. 31, Elsevier, pp. 170 -204.
- Phillips, G. N., Groves, D.I., and Brown, I.J., 1987, Source requirements for the Golden Mile, Kalgoorlie: Significance to the metamorphic replacement model for Archean gold deposits: *Canadian Journal of Earth Sciences*, v. 24, pp. 1,643-1,651.
- Phillips, G.N., and Hughes, M.J., 1998, Victorian gold deposits, *AGSO Journal of Australian Geology and Geophysics*, v. 17, No. 4, pp. 213-216.
- Proctor, W.D., 1972, Geology and Mineral Resources Benta area, Pahang. *Geological Survey of Malaysia. Map Bulletin 4*, 25p.
- Reich, M., Kesler, S.E., Utsunomiya, S., Palenik, C.S., Chryssoulis, S.L., and Ewing, R., 2005, Solubility of gold in arsenian pyrite: *Geochemica et Cosmochimica Acta*, v. 69, pp. 2,781-2,796.
- Richardson, J.A., 1939, The Geology and mineral resources of the neighbourhood of Raub, Pahang with an account of the Geology of the Raub Australian Gold Mine. *Geological Survey of Malaysia, Kuala Lumpur*, 3, 166p.
- Richardson, J.A., 1949, The Geology and mineral resources of the neighbourhood of Chegar Perah and Merapoh, Pahang. *Geological Survey Department, Federation of Malaya, Memoir No. 4*, 162p.
- Ridley, J.R., and Diamond, L.W., 2000, Fluid chemistry of orogenic lode gold deposits and implications for genetic models, in Hagemann, S. E and Brown, P. E (Eds), *Gold in 2000, Reviews in Economic Geology*, v. 13, pp. 141-162.
- Robinson, B.W., and Kusakabe, M., 1975, Quantitative preparation of SO₂ for ³⁴S/³²S analyses from sulphides by combustion: *Analytical Chemistry*, v. 47, pp. 1,179-1,181.

- Rocky, R., 1980, Stratigraphy and palaeontology of the Temerloh Mentakab-Kerdau area, Central Pahang, West Malaysia: BSc thesis, University of Malaya, 40p.
- Roedder, E., 1984, Fluid inclusions. Mineralogical Society of America, Rev. Mineralogy, 644p.
- Rollinson, H.R., 1996, Using geochemical data: evaluation, presentation, interpretation, Longman, Singapore, pp. 1 – 314.
- Rye, R. O., and Ohmoto, H., 1974, Sulphur and carbon isotopes and ore genesis: A review: Economic Geology, v. 69, pp. 826 - 842.
- Sangster, A.L., 1992, Light stable isotope evidence for a metamorphogenic orogen for bedding-parallel, gold-bearing veins in Cambrian flysch, Meguma Group, Nova Scotia: Exploration and Mining Geology, v. 1, pp. 69 - 79.
- Schwartz, M.O., Rajah, S.S., Askury, A.K., Putthapiban, P., and Djaswadi, S., 1995, The Southeast Asian Tin Belt: Earth Science Review, v. 38, issue 2-4, pp. 95 -293. Elsevier Science.
- Sevastjanova, I., Clements, B., Hall, R., Belousova, E. A., William, L. G., and Pearson, N., 2010, Granitic magmatism, basement ages, and provenance indicators in the Malay Peninsula: Insights from detrital zircon U-Pb and Hf-isotope data, Gondwana Research (2010), doi: 10.1016/j.gr.2010.10.010.
- Scrivenor, J.B., 1928, The Geology of Malayan Ore Deposits. Macmillan, London, 216p.
- Sengor, A.M.C., 1984, The Cimmeride Orogenic System and the tectonics of Eurasia. The Geological Society of American, special paper 195, 82p.
- Seward, T.M., and Barnes, H.L., 1997, Metal transport by hydrothermal ore fluids, in Barnes, H. L (Ed), Geochemistry of hydrothermal ore deposits, 3th ed.: New York, John Wiley & Sons, pp. 435 - 486.
- Shepherd, T.J., Rankin, A.H., and Alderton, D.H.M., 1985, A practical guide to fluid inclusion studies, Blackie, Glasgow, 235p.
- Stacey, J.S., and Kramer, J.D., 1975, Approximation of terrestrial lead isotope evolution by a two-stage model: Earth and Planetary Science Letters, v. 26, pp. 207 - 221.
- Stauffer, P.H., and Lee, C.P., 1986, Late Palaeozoic glacial marine facies in Southeast Asia and its implications. In: Proceedings of GEOSEA V, Bulletin of the Geological Society of Malaysia, No. 20, pp. 363 - 397.

- Stephenson, B., Ghazali, S.A and Widjaya, H., 1982, Regional geochemical Atlas Series of Indonesia: 1. Northern Sumatra. Institute of Geological Sciences, Keyword; Directorate of Mineral Resources, Bandung.
- Tan, B.K., 1984. The Tectonic framework and evaluation of the Central Belt and its margin, Peninsular Malaysia. Geological Society of Malaysia. Bulletin 17, pp. 307 - 322.
- Sonny Lim Teng Chye, Sharafuddin, M., Sulaiman, M., Teh, G.H., and Jasmi Hafiz Abdul Aziz., 2007. In: Teh, G. H., Mohd Shafeea Leman., and Ng, T. F (Eds), Geology, structure, mineralisation and geochemistry of the Penjom gold deposit, Penjom, Pahang, Geological Society of Malaysia, Annual Geological Conference 2001, Pangkor Island, Malaysia, pp. 59 - 63.
- Thomas, H.V., Large, R.R., Bull, S.W., Maslennikov, V., Berry, R.F., Fraser, R., and Froud, S., Moye, R., 2011, Pyrite and pyrrhotite textures and composition in sediments, laminated quartz veins and reefs, at Bendigo Gold Mine, Australia; Insights for ore genesis: Economic Geology, v. 106, pp. 1 - 31.
- Tjia, H.D., 1987, Complex deformations and probable fold nappe in Upper Silurian metasediments near Kuala Sawah, Negeri Sembilan: Sains Malaysiana 16 (1): pp. 33 - 47.
- Todheide, K., and Franck, E.U, 1963, Das Zweiphasengebiet und die kritische Kurve im System Kohlendioxid-Wasser bis zu Drucken von 3500 bar. Zeitschrift fur Physikalische Chemie Neue Folge 37, pp. 387 - 401.
- Wakita, K., and Metcalfe, I., 2005, Ocean plate stratigraphy in East and Southeast Asia: Journal of Asian Earth Sciences, v. 24, pp. 679 - 702.
- Wan Fuad, W.H., and Heru Sigit, P., 2001, Possible source rocks of gold mineralisation in Peninsular Malaysia, Proceedings, IAGI GEOSEA Annual Convention, 10-12 September, Yogyakarta, Indonesia.
- Wan Fuad, W.H., and Heru Sigit, P., 2002, Type deposits of Primary Gold Mineralisation in the Central Belt, Peninsular Malaysia. Buletin Persatuan Geologi Malaysia, 45, pp. 111 - 116.
- Wiedenbeck, M., Alle, P., Corfu, F., Griffin, W.L., Meier, M., Oberli, F., Vonquadt, A., Roddick, J.C., and Spiegel, W., 1995, 3 Natural Zircon Standards for U-Th-Pb, Lu-Hf, Trace-Element and REE Analyses. Geostandards Newsletter 19, pp. 1 - 23.

- Wilson, A.J., Cooke, D.R., Harper, B.J., and Deyell, C.L., 2007, Sulphur isotope zonation in the Cardia District, south-eastern Australia: exploration significance and implications for the genesis of alkalic porphyry gold-copper deposits: *Mineralium Deposita*, v. 42, pp. 465 - 487.
- Winchester, J.A., and Floyd, P.A., 1977, Geochemical discrimination of different magma series and their differentiation products using immobile elements: *Chemical Geology*, v. 20, pp. 325 - 343.
- Yeap, E.B., 1993, Tin and gold mineralization in Peninsular Malaysia and their relationships to the tectonic development: *Journal of Southeast Asian Earth Sciences*, v. 8, pp. 329 - 348.
- Zatman, R.E., and Doe, B.R., 1981, Plumbotectonics – the model: *Tectonophysics*, v. 75, pp. 135 - 162.
- Zatman, R.E., and Stacey, J.S., 1971, Lead isotope and mineralisation ages in belt supergroup rocks, Northwestern Montana and Northern Idaho, v. 66, pp. 849 - 860.
- Zhang, X.C., Hofstra, A.H., Hu, R.Z., Emsbo, P., Su, W.C., and Ridley, W.L., 2005, Geochemistry and delta 34 S of ores and ore stage iron sulphides in Carlin-type gold deposits, Dian-Qian-Gui area, China: Implications for ore genesis., In: Mao, J.W., and Bierlein, F.P (Eds), 8th Biennial SGA Meeting, Mineral deposit research: meeting the global challenge: Beijing, P.R. China, Springer, pp. 1107 - 1110.

Appendix D
Statistical analysis of gold in pyrite
and silicates

Statistical analysis of gold in pyrite and silicate

Deposit	Count numeric	Au_ppm	Average ppm	Sum ppm for all pixel gold (%)	Percentage
	all	77572 Mean : [Visible]	1.18	91787	100%
Tersang	Count Numeric : Gold in inclusions	14 Mean : Gold in inclusions	8.77	123	0.1%
Tersang	Count Numeric : silicate	36774 Mean : silicate	0.14	5084	5.5%
Tersang	Count Numeric : core	2046 Mean : core	0.09	193	0.2%
Tersang	Count Numeric : edges pyrite	1728 Mean : edges pyrite	2.02	3486	3.8%
Tersang	Count Numeric : main pyrite high Au	15360 Mean : main pyrite high Au	3.79	58208	63.4%
Tersang	Count Numeric : Main Low Au	16330 Mean : Main Low Au	0.14	2227	2.4%
Tersang	Count Numeric : high As high Au	939 Mean : high As high Au	15.32	14382	15.7%
Tersang	Count Numeric : high As low Au	1448 Mean : high As low Au	0.32	460	0.5%
Tersang	Count Numeric : outer rim	2933 Mean : outer rim	2.60	7624	8.3%
	all	28350	5.74	162729	100.0%
Selinsing	Py1 : Count Numeric	2 Pyrite 1	0.25	0.5	0.0%
Selinsing	Py2 : Count Numeric	3 Pyrite 2	0.47	1.41	0.0%
Selinsing	Py3 : Count Numeric	415 Pyrite 3	41.2	17098	10.5%
Selinsing	Py4 : Count Numeric	4075 Pyrite 4	0.53	2159.75	1.3%
Selinsing	Py5 : Count Numeric	5827 Pyrite 5	0.36	2097.72	1.3%
Selinsing	Py6 : Count Numeric	15616 Pyrite 6	7.62	118993.9	73.1%
Selinsing	Py7 : Count Numeric	2412 Pyrite 7	0.82	1977.84	1.2%

Appendix C

LA ICP-MS data

Trace element analysis in pyrite at Tersang

77575 rows - Univariate	As_ppm	Co_ppm	Ni_ppm	Cu_ppm	Zn_ppm	Se_ppm	Mo_ppm	Ag_ppm	Sb_ppm	Te_ppm
[Visible] : Count Numeric	38011.00	38011.00	38011.00	38011.00	38011.00	38011.00	38011.00	38011.00	38011.00	38011.00
[Visible] : Mean	9896.98	66.51	93.54	69.77	7.40	34.54	0.03	1.33	80.17	0.35
Core of pyrite 2 : Count Numeric	1888.00	1888.00	1888.00	1888.00	1888.00	1888.00	1888.00	1888.00	1888.00	1888.00
Core of pyrite 2 : Mean	647.69	1.95	3.29	520.57	4.11	49.27	0.15	0.22	48.10	1.00
edges pyrite : Count Numeric	1681.00	1681.00	1681.00	1681.00	1681.00	1681.00	1681.00	1681.00	1681.00	1681.00
edges pyrite : Mean	26077.41	5.72	7.03	422.98	18.05	40.46	0.09	7.28	201.31	0.62
Py1 : Count Numeric	17347.00	17347.00	17347.00	17347.00	17347.00	17347.00	17347.00	17347.00	17347.00	17347.00
edges pyrite : Mean	26077.41	5.72	7.03	422.98	18.05	40.46	0.09	7.28	201.31	0.62
Py1 : Mean	8496.14	93.19	148.50	21.71	10.04	19.29	0.03	1.64	35.09	0.26
Py2 : Count Numeric	14851.00	14851.00	14851.00	14851.00	14851.00	14851.00	14851.00	14851.00	14851.00	14851.00
Py2 : Mean	3594.38	57.93	61.01	16.14	3.41	20.87	0.01	0.06	14.89	0.28
Py2 : Median	3284.04	3.59	16.00	2.45	1.12	11.67	0.01	0.01	0.24	0.02
Py3 : Count Numeric	915.00	915.00	915.00	915.00	915.00	915.00	915.00	915.00	915.00	915.00
Py3 : Mean	93838.65	4.02	4.92	240.29	12.52	447.36	0.14	8.89	1597.83	0.58
Py4 : Count Numeric	1315.00	1315.00	1315.00	1315.00	1315.00	1315.00	1315.00	1315.00	1315.00	1315.00
Py4 : Mean	33847.26	25.94	38.81	92.54	5.22	74.52	0.02	0.24	247.49	0.82

Trace element analysis in pyrite at Tersang

77575 rows - Univariate	Au_ppm	Tl_ppm	Pb_ppm	Bi_ppm	Na_ppm	Mg_ppm	Al_ppm	Si_ppm	K_ppm	Ca_ppm	Ti_ppm
[Visible] : Count Numeric	38011.00	38011.00	38011.00	38011.00	38011.00	38011.00	38011.00	38011.00	38011.00	38011.00	38011.00
[Visible] : Mean	2.09	2.32	22.49	0.97	0.01	112.55	2122.21	2938.54	1099.96	1085.65	884.02
Core of pyrite 2 : Count Numeric	1888.00	1888.00	1888.00	1888.00	1888.00	1888.00	1888.00	1888.00	1888.00	1888.00	1888.00
Core of pyrite 2 : Mean	0.10	1.60	218.64	4.05	0.01	74.22	1422.14	4032.34	773.05	559.94	154.10
edges pyrite : Count Numeric	1681.00	1681.00	1681.00	1681.00	1681.00	1681.00	1681.00	1681.00	1681.00	1681.00	1681.00
edges pyrite : Mean	2.01	6.59	31.39	2.27	0.01	1005.42	20112.79	29065.74	10412.72	1218.14	1619.17
Py1 : Count Numeric	17347.00	17347.00	17347.00	17347.00	17347.00	17347.00	17347.00	17347.00	17347.00	17347.00	17347.00
edges pyrite : Mean	2.01	6.59	31.39	2.27	0.01	1005.42	20112.79	29065.74	10412.72	1218.14	1619.17
Py1 : Mean	3.42	0.57	13.86	1.10	0.01	66.90	1211.75	1480.09	685.83	1241.66	1268.33
Py2 : Count Numeric	14851.00	14851.00	14851.00	14851.00	14851.00	14851.00	14851.00	14851.00	14851.00	14851.00	14851.00
Py2 : Mean	0.12	0.38	6.86	0.37	0.01	32.25	574.03	1062.40	270.89	961.75	523.36
Py3 : Count Numeric	915.00	915.00	915.00	915.00	915.00	915.00	915.00	915.00	915.00	915.00	915.00
Py3 : Mean	15.55	55.53	29.89	0.34	0.01	240.65	4465.01	3628.05	1996.36	611.32	260.20
Py4 : Count Numeric	1315.00	1315.00	1315.00	1315.00	1315.00	1315.00	1315.00	1315.00	1315.00	1315.00	1315.00
Py4 : Mean	0.30	5.86	14.84	0.26	0.01	428.65	7619.18	7235.09	3665.01	1351.52	430.25

Trace element analysis in pyrite at Tersang

77575 rows - Univariate	V_ppm	Mn_ppm	Fe_ppm	W_ppm	Pt_ppm	Hg_ppm	U_ppm
[Visible] : Count Numeric	38011.00	38011.00	38011.00	38011	38011	38011	38011
[Visible] : Mean	3.74	7.80	437453.10	5.79	0.03	0.01	6.03
Core of pyrite 2 : Count Numeric	1888.00	1888.00	1888.00	1888.00	1888.00	1888.00	1888.00
Core of pyrite 2 : Mean	2.28	2.03	428010.45	1.41	0.02	0.01	0.69
edges pyrite : Count Numeric	1681.00	1681.00	1681.00	1681.00	1681.00	1681.00	1681.00
edges pyrite : Mean	23.39	10.83	185811.33	14.22	0.05	0.01	31.17
Py1 : Count Numeric	17347.00	17347.00	17347.00	17347.00	17347.00	17347.00	17347.00
edges pyrite : Mean	23.39	10.83	185811.33	14.22	0.05	0.01	31.17
Py1 : Mean	3.36	5.05	450829.61	6.51	0.03	0.01	1.28
Py2 : Count Numeric	14851.00	14851.00	14851.00	14851.00	14851.00	14851.00	14851.00
Py2 : Mean	1.57	2.96	457571.41	4.86	0.03	0.01	10.23
Py2 : Median	0.01	1.02	457560.54	0.01	0.01	0.01	0.01
Py3 : Count Numeric	915.00	915.00	915.00	915.00	915.00	915.00	915.00
Py3 : Mean	6.19	139.51	398461.52	2.15	0.06	0.01	0.67
Py4 : Count Numeric	1315.00	1315.00	1315.00	1315.00	1315.00	1315.00	1315.00
Py4 : Mean	8.46	11.67	400531.29	4.94	0.08	0.01	0.58

Trace element analysis in pyrite at Selinsing

35643 rows - Univariate	Na_ppm	Mg_ppm	Al_ppm	Si_ppm	K_ppm	Ca_ppm	Ti_ppm	V_ppm	Cr_ppm	Mn_ppm	Fe_ppm
[Visible] : Count Numeric	35636.00	35642.00	35642.00	35636.00	35636.00	35636.00	35642.00	35642.00	35636.00	35642.00	35642.00
[Visible] : Mean	72.28	963.40	3760.72	4338.53	936.69	468.96	930.61	3.08	11.46	60.13	456738.05
Py1 : Count Numeric	0.00	3.00	3.00	0.00	0.00	0.00	3.00	3.00	0.00	3.00	3.00
Py1 : Mean	0.00	4573.53	6188.58	0.00	0.00	0.00	4431.34	8.43	0.00	440.89	465000.00
Py2 : Count Numeric	0.00	3.00	3.00	0.00	0.00	0.00	3.00	3.00	0.00	3.00	3.00
Py2 : Mean	0.00	2339.82	8540.22	0.00	0.00	0.00	2246.93	12.43	0.00	701.74	465000.00
py3 : Count Numeric	415.00	415.00	415.00	415.00	415.00	415.00	415.00	415.00	415.00	415.00	415.00
py3 : Mean	0.01	0.32	2.61	467.31	9.79	1403.75	0.01	0.01	10.80	2.62	453404.90
py4 : Count Numeric	4075.00	4075.00	4075.00	4075.00	4075.00	4075.00	4075.00	4075.00	4075.00	4075.00	4075.00
py4 : Mean	198.71	923.84	3056.35	4814.03	1037.40	364.67	809.86	3.10	9.77	139.82	453397.05
py5 : Count Numeric	5827.00	5827.00	5827.00	5827.00	5827.00	5827.00	5827.00	5827.00	5827.00	5827.00	5827.00
py5 : Mean	43.38	428.07	1908.25	2738.47	584.94	248.90	686.12	1.65	9.27	34.54	466476.34
py6 : Count Numeric	15616.00	15616.00	15616.00	15616.00	15616.00	15616.00	15616.00	15616.00	15616.00	15616.00	15616.00
py6 : Mean	95.66	1534.28	5651.94	6113.17	1169.87	634.97	959.15	4.67	15.03	83.52	461415.63
py7 : Count Numeric	2412.00	2412.00	2412.00	2412.00	2412.00	2412.00	2412.00	2412.00	2412.00	2412.00	2412.00
py7 : Mean	8.00	393.47	3879.60	4106.87	1327.87	193.77	617.87	1.60	11.23	14.31	451151.16

Trace element analysis in pyrite at Selinsing

35643 rows - Univariate	Co_ppm	Ni_ppm	Cu_ppm	Zn_ppm	As_ppm	Se_ppm	Mo_ppm	Ag_ppm	Sb_ppm	Te_ppm	W_ppm
[Visible] : Count Numeric	35642.00	35642.00	35642.00	35642.00	35642.00	35637.00	35642.00	35642.00	35642.00	35639.00	35640.00
[Visible] : Mean	118.03	176.52	85.91	538.64	4901.75	14.66	0.10	2.15	20.69	4.65	2.30
Py1 : Count Numeric	3.00	3.00	3.00	3.00	3.00	1.00	3.00	3.00	3.00	2.00	2.00
Py1 : Mean	311.46	204.61	382.24	95.84	202.25	10.37	1.18	7.64	55.55	3.04	4.18
Py2 : Count Numeric	3.00	3.00	3.00	3.00	3.00	0.00	3.00	3.00	3.00	1.00	2.00
Py2 : Mean	522.92	193.17	352.02	191.94	267.28	0.00	3.71	2.74	34.50	1.80	3.04
py3 : Count Numeric	415.00	415.00	415.00	415.00	415.00	415.00	415.00	415.00	415.00	415.00	415.00
py3 : Mean	906.82	2351.97	6.39	0.27	22101.42	11.46	0.01	0.12	0.25	0.50	0.01
py4 : Count Numeric	4075.00	4075.00	4075.00	4075.00	4075.00	4075.00	4075.00	4075.00	4075.00	4075.00	4075.00
py4 : Mean	86.03	171.18	27.36	1063.02	2524.22	2.04	0.11	2.27	15.87	2.41	2.09
py5 : Count Numeric	5827.00	5827.00	5827.00	5827.00	5827.00	5827.00	5827.00	5827.00	5827.00	5827.00	5827.00
py5 : Mean	63.98	108.08	13.93	183.89	3187.98	4.70	0.06	2.55	8.97	2.62	1.95
py6 : Count Numeric	15616.00	15616.00	15616.00	15616.00	15616.00	15616.00	15616.00	15616.00	15616.00	15616.00	15616.00
py6 : Mean	92.18	88.03	21.87	148.04	6927.98	21.40	0.04	2.15	32.98	7.08	3.12
py7 : Count Numeric	2412.00	2412.00	2412.00	2412.00	2412.00	2412.00	2412.00	2412.00	2412.00	2412.00	2412.00
py7 : Mean	422.20	418.31	40.60	14.16	626.79	18.27	0.80	5.94	29.34	11.58	1.98

Trace element analysis in pyrite at Selinsing

35643 rows - Univariate	Pt_ppm	Au_ppm	Hg_ppm	Tl_ppm	Pb_ppm	Bi_ppm	U_ppm
[Visible] : Count Numeric	35636.00	35641.00	35636.00	35642.00	35642.00	35642.00	35641.00
[Visible] : Mean	0.02	4.06	0.01	0.10	169.15	34.52	1.29
Py1 : Count Numeric	0.00	2.00	0.00	3.00	3.00	3.00	2.00
Py1 : Mean	0.00	0.25	0.00	1.41	448.76	9.67	7.95
Py2 : Count Numeric	0.00	3.00	0.00	3.00	3.00	3.00	3.00
Py2 : Mean	0.00	0.47	0.00	0.92	337.40	4.66	10.55
py3 : Count Numeric	415.00	415.00	415.00	415.00	415.00	415.00	415.00
py3 : Mean	0.03	41.21	0.01	0.01	3.36	1.32	0.01
py4 : Count Numeric	4075.00	4075.00	4075.00	4075.00	4075.00	4075.00	4075.00
py4 : Mean	0.01	0.54	0.01	0.08	155.18	26.14	1.29
py5 : Count Numeric	5827.00	5827.00	5827.00	5827.00	5827.00	5827.00	5827.00
py5 : Mean	0.01	0.36	0.01	0.04	186.54	20.39	0.85
py6 : Count Numeric	15616.00	15616.00	15616.00	15616.00	15616.00	15616.00	15616.00
py6 : Mean	0.02	7.62	0.01	0.16	214.25	54.72	1.86
py7 : Count Numeric	2412.00	2412.00	2412.00	2412.00	2412.00	2412.00	2412.00
py7 : Mean	0.01	0.83	0.01	0.11	322.73	54.92	0.98

Appendix B

X-ray fluorescence (XRF) data

Penjom and Tersang deposits, Malaysia

Charles
13/12/2010

XRF ANALYSIS **CODES-SES, University of Tasmania**
Analyst: Phil Robinson
XRF sample preparation: Katie McGoldrick
Samples ground in tungsten carbide mill by Michelle Makoundi

Sample ID	Major elements in wt % and trace elements in ppm											(S- is sulphide sulphur)		
	SiO2	TiO2	Al2O3	Fe2O3	MnO	MgO	CaO	Na2O	K2O	P2O5	As2O3	Loss inc.S-	Total	Total S
PEN-R04	81.01	0.04	9.77	0.42	0.06	0.15	2.00	1.19	2.25	0.01	0.00	2.86	99.76	0.09
PEN-R14	74.71	0.05	12.54	0.63	0.09	0.25	2.47	5.09	1.14	0.01	0.07	2.99	100.04	0.06
PEN-S1	56.13	0.94	11.49	4.72	0.08	6.57	5.96	3.70	0.06	0.38	0.01	9.51	99.54	0.31
PEN-S2	76.93	0.04	14.16	0.52	0.02	0.26	0.28	3.89	2.15	0.01	0.05	1.60	99.90	0.08
TER-R007	64.01	0.67	17.00	4.92	0.00	1.17	0.02	<0.03	5.49	0.02	1.45	5.49	100.24	2.94
TER-R010	78.76	0.01	13.99	0.60	0.00	0.23	<0.01	0.07	4.13	0.01	0.03	2.08	99.91	<0.01
TER-R028	74.73	0.37	14.84	2.56	0.00	0.30	<0.01	0.15	4.12	0.04	0.08	2.56	99.75	<0.01
TER-R033	77.46	0.01	13.20	2.72	0.01	0.18	<0.01	0.17	3.69	0.01	0.35	2.54	100.33	0.02
	Sc	V	Cr	Ni	Cu	Zn	As	Rb	Sr	Y	Zr	Nb	Sn	Ba
PEN-R04	6	<3	2	2	3	8	5	241	85	11	33	19	10	96
PEN-R14	7	<3	3	2	3	14	504	179	280	15	42	27	11	51
PEN-S1	19	123	567	156	3	53	44	6	676	26	387	24	12	49
PEN-S2	5	2	2	1	1	15	367	335	194	15	44	43	17	209
TER-R007	16	119	47	9	31	10	9450	389	18	15	174	21	13	333
TER-R010	7	<3	2	1	2	6	217	264	13	68	70	13	20	220
TER-R028	11	61	17	3	18	21	565	212	67	24	129	3	2	282
TER-R033	9	<3	<1	4	29	9	2280	403	8	52	55	24	35	168
detection limit (ppm)	1.5	3	1	1	1	1	3	1	1	1	1	0.5	2	4
PEN-R04	La	Ce	Nd	Pb	Bi	Th	U							
PEN-R14	5	8	4	13	4	12	26							
PEN-S1	5	13	6	123	5	14	32							
PEN-S2	33	81	47	12	<2	55	15							
TER-R007	7	13	5	245	4	21	43							
TER-R010	22	0	26	52	<2	10	8							
TER-R028	18	46	28	64	4	22	4							
TER-R033	17	36	19	20	<2	10	8							
detection limit (ppm)	105	244	131	96	37	12	8							
	2	4	2	1.5	2	1.5	1.5							

Appendix A

Rock catalogue

Rock Catalogue

Utas#	Field Number	Rock Name	Northing	Easting	Drill Hole	Depth (m)	Location
174253	TER-R007	Sandstone	440918	812851			Tersang, Malaysia
174254	TER-R033	Rhyolite	441160	812858			Tersang, Malaysia
174255	TER-R032	Breccia	441210	812782			Tersang, Malaysia
174256	TER-R029	Quartz	441071	812689			Tersang, Malaysia
174257	TER-R027	Quartz	440898	812894			Tersang, Malaysia
174258	TER-R035	Quartz	441120	812826			Tersang, Malaysia
174259	TER-R042	Quartz	440885	812935			Tersang, Malaysia
174260	TER-R008	Quartz	440890	812719			Tersang, Malaysia
174261	TER-R030	Quartz	441009	812753			Tersang, Malaysia
174262	TER-R041	Quartz	440875	812925			Tersang, Malaysia
174263	TER-R025	Quartz	440930	812881			Tersang, Malaysia
174264	TER-R039	Quartz	440904	812928			Tersang, Malaysia
174265	TER-R022	Quartz	440918	812889			Tersang, Malaysia
174266	TER-R009	Quartz	440890	812719			Tersang, Malaysia
174267	SR12	Phyllite	470103	421456			Selinsing, Malaysia
174268	SR12B	Phyllite	470103	421456			Selinsing, Malaysia
174269	SEL-R032	Breccia	470060	421670	SEL-DD002	89.9	Selinsing, Malaysia
174270	SEL-R008	Mylonite	470050	421700	SEL-DD001	32.4	Selinsing, Malaysia
174271	SEL-R009	Mudstone	470050	421700	SEL-DD001	35.3	Selinsing, Malaysia
174272	SR61	Limestone	470147	420851			Selinsing, Malaysia
174273	SR60	Limestone	422174	469525			Selinsing, Malaysia
174274	SELDD1-102m	Siltstone	470050	421700			Selinsing, Malaysia
174275	SM09-07	Phyllite	469896	421440			Selinsing, Malaysia
174276	SEL-R091	Breccia	470041	421611	SEL-DD008	156	Selinsing, Malaysia
174277	SEL-R038	Siltstone	470060	421720	SEL-DD003	39.9	Selinsing, Malaysia
174278	SEL-R019	Mylonite	470050	421700	SEL-DD001	98.5	Selinsing, Malaysia
174279	SEL-R026	Siltstone	470050	421700	SEL-DD001	98.1	Selinsing, Malaysia
174280	SEL-R012	Mylonite	470050	421700	SEL-DD001	52.3	Selinsing, Malaysia
174281	SEL-R027	Breccia	470060	421670	SEL-DD002	60	Selinsing, Malaysia
174282	SEL-R047	Breccia	470060	421720	SEL-DD003	121.3	Selinsing, Malaysia
174283	SEL-R036	Siltstone	470060	421720	SEL-DD003	31.9	Selinsing, Malaysia
174284	SEL-R039	Siltstone	470060	421720	SEL-DD003	42.4	Selinsing, Malaysia
174285	SEL-R094	Phyllite	470044	421613	SEL-DD009	30	Selinsing, Malaysia
174286	SEL-R001	Quartz	470050	421700	SEL-DD001	7.8	Selinsing, Malaysia
174287	SEL-R054	Phyllite	470350	421680	SEL-DD004	58.1	Selinsing, Malaysia
174288	SEL-R025	Breccia	470060	421670	SEL-DD002	51.1	Selinsing, Malaysia

Rock Catalogue

Utas#	Field Number	Rock Name	Northing	Easting	Drill Hole	Depth (m)	Location
174289	SEL-R042	Quartz	470060	421720	SEL-DD003	85.6	Selinsing, Malaysia
174290	SEL-R024	Quartz	470060	421670	SEL-DD002	41	Selinsing, Malaysia
174291	SEL-R055	Phyllite	470350	421680	SEL-DD004	60.7	Selinsing, Malaysia
174292	SEL-R006	Siltstone	470050	421700	SEL-DD001	23	Selinsing, Malaysia
174293	PEN-S3	Siltstone	458141	443546			Penjom, Malaysia
174294	PEN-S5	Siltstone	458141	443546			Penjom, Malaysia
174295	PEN-R04	Trachyte	458137	443572			Penjom, Malaysia
174296	PEN-R009	Shale	458248	443595			Penjom, Malaysia
174297	PEN-R12	Trachyte	457671	443424			Penjom, Malaysia
174298	PEN-S2	Trachyte	458092	443558			Penjom, Malaysia
174299	PEN-S1	Trachyte	457653	443496			Penjom, Malaysia
174300	PEN-R16	Quartz	457653	443496			Penjom, Malaysia